Search for heavy charged diboson resonances in events with light leptons (e, μ) and τ leptons with 2016 CMS data

Von der Fakultät für Mathematik, Informatik und Naturwissenschaften der RWTH Aachen University zur Erlangung des akademischen Grades eines Doktors der Naturwissenschaften genehmigte Dissertation

vorgelegt von

Thomas Esch, M. Sc. RWTH

aus Troisdorf

Berichter:
Univ.-Prof. Dr. rer. nat. Thomas Hebbeker
Priv.-Doz. Dr. rer. nat. Oliver Pooth

Tag der mündlichen Prüfung: 22.01.2019

Abstract

This thesis presents a search for narrow heavy charged resonances $V^{\pm}$ with spin-1 and masses between 0.6 and 4.0 TeV decaying to a W boson and a Standard Model Higgs (h) or Z boson. The analysis considers $W \to \ell\nu$ and $Z/h \to \tau\tau$ decay channels with fully hadronic and semileptonic $\tau\tau$ decays. It is based on the full 2016 dataset from proton-proton collisions with a center-of-mass energy of $\sqrt{s} = 13$ TeV collected by the CMS experiment, corresponding to an intergrated luminosity of 35.9 fb^{-1}. The resonance masses exceed the TeV scale and thus, special techniques for the reconstruction of boosted bosons decaying to adjacent tau lepton pairs are applied to obtain a high signal selection efficiency. No deviation between data and Standard Model background is found. Therefore, upper limits on the cross section times branching fractions $\sigma \times B(V \to Wh)$ and $\sigma \times B(V \to WZ)$ are set with 95 % confidence level. An interpretation of these limits is done in context of the Heavy Vector Triplet (HVT) model, resulting in mass limits of $M_V > 1.7$ TeV for a weakly coupling extended gauge symmetry and $M_V > 1.9$ TeV for a strongly coupling composite Higgs model. The cross section limits are finally reinterpreted in terms of the coupling parameters $g_V c_h$ and $g^2 c_F / g_V$ depending on the resonance mass in the HVT model.

Zusammenfassung

Diese Dissertation präsentiert eine Suche nach schmalen, schweren und geladenen Resonanzen $V^{\pm}$ mit Spin-1 und Massen zwischen 0.6 und 4.0 TeV, die in ein W-Boson und in ein Standardmodell Higgs- (h) oder Z-Boson zerfallen. The Analyse betrachtet die Zerfallskanäle $W \to \ell\nu$ und $Z/h \to \tau\tau$ mit vollhadronischen und semileptonischen $\tau\tau$ Zerfällen. Sie basiert auf dem vollen Datensatz von Proton-Proton-Kollisionen bei einer Schwerpunktsenergie von $\sqrt{s} = 13$ TeV, der 2016 vom CMS Experiment gesammelt wurde und entspricht einer integrierten Luminosität von 35.9 fb^{-1}. Die Resonanzmassen übersteigen die TeV Skala, weshalb spezielle Techniken zur Rekonstruktion von geboosteten Bosonen, die in nahe beieinanderliegende Tau-Leptonpaare zerfallen, angewendet werden, um eine hohe Selektionseffiezienz des Signals zu erhalten. Es wurde keine Abweichung zwischen den Daten und dem Standardmodelluntergrund gefunden. Deshalb werden obere Grenzwerte auf den Wirkungsquerschnitt multipliziert mit den Verzweigungsverhältnissen $\sigma \times B(V \to Wh)$ und $\sigma \times B(V \to WZ)$ mit einem Konfidenzniveau von 95 % gesetzt. Die Grenzwerte werden im Kontext des Heavy Vector Triplett (HVT) Modells interpretiert und resultieren in Massengrenzwerte von $M_V > 1.7$ TeV für ein schwach koppelndes erweitertes Eichsymmetrie Modell und $M_V > 1.9$ TeV für ein stark koppelndes composite Higgs (Higgs mit Substruktur) Modell. Am Ende werden die Grenzwerte auf den Wirkungsquerschnitt bezüglich der Kopplungsparamter $g_V c_h$ und $g^2 c_F / g_V$ in Abhängigkeit von der Resonanzmasse im HVT Modell reinterpretiert.

Table of Contents

1. Introduction **1**

2. Theoretical Foundation **3**
2.1. The Standard Model of Particle Physics . . . 3
2.2. Physics Beyond the Standard Model . . . 7
2.3. The Heavy Vector Triplet Model . . . 8
2.3.1. Phenomenological Description . . . 8
2.3.2. Production and Decay . . . 11
2.3.3. Characteristics of Model A and B . . . 15
2.3.4. Existing Limits . . . 18

3. Experimental Setup **21**
3.1. The Large Hadron Collider . . . 21
3.2. The Compact Muon Solenoid . . . 23
3.2.1. Inner Tracker . . . 24
3.2.2. Calorimeters . . . 25
3.2.3. Solenoid Magnet . . . 26
3.2.4. Muon System . . . 27
3.2.5. Trigger and Data Acquisition . . . 31
3.2.6. Computing and Analysis Framework . . . 32

4. Signal Properties **33**

5. Object Reconstruction and Identification **43**
5.1. Particle-Flow Algorithm . . . 43
5.2. Electrons . . . 44
5.2.1. Reconstruction . . . 44
5.2.2. Identification . . . 45
5.3. Muons . . . 46
5.3.1. Reconstruction . . . 46
5.3.2. Identification . . . 48
5.4. Hadronic Tau Leptons . . . 50
5.4.1. Properties of the Tau Lepton . . . 50
5.4.2. Separated Tau Leptons . . . 51
5.4.3. Nearby Tau Leptons . . . 54
5.5. Correction of the Electron and Muon Isolation . . . 60
5.6. Jets and B-Tagging . . . 63
5.7. Missing Transverse Energy . . . 65

6. Analysis **67**
6.1. The 2016 CMS Dataset . . . 67
6.2. Monte-Carlo Simulation . . . 67
6.2.1. Parton Distribution Functions . . . 68
6.2.2. Background Processes . . . 69

6.2.3. Signal Samples . . . 73
6.3. Event Selection . . . 73
6.3.1. Categorisation of the Channels . . . 75
6.3.2. Trigger Requirement . . . 75
6.3.3. Event Filters for E_T^{miss} . . . 79
6.3.4. Preselection . . . 79
6.3.5. Kinematic Selection . . . 82
6.3.6. Signal Efficiencies . . . 87
6.4. Standard Model Background Estimation . . . 89
6.4.1. V+Jets and $t\bar{t}$ Control Regions . . . 89
6.4.2. Corrections to the SM Background . . . 90
6.4.3. Backgrounds from Tau Misidentification . . . 95
6.5. Systematic Uncertainties . . . 101
6.6. Final Distributions . . . 106

7. Statistical Interpretation **113**
7.1. Bayesian Statistics . . . 113
7.2. Maximum Likelihood Fit, Uncertainty Impacts and Significances . . . 114
7.3. Exclusion Limits . . . 124
7.3.1. Cross Section Limits . . . 124
7.3.2. Limits on the Model Parameters . . . 130

8. Conclusion **133**

A. Derivation of Formula $\Delta R \approx 2\,M_V/p_T^V$ **135**

B. Dataset and Background Samples **137**
B.1. The 2016 CMS Datasets . . . 137
B.2. Background Samples and Cross Sections . . . 138

C. Supplementary Tables and Figures **141**
C.1. Candidate Event List . . . 141
C.2. Missing E_T triggers . . . 144
C.3. Data/MC Control Distributions . . . 145
C.4. Data Driven Control Distributions . . . 151
C.5. Cross Section Limits . . . 152

Bibliography **155**

Acknowledgements **165**

CHAPTER 1

Introduction

The Standard Model of Particle Physics (SM) was tested and proven to describe the electromagnetic, weak, and strong interaction with high precision [1]. However, some observations, for example of the Higgs mass and the resulting so called hierarchy problem, indicate new physics beyond the TeV scale that is not yet included in the SM. Many models postulate new so called Beyond the Standard Model (BSM) physics, predicting for example the production of additional heavy resonances [2]. Depending on the model, these resonances may have varying characteristics, e.g. the decay widths of processes or the production cross section, as well as the underlying interaction, resulting in a large number of interesting final states. Some of these models predict the decay of heavy resonances to two bosons. Due to the large resonance masses (> 1 TeV), these bosons can be highly boosted and therefore, the decay products can be collimated. In the past few years, a great progress in the reconstruction of nearby objects was achieved by the experiments CMS [3] and ATLAS [4], including the possibility to tag single b-jets who itself lie within a large cone size jet. In addition to that, the CMS experiment was able to develop an algorithm that allows to identify and select hadronic tau leptons arising from boosted boson decays. This is especially complicated because of the large number of possible tau decay modes and their overlapping constituents. With the development of these methods, the sensitivity for resonance decays to two bosons was highly increased, allowing to analyse many of the possible final states.

In this thesis, a heavy charged resonance decaying to two Standard Model bosons via $V^{\pm} \rightarrow WV$ (V = Z, h) is considered. Here, h denotes the SM Higgs boson with a mass of 125 GeV and W and Z are the SM gauge bosons. The bosons are assumed to subsequently decay via $W \rightarrow \ell\nu$ and $Z/h \rightarrow \tau\tau$, resulting in final states with one lepton ℓ, two tau decay products - hadronic τ_h and leptonic τ_ℓ - and missing transverse energy (E_T^{miss}) from neutrinos leaving the experiment undetected. It is the first search for charged resonances in this specific decay channel at the TeV scale. However, searches for these resonances have been performed in many other channels by the CMS and ATLAS experiments, namely the two fermion decays $\ell\nu$ (ℓ = e, μ, τ) [5–8] and qq [9–13], the WZ final states qqqq [14,15], $\ell\nu$qq [16, 17], $\ell\ell$qq [18, 19], $\ell\nu\ell\ell$ [20] and qq$\nu\nu$ [19, 21], and the Wh final states qqbb [22, 23], $\ell\nu$bb [24, 25], and qq$\tau\tau$ [26]. Two fermion (difermion) decays are more sensitive to weakly interacting models, e.g. extended gauge symmetry models while two boson (diboson) decays dominate strongly interacting models, e.g. composite Higgs models. In context of these models, the term strongly interacting is not to be confound with the strong interaction QCD from the SM.
Typically, leptonic final states give better results at low masses because of the lower trigger threshold and the smaller SM background while hadronic final states are more sensitive at high masses where the full potential of their enhanced branching fraction can be used. The $\ell\tau\tau + E_T^{miss}$ final state analysed in this thesis is expected to provide a good discrimination against the background and thus good cross section limits for low resonance masses. In addition to that, the analysis works also as a cross check for the boosted boson to $\tau\tau$ reconstruction algorithm as only a few analyses utilize it. For 2016 data, only one other analysis, namely the qq$\tau\tau$ resonance search, is known to rely on this reconstruction method. The analysis described in this thesis is based on the full 2016

dataset corresponding to an integrated luminosity of 35.9 fb^{-1} collected in proton-proton collisions at $\sqrt{s}$ = 13 TeV.

The thesis is split in several chapters. In Chap. 2, the theoretical foundation will be discussed, namely the SM, its shortcomings in the description and inclusion of some observations, and the discussion of the Heavy Vector Triplet (HVT) model [2] that is used as a benchmark model for the search. At the end of the chapter, existing limits in the HVT model will be discussed. Chap. 3 summarises the experimental setup, the parameters of the Large Hadron Collider (LHC) and the Compact Muon Solenoid (CMS) experiment and its subdetectors. Afterwards, the properties of the signal will be discussed, especially its effect on kinematic variables. This chapter is important for the following analysis, as the signal kinematics affect the reconstruction and identification of final state objects which is summarised in Chap. 5. Here, the selection of electrons, muons, and hadronic taus will be discussed, but also the impact of the nearby topology on their isolation variables. In Chap. 6, the whole analysis chain will be described, starting with the used dataset and background samples and followed by the event selection, background estimation and systematic uncertainties. Afterwards, a statistical interpretation will be performed in Chap. 7, including the discussion of the impact of systematic uncertainties and the observed significances before a limit on the cross section and HVT model parameters will be calculated. In the end, everything will be summarised in a final conclusion (Chap. 8).

CHAPTER 2

Theoretical Foundation

This thesis describes the analysis for a search for heavy charged resonances decaying to two bosons. However, before such an analysis can be performed, the theory behind it needs to be understood. The theoretical foundation depends on two main parts: The Standard Model of Particle Physics (SM) that characterizes the known particles and interactions and the new Beyond the Standard Model (BSM) theory that suggests possible solutions for observations that cannot be described within the SM. A thorough definition of both SM and BSM theory are necessary to characterize the expected background and its differences with respect to (w.r.t) changes due to the signature from the postulated new model. Since not all parts of the SM are important to understand the BSM theory and describing the whole SM would be out of the scope of this thesis, only a brief introduction will be given including the important aspects for the BSM theory, namely the particles and forces, the electroweak interaction, the Higgs mechanism, and some aspects of the strong interaction. The summary of the SM is mainly based on [1]. A detailed discussion of the other aspects of the SM can be found in [1, 27].

2.1. The Standard Model of Particle Physics

The SM is a very well tested and therefore successful theory used to describe the formation of matter based on observed particles and forces [1]. The particles in the SM can be split in two categories, namely the bosons with integer spin that are used as mediators to transmit certain forces and the fermions with spin-1/2. Three of the four known forces found in nature are characterized in the SM: The strong, weak, and electromagnetic interaction, meaning that only gravity is not yet included. Based on a relativistic local gauge theory (a quantum field theory), the SM is summarized by a $\mathrm{U}(1)_\mathrm{Y} \times \mathrm{SU}(2)_\mathrm{L} \times \mathrm{SU}(3)_\mathrm{C}$ symmetry group where $\mathrm{U}(1)_\mathrm{Y} \times \mathrm{SU}(2)_\mathrm{L}$ represents the combination of electromagnetic and weak interaction, named electroweak interaction, and $\mathrm{SU}(3)_\mathrm{C}$ stands for the strong interaction. A combined formalism for all three forces is yet to be achieved [1]. Each of the three forces has its own mediators: The massless photon (γ) is the mediator of the electromagnetic, the massive $\mathrm{W}^\pm/\mathrm{Z}^0$ bosons of the weak and massless gluons (g)[1] of the strong interaction. Particles only interact with each other using a certain force if they carry the corresponding quantum number. Electrically charged particles can interact electromagnetically, color charged particles via strong, and particles with weak-isospin via weak interaction. Due to this setup, the weak force can interact with all fermions in the SM while the strong force only interacts with so called quarks and the electromagnetic force with every particle except neutrinos. A summary of all particles of the SM and their properties can be found in Tab. 2.1.

In addition to the categorization of bosons and fermions, additional groups can be formed for fermions, namely leptons and quarks. Both groups can be split in three generations/families with

[1] There are 8 types of gluons with variating color charge combinations

		Type/Generation	Particle		Mass	Charge	Spin
Fermions	Leptons	I.	Electron	e	511 keV	-1/2	1/2
			Electron neutrino	ν_e	< 2 eV	0	1/2
		II.	Muon	μ	105.7 MeV	-1/2	1/2
			Muon neutrino	ν_μ	< 2 eV	0	1/2
		III.	Tau	τ	1.78 GeV	-1/2	1/2
			Tau neutrino	ν_τ	< 2 eV	0	1/2
	Quarks	I.	Up	u	2.2 MeV	2/3	1/2
			Down	d	4.7 MeV	-1/3	1/2
		II.	Charm	c	1.3 GeV	2/3	1/2
			Strange	s	96 MeV	-1/3	1/2
		III.	Top	t	173 GeV	2/3	1/2
			Bottom	b	4.7 GeV	-1/3	1/2
Bosons	Gauge	Electromagnetic	Photon	γ	0	0	1
		Weak	W bosons	W^+/W^-	80.4 GeV	1 / -1	1
			Z boson	Z^0	91.2 GeV	0	1
		Strong	8 Gluons	g	0	0	1
			Higgs	h	125 GeV	0	0

Table 2.1.: Summary of all the particles of the SM particles and their most important characteristics [28].

increasing masses, each of them containing two particles and their anti-particles with inverse characteristics. For leptons, each generation contains one charged lepton, named electron (e), muon (μ) and tau lepton (τ) and one neutral lepton, called neutrino (ν_e, ν_μ, ν_τ). Leptons carry a specific quantum number, the lepton number, which is conserved in particle decays. Due to the lack of color charges, charged leptons interact only via electromagnetic and weak force. Neutrinos do not carry any electric charge and can therefore only interact weakly.

Quarks have a different structure as leptons. Each generation contains one up-like quark and one down-like quark with electric charges of 2/3 and -1/3. Quarks carry a color charge and therefore, they can interact via strong interactions. As they also have an electric charge and weak isospin, all three interactions described in the SM are possible. In contrast to leptons, quarks and other color charged particles were only observed in bound states indicating that free states with non-zero color charges are not possible. This effect is named *color confinement* and believed to arise from the self-coupling of gluons [1]. Color confinement leads to a direct consequence for the observation of quarks at colliders as they can only be reconstructed as so called jets. Jets arise from the strong interaction between the quarks within an event. The energy of the strong interaction between several color charged particles is large enough to produce additional quarks and gluons resulting in particle avalanches in the flight directions of the initial quarks. This effect is called hadronisation. In the end, the jets have a neutral color charge. However, their initial quark flavour can still be reconstructed as it affects the shape and the origin of the jet. This is important to distinguish jets arising from light and heavy quarks.

As described above, the electromagnetic and weak force have been unified in one formalism based on a $U(1)_Y \times SU(2)_L$ gauge group, called electroweak interaction. This unification is a consequence of observations of Z bosons interacting with right-handed fermions which should not be possible according to the weak interaction [1]. Since electromagnetic currents couple to left- and right-handed particles, the combination of these two forces is used as an explanation for this observation. Neutral

currents arise then as a combination of the left-handed weak current and the right-handed electromagnetic current. In the electroweak unification, the electric charge Q is related to the third component of the weak-isospin I_3 and the hypercharge Y via the Gell-Mann-Nishijima formula [27]

$$Q = I_3 + \frac{Y}{2}. \tag{2.1}$$

Four bosons are predicted in the $U(1)_Y \times SU(2)_L$ gauge group, namely W^1_μ, W^2_μ, W^3_μ, and B_μ. The experimentally observed bosons, the W bosons $W^\pm_\mu$, the Z boson Z_μ, and the photon Z_μ can then be described as combinations of the two charged bosons W^1_μ, W^2_μ and the neutral bosons W^3_μ, and B_μ:

$$\begin{aligned} W^\pm_\mu &= \frac{1}{\sqrt{2}}\left(W^1_\mu \mp iW^2_\mu\right) \\ A_\mu &= B_\mu \cos\theta_W + W^3_\mu \sin\theta_W \\ Z_\mu &= -B_\mu \cos\theta_W + W^3_\mu \sin\theta_W \end{aligned} \tag{2.2}$$

where θ_W is the electroweak mixing angle or Weinberg angle that has been experimentally measured to be $\sin^2\theta_W = 0.2315 \pm 0.0001$. The couplings of the interactions are also related based on the Weinberg angle:

$$e = g_W \sin\theta_W = g_Z \sin\theta_W \cos\theta_W \tag{2.3}$$

where e is the electron charge, and g_W and g_Z are the couplings to the W and Z bosons. Without additional corrections to the theory, all bosons are massless. However, observations have shown that the W bosons (80.4 GeV) and the Z boson (91.2 GeV) are massive particles. Due to their mass, the scattering process $W^+W^- \to W^+W^-$ would violate unitarity at high energies. This inconsistency is solved introducing the Higgs mechanism to the SM, resulting in a new heavy scalar particle adding destructively interfering contributions to the W^+W^- scattering process. In addition, it describes the generation of masses to SM bosons and charged fermions, but not of neutrinos. In the Higgs mechanism, two new complex scalar fields ϕ^+ (with $(\phi^+)^\dagger = \phi^-$) and ϕ^0 are added as an isospin doublet to the SM [1]:

$$\phi = \begin{pmatrix} \phi^+ \\ \phi^0 \end{pmatrix} = \frac{1}{\sqrt{2}} \begin{pmatrix} \phi_1 & + & i\phi_2 \\ \phi_3 & + & i\phi_4 \end{pmatrix} \tag{2.4}$$

These scalar fields add a new term to the SM Lagrangian, given by

$$\mathcal{L} = \left(\partial_\mu \phi\right)^\dagger \left(\partial^\mu \phi\right) - V(\phi) \tag{2.5}$$

where $V(\phi) = \mu^2 \phi^\dagger \phi + \lambda\left(\phi^\dagger \phi\right)$ is the so called Higgs potential. For $\mu^2 < 0$ and $\lambda > 0$, the Higgs potential has the form of a Mexican hat and its minima lie at the vacuum expectation value

$$\pm\nu = \pm\left|\sqrt{\frac{-\mu^2}{\lambda}}\right| = 246 \text{ GeV}. \tag{2.6}$$

This value also corresponds to the mass or energy scale of the electroweak interaction. The potential is gauge invariant, but it breaks the local gauge symmetry. If this spontaneous symmetry breaking is applied to the electroweak interaction, the masses of the W and Z boson can be explained. They are given by the formula

$$m_W = m_Z \cos\theta_W = \frac{1}{2} g_W \nu. \tag{2.7}$$

The Higgs mechanism can also be used to introduce fermion masses to the SM. Its corresponding application to SM fermions results in the Lagrangian

$$\mathcal{L} = -g_f \left[\bar{L}\phi R + \left(\bar{L}\phi R\right)^\dagger \right] \tag{2.8}$$

for each fermion, where g_f are the so called Yukawa couplings of the fermions to the Higgs field. In general, the coupling value is not predicted by the Higgs mechanism. However, to reproduce the fermion masses m_f in the SM, it is set to

$$g_f = \sqrt{2}\,\frac{m_f}{\nu}. \tag{2.9}$$

If the Higgs mechanism is simply applied to the fermions, it can only generate the masses of charged leptons and down-type quarks. For the inclusion of masses of up-type quarks, a second, conjugate doublet ϕ_c needs to be constructed, satisfying the condition

$$\phi_c = \begin{pmatrix} -\phi^{0*} \\ \phi^- \end{pmatrix} = \frac{1}{\sqrt{2}} \begin{pmatrix} -\phi_3 + i\phi_4 \\ \phi_1 - i\phi_2 \end{pmatrix}. \tag{2.10}$$

It transforms in the same way as ϕ, resulting in the Lagrangian

$$\mathcal{L} = g_f \left[\bar{L}\phi_c R + \left(\bar{L}\phi_c R\right)^\dagger \right] \tag{2.11}$$

which can be used to describe the generation of up-type quark masses. However, this mechanism does not include the description of neutrino masses, as right-handed neutrinos do not couple to SM bosons. A corresponding formalism for neutrino masses needs still to be achieved.

One consequence of the introduction of the complex scalar fields is that an additional massive scalar (spin-0) particle is expected in the SM. This particle, called Higgs boson, was found in Run-1 (2009-2012) of the Large Hadronic Collider [29] by the experiments CMS [3] and ATLAS [4] at a mass of about 125 GeV [30, 31]. Additional measurements have shown that it is consistent with expected characteristics of the SM Higgs boson, e.g. the spin or branching fractions to fermions and bosons.

2.2. Physics Beyond the Standard Model

Although the SM was measured and tested with high accuracy, it still has some shortcomings. On one hand, some cosmological observations indicate for example the existence of dark matter which is not yet included [1]. On the other hand, some measurements within the SM, e. g. the Higgs mass, are not compatible with other observations or known energy scales, like in the so called hierarchy problem. To solve these inconsistencies, additional theories need to be developed and tested, and, if they prove to describe a certain behaviour, to be implemented in the SM. These physics models are called Beyond the Standard Model (BSM) physics. Some inconsistencies that are addressed by BSM physics are:

- The so called hierarchy problem: The energy scale of the electroweak interaction $\mathcal{O}\left(10^2 \text{ GeV}\right)$ is much smaller than the Planck scale $\mathcal{O}\left(10^{19} \text{ GeV}\right)$. The energy of loop corrections of processes needs to be integrated up to the energy scale where the theory is still valid. The impact of these additional terms can be removed based on renormalization. However, in case of the Higgs boson which is a scalar particle, the added terms are squared, resulting in large energy corrections. Due to the relatively low mass of the Higgs boson w.r.t. the Planck scale, a specific fine tuning is needed to renormalize these terms. Typical models that address the hierarchy problem are SUSY and composite Higgs models [32, 33] that introduce energy corrections based on new particles at the TeV scale.

- The differences in the masses of the fermion families is not explained in the Higgs mechanism. In addition, the charged particles of the same generation have masses in the same order of magnitude, except for the much heavier top quark (factor 100). In contrast to that, the uncharged neutrinos are much lighter (factor up to 10^{-9}) [1]. The question arises why the Yukawa couplings generate this general structure with such a large top quark mass. On the other hand, it is not clear why the neutrinos masses are so much lighter. In context of the neutrino masses, an additional formalism describing how they are generated needs to be developed. Other questions address the observation of exactly three generations, and if the fermions are elementary particles or if they contain an underlying substructure [1].

- It is possible to unify the electromagnetic and the weak interaction via electroweak interaction in the SM. However, the inclusion of the strong interaction in a Grand Unified Theory was not successful yet. Additional particles at the TeV scale could change the coupling values of the interactions at high energies, resulting in a possible unification of all three couplings at a certain energy scale (estimated at 10^{15} – 10^{17} GeV). One theory addressing this question is Supersymmetry (SUSY) [1, 34].

- Measurements of cosmic energies have shown that additional particles and energies exist in the universe, namely dark matter and dark energy [1]. These are not included in the SM yet. Searches for dark matter at hadron colliders are typically performed in events where the dark matter candidate leaves the experiment undetected, resulting in an offset in the energy balance of the event, called missing transverse energy (E_T^{miss}).

As one can see from this list, several problems are addressed by SUSY. However, experimental searches have excluded SUSY in a large phase space which motivates an increased interest in alternative approaches. One of these theories is based on a substructure of the Higgs boson, called composite Higgs. This substructure could result in new resonances at the TeV scale, leading to energy corrections that could solve some of the inconsistencies. In this analysis, a search for heavy charged resonances decaying to two bosons will be performed. As a benchmark model, the Heavy

Vector Triplet model [2, 35] will be used which is a generalization of a large number of models containing heavy resonances, including composite Higgs models.

2.3. The Heavy Vector Triplet Model

Many models for BSM physics predict heavy spin-1 resonances decaying to SM particles. Although these models are based on different assumptions, they have much in common. The Heavy Vector Triplet (HVT) framework combines these models in one framework based on a simplified Lagrangian, using as few model parameters as possible [2]. This allows to reproduce the phenomenologies of a large number of models containing heavy vector triplets, for example weakly coupled (extended gauge symmetry) [36–40] and strongly coupled (composite Higgs) [32, 33, 41–45] scenarios which will be discussed in more detail later. As the HVT model is optimized for the search of resonances, it concentrates on the main parameters that are important for the characterisation of these resonances, controlling their masses and interactions with other particles.

2.3.1. Phenomenological Description

In the HVT model, a real vector V^a_μ (a = 1, 2, 3) with vanishing hypercharge is considered as a part of a $SU(2)_L$ group. The vector describes three heavy spin one particles, two charged and one neutral boson with charge eigenstates [2]

$$V^\pm_\mu = \frac{V^1_\mu \mp iV^2_\mu}{\sqrt{2}} \quad \text{and} \quad V^0_\mu = V^3_\mu. \tag{2.12}$$

The simplified Lagrangian that describes the dynamic of the new vector is given by

$$\begin{aligned}\mathscr{L}_V = &-\frac{1}{4}D_{[\mu}V^a_{\nu]}D^{[\mu}V^{\nu]a} + \frac{m_V^2}{2}V^a_\mu V^{\mu a} + ig_V c_H V^a_\mu H^\dagger \tau^a \overleftrightarrow{D}^\mu H + \frac{g^2}{g_V}c_F V^a_\mu J^{\mu a}_F \\ &+ \frac{g_V}{2}c_{VVV}\epsilon_{abc}V^a_\mu V^b_\nu D^{[\mu}V^{\mu]c} + g_V^2 c_{VVHH}V^a_\mu V^{\mu a}H^\dagger H - \frac{g}{2}c_{VVW}\epsilon_{abc}W^{\mu\nu a}V^b_\mu V^c_\nu.\end{aligned} \tag{2.13}$$

where $D_{[\mu}V^a_{\nu]} = D_\mu V^a_\nu - D_\nu V^a_\mu$ and $D_\mu V^a_\nu = \partial_\mu V^a_\nu + g\epsilon^{abc}W^b_\mu V^c_\nu$. The first two terms of Eq. 2.13 describe the kinetic energy and mass of the new bosons, as well as trilinear and quadrilinear interactions with the vector bosons from the SM, W^a_μ. In this context, the parameter g stands for the $SU(2)_L$ gauge coupling at the energy scale of the new bosons. As the new fields V^a_μ mix with the SM vector boson fields W^a_μ after electroweak symmetry breaking (EWSB), they are no mass eigenstates and the mass parameter m_V does not coincide with the physical mass of the new resonances [2].

The third and the fourth term are important for the interaction with SM particles as they control the vertices and couplings for these processes. The third term where $iH^\dagger\tau^a\overleftrightarrow{D}^\mu H = iH^\dagger\tau^a D^\mu H - iD^\mu H^\dagger\tau^a H$ represents the direct interaction of the vector with the Higgs currents, while the fourth term describes the interaction with the SM left-handed fermionic currents $J^{\mu a}_F = \sum_f \bar{f}_L\gamma^\mu\tau^a f_L$. In both equations $\tau^a = \sigma^a/2$, where σ^a are the Pauli matrices. In these two terms, three new parameters are introduced, namely g_V which denotes the coupling strengths of the new vector bosons, c_H which controls the interaction with SM vector bosons and the Higgs boson, and c_F which does the same for left-handed fermions. As g_V is present in both terms, it can be viewed as the general strength of

the interaction while the parameters c_H and c_F are important to model its preference for one of the possible decay modes. Since it is also possible that the parameters c_H and c_F depend on the coupling g_V, it can be helpful to combine these parameters and use $g_V c_H$ and $g^2 c_F/g_V$ instead of c_H and c_F in the final discussion of the results. While c_F is taken as an universal coupling in the Lagrangian, it can also be transferred to separated couplings for leptons, light quarks and third generation quarks:

$$c_F V \cdot J_F \rightarrow c_\ell V \cdot J_\ell + c_q V \cdot J_q + c_3 V \cdot J_3. \tag{2.14}$$

where c_ℓ, c_q, and c_3 control the coupling strengths to leptons, light quarks and third generation quarks while J_ℓ, J_q, and J_3 denote the corresponding left-handed currents. Although it is possible to split these couplings, this analysis will only use one universal parameter c_F for the fermion couplings.

The last three terms of the Lagrangian from Eq. 2.13 introduce three additional parameters, namely c_{VVV}, c_{VVHH}, and c_{VVW}. The corresponding terms do not contain vertices between the new vector V and light SM fields and therefore, they do not contribute to these decays and also not to the corresponding production process ($qq \rightarrow V$) as it will be discussed in Sec. 2.3.2. On the other hand, these terms contribute to the mixing between the new vector and the SM vector bosons. Since the effect of the mixing is typically small, their contribution is marginal and the last three terms can be approximately neglected. With this taken into account, the whole phenomenology of the model can be described by three terms, namely $g_V c_H$, $g^2 c_F/g_V$, and the mass term m_V.

Within the Lagrangian from Eq. 2.13, one invariant low-dimension operator is missing, namely

$$D_{[\mu} V^a_{\nu]} W^{\mu\nu a} \tag{2.15}$$

which describes the W-V kinetic mixing [2]. This operator is not included as it can be canceled using the field redefinitions [46]

$$\begin{cases} W^a_\mu \rightarrow W^a_\mu + \alpha V^a_\mu \\ V^a_\mu \rightarrow \beta V^a_\mu \end{cases} \tag{2.16}$$

where α and β are parameters that contain information about the couplings. To perform these field redefinitions, the parameters of the HVT model in the Lagrangian from Eq. 2.13 are replaced by the so called "tilded basis" according to

$$c \rightarrow \tilde{c} \tag{2.17}$$

and an additional kinetic mixing term is introduced, given by:

$$c_{\tilde{VW}} \frac{g}{2 g_V} D_{[\mu} V^a_{\nu]} W^{\mu\nu a}. \tag{2.18}$$

If the field redefinition from Eq. 2.16 is applied using the parameters

$$\alpha = \frac{g \tilde{c}_{VW}}{\sqrt{g_V^2 - \tilde{c}^2_{VW} g^2}} \quad \text{and} \quad \beta = \frac{g_V}{\sqrt{g_V^2 - \tilde{c}^2_{VW} g^2}} \tag{2.19}$$

the following transformations between the coupling parameters in the two bases are obtained [2]:

$$
\begin{aligned}
c_F &= \frac{g_V}{\sqrt{g_V^2 - \tilde{c}_{VW}^2 g^2}} \left[\tilde{c}_F + \tilde{c}_{VW}\right], \\
c_H &= \frac{g_V}{\sqrt{g_V^2 - \tilde{c}_{VW}^2 g^2}} \left[\tilde{c}_H + \frac{g^2}{g_V^2}\tilde{c}_{VW}\right], \\
c_{VVW} &= \frac{g_V^2}{g_V^2 - \tilde{c}_{VW}^2 g^2} \left[\tilde{c}_{VVW} - \frac{g^2}{g_V^2}\tilde{c}_{VW}^2\right], \\
c_{VVV} &= \frac{g_V^3}{\left(g_V^2 - \tilde{c}_{VW}^2 g^2\right)^{3/2}} \left[\tilde{c}_{VVV} - \frac{g^2}{g_V^2}\tilde{c}_{VW}\left(\tilde{c}_{VVW} + 2\right) + 2\frac{g^4}{g_V^4}\tilde{c}_{VW}^3\right], \\
c_{VVHH} &= \frac{g_V^2}{g_V^2 - \tilde{c}_{VW}^2 g^2} \left[\tilde{c}_{VVHH} + \frac{g^2}{2g_V^2}\tilde{c}_{VW}\tilde{c}_H + \frac{g^4}{4g_V^4}\tilde{c}_{VW}\right].
\end{aligned}
\tag{2.20}
$$

Two explicit models are interpreted in this thesis using the HVT model framework. The first one, called HVT model A, describes the phenomenology of weakly coupling resonances that extend the SM gauge group, as described in model [39]. The characteristics of these resonances are similar to SM gauge bosons with some additional decay modes due to the higher mass. For neutral resonances, these modes are the diboson decays WW and Zh and the diquark decay to $t\bar{t}$ while for charged resonances, decays to WZ, Wh and $t\bar{b}$ are added. The model parameters slightly differ from the often used Sequential Standard Model (SSM) where for example decays to dibosons are suppressed.

In the weakly coupled scenario, the parameters in the tilded basis are set to [2]

$$
\tilde{c}_{VW} = -\tilde{c}_{VVW} = \tilde{c}_{VVV} = -1 \quad \text{and} \quad \tilde{c}_H = \tilde{c}_F = \tilde{c}_{VVHH} = 0. \tag{2.21}
$$

According to the relations summarized in Eq. 2.20, the parameters c_F and c_H are then defined by

$$
c_F = -\frac{1}{\sqrt{1 - \frac{g^2}{g_V^2}}} \quad \text{and} \quad c_H = -\frac{1}{\sqrt{1 - \frac{g^2}{g_V^2}}}\frac{g^2}{g_V^2} = c_F\frac{g^2}{g_V^2} \tag{2.22}
$$

in this scenario, meaning that c_H is suppressed by a factor g^2/g_V^2 with respect to c_F. The parameter g depends on the energy scale and therefore on the resonance mass. However, for resonance masses from 1 TeV to 4 TeV, $g \approx 0.65$. The coupling g_V is set to one, and therefore the parameter values of c_F and c_H to describe the extended gauge symmetry in the HVT model are found to be $c_F = -1.316$ and $c_H = -0.556$. For completeness, the other parameters are calculated based on Eq. 2.20 to be $c_{VVW} = 1$, $c_{VVHH} = 0.077$, and $c_{VVV} = -0.204$.

The second model interpretation is a strongly coupled scenario that mimics the phenomenology of composite Higgs models, or more detailed the one described in [33]. This parameter selection is called HVT model B. In this model, the Higgs boson is a pseudo Nambu-Goldstone boson (comparable to the pion in quantum chromodynamics) emerging as the light state from the symmetry breaking due to an underlying strongly coupling substructure. As a result, additional resonances at masses above the TeV scale are expected from excited states of the underlying substructure. In general, more than one set of additional resonances could be produced at even higher energy scales.

However, only the dynamics of the lightest resonances will be discussed here. Composite Higgs models provide an interesting solution to the hierarchy problem, as the Higgs would dissolve for energies above the compositeness scale which is expected to lie at the TeV scale and therefore, the inconsistencies between the energy scales of the electroweak and the Planck scale would be solved [32].

Same as for model A, the parameter values can be estimated based on the tilded basis. Here, the tilded parameters are set to [2]

$$\tilde{c}_{VW} = -\tilde{c}_{VVW} = \tilde{c}_{VVV} = 1 \qquad \tilde{c_H} = -a_\rho^2, \qquad \text{and} \qquad \tilde{c}_F = \tilde{c}_{VVHH} = 0. \tag{2.23}$$

where a_ρ is a free parameter defined in the composite higgs model [33] which is set to 1, meaning that $\tilde{c}_H = -1$. Using these relations, the parameters c_F and c_H in the composite higgs model are defined by

$$c_F = \frac{1}{\sqrt{1 - \frac{g^2}{g_V^2}}} \qquad \text{and} \qquad c_H = \frac{1}{\sqrt{1 - \frac{g^2}{g_V^2}}} \left[\frac{g^2}{g_V^2} - 1\right] = c_F \left[\frac{g^2}{g_V^2} - 1\right]. \tag{2.24}$$

The coupling g is again approximately 0.65 for resonance masses between 1 TeV and 4 TeV and the coupling strength of the new heavy vector bosons g_V is set to 3. Using these values, the parameters c_F and c_H are given by $c_F = 1.024$ and $c_H = -0.976$ in model B. The additional parameters values are obtained to be $c_{VVW} = 1$, $c_{VVHH} = -0.024$, and $c_{VVV} = 0.928$.

2.3.2. Production and Decay

In the HVT model, the heavy spin-1 particle can be produced via Drell-Yan (DY), Vector boson fusion (VBF), and associated production with an additional vector boson. The rate of the associated production is negligible for resonance masses above the TeV scale and therefore, it is not discussed in the following. The feynman diagrams of the two dominant processes are shown in Fig. 2.1. If only the production vertices $qq \to V$ and $V_{SM}V_{SM} \to V$ (V_{SM} = W, Z) of the resonances are taken into account, these processes are $2 \to 1$ processes and their leading order cross section is given by:

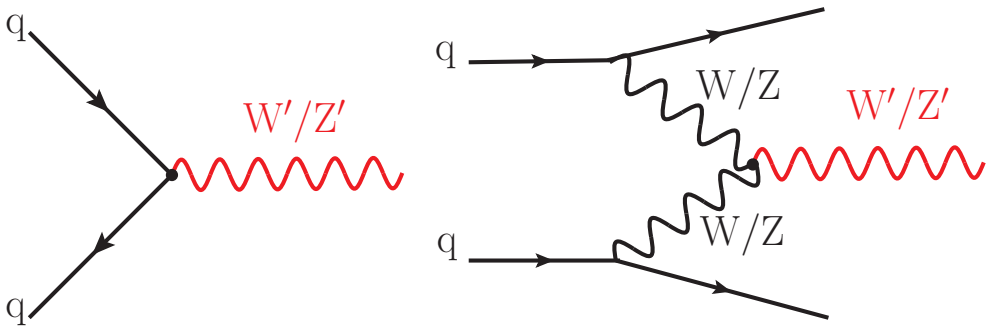

Figure 2.1.: The two dominant production processes for heavy spin-1 particles in the HVT model in pp-collisions. Left: Drell-Yan, Right: Vector Boson Fusion

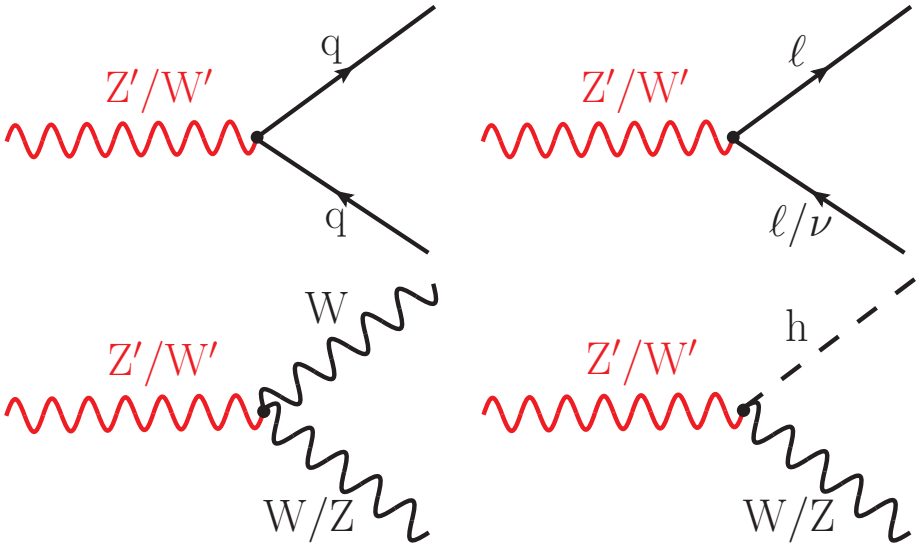

Figure 2.2.: Feynman diagrams of possible decay channels of heavy diboson resonances, charged and neutral resonances combined. Top left: $V \to qq$; top right: $V \to \ell\nu$; bottom left: $V \to V_{SM}V_{SM}$ (V_{SM} = W, Z); bottom right: $V \to V_{SM}h$.

$$\sigma\left(pp \to qq/V_{SM}V_{SM} \to\to V\right) = \sum_{i,j\,\epsilon\,p} \frac{\Gamma_{V\to ij}}{M_V} \frac{16\pi^2\,(2J+1)}{(2J_i+1)\,(2J_j+1)} \frac{C}{C_iC_j} \frac{dL_{ij}}{d\hat{s}}\,|_{\hat{s}=M_V^2} \tag{2.25}$$

where $i,j = \{q,\bar{q},W,Z\}$ are the colliding particles or radiated bosons from the hard interaction, $\Gamma_{V\to ij}$ is the decay width of the inverse process $V \to ij$, J and $J_{i,j}$ are the spin of the resonance and the initial particles, C and $C_{i,j}$ are the color factors for these particles, and $dL_{ij}/d\hat{s}|_{\hat{s}=M_V^2}$ is the parton luminosity for the initial particles evaluated at the resonance mass. It is important to note that for a given resonance mass M_V, the only term that depends on the model parameters is the decay width $\Gamma_{V\to ij}$ for the inverse process. This means that the production cross section has the same dependencies on the theory parameters, making it easy to analytically reinterpret results for different model parameters. As the decay widths play an important role in the production of the heavy vector bosons, they will be discussed before taking a more detailed look at the differences of the production processes.

The resonances can decay in three ways, namely in dilepton, diquark and diboson pairs, as shown in Fig. 2.2. Starting with the fermionic decay (dilepton and diquark), the decay width in asymptotic approximation is given by [2]:

$$\Gamma_{V_\pm\to f\bar{f}'} \simeq 2\cdot\Gamma_{V_0\to f\bar{f}} \simeq N_c\,[f]\left(\frac{g^2c_F}{g_V}\right)^2 \frac{M_V}{48\pi}. \tag{2.26}$$

where $N_c\,[f]$ is the number of colors which is $N_c\,[q] = 3$ for diquark and $N_c\,[\ell] = 1$ for dilepton decays. As discussed already in Sec. 2.3.1, the decay to fermions depends mainly, except for the resonance mass M_V, on the parameter combination g^2c_F/g_V which is squared in the calculation of the partial decay width. The parameter c_F can be split in leptons, light quarks and third generation quarks if necessary. Since this decay width does also control the production rate via Drell-Yan from $q\bar{q}$, the production has the same dependence.

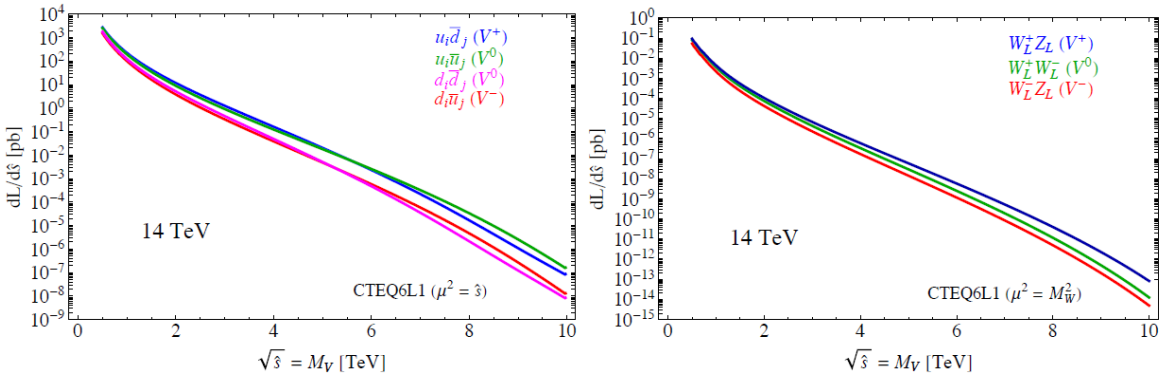

Figure 2.3.: Parton luminosity for the production via DY ($qq \to V$, left) and VBF ($V_{SM}V_{SM}qq \to qqV$, right) for a center-of-mass energy of $\sqrt{s}$ = 14 TeV at pp collider, taken from [2].

The dynamic of the diboson decay is slightly different as there is a contribution from the mixing with SM particles. The decay widths for the diboson decays to W, Z, and h (Higgs) bosons are given by [2]:

$$\begin{aligned}
\Gamma_{V_0 \to W_L^+ W_L^-} &\simeq \Gamma_{V_\pm \to W_L^\pm Z_L} \simeq \frac{g_V^2 c_H^2 M_V}{192\pi} \frac{\left(1 + c_H c_{VVV} \varsigma^2\right)^2}{\left(1 - c_H^2 \varsigma^2\right)^2} = \frac{g_V^2 c_H^2 M_V}{192\pi} \left[1 + \mathcal{O}\left(\varsigma^2\right)\right], \\
\Gamma_{V_0 \to Z_L h} &\simeq \Gamma_{V_\pm \to W_L^\pm h} \simeq \frac{g_V^2 c_H^2 M_V}{192\pi} \frac{\left(1 + 4 c_{VVHH} \varsigma^2\right)^2}{1 - c_H^2 \varsigma^2} = \frac{g_V^2 c_H^2 M_V}{192\pi} \left[1 + \mathcal{O}\left(\varsigma^2\right)\right]
\end{aligned} \tag{2.27}$$

In these equations, $\varsigma = g_V \hat{\nu}/(2\hat{m}_V)$ is a parameter that includes information about the energy scale of the EWSB, with $\hat{\nu}$ denoting the Higgs field vacuum expectation value that can differ from the EWSB in the SM where ν = 246 GeV and $\hat{m}_V^2 = m_V^2 + g_V^2 c_{VVHH} \hat{\nu}^2$. In principle, ς is a measure for the mixing with SM particles. It can be used to reproduce the SM vector boson masses within the HVT model using the equations:

$$\begin{aligned}
m_Z^2 &= \hat{m}_Z^2 \left(1 - c_H^2 \varsigma^2\right) \left(1 + \mathcal{O}\left(\hat{m}_Z^2/\hat{m}_V^2\right)\right) \\
m_W^2 &= \hat{m}_W^2 \left(1 - c_H^2 \varsigma^2\right) \left(1 + \mathcal{O}\left(\hat{m}_W^2/\hat{m}_V^2\right)\right)
\end{aligned} \tag{2.28}$$

where $\hat{m}_Z = e\,\hat{\nu}/(2\sin\theta_W \cos\theta_W)$ and $\hat{m}_W = \cos\theta_W\, \hat{m}_Z$. In most cases, except for very strongly coupled scenarios with very large g_V, $\varsigma \ll 1$ [2] and therefore, the second term can be neglected in these cases also following the argumentation of Sec. 2.3.1. The authors of the theory paper have tested these widths and proven that they reproduce the exact widths up to $\mathcal{O}\left(\hat{m}_{W,Z}^2/\hat{m}_V^2\right)$ corrections. Other decay channels, like hh, $\gamma\gamma$ or ZZ are forbidden due to CP violation. Decays of heavy charged bosons to Wγ are possible, but also highly suppressed in most models. Therefore, this decay will also be neglected. For $\varsigma \ll 1$, the parameter combination $g_V c_H$ describes the entire production and decay via diboson processes. In conclusion, the whole model can be described approximately by the three parameter combinations M_V, $g_V c_H$, and $g^2 c_F/g_V$ since they control the production as well as the decay of the resonance.

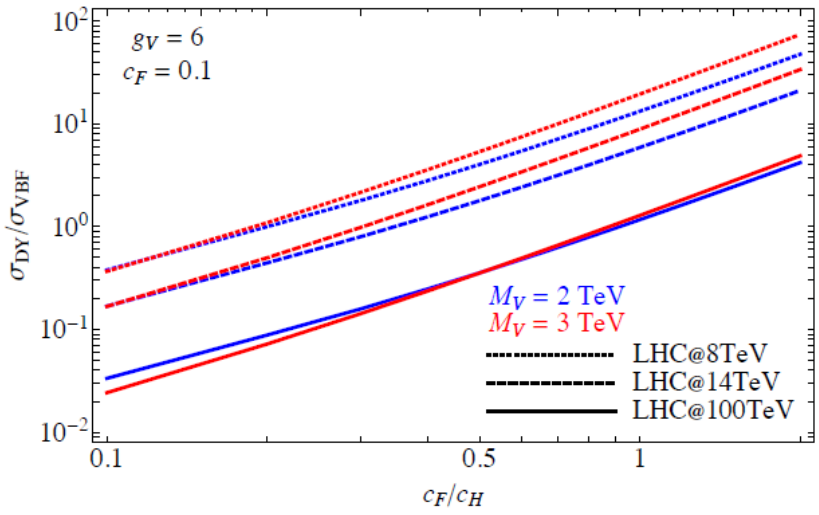

Figure 2.4.: Ratio of the DY over VBF production cross section as a function of the ratio c_F/c_H for a center-of-mass energy of $\sqrt{s}$ = 8/14/100 TeV at a pp collider for two resonance masses, taken from [2]. The value of c_F is set to 0.1, the value of g_V is set to 6.

Now that the decay widths are known, it is possible to compare the two production mechanisms. In Eq. 2.25, it is visible that both production processes depend on two main parts: The parton luminosity for the corresponding process which is independent from the model parameters and the partial width that depends on them. Fig. 2.3 shows the parton luminosity for the two production processes as a function of the resonance mass for a center of mass energy of 14 TeV. Depending on the resonance mass, the parton luminosity for production via DY is four to six orders of magnitude larger than the production via VBF. This difference leads to a dominance of the DY production mechanism for most of the parameter combinations. To compensate for this effect, the value of g_V needs to be very large or c_H needs to be unsuppressed. This is the case in strongly coupled scenarios where $c_H \approx 1$, like in the previous discussed model B. Fig. 2.4 shows a comparison between the production cross section via DY and VBF for a coupling of $g_V = 6$ as a function of the ratio c_F/c_H. In this particular case, the production via DY would still be stronger for ratios above 0.5, but the production via VBF would play an important role in the whole parameter space. Model B, for example, has values of $c_F \approx c_H \approx 1$. However, the value of g_V is only 3 in model B. While the production via DY goes with $1/g_V^2$, the production via VBF is proportional to g_V^2, meaning that the ratio between DY and VBF would be 16 times higher by only switching from $g_V = 6$ to $g_V = 3$. Therefore, the production via DY will be the dominant production mechanism for couplings of $g_V \leq 5$ [2].

Another important aspect of the production and decay is the total width of the resonance. Since this search concentrates on narrow resonances, it is important to keep an eye on the relative resonance width Γ_{tot}/M_V. In general, it should not exceed the resolution of the CMS detector. The full decay width is the sum of the partial widths and therefore, the sum of the difermion and diboson decay widths. In asymptotic approximation, the relative width is independent of the resonance mass and should therefore just depend on the parameter combinations $c_H g_V$ and $g^2 c_F/g_V$. Fig. 2.5 shows two examples how the decay width changes as a function of the resonance mass and the strength g_V. On the left side, the weakly coupled scenario (like model A) is shown while the right side represents the strongly coupled scenario (like model B). In case of weakly coupled scenarios where c_F is in the order of one and c_H is suppressed, the resonance width is dominated by the fermionic decay modes. Since their width is inversely proportional to the strength g_V, the highest value is reached

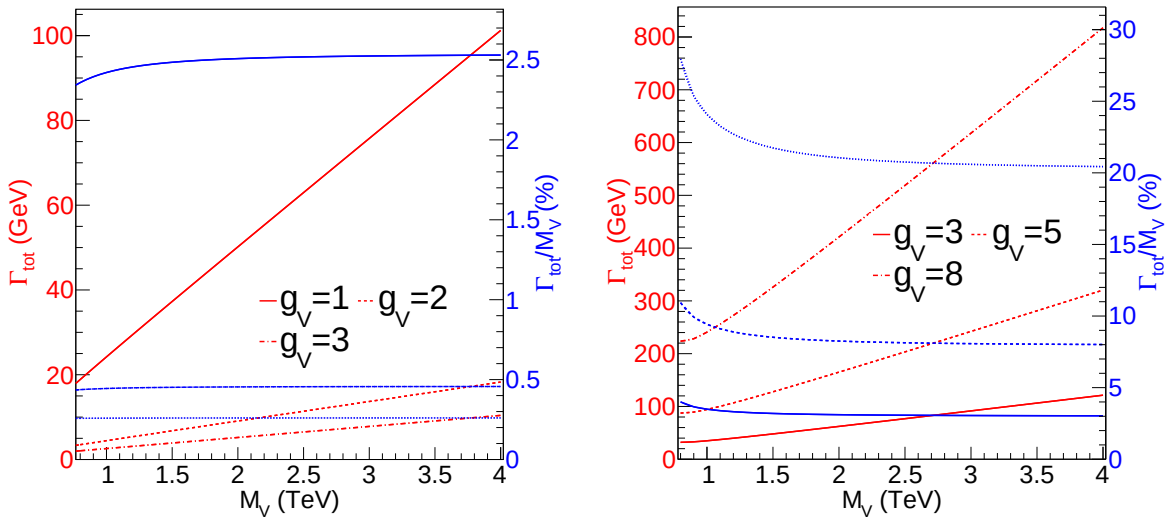

Figure 2.5.: Absolute (red line) and relative (blue line) decay widths as a function of the resonance mass for heavy charged $V^{\pm}$ with parameters for the weakly coupled case (left) and the strongly coupled case (right) for different strengths g_V, based on [2]. In these plots, the decay widths are based on the exact calculation and can therefore slightly differ w.r.t Eq. 2.26 and Eq. 2.27 for low mass as they are estimated in asymptotic approximation.

for small g_V. In the case $g_V = 1$, the relative decay width is about 2.5 % which is on the edge of the detector resolution that is also in the order of a few percent. For the strongly coupled scenario, the resonance width is dominated by the diboson decays and therefore is proportional to the strength g_V in first approximation. While $g_V = 3$ is still within the narrow width approximation, higher values of the strength might be beyond the detector resolution. For $g_V = 5$, the relative width is in the order of 10 % and therefore not smaller than the detector resolution anymore. As long as the narrow width approximation is kept, the relative width should stay below 10 % and therefore, the strength g_V is restricted to be ≤ 5 for the strongly coupled scenario in this search. As the narrow width approximation restricts the search to relatively low g_V values, the production via DY will always be dominant, also in the strongly coupled scenario. Therefore, this analysis will stick to the production via DY.

2.3.3. Characteristics of Model A and B

At the end of Sec. 2.3.1, two explicit model interpretation where introduce, namely HVT model A, mimicking weakly coupled scenarios like extended gauge symmetries and HVT model B, doing the same for strongly coupled scenarios like composite Higgs models. In model A, the three important parameters g_V, c_F, and c_H are set to $g_V = 3$, $c_F = 1.316$, and $c_H = -0.556$. As discussed in Sec. 2.3.2, $\varsigma \ll 1$ for weakly coupled scenarios, and thus the impact of the additional parameters on the branching fractions is very low and only visible for low mass resonances. Fig. 2.6 shows the characteristic distributions of the model A, namely the branching fractions for the neutral resonances (top left), charged resonances (top right), and their cross sections and decay widths (bottom) as a function of the resonance mass. Due to the large value of c_F, the coupling to fermions is enhanced and therefore, the corresponding decay fraction. Diboson decays have only a branching fraction of about 2 % per decay mode. For low masses, the WW/Wh decay has a slightly higher branching

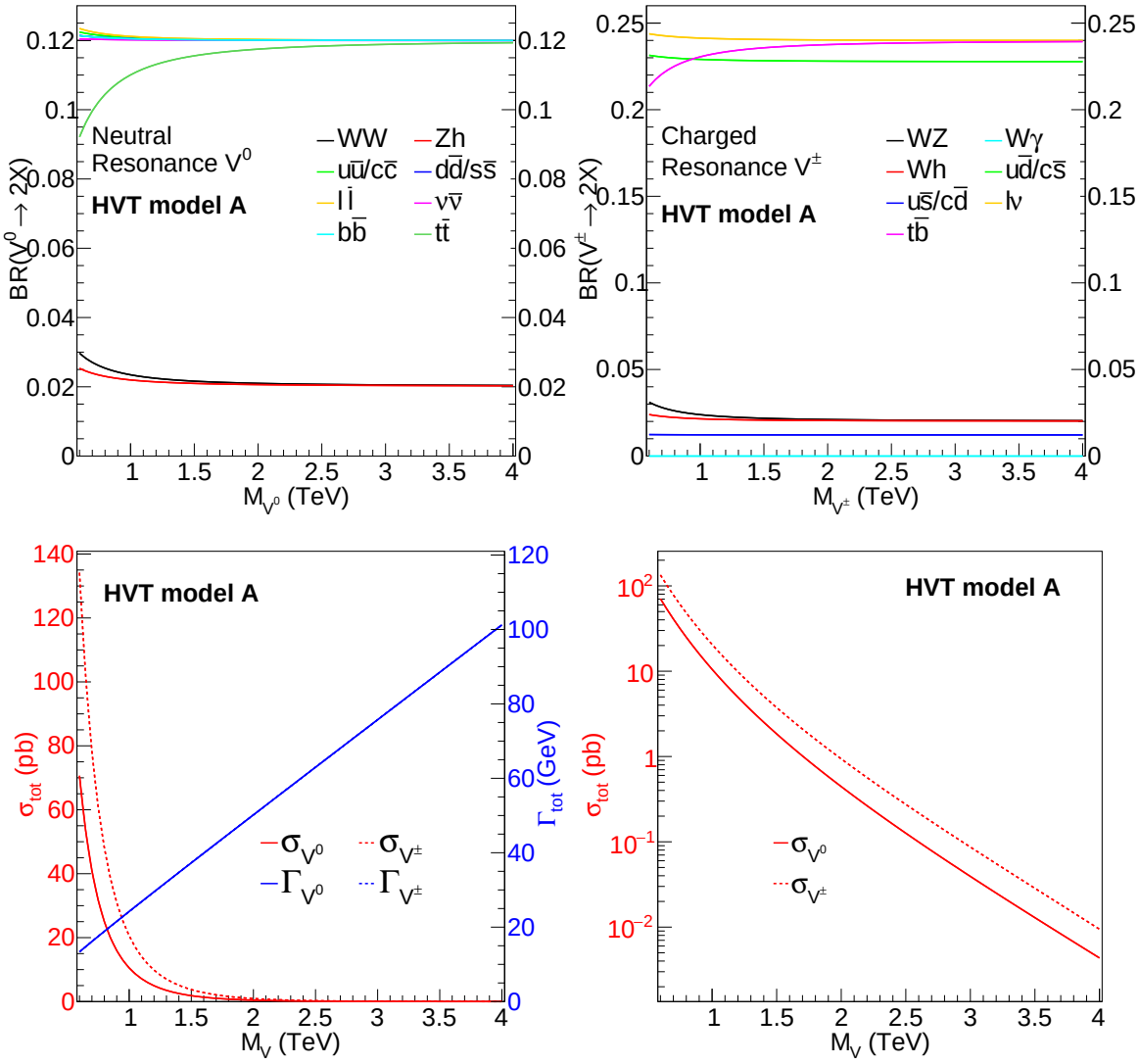

Figure 2.6.: Characteristic distributions of the HVT model A as a function of the resonance mass, based on [2]. Top left: Branching fraction of the neutral resonance, top right: Branching fraction of the charged resonance, bottom left: cross sections for charged and neutral resonances (red) and their width (blue) for a center-of-mass energy $\sqrt{s}$ = 13 TeV, bottom right: the same cross section with logarithmic y-axis. The lines of the decay widths of neutral and charged resonances are indistinguishable.

fraction as the Zh/Wh decay. However, for masses above 1.5 TeV, both decay modes have nearly the same value. In decays to two quarks, small differences between the third generation and the first two generations can be observed for neutral and charged resonances. For neutral resonance decays, these differences arise from the large top mass and the resulting turn-on in the branching fraction while for charged resonance decays, they arise from the quark mixing based on the CKM matrix.
Another effect of the large coupling to fermions is the large production cross section from $q\bar{q}$ annihilation. For a 1 TeV resonance, it is about 20 pb, resulting in about 720 000 hypothetically produced charged or neutral resonances for the full 2016 CMS dataset corresponding to 36 fb^{-1}. The decay width has been discussed above, the relative decay width in HVT model A is about 2.5 % over the

full mass spectrum.

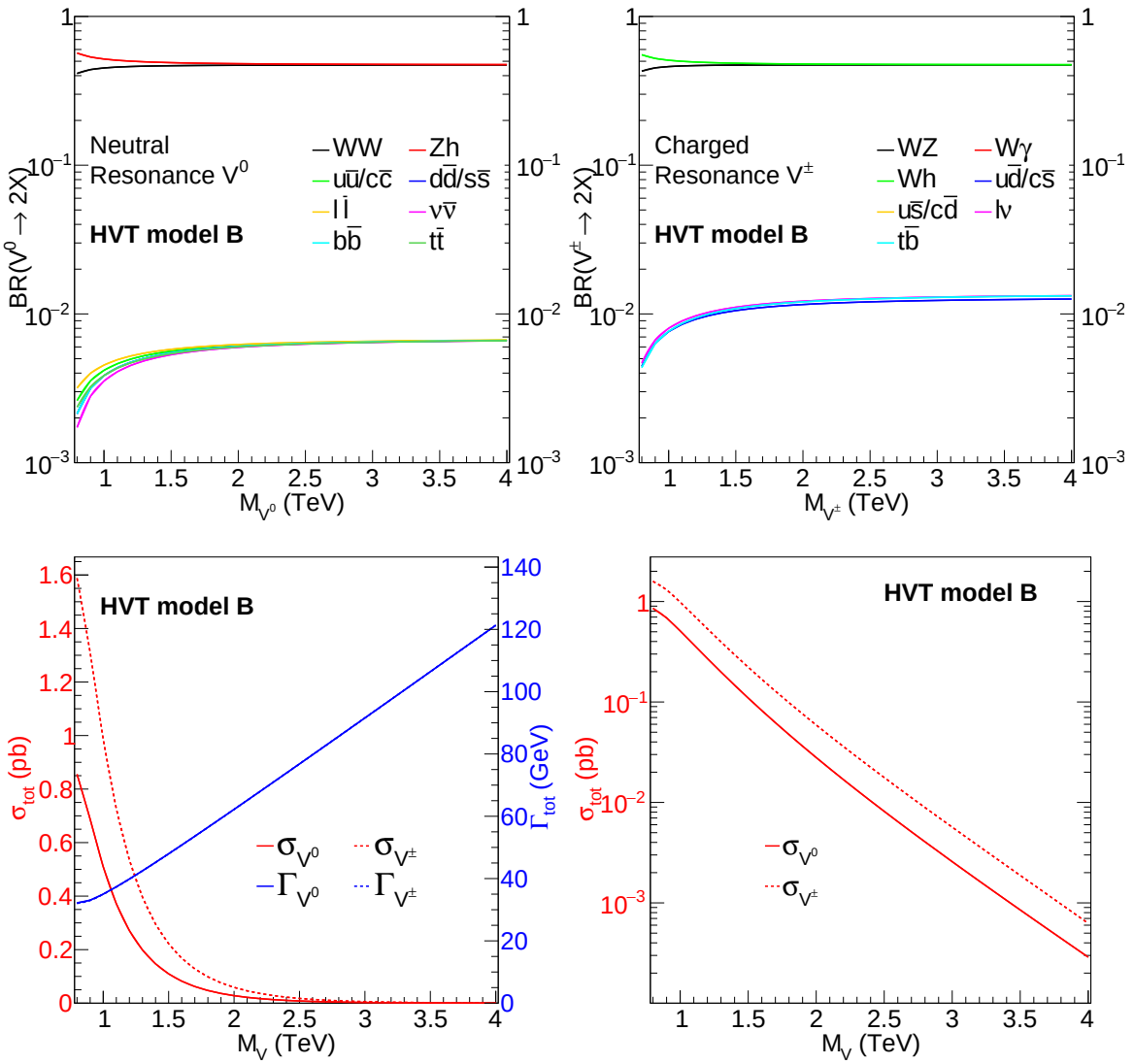

Figure 2.7.: Characteristic distributions of the HVT model B as a function of the resonance mass, based on [2]. Top left: Branching fraction of the neutral resonance, top right: Branching fraction of the charged resonance, bottom: cross sections for charged and neutral resonances (red) and their width (blue) for a center-of-mass energy $\sqrt{s}$ = 13 TeV, bottom right: the same cross section with logarithmic y-axis. The lines of the decay widths of neutral and charged resonances are indistinguishable.

In model B, the three important parameters g_V, c_F, and c_H are set to $g_V = 3$, $c_F = 1.316$, and $c_H = -0.556$. Fig. 2.7 summarizes the characteristics for neutral and charged resonances in the model B. Due to the large value of c_H and g_V, the decay width to diboson decays is enhanced, summing their impact up to about 96 % of the full branching fraction. In comparison to model A, the production cross section is decreased, as the coupling to fermions c_F is reduced and the coupling strength g_V is increased, resulting in a smaller width $\Gamma_{V\to qq}$. Since the coupling strength is larger, the parameter ς has a larger impact than in model A, resulting in large differences in the WW/WZ and Zh/Wh branching fraction at low masses. In addition, the mixing with SM gauge bosons is slightly enhanced,

resulting in already theoretically excluded masses below 800 GeV from SM precision measurements [2, 47]. The total decay width is also increased with relative values of 3-4 % w.r.t. the resonance mass. Overall, the constraints on model B are stricter than for model A, meaning that it needs to be interpreted more carefully.

2.3.4. Existing Limits

As mentioned in the introduction of this thesis, searches for heavy charged resonances are performed in various decay channels as they are predicted by many BSM physics theories. Here, the most stringent bounds on the cross section times branching fraction for the different analyses based on diboson resonances will be listed, including a brief overview about their characteristics. The analyses are split in WZ and Wh resonances and the limits stated here are calculated with respect to the branching ratio to WZ or Wh $\left(\sigma \times \mathrm{B}\left(\mathrm{V}^{\pm} \rightarrow \mathrm{WZ/Wh}\right)\right)$. In all cases, the best limits arise from LHC measurements by the CMS and ATLAS collaborations and they are estimated with 95 % confidence level.

Limits on $\mathrm{W}' \rightarrow \mathrm{WZ}$ Resonances

Searches for WZ resonances have been performed in the following channels:

- qqqq: Searches for WZ resonances decaying to four quarks were done by CMS and ATLAS using two merged large cone size jets [14, 15]. With a combined branching fraction of about 47 %, the decay to four quarks has the highest production rate of all WZ channels. However, since the LHC is a proton-proton collider, it also has the highest SM background and thus, the highest trigger threshold. As a consequence, these searches start only at resonance masses above 1.2 TeV. HVT model A is excluded up to $\mathrm{M}\left(\mathrm{W}'_{\mathrm{HVT\ A}}\right) > 3.0$ TeV and $\mathrm{M}\left(\mathrm{W}'_{\mathrm{HVT\ B}}\right) > 3.3$ TeV by both experiments if the WZ decay is considered. The limit on $\sigma \times \mathrm{B}\left(\mathrm{V}^{\pm} \rightarrow \mathrm{WZ}\right)$ lies at about $2 \cdot 10^{-3}$ pb for resonance masses above 3 TeV.

- $\ell\nu$qq (ℓ = e, μ): In comparison to the four quark final state, searches for resonances decaying to $\ell\nu$qq have the advantage of a lower trigger threshold because of the additional lepton in the event. Thus, the search region can be extended below the TeV scale. In its analysis, the ATLAS experiment combines results from merged large cone size jets and resolved jets, resulting in limits on $\sigma \times \mathrm{B}\left(\mathrm{V}^{\pm} \rightarrow \mathrm{WZ}\right)$ ranging from 50 pb ($\mathrm{M}_{\mathrm{V}^{\pm}} = 0.3$ TeV) to $2 \cdot 10^{-3}$ pb for high masses [17]. The CMS experiment does not use the resolved category and therefore, their analysis starts at 1 TeV [16]. The individually observed limits on the HVT models from both experiments are $\mathrm{M}\left(\mathrm{W}'_{\mathrm{HVT\ A}}\right) > 2.8$ TeV and $\mathrm{M}\left(\mathrm{W}'_{\mathrm{HVT\ B}}\right) > 3.0$ TeV.

- qq$\ell\ell$ (ℓ = e, μ): Due to the two leptons in the event, this analysis has a good suppression of the SM background. However, since the Z boson is required to decay to two electrons or muons, the branching fraction of this channel is about an order of magnitude smaller in comparison to the qqqq final state. Both experiments have combined searches in resolved and merged categories [18, 19]. The CMS experiment sets limits of 1 pb - $5 \cdot 10^{-3}$ pb (0.5 TeV < $\mathrm{M}_{\mathrm{V}^{\pm}}$ < 4.5 TeV) on the cross section and $\mathrm{M}\left(\mathrm{W}'_{\mathrm{HVT\ A}}\right) > 2.4$ TeV and $\mathrm{M}\left(\mathrm{W}'_{\mathrm{HVT\ B}}\right) > 2.7$ on the masses in the HVT model. In the ATLAS experiment, a drop in the signal efficiency is observed for masses above 3 TeV, resulting in a worse limit on $\sigma \times \mathrm{B}\left(\mathrm{V}^{\pm} \rightarrow \mathrm{WZ}\right)$. However, the rounded mass limits are approximately the same as obtained by the CMS measurement.

- qq$\nu\nu$: This channel has a high branching fraction, comparable to the $\ell\nu$qq channel. The low number of objects, namely only one merged jet plus E_T^{miss} results in a high signal selection efficiency. The signature can be triggered based on the E_T^{miss} where the threshold typically lies at about 200 GeV, giving rise to resonance masses above 800 GeV. Therefore, no resolved jet selection is performed by the two experiments. The cross section limits range from 0.1 pb - $2 \cdot 10^{-3}$ pb for masses between 0.8 and 4.5 TeV in both experiments [19, 21] which can be translated to mass limits of 3.0 TeV (HVT model A) and 3.3 TeV (HVT model B).
- $\ell\nu\ell\ell$ (ℓ = e, μ): An analysis in this channel has only been performed by the ATLAS experiment [20]. It is the channel with the lowest branching fraction, but with the highest discrimination against the background, resulting in good limits for low mass resonances. The limits on $\sigma \times B\left(V^{\pm} \to WZ\right)$ range from 4 pb to 10^{-2} pb for 0.5 TeV < $M_{V^{\pm}}$ < 3.0 TeV and masses $\leq$ 2.25 TeV (HVT model A) and $\leq$ 2.45 TeV (HVT model B) can be excluded. This analysis does not include hadronic tau decays as it is done the analysis presented in this thesis.

Limits on $W' \to Wh$ Resonances

Searches for Wh resonances have been performed in the following channels:

- qqbb: This channel is similar to the qqqq final state for WZ resonances. However, the usage of b-tagged jets results in some additional discrimination power against the background. The branching fraction is about 39 % and therefore it is the dominant decay channel regarding the event production rate. Due to the large trigger thresholds, the analyses start at masses of 1 TeV [22, 23]. The limits on $\sigma \times B\left(V^{\pm} \to Wh\right)$ are found to be between $8 \cdot 10^{-2}$ pb and $2 \cdot 10^{-3}$ pb while the observed lower mass limits are at about 2.4 TeV (HVT model A) and 2.6 TeV (HVT model B).
- $\ell\nu$bb (ℓ = e, μ): This analysis starts at 0.8 TeV in CMS and 0.5 TeV in ATLAS where an additional analysis in a resolved b-jet category is performed [24, 25]. Here, the limits are stated with respect to the branching fraction $B\left(V^{\pm} \to Wh \to bb\right)$. The limits range from 0.25 pb (0.5 TeV ATLAS) to 10^{-3} pb (both experiments) and result in mass limits of 2.7 TeV (HVT model A) and 2.8 TeV (HVT model B).
- qq$\tau\tau$: This channel is only analysed by the CMS experiment due to the requirement of reconstructed hadronic tau leptons in boosted topologies [26]. The branching fraction of SM Higgs decay to two taus is approximately 9 times smaller in comparison to bb decays. However, the discrimination power against the SM background is better. This signature can be triggered using the E_T^{miss} from the tau decays. The limits on the cross section range from 0.15 pb to 10^{-2} pb for masses between 0.9 TeV and 4.0 TeV, resulting in mass limits of 2.1 TeV (HVT model A) and 2.4 TeV (HVT model B).

In addition to the single channel analyses, the ATLAS experiment has published a combined result of all decay channels, including neutral resonances and two fermion decays, to set a limit on the HVT model [47]. The limits in this publication are found to be 4.2 TeV (HVT model A) and 4.4 TeV (HVT model B).

CHAPTER 3

Experimental Setup

This chapter gives a brief summary of the experimental setup used to take the data for the performed analysis. The experimental setup is based on two important parts: The Large Hadronic Collider (LHC) [29] that provides the physical input for the data with proton-proton collisions and the Compact Muon Solenoid (CMS) experiment [3] which measures the output of the collisions and therefore takes the data. Both parts will be discussed in the following sections. Changes on the detector after the data taking in 2016 are not included.

3.1. The Large Hadron Collider

This section is based on the "The LHC machine" [29]. The basis for the analysis presented in this thesis is the Large Hadronic Collider (LHC) located at CERN at the border of France and Switzerland near Geneva. The LHC is a circular particle accelerator which is designed to accelerate and collide ionized atoms with high energies and high instantaneous luminosity. Although the LHC did also run successfully with ionized lead and xenon atoms in the past, the main machine mode that is also used for this analysis, produces proton-proton collisions, where the protons are taken from ionized hydrogen. Within the years, the center of mass energy for these collisions was increased starting from $\sqrt{s}$ = 7 TeV in 2011 and $\sqrt{s}$ = 8 TeV in 2012 up to $\sqrt{s}$ = 13 TeV from 2015 to 2018 and is therefore close to the designed center-of-mass energy of 14 TeV which would correspond to a beam energy of 7 TeV.

The LHC was built in the tunnel of the Large Electron-Positron collider (LEP) [48] and has a circumference of 26.7 km. It is part of the CERN accelerator chain (see Fig. 3.1) which is used to accelerate and inject the protons in the LHC. These protons are not injected one-by-one, but in groups of many protons, also called bunches. Starting from the Linear Accelerator 2 (LINAC2) where the bunches are accelerated to 50 GeV, they are led to the Proton Synchrotron Booster (PSB), the Proton Synchrotron (PS) and the Super Proton Synchrotron (SPS). At the end of the accelerator chain, the bunches reach an energy of 450 GeV before they are injected in the LHC accelerator where they reach energies beyond the TeV scale.

One important factor for particle accelerators is the instantaneous luminosity defined by

$$\mathscr{L} = \frac{N_b^2 n_b f_{rev} \gamma_r}{4\pi \epsilon_n \beta^*} F \tag{3.1}$$

where N_b is the number of particles per bunch, n_b the number of bunches per beam, f_{rev} the revolution frequency, γ_r the relativistic gamma factor, ϵ_n the normalized transverse beam emittance, β^* the beta function at the collision point, and F the geometric luminosity reduction factor given by

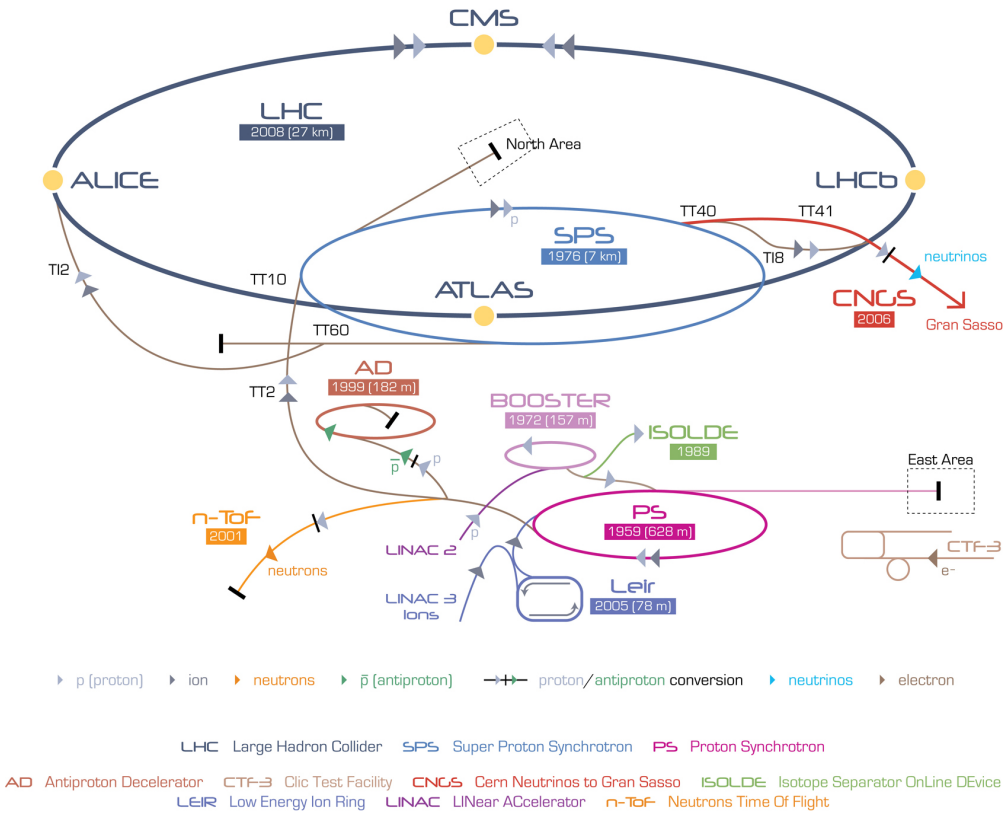

Figure 3.1.: The CERN accelerator complex with its experiments and injectors [49].

$$F = \left(1 + \left(\frac{\theta_c \sigma_z}{2\sigma^*}\right)^2\right)^{-1/2} \approx 1 - \frac{1}{2}\left(\frac{\theta_c \sigma_z}{2\sigma^*}\right)^2 . \tag{3.2}$$

Here, θ_c is the crossing angle at the interaction point, σ_z the RMS bunch length, and σ^* the transverse RMS beam size. The LHC is designed to contain 2 808 bunches in each proton beam with a bunch spacing of 25 ns. With these parameters, the design luminosity is $\mathscr{L} = 10^{34}\ \mathrm{cm}^{-2}\ \mathrm{s}^{-1}$ (10 Hz/nb) [29]. Due to optimizations in the past few years, the instantaneous luminosity has reached $\mathscr{L} \approx 1.5 \cdot 10^{34}\ \mathrm{cm}^{-2}\ \mathrm{s}^{-1}$ in 2016 and is therefore already 50 % higher than the design luminosity [50]. The event production rate is then defined by

$$\dot{N} = \mathscr{L} \cdot \sigma \tag{3.3}$$

where σ is the cross section. If this formula is integrated with respect to time, the full number of produced events is given by $N = \mathscr{L}_{\mathrm{int}} \cdot \sigma$. Here, $\mathscr{L}_{\mathrm{int}}$ is the integrated luminosity, a measure for the amount of data collected in a certain time period.

Several experiments are placed at the interaction points of the LHC. The four most important ones are the two general purpose detectors ATLAS [4] and CMS [3], the LHCb [51] experiment, which is optimized for b-physics, and ALICE [52], an experiment that is optimized for heavy ion collisions. ATLAS and CMS target similar physical processes by using different detector approaches. Since this thesis is based on 2016 CMS data, the CMS experiment will be discussed more detailed in the following section.

3.2. The Compact Muon Solenoid

The information used here is mainly taken from [3]. The Compact Muon Solenoid (CMS) experiment is a multi-purpose detector located on the french site of the LHC, 100 meters underground at Interaction Point 5 (IP5) of the LHC. It has a diameter of 14.6 m, a length of 16 m, and is optimized to reconstruct and measure all kinds of particles over a large energy scale starting from a few GeV up to above the TeV scale. It is built out of many subdetectors that form the different layers of the full CMS experiment, starting with the pixel detector in the most inner layer, followed by the silicon tracker, the electromagnetic calorimeter (ECAL), the hadronic calorimeter (HCAL), the solenoid magnet with a field strength of 3.8 T, and the muon system. The CMS detector can be split in three parts, the central part which is called the "barrel" region and the two forward parts named "endcap" regions. Fig. 3.2 shows a schematic view of the CMS detector and all of its subdetectors which will be described later based on their technical design reports.

The CMS experiment uses its own coordinate system to define the positions and directions of particles from the interaction. The center of the CMS coordinate system is the placed in the nominal collision point at the center of the beam pipe. While the x-axis points radially to the center of the LHC, the y-axis shows vertically to the surface of the earth. The z-axis is orientated along the beam direction, pointing to the Jura mountains. The azimuthal angle ϕ is measured in the x-y plane, starting from the x-axis while the polar angle θ is measured in the y-z plane, based on the z-axis. Instead of the polar angle θ, a variable more commonly used is the pseudorapidity η which is defined as

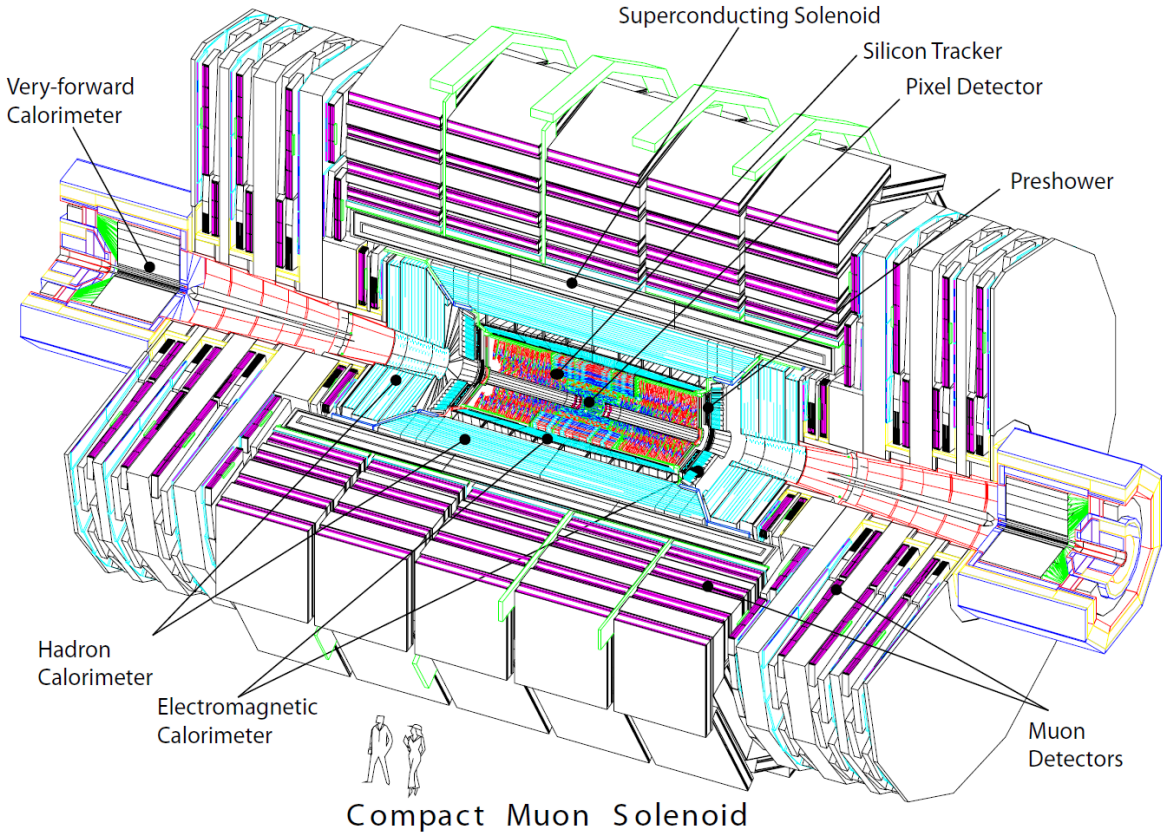

Figure 3.2.: Schematic view of the CMS detector, showing the general construction and the various subdetectors. The picture is taken from [53].

$$\eta = -\ln \tan\left(\frac{\theta}{2}\right). \tag{3.4}$$

The advantage of the pseudorapidity is that it is invariant under Lorentz transformation in z-direction for spatial differences $\Delta\eta = \eta_1 - \eta_2$ for highly boosted objects with $E \gg m$. An additional important variable is ΔR which can be used to describe the distance of two objects within the detector. It is defined as

$$\Delta R = \sqrt{(\Delta\eta)^2 + (\Delta\phi)^2} \tag{3.5}$$

and can be used for several purposes, for example the calculation of isolation variables or the definition of the jet cone size.

3.2.1. Inner Tracker

The inner tracker [54] is the most central subdetector of the CMS experiment. It consists of two parts: The pixel detector and the strip detector. A schematic overview of the tracker system can be found in Fig. 3.3. The inner tracker is optimized for a precise measurement of charged particle tracks based on the bending of particle trajectories by the magnetic field up to $|\eta| < 2.5$ and for a detailed reconstruction of primary and secondary vertices. Due to its impact on the vertex reconstruction, the tracker plays an important role in the reduction of effects from additional proton-proton interactions per bunch crossing, called pileup. The tracker system is built as close as possible to the interaction point with a distance of only 4.4 cm. Overall, it has a length of 5.8 m and a diameter of 2.5 m. To reach its physics goals of high precision momentum measurements and vertex reconstruction for each bunch crossing ($\approx$ 25 ns), a high granularity with fast response times is needed. At the same time, the effects of radiation damage in the busy environment close to the beam pipe should be as small as possible for a long lifetime of the tracker. Therefore, the system is based on silicon detector technology.

The Pixel Detector

The pixel detector is the innermost part of the tracking system. It is built out of 66 million silicon pixels, each of them having a size of 100×150 μm^2, distributed over three layers in the barrel region and two discs in the endcap region. The main target of the pixel detector is a good reconstruction of production and decay vertices. Therefore, it is important for the reconstruction of b-jets, hadronic tau decays, the suppression of pileup, and also for the measurement of the luminosity. The pixel detector can measure coordinates in r – ϕ- and z-direction and it reaches a spatial resolution of 15 μm.

The Strip Detector

The pixel detector is surrounded by the strip detector. The main goal of the strip detector is a precise measurement of the transverse momentum of particles using the bending by the magnetic field. It has a lower density of layers than the pixel detector, but it covers a larger area. The strip detector consists of several components. In the barrel region ($|\eta| < 0.9$), there are the tracker inner barrel (TIB), the tracker inner discs (TID), and the tracker outer barrel (TOB). In addition to the barrel system,

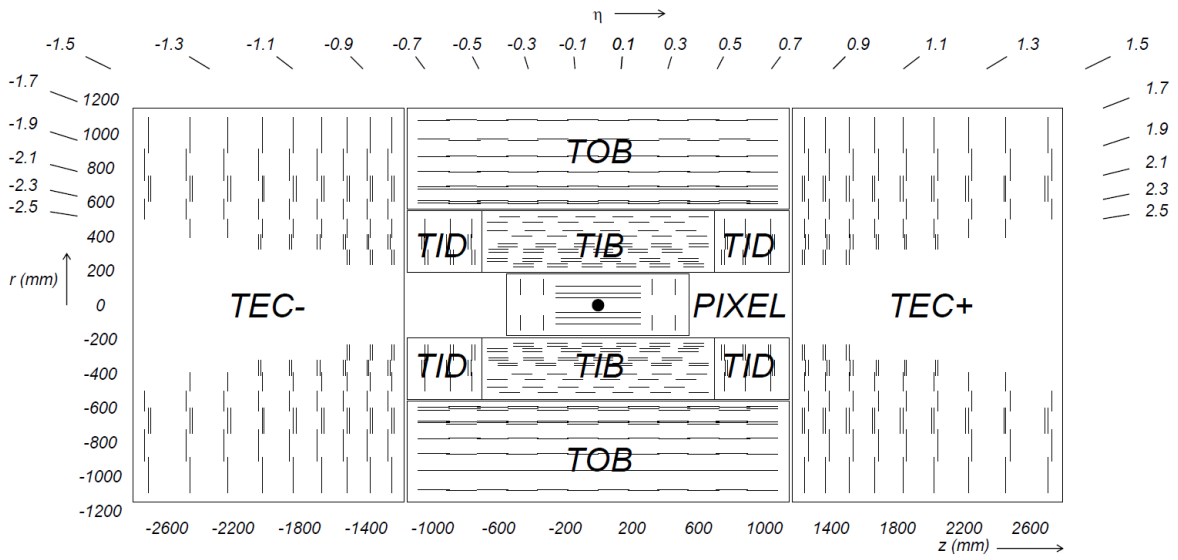

Figure 3.3.: Schematic overview of the CMS inner tracking system [3].

there are two tracker endcaps (TEC), covering a pseudorapidity of $0.9 < |\eta| < 2.5$. The position of the subcomponents can also be found in Fig. 3.3.

While the pixel detector can measure coordinates in two directions, the strip detector can only measure them in one direction. To compensate for this effect, some additional strip modules are added with a stereo angle of 100 mrad. With these modules, a measurement in z-direction is possible. Overall, the resolution of charged particles in the barrel region is about 1-2 % for a transverse momentum of 100 GeV [54]. For higher transverse momenta, the resolution decreases due to the smaller bending of the particle track by the magnetic field ($\frac{\sigma_{p_T}}{p_T} \propto p_T$). For outer regions of the strip detector, the resolution also decreases since the distance between the tracker layers increases.

3.2.2. Calorimeters

Two types of calorimeters are built in the CMS detector: The electromagnetic calorimeter (ECAL) which is the more central one and the hadronic calorimeter (HCAL). While the ECAL and the innermost part of the HCAL are covered completely by the inner magnetic field, some additional components of the HCAL are placed outside of the iron yoke of the magnet. Most particles produced in a collision shower due to interactions with matter and end up in the calorimeters where their energy is measured. The only exceptions are muons (measured in tracker and muon system) that have only small energy deposits in the calorimeters and neutrinos as they only interact weakly and therefore leave the experiment undetected.

Electromagnetic Calorimeter

The electromagnetic calorimeter (ECAL) [55] is built to measure the energy deposits of electrons and photons within a pseudorapidity range of $|\eta| < 3.0$. It is constructed out of about 76 000 tungstate ($PbWO_4$) crystals with a density of 8.28 g/cm^3 and a length of 230 mm. The radiation length of tungstate is $X_0 = 0.89$ cm, resulting in 26 radiation lengths for each of them. Same as for the silicon tracker, the ECAL aims for a fast response time while keeping a precise measurement of the energy

deposits of electrons and photons. The second one is achieved with the high density of the tungstate crystals. The energy in the ECAL is measured using the scintillated light of the tungstate crystals. Within one bunch crossing of the LHC (25 ns), about 80 % of the light is radiated. While in the barrel region avalanche photodiods are used to detect light, the endcaps utilize vacuum phototriods. In addition, preshower detectors are placed in front of the ECAL in the endcaps. These preshower detectors have an even higher granularity than the ECAL to distinguish between photons from boosted π^0 decays and photons from the hard primary interaction.

Since the measurement of the energy depends on the electromagnetic shower and therefore on the number of particles in the shower, the resolution increases as a function of the transverse momentum. It is given by

$$\left(\frac{\sigma_E}{E}\right)^2 = \left(\frac{2.8\%}{\sqrt{E/GeV}}\right)^2 + \left(\frac{12\%}{E/GeV}\right)^2 + (0.3\%)^2 \tag{3.6}$$

where the constant values a = 2.8 %, b = 12 %, and c = 0.3 % have been measured in beam tests without magnetic field and additional material (like the silicon tracker) in front of the ECAL. While the first term takes the stochastic effects into account, the second one contains the noise of the ECAL and pileup effects, and the third one represents uncertainties due to calibration.

Hadronic Calorimeter

The main task of the hadronic calorimeter (HCAL) [56] which surrounds the ECAL is to reconstruct the energy deposits of hadronic jets that have passed the ECAL. An exact measurement of the hadronic energy deposits of an event is crucial for many physics processes containing hadrons, but also for the reconstruction of missing transverse energy which relies much on the information from the calorimeters.

The HCAL consists of two parts which are divided by the magnetic coil that functions as an additional absorber material: The inner and the outer hadronic calorimeter. The inner HCAL is split in three parts: The hadronic barrel (HB), endcap (HE) and forward (HF) calorimeter. The outer HCAL (HO) on the other hand is only placed in the barrel region. A schematic overview of the hadronic calorimeter and its subsystems is presented in Fig. 3.4. The HCAL is built out of alternating layers with absorption material like brass and steel and plastic scintillators for the energy measurement. Overall, the absorber depth of the HCAL is about 5.8 radiation lengths at a pseudorapidity of $\eta = 0$. Hadronic showers that are not completely reconstructed in the inner HCAL can then be analysed in the HO. The resolution of the HCAL has also been measured in test beams and it is given by

$$\left(\frac{\sigma}{E}\right)^2 = \left(\frac{100\%}{\sqrt{E/GeV}}\right)^2 + (4.5\%)^2 \,. \tag{3.7}$$

3.2.3. Solenoid Magnet

For the reconstruction of the momentum and charge of particles, their bending by the magnetic field in the tracker and muon system is used. Therefore, it is important to have a magnetic field with a high strength to guarantee a good resolution and charge reconstruction also at high transverse momenta. This is realized in the CMS experiment by implementing a superconducting solenoid magnet [3] with an inner field strength of 3.8 T. A complete field map based on cosmic ray measurements can

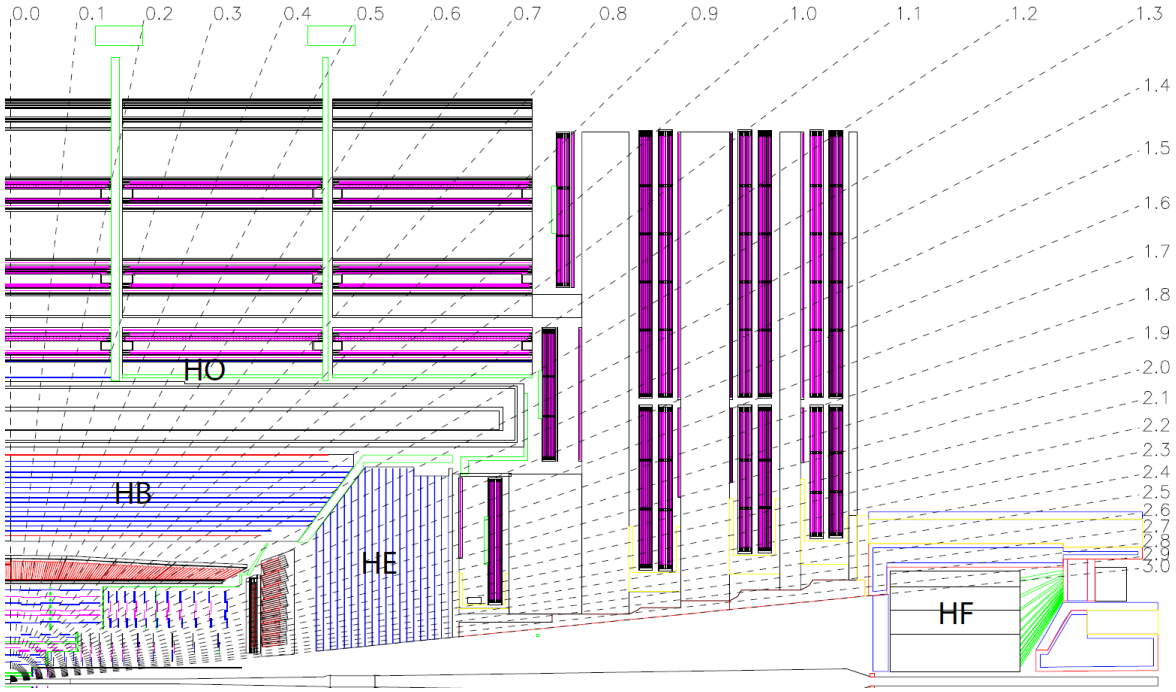

Figure 3.4.: Schematic overview of the HCAL [3] and its subsystems, the hadron barrel (HB), endcap (HE), outer (HO), and forward (HF) calorimeter.

be found in Fig. 3.5.
The magnet divides the HCAL in two parts and includes the tracker system, the ECAL and the inner HCAL and is returned by an iron yoke. The cooling system is based on liquid helium and operates at a temperature of 4.65 K. The magnetic field is parallel to the beam axis, therefore the transverse momentum of a particle based on its bending is given by

$$\frac{p_T}{\mathrm{GeV}} \approx 0.3 \cdot \frac{B}{\mathrm{T}} \frac{r}{\mathrm{m}}$$

with the magnetic field strength B and the bending radius r.

3.2.4. Muon System

The outermost part of the CMS detector is the muon system [58–60]. It plays an important role in SM measurements and in the search for new physics. Since muons are close to be minimum ionizing particles, their interaction with the ECAL, HCAL and magnet material is very small and therefore, their energy cannot be measured in the calorimeters. Due to their relatively long lifetime and small interaction with detector material, muons are typically the only charged particles that pass the inner detector and reach the outer muon system. The muon system works in a comparable way to the inner tracker: A muon interacts with the muon system and places hits in different layers. These hits can be combined to reconstruct the muon track and measure its transverse momentum. To guarantee the best possible resolution for muons, the measurement from the muon system is combined with the one from the silicon tracker. For a high-p_T muon ($\approx$ 1 TeV), the p_T resolution is about 5 %. The muon system consists of three parts, namely the drift tubes (DT), cathode strip

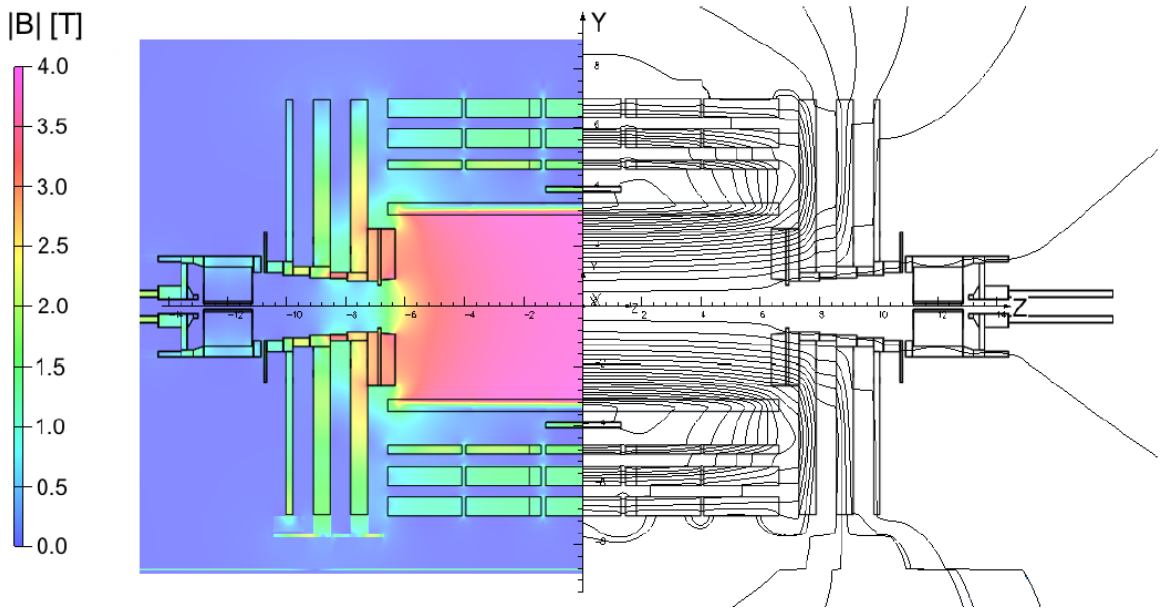

Figure 3.5.: Field map of the magnetic field of CMS measured using cosmic rays [57].

chambers (CSC), and resistive plate chambers (RPC), covering a range of $|\eta| < 2.4$. A schematic overview of the muon system and its subsystems can be found in Fig. 3.6.

Drift Tubes

In the barrel region ($|\eta| < 1.2$) of the muon system, the magnetic field is nearly homogeneous and the muon rate is small in comparison to the forward region. Therefore, a system based on drift tubes is used in this region. They are placed on four concentric cylinders, called muon stations, which are arranged between HCAL and iron yoke (MB1), inside the iron yoke (MB2 and MB3), and on the outermost part of the CMS detector (MB4). All muon stations constist of 60 drift tube chambers, except for MB4, which has 70. Four layers of drift cells are formed to one so called superlayer. The drift cells are constructed out of 50 μm anode wires operating with a voltage of +3600 V, two cathodes with a voltage of -1200 V, and two electrodes with a voltage of +1800 V (see Fig. 3.7). The gas used in the DTs consists of 85 % Argon and 15 % CO2. Charged particles that travel through the DTs ionize the gas. The resulting ions and electrons reach the anode and the cathode and produce an electric pulse which is used to measure the drift time of the ions. Based on the measured drift-time and the drift-velocity v_D which depends e.g. on the gas mixture and the voltage, the muon trajectory is estimated. The three inner muon stations consist of three super layers, while the most outer station has only two. For the three inner stations, the innermost superlayer is used for the measurement in the z-direction and the two outer ones measure the r-ϕ component of an incoming particle. In case of the fourth muon station, the two superlayers only measure the r-ϕ component, meaning that there is no z-direction measurement in the outermost muon station.

Cathode Strip Chambers

While the barrel region of the detector is covered by DTs, the muon system in the endcaps ($0.9 < |\eta| < 2.4$) is based on cathode strip chambers (CSC). Since the DTs are placed up to $|\eta| < 1.2$, there

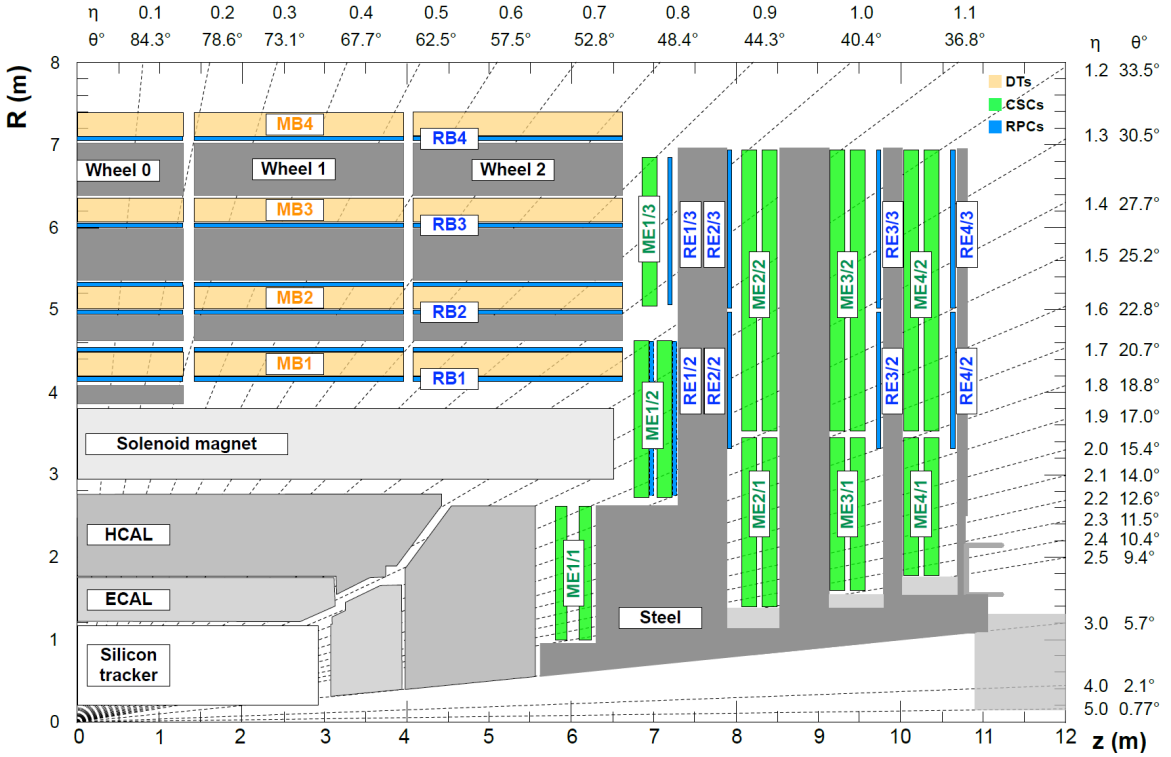

Figure 3.6.: Longidutinal schematic overview of the CMS detector showing the muon system and its subsystems, namely the drift tubes (DT), cathode strip chambers (CSC) and resistive plate chambers (RPC) [61].

is an overlay region between the two subsystems. CSCs are used instead of DTs because they have a faster response time and perform better in inhomogeneous magnetic fields than DTs, both important aspects in the muon endcaps where the expected rate is high and the magnetic field inhomogeneous. The CSCs have a trapezoidal shape consisting of seven panels with cathode strips placed radially to guarantee a precise measurement in ϕ direction. Fig. 3.8 shows a schematic view of the CSCs (left). In the gaps between the panels, six planes of anode wires are installed perpendicular to reconstruct the radial component of the muon momentum. The gaps are filled with a gas mixture based on argon (40 %), carbon dioxide (50 %), and carbon tetrafluoride (10 %). In each endcap, four CSC stations are placed perpendicularly to the beam pipe. Overall, 540 chambers are installed in CMS of which 72 where included before the start of Run-2 of the LHC (2015) in the outermost disc [61]. In general, the CSCs working principle is similar to the DTs and based on ionization of the gas mixture by an incoming muon. The expected spatial resolution ranges from 75 μm close to the beam pipe up to 150 μm if they are further away. The working principle of CSCs is also shown in Fig. 3.8 (right).

Resistive Plate Chambers

In addition to DTs and CSCs, a third subsystem is part of the muon system: Resistive plate chambers (RPCs). The advantage of RPCs in comparison to CSCs and DTs is their much better response time of a few ns. On the other hand, RPCs have a worse spatial resolution. Due to the good time resolution, RPCs are important for the muon trigger system since they can distinguish between different bunch crossings and match detected muons to their origin bunch crossing. A total number of 480 chambers in the barrel and 576 chambers in the endcaps are implemented in CMS. In the barrel, two RPC layers

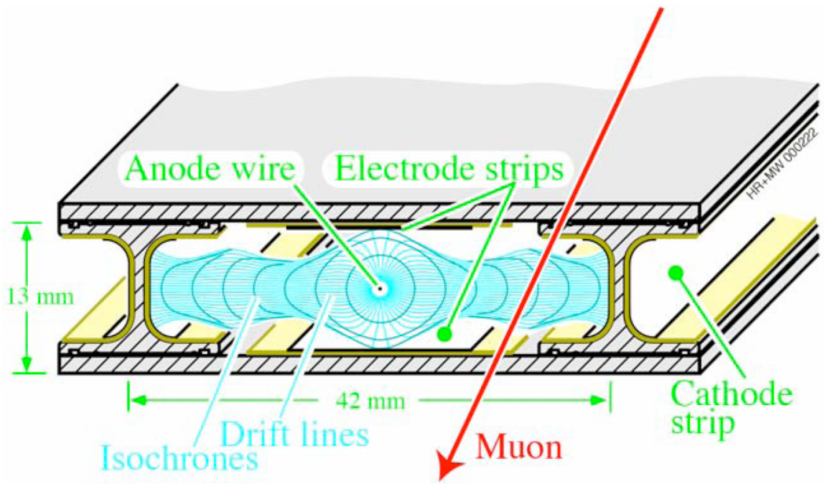

Figure 3.7.: Cross-section of a drift cell, taken from [3].

are placed on MB1 and MB2, and one is placed on MB3 and MB4, overall resulting in six installed layers. This arrangement increases the chances to detect low-p_T muons that do not travel trough the whole muon system. In the endcaps, three layers of RPCs are installed, covering an overall range of $|\eta| < 1.9$. RPCs are built out of two chambers filled with gas that have a small gap of 2 mm where read-out strips are located. They are based on an avalanche principle: Charged particles travelling through the RPCs ionize the gas. The detached electrons do the same, resulting in an avalanche of charged particles that reaches the read-out strips and creates a strong signal.

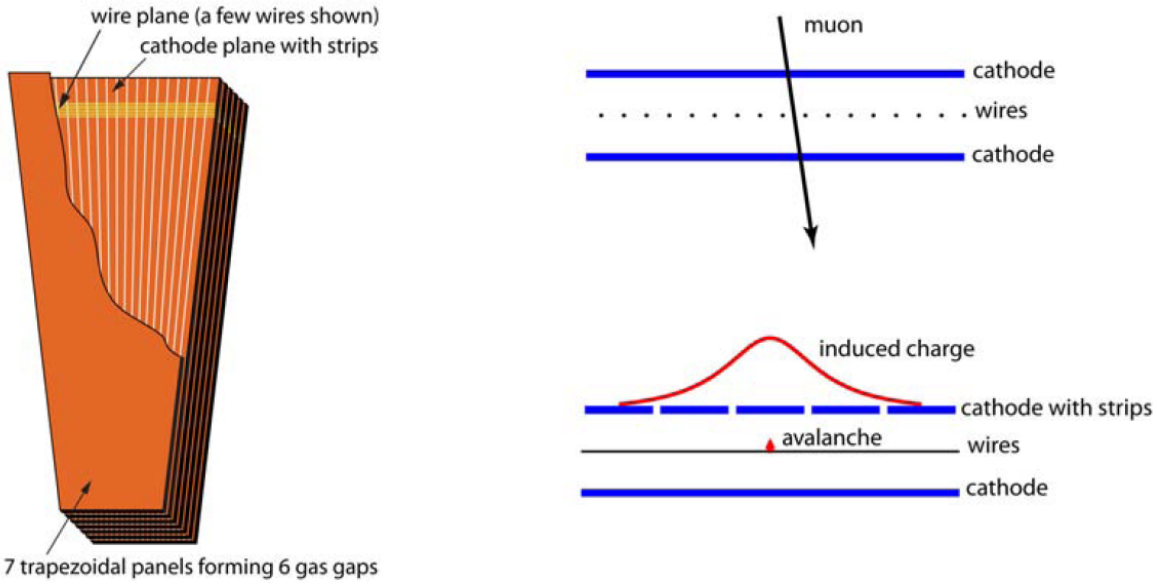

Figure 3.8.: Illustration of a cathode strip chamber (left) and its working principle (right) in CMS [3].

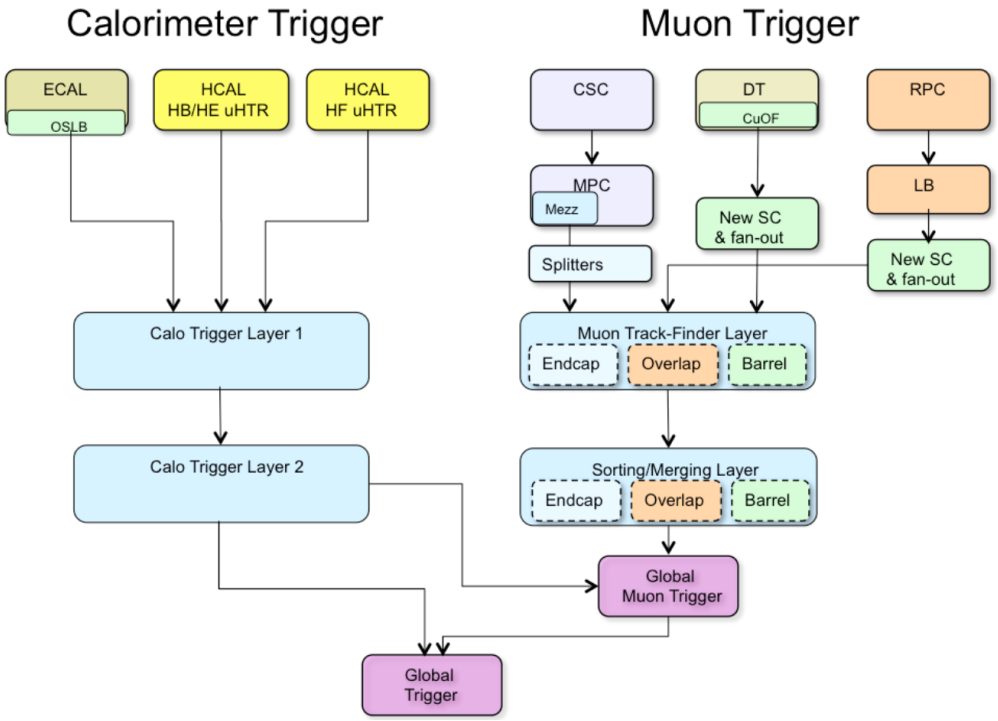

Figure 3.9.: Summary of the level-1 trigger structure as it was used by the CMS experiment in run-2 [64].

3.2.5. Trigger and Data Acquisition

The LHC operates with a bunch crossing time of 25 ns which corresponds to an event rate of 40 MHz. Due to limited computing and storage capabilities, a preselection of events needs to be performed to keep the event rate low. Therefore, the CMS experiment works with a trigger system [62] that selects as many events as possible with a rate that can be processed by the computing farms. The CMS trigger is split in two levels: The hardware based level-1 trigger (L1) and the software based high level trigger (HLT).

The level-1 trigger is the first part of the CMS trigger system. It depends on the electronics of the calorimeters and the muon system. The tracker does not yet contribute to the L1 system, but a level-1 track trigger is planned for the phase-II of the LHC [63]. The L1 trigger does not use the full object information, but only some characteristic information like the energy deposit in the calorimeter and the hits in the muon system. The information of the local muon and calorimeter triggers are then combined in the global muon and calorimeter triggers. Afterwards, it is send to the global trigger which finally decides if an event passes the L1 trigger or not. The L1 trigger reduces the output rate from 40 MHz to 100 kHz. Events that pass the L1 trigger are collected by the data acquisition (DAQ) subsystem and passed on to computer farms for further event processing. A summary of the L1 trigger system in Run-2 is shown in Fig. 3.9.

After the events are send to the computer farms, they are processed in the high level trigger (HLT). The high level trigger is software based and includes the full event information. For example, while the L1 trigger only depends on the calorimeter and muon system, the HLT does also include tracker information. Based on the L1 trigger object (electron/photon, muon, jet), a more advanced selection is performed. In this analysis, muon, electron, photon, and missing transverse energy HLT will be

used. The HLT also decides with which rate events with a certain object are selected. If all events are selected like it is done for triggers in this analysis, the trigger type is called "unprescaled". If only some of the events are selected, the trigger is called "prescaled". The HLT reduces the event rate further to about 100 Hz.

3.2.6. Computing and Analysis Framework

All the data passing the HLT are sent to computer centers (Tiers) [65] distributed around the world where they are stored and further reconstruction steps are done. One copy of the raw data is saved at the Tier-0 at CERN. Tier-1 computer centers are used to save and process the data, while Tier-2 computer centers are used for a smaller amount of reconstructed data and simulated events and to store finished samples. The data of the CMS experiment is reconstructed and analysed based on the CMS Software (CMSSW) [66] which is also used for the simulation and reconstruction of background processes. There are different data formats that can be used depending on the level of reconstruction that is needed. For analyses that need fully reconstructed events, the AOD (Analysis Object Data) [67] or MINIAOD format is used. The AOD format includes the full reconstruction and Physics Analysis Toolkit (PAT) [68, 69] sequence of CMS, resulting in high level objects where only identification variables need to be applied. The MINIAOD format has a reduced number of information, only including the most important variables. Since this is all that is needed for this analysis, the MINIAOD format is used. The MINIAOD format is then further analysed within the "Three A Physics Analysis Software" (TAPAS) [70] framework developed at the III. Physics Institute A at the RWTH Aachen University. The TAPAS skimming software extracts the important information from the MINIAOD format and saves them in .pxlio files [71, 72] on the dCache [73] in Aachen. These .pxlio files can then be analysed with the PxlAnalyzer of the TAPAS framework. The analysis ran on the Tier-2 center in Aachen, resulting in ROOT [74] files that are used for the plotting of the final distributions and the calculation of the final results.

CHAPTER 4

Signal Properties

Before the details of the object reconstruction and identification will be discussed, it is important to take a look at the signal properties since they have a large influence on the object selection. For this purpose, characteristic distributions of the signal will be shown and discussed in this chapter.

As described earlier in this thesis, a search for heavy charged resonances $V^{\pm}$ with spin-1 that decay subsequently to two bosons, namely a WZ or Wh pair, which then decay via $W \to \ell\nu_\ell$ and $Z/h \to \tau\tau$ is performed. The final state that results from this decay cascade consists of one charged lepton from the W decay and two tau leptons [1]. The two tau leptons can afterwards also decay either to hadronic taus ($\tau \to \tau_h\nu_\tau$) or leptons ($\tau \to \tau_\ell\nu_\ell\nu_\tau$)[2]. In the following plots, τ_h refers to the visible hadronic part of tau decays and τ_ℓ to the visible leptonic part. In principle, 18 final states are possible with this signature. Events with hadronic tau decays from the W are not included in the analysis since they are suppressed by 35 % due to the branching fraction of hadronic tau decays and they have a lower reconstruction efficiency, decreasing the sensitivity of these channels. This is also the case for events with fully leptonic $h \to \tau\tau$ decays since they make up only 12 % of the full branching fraction. Taking this into account, six channels are left for this analysis, namely the channels with W decays to electrons and muons and fully hadronic or semileptonic $Z/h \to \tau\tau$ decays. However, the branching fractions of the channels that are not analysed are still included. Tab. 4.1 summarizes the final states and shows if they are analysed or not. The neutrinos will not be reconstructed, but they influence the missing transverse energy of the event. Since the kinematics of the Z and h boson are similar in this analysis, in most cases only the characteristics of the Wh decay will be shown.

	$W \to e\nu$	$W \to \mu\nu$	$W \to \tau\nu$
$Z/h \to \tau_h\tau_h 2\nu$	**YES**	**YES**	**NO**
$Z/h \to \tau_e\tau_h 3\nu$	**YES**	**YES**	**NO**
$Z/h \to \tau_\mu\tau_h 3\nu$	**YES**	**YES**	**NO**
$Z/h \to \tau_e\tau_e 4\nu$	**NO**	**NO**	**NO**
$Z/h \to \tau_\mu\tau_\mu 4\nu$	**NO**	**NO**	**NO**
$Z/h \to \tau_\mu\tau_e 4\nu$	**NO**	**NO**	**NO**

Table 4.1.: List of possible final states and if they are analysed within this thesis.

After discussing which final states are analysed, one can have a more detailed look at the signal kinematics. Since the kinematics in most channels are the same, they are split into two categories: Fully hadronic, including $\ell\tau_h\tau_h + E_T^{miss}$ final states and semileptonic, including $\ell\tau_\ell\tau_h + E_T^{miss}$ final states. The additional neutrino in the semileptonic final states slightly changes the signal kinematics.

[1] Leptons from the decay chain $W \to \tau\nu \to \ell\nu_\tau\nu_\tau\nu_\ell$ are treated as leptons directly arising from the W decay

[2] Starting from now, there will be no distinction between the lepton families for neutrinos, since they have the same influence on the analysis.

The heavy charged particle, from now on called W′, is expected to be produced in the center of the interaction point due to its large mass. It then decays to two boson, one W boson and one Z/h boson. The Higgs boson is expected to have a mass of 125 GeV. If the mass of the W′ increases, the two bosons are effected in two ways: First, they are produced more and more back-to-back, their $\Delta\phi$ gets close to π, and second, they both get a high transverse momentun since $M_{W'} \gg M_V$. Fig. 4.1 shows the transverse momenta of the W, Z, and Higgs (h) boson and the $\Delta\phi$ between the W and the Higgs boson for different W′ masses on generator level. It can be seen that for high masses the transverse momenta of the bosons peak at $M_{W'}/2$ and more importantly, that it exceeds the threshold of 500-600 GeV. For transverse momenta above this threshold, the decay products are collimated, as it will be discussed later in this chapter. It is also visible that the two bosons are produced back-to-back as expected which is also important since it influences the reconstruction of the missing transverse

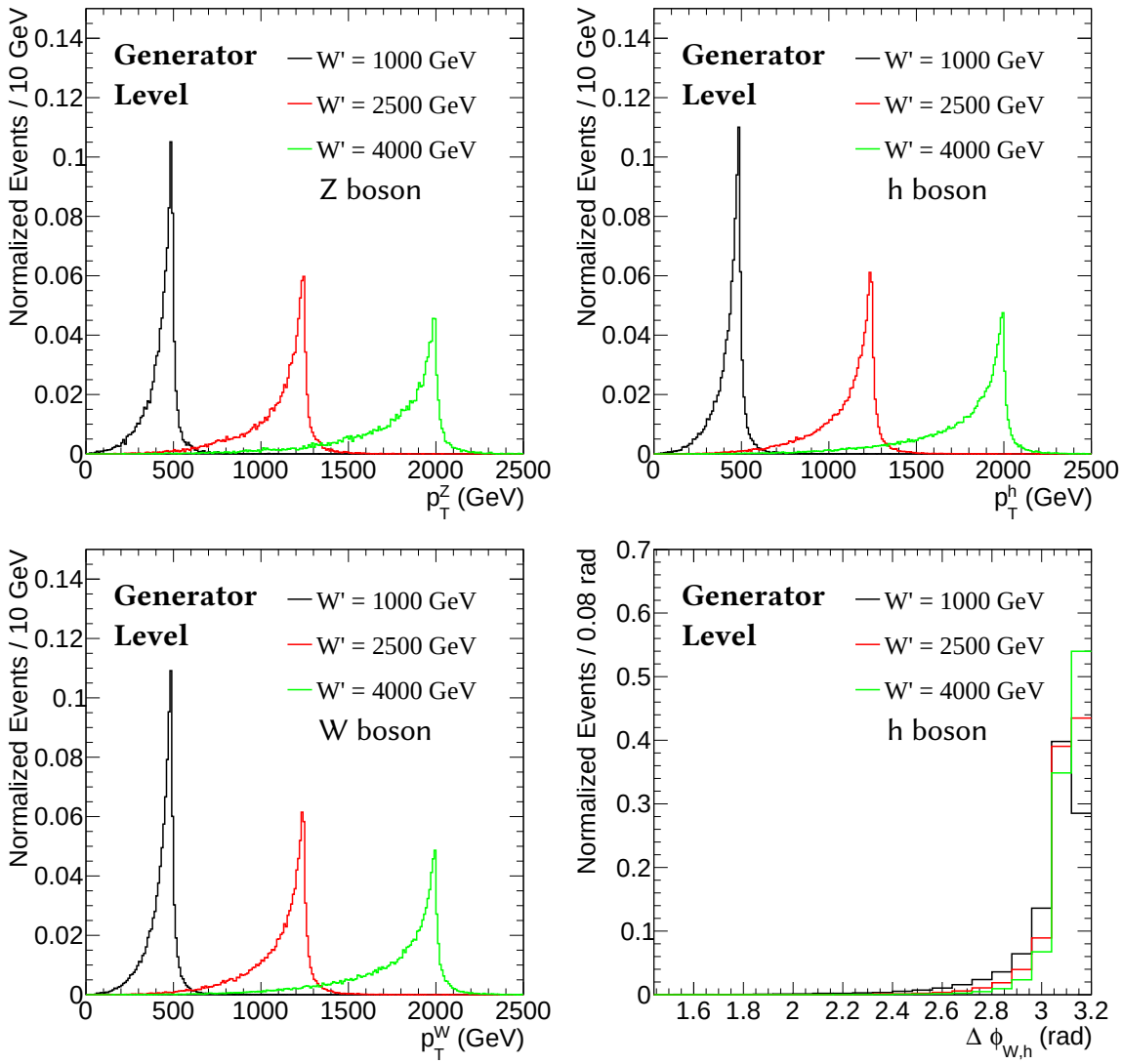

Figure 4.1.: Characteristic distributions of the two bosons from the W′ decay for different W′ masses on generator level. Top left: Transverse momentum of the Z boson, top right: Transverse momentun of the Higgs boson, bottom left: Transverse momentum of the W boson, bottom right: $\Delta\phi$ between the W boson and the h boson.

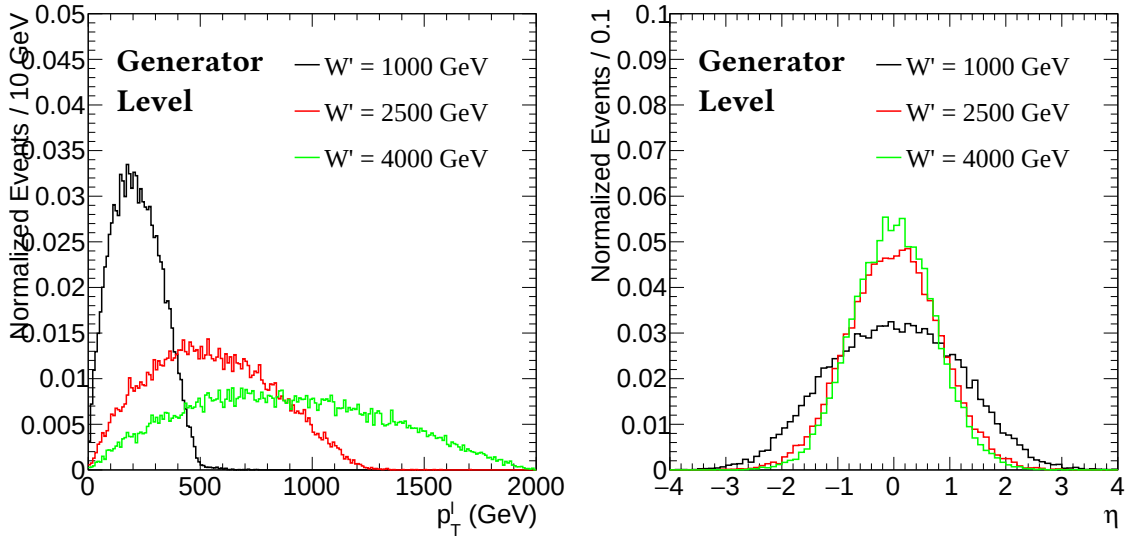

Figure 4.2.: Kinematic characteristics of the lepton from the W decay for different W′ masses on generator level. Left: Transverse momentum p_T^ℓ, right: Pseudorapidity η.

energy.

After the kinematics of the bosons have been discussed, the next step is to describe their decay particles, starting with the charged lepton from the W decay. Fig. 4.2 shows the transverse momentum and the pseudorapidity of this lepton for different W′ masses. Since the W decay is a two-body decay and the masses of the charged lepton and the neutrino are much smaller than the W mass, their transverse momenta peak a bit below 1/2 of the boson p_T and 1/4 of the W′ mass. The transverse momentum of the lepton is mostly above the trigger threshold for single lepton triggers which is 115 GeV for the highest non-isolated single lepton trigger. The lepton from the W decay should be well isolated since the decay products of the Z/h boson end up in the opposite direction and therefore, it can be used to trigger the signature. In case of the pseudorapidity, the lepton from the W decay is produced more centrally for increasing W′ masses. This is a consequence of the W′ production, which is also produced more centrally since most of the energy from the parton interaction is used to generate the larger masses.

In case of the decay of the Z/h boson, the semileptonic and hadronic final states need to be seperated. In the fully hadronic case, the decay of the boson results in two hadronic taus (τ_h) and some additional neutrinos. Fig. 4.3 shows the transverse momenta and the pseudorapidity of the fully hadronic case for the leading and the subleading hadronic tau. While the average transverse momentum of the leading hadronic tau peaks in the medium-p_T region although it has an additional decay chain included ($\tau \to \tau_h \nu$), the subleading hadronic tau has a constantly falling shape with its maximum at 0. To keep the signal efficiency high, it will be important to decrease the p_T threshold of the subleading tau as much as possible.
For the pseudorapidity, it can be seen that most of the hadronic taus end up in the detector acceptance ($|\eta| < 2.3$) so that only a small loss of efficiency due to the acceptance can be expected.

In the semileptonic case, it can be distinguished between the hadronic and the leptonic tau. Fig. 4.4 shows the transverse momenta and the pseudorapidity for the leptonic and the hadronic tau from the Z/h decay for different W′ masses. It can be seen that the kinematic differs much in comparison to the fully hadronic decay channel. Since there is only one hadronic tau, it does not have a peak

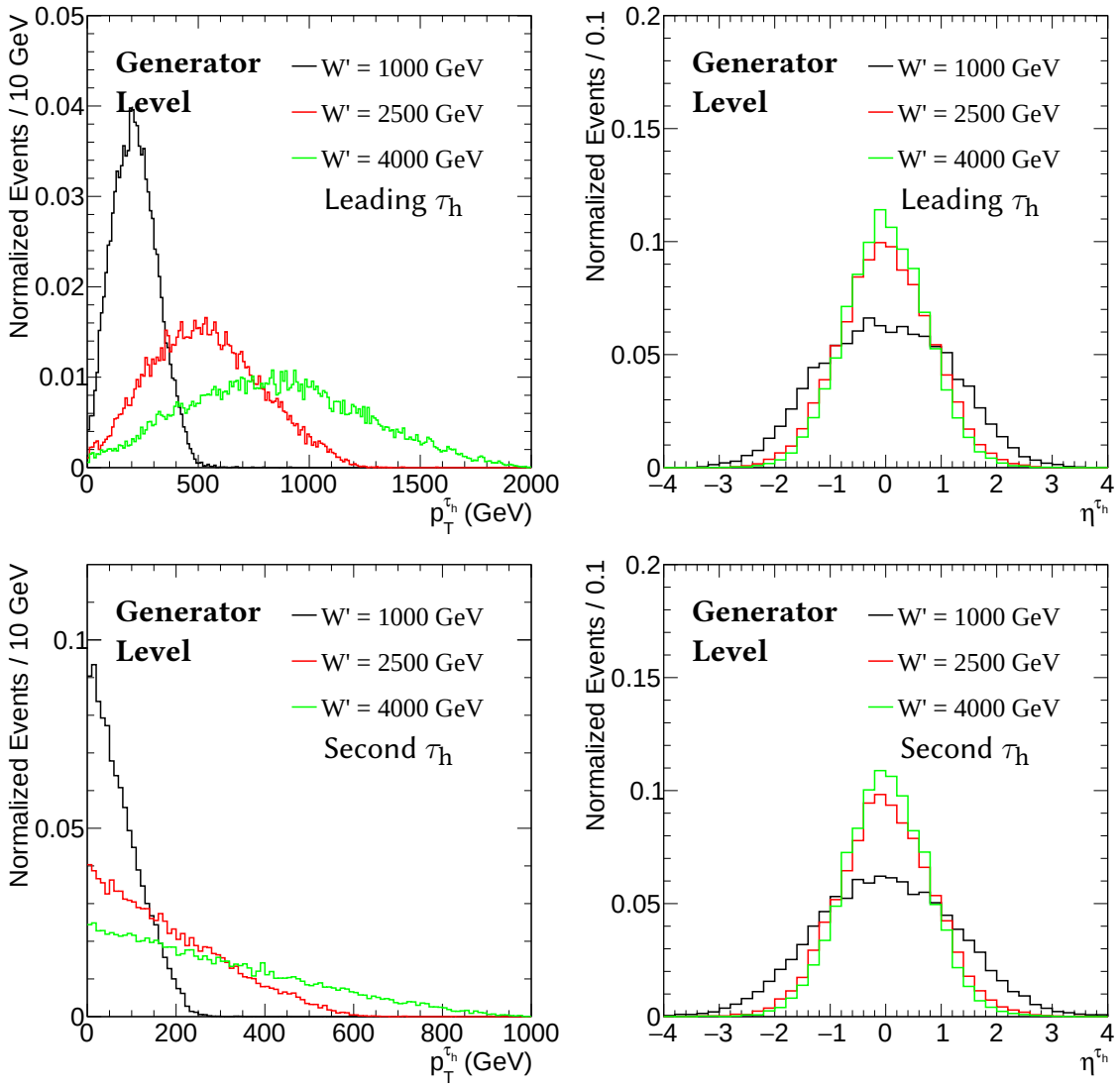

Figure 4.3.: Kinematic characteristics of the hadronic taus from the Z/h decay for different W′ masses in the fully hadronic case on generator level. Top left: Transverse momentun of the leading hadronic tau, top right: Pseudorapidity of the leading hadronic tau, bottom left: Transverse momentum of the second leading hadronic tau, bottom right: Pseudorapidity of the second leading hadronic tau.

like structure as the leading tau in the fully hadronic final state, but it shows a falling p_T spectrum. However, the slope of the distribution is flatter than for the subleading tau in the fully hadronic channel, resulting in a larger fraction of hadronic taus in the medium-p_T region.
As the leptonic decay of a tau is a three body decay, less energy transfers to the tranverse momentum of the lepton. Therefore, its p_T-distribution has a constantly falling shape with a high slope and a large fraction of events in the low-p_T region. For this reason, the p_T threshold of these leptons needs to be as small as possible.
Same as for the hadronic final states, it can be expected that most of the particles pass the detector acceptance which is $|\eta| < 2.5$ for electrons and $|\eta| < 2.4$ for muons.

After discussing the characteristics of the charged leptons, the next step is to describe the influence

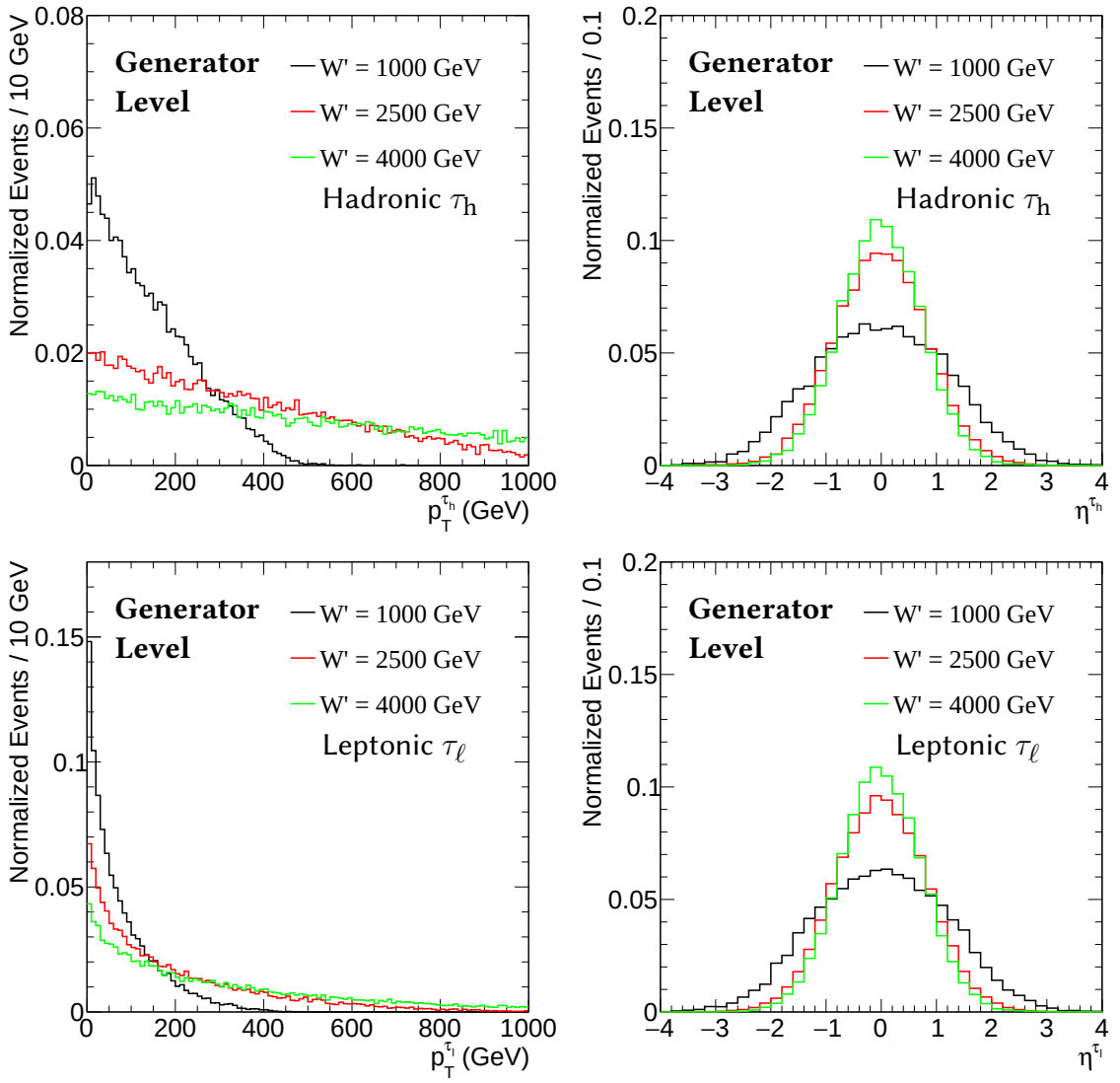

Figure 4.4.: Kinematic characteristics of the tau decays from the Z/h decay for different W′ masses in the semileptonic case on generator level. Top left: Transverse momentun of the hadronic tau, top right: Pseudorapidity of the hadronic tau, bottom left: Transverse momentum of the leptonic tau, bottom right: Pseudorapidity of the leptonic tau.

of the neutrinos. Neutrinos cannot be detected by the CMS experiment as they are only weakly interacting particles. Since neutrinos end up as a difference in the transverse momentum balance, they are often visible as missing transverse energy. However, in the analysed signature, there are two sources of neutrinos per event, namely one neutrino from the W decay and two or three (only taking into account fully hadronic and semileptonic final states) neutrinos from the two tau leptons. In contrast to searches for $W' \to \ell\nu$ or $W' \to Wh \to qq\tau\tau$ where all neutrinos are boosted in the same direction, the neutrinos in the here analysed signature are boosted in opposite directions. As a result, the missing transverse energy does not represent the full transverse energy or momentum of the neutrinos, but their difference. Fig. 4.5 shows the missing transverse energy and the $\Delta\phi$ between the E_T^{miss} direction and the lepton from the W decay for the semileptonic and fully hadronic final states. As one can see, the E_T^{miss} distribution peaks already at about 50-100 GeV for W′ masses above

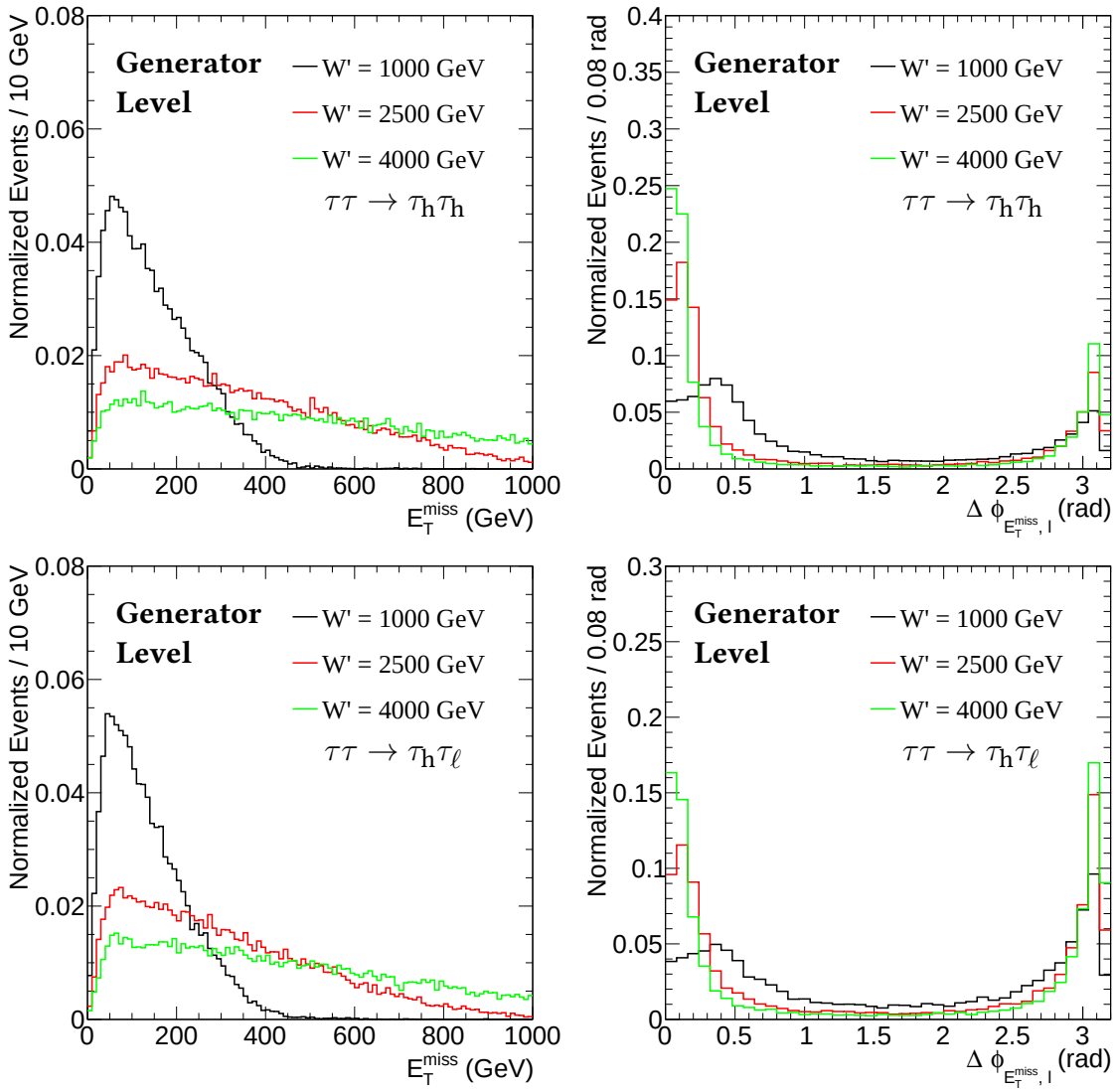

Figure 4.5.: Influence of the neutrinos on the missing transverse energy E_T^{miss} for the fully hadronic (top) and semileptonic (bottom) final states for different W′ masseson generator level. Left: Missing transverse energy E_T^{miss}, right: $\Delta\phi$ between the missing transverse energy and the lepton from the W decay.

1 TeV, although about 50 % (a bit more in the semileptonic channels) of the final state particles are neutrinos. In contrast to the lepton, there is no real difference visible between the semileptonic and the fully hadronic analyses for the expected missing transverse energy. However, this is not the case for the angle between the lepton and the E_T^{miss}. The $\Delta\phi$ distribution shows some small differences. In the hadronic case, there are more events expected with $\Delta\phi$ in the direction of the W boson ($\Delta\phi <$ 1) than in the direction of the Z/h boson ($\Delta\phi >$ 2). This effect arises due to the different numbers of neutrinos from the Z/h boson decay chain in the semileptonic channels leading to a different energy distribution. In the semileptonic case, the Z/h leg dominates due to the additional neutrino from the leptonic tau decay. In general, it is visible which direction of the missing transverse energy is prefered for each channel, but the differences are too small to use this distribution for further selections.

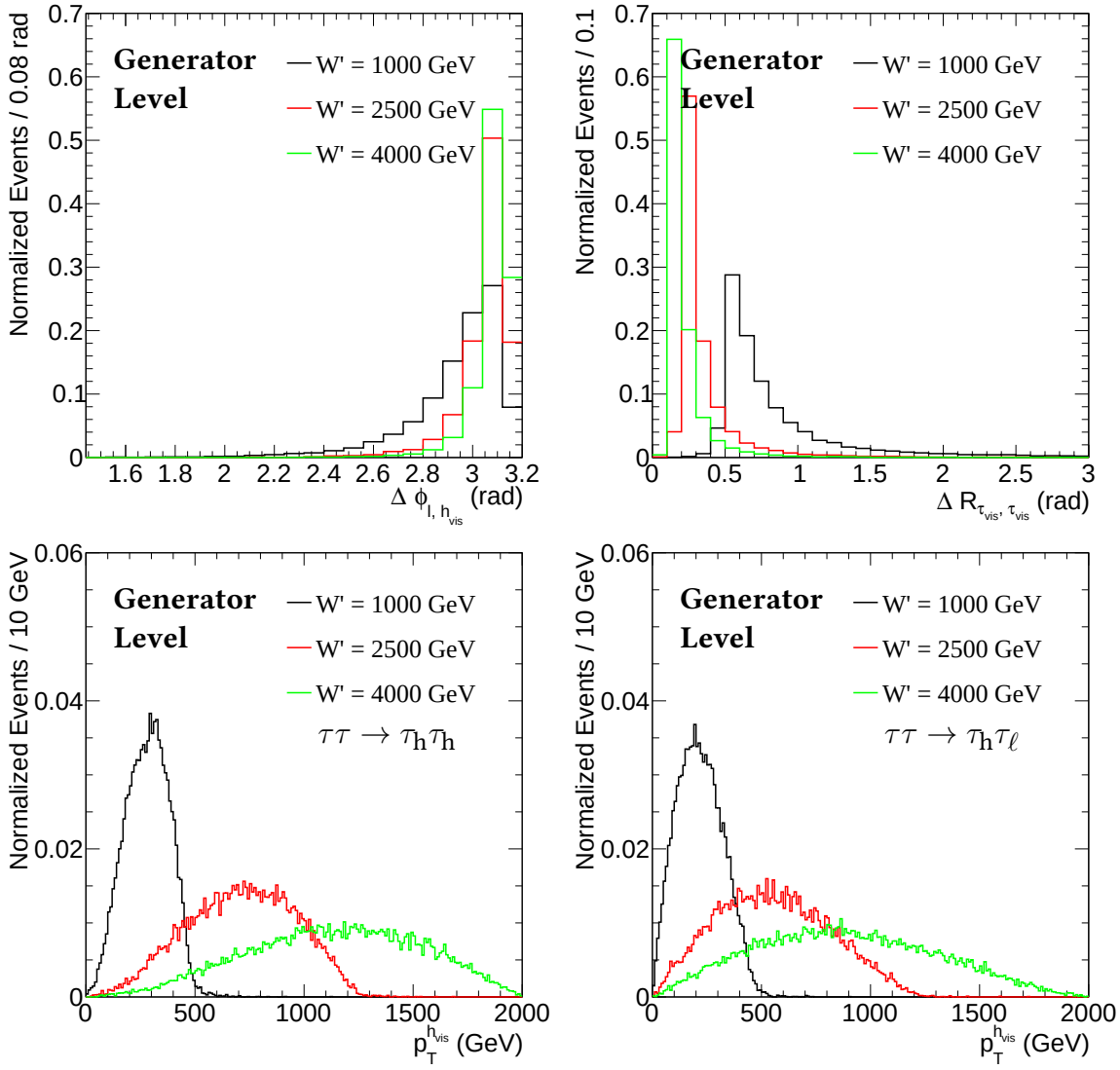

Figure 4.6.: Kinematic distributions on generator level for the final state objects for different W′ masses on generator level. Top left: $\Delta\phi$ between the lepton from the W decay and the reconstructed visible Higgs, top right: ΔR between the two tau decay products, bottom left: Visible p_T of the hadronic Higgs boson decay chain $h \to \tau\tau \to \tau_h\tau_h 2\nu$, bottom right: Visible p_T of the semileptonic Higgs boson decay chain $h \to \tau\tau \to \tau_h\tau_\ell 3\nu$.

The absence of the full neutrino information has additional effects on the analysis. While other analyses like $W' \to Wh \to qq\tau\tau$ or $W' \to Wh \to \ell\nu qq$ can use the boosted topology and the E_T^{miss} to reconstruct the Z/h or W mass, this is not possible in this analysis. Therefore, it is mainly based on the visible objects. Fig. 4.6 shows some of the most important distributions of the visible objects: The angle $\Delta\phi$ between the lepton from the W decay and the combination of the visible part of the h boson, the transverse momentum of the visible h boson, and the angle ΔR between the two visible tau decay products. While the $\Delta\phi$ confirms the back-to-back signature also for the combination of the decay products, the visible p_T distributions show a peak at about 1/4 to 1/3 of the resonance mass. Here, one can also see that the momentum in the semileptonic channel is slightly shifted to lower energies, as one would expect due to the additional neutrino. The ΔR distribution is the most important one shown here. It is visible that the distance between the two tau decay products gets

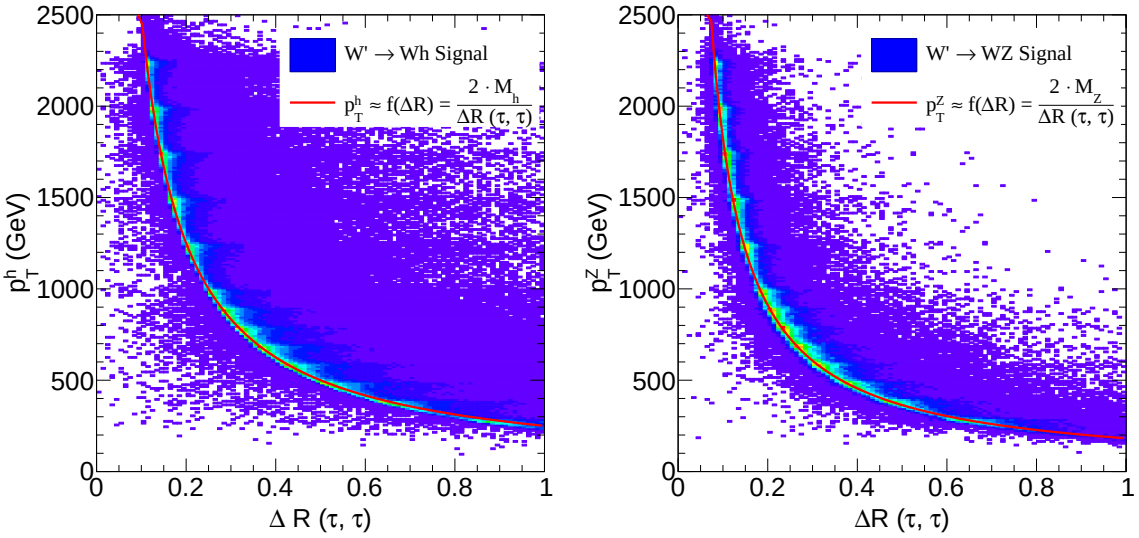

Figure 4.7.: Two-dimensional $\Delta R - p_T^V$ distributions for Wh (left) and WZ (right) signal on generator level. The red graph corresponds to the approximation $p_T^V \approx 2 \cdot M_V / \Delta R(\tau, \tau)$.

smaller than 0.5 for resonance masses above 1 TeV for a huge amount of events. This effect arises from the boost of the Z/h boson. Fig. 4.7 shows the two-dimensional ΔR-p_T distribution for Wh (left) and WZ (right) events. The main part of the events lies on the red line based on the formula $p_T^V \approx 2 \cdot M_V / \Delta R(\tau, \tau)$ meaning that the ΔR depends on the inverse transverse momentum and on the mass of the vector boson. The derivation of this formula can be found in App. A. If one compares Higgs and Z boson decays, the decay products of the Z decay are expected to be 35 % closer. This effect is important for the signal efficiency of both signal hypothesis, as it will be discussed in Sec. 6.3.6. In CMS, isolation requirements are applied for each object. In most cases, these isolation requirements fail if additional particles are detected within a distance $\Delta R < 0.4$. This means that a decrease of efficiency can be expected for resonance masses above the TeV scale if the standard CMS identification and isolation criteria are applied. The solution to compensate this effect will be presented in Chap. 5.

In the end, it needs to be discussed which kinematic distribution is the most sensitive for this charged resonance search and therefore should be used for the final statistical interpretation of the analysis. As there is some information about the energy missing, a full invariant mass reconstruction is not possible. Therefore, one has to use another mass variable. For this analysis, three candidates have been tested:

1. The visible mass M_{vis}, reconstructed from the visible objects of the event, namely the lepton from the W decay and the two visible tau decay products. The visible mass does not include the information from the missing transverse energy.

2. The transverse mass M_T, calculated based on the combination of the visible objects and the measured E_T^{miss}. It uses the full event information.

3. The sum of the transverse momenta $\sum p_T$, calculated by adding up the transverse momenta of the visible objects and the E_T^{miss}. Same as the transverse mass, it uses the full event information.

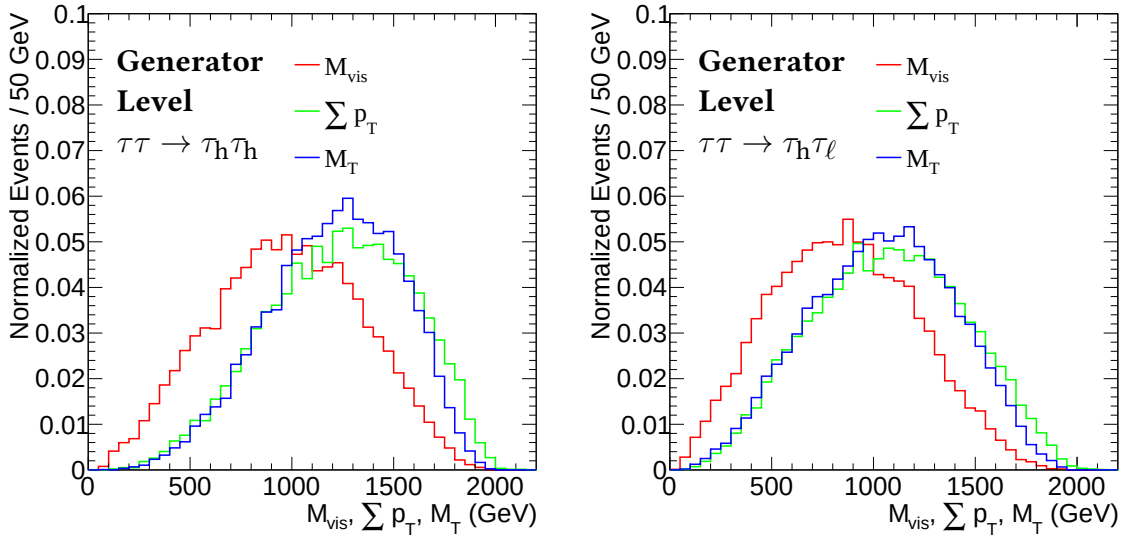

Figure 4.8.: Comparison of the three mass variable for a W′ mass of 2 TeV on generator level. Left: Fully hadronic final states, right: semileptonic final states.

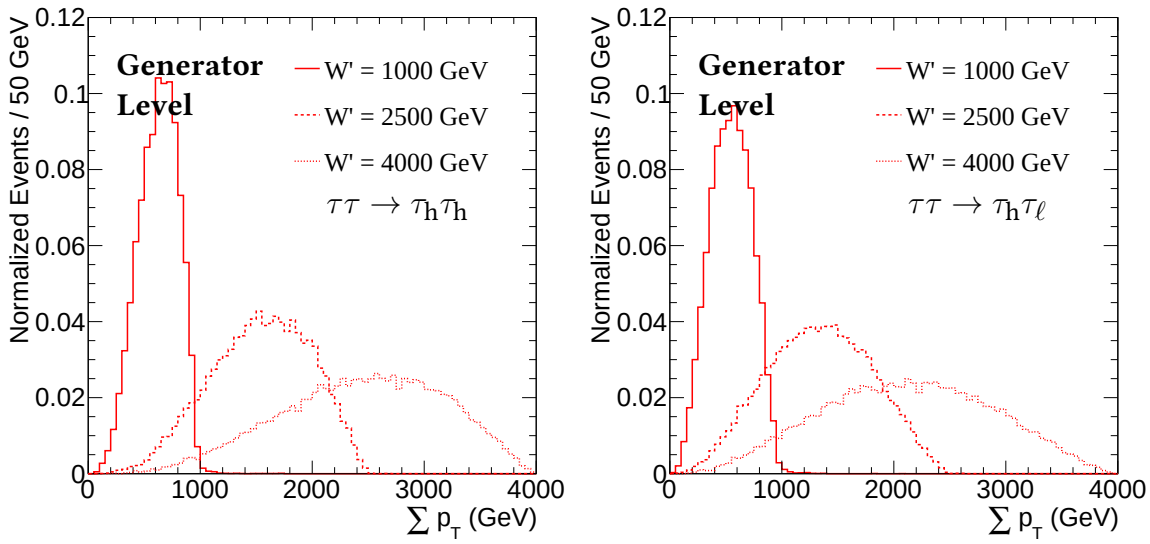

Figure 4.9.: $\sum p_T$ distribution for different W′ masses on generator level. Left: Fully hadronic final states, right: semileptonic final states.

Fig. 4.8 shows a comparison between the three mass variables for fully hadronic and semileptonic channels. The M_T and the $\sum p_T$ look quite similar while the visible mass distribution is shifted to lower masses due to the absence of E_T^{miss}. Since the visible mass does include less information and peaks at lower p_T values, it is not used for the final result. In case of the M_T and the $\sum p_T$, the differences are very small. The $\sum p_T$ goes to slightly higher values, but it has a broader peak. The M_T distribution has a more narrow resonance peak. As both distributions show a similar behaviour, the final result is not really effected by the choice of the distribution. Since the tail of the $\sum p_T$ distribution goes to slightly higher values, it will be used in the end. Fig. 4.9 shows the $\sum p_T$ distribution for different W′ masses for both final states. In the hadronic channel, the $\sum p_T$ peaks at

about 70 % of the resonance mass. In the semileptonic channel where the visible part of the events is lower, but the E_T^{miss} is not much larger, the distribution is shifted to lower masses, resulting in a peak at about 60 % of the resonance mass.

CHAPTER 5

Object Reconstruction and Identification

In this chapter, the reconstruction and identification requirements for the physics objects will be described. This also includes special reconstruction techniques for nearby objects.

5.1. Particle-Flow Algorithm

Modern particle detectors are built based on an onion-like structure with different subdetectors. This is also the case for the CMS detector, as discussed in Sec. 3.2. Particles travel trough the detector and leave characteristic information in the subdetectors. For example, a muon produces hits in the silicon tracker and in the muon chambers, but leaves also small energy deposits in the two calorimeters. Electrons on the other hand produce hits in the silicon tracker and showers in the ECAL, but they do not reach the outer detector system. Based on this concept, all particles have their own signature and therefore, from an historical point of view, each particle has its own combination of subdetectors that is used for its reconstruction. The CMS experiment follows a different approach, called Particle-Flow (PF) [75–77]. In contrast to other experiments where particles are reconstructed more independent from each other, the PF algorithm leads to a particle reconstruction based on the global event description. This results in very high performances in the jet and hadronic tau reconstruction, the measurement of missing transverse energy, and the identification of electrons and muons. Due to the global event description, a precise identification of particles from pileup is possible leading to an efficient pileup mitigation. The PF approach also affects the isolation requirements, as all energy deposits within the isolation cone are taken into account. In this particular analysis, the PF algorithm helps to handle energy deposits from hadronic tau decays within the lepton isolation cone in highly boosted boson decays. This would not be possible with an independent particle reconstruction.

The PF algorithm collects the tracks from charged particles, energy deposits in the calorimeters and tracks from muons in the muon system. As muons are the easiest to identify, the algorithm starts by removing tracks from the tracker and the muon system that can be matched and identified as muons. Energy deposits in the calorimeters that can be matched with the muon trajectory are also taken into account and removed from the collection. Afterwards, electrons are identified by matching tracks to energy deposits in the ECAL. The tracks and deposits that are left are then sorted into charged hadrons, neutral hadrons, and photons. While charged hadrons can be identified using the corresponding track, neutral hadrons and photons are distinguished based on their expected resolution in the calorimeters.

5.2. Electrons

5.2.1. Reconstruction

The summary of the electron reconstruction is based on [78]. In the electron reconstruction, tracks from the silicon detector are matched to energy deposits in the ECAL. Two approaches are combined: The standalone approach where just the tracks and the ECAL deposits are taken into account, and the PF approach where the global event information is taken.

Energy Clustering in the ECAL

For the clustering of the energy, two main effects need to be considered: The impact of photon radiation while the electron travels trough the detector, especially the tracking system, and the energy loss due to bremsstrahlung in the ECAL. While the consequences of the second effect are rather small (97 % of the energy of an electron with p_T = 120 GeV are deposit in a 5×5 crystal array), the first effect has a large impact. In regions where the intervening material is minimal ($\eta \approx 0$), 33 % of the electron energy is radiated before the electron reaches the ECAL while in regions with thick material ($|\eta| < 1.4$), 86 % are radiated [78]. These energy losses are spread mainly in ϕ direction, the impact in η direction is negligible, except for very low energy electrons. For an accurate energy measurement, these energy losses due to photon radiation need also to be measured.
In the ECAL barrel (EB), the so called hybrid algorithm is used. The starting point is the crystal that contains the highest energy, the "seed crystal". Around this crystal, arrays of 5×1 crystals in $\eta \times \phi$ direction are added if their energy deposit is higher than the minimum value. These arrays are then combined to clusters, and afterwards to superclusters (SC), if the energy of a cluster is above 0.35 GeV.
In the endcaps, a different algorithm, called multi-5×5 algorithm, needs to be used since the crystals are not arranged in an $\eta \times \phi$ geometry, starting again based on the crystal with the largest energy deposit. Around this initial seed, the energy is collected in clusters of 5×5 crystals. These crystals are then again grouped in SC, and later the energy weighted positions of all clusters that are part of the SC are extrapolated to planes of the preshower. Preshower energies within $\eta \pm 0.15$ and $\phi \pm 0.15$ rad around these clusters are in the end added to the SC energy.
In both cases, barrel and endcap, the SC energy corresponds to the sum of energies in the clusters they are built off, and the position is reconstructed based on the energy weighted mean of these clusters.

Track Reconstruction

In principle, electron tracks can be reconstructed in the same way as for the other particles, based on a Kalman filter [79]. However, since electrons radiate a large amount of their energy in the tracker, this procedure would result in a lower hit-collection efficiency. Therefore, a slightly different method for the electron tracking is used.

The seeding step starts by selecting the innermost two or three hits in the tracker system as a starting point for the track reconstruction. For the selection of this initial seed, two different complementary approaches are used, namely the ECAL and the tracker based seeding. In the ECAL based seeding algorithm, the energy and position measurement in the SC is used for an estimation of the electron trajectory in the first tracker layers by extrapolating it towards the collision point. Based on a comparison between SC and tracker hits, seeds for each SC are produced and selected for the electron

track reconstruction. The tracker based seeding algorithm makes use of the Kalman filter algorithm for charged particles, but with an additional extrapolation to a SC. If the effect of bremsstrahlung is negligible, the tracker based seeding is very accurate. Therefore, it is especially reliable for low-p_T, but also for non-isolated electrons in busy environments.

In the tracking step, the electron seeds are taken as the base for the track building and fitting. The track is reconstructed based on a combinatorial Kalman filter method with an additional modelling of the energy loss due to bremsstrahlung with help of a Bethe-Heitler function. Since bremsstrahlung can affect the electron trajectory, the compatibility restriction between predicted and found hits per layer is loosened. This method helps to improve the reconstruction efficiency.
After the collection of the hits, a Gaussian sum filter (GSF) [80] fit is done as an estimation of the track parameter, taking into account the energy losses in each tracker layer using Gaussian distributions. The result of this fitting method are so called GSF-tracks which are used as the base for the electron reconstruction.

5.2.2. Identification

In addition to the reconstruction of electrons, several quality selection criteria are applied to ensure a high electron purity and a small misidentification rate from other objects that are reconstructed as electrons. These quality criteria are called identification criteria (ID). There are four ID working points for electrons and each working point was developed for a special purpose. The four working points are, in order of their discrimination power against misidentified electrons, the tight, medium, loose, and veto ID [81]. All of them are using variables to select good electrons based on the shower shape, the tracking, and the isolation with respect to other objects. The tight ID is used in regions where it is likely to get electrons from misidentified jets, for example in analyses with low-p_T electrons or low lepton multiplicities, aiming for a good discrimination against other objects. However, the high discrimination power results in a lower identification efficiency of prompt electrons. The medium ID has some looser selection criteria and is therefore important in regions where one needs a high signal efficiency and good background discrimination at the same time like for W and Z events. The loose ID is then used in analyses where a high signal efficiency is very important and the background does also mainly arise from prompt electrons. A good example for such analyses are multilepton final states where the background mainly arises from multiboson interactions, but not from jets, and where a loss of efficiency for each electron has a higher impact than in events with low lepton multiplicity. The veto ID is used, as its name indicates, to veto against additional electrons in the event. It is typically not used for the selection of signal events. All working points are split in barrel region ($|\eta| < 1.479$) and endcap region ($1.479 < |\eta| < 2.5$) [81]. The different working points and their selection values are summarized in Tab. 5.1. For high-p_T electrons there is a dedicated identification selection, called HEEP (High energy electron photon) ID, which will not be used in this analysis since it does not rely on the standard PF isolation that is needed later to correct the isolation value by removing contributions from hadronic tau decays (see Sec. 5.5).

In case of electrons, the isolation is part of the ID. An electron is defined as well isolated if it passes the relative PF isolation requirement with the so called effective area (EA) pileup correction [82]. The isolation variable for the requirement is given by:

$$I_{PF}^{rel} = \left(\sum_{\text{charged had.}} p_T + \max \left[0, \sum_{\text{neutral had.}} p_T + \sum_{\gamma} p_T - \rho \cdot A_{eff} \right] \right) / p_T^e \tag{5.1}$$

Variable	Tight ID	Medium ID	Loose ID	Veto ID
$\sigma^{5\times5}_{i\eta i\eta}$ <	0.00998 (0.0292)	0.00998 (0.0298)	0.011 (0.0314)	0.0115 (0.037)
$\lvert d\eta_{In}\rvert$ <	0.00308 (0.00605)	0.00311 (0.00609)	0.00477 (0.00868)	0.00749 (0.00895)
$\lvert d\phi_{In}\rvert$ <	0.0816 (0.0394)	0.103 (0.045)	0.222 (0.213)	0.228 (0.213)
H/E <	0.0414 (0.0641)	0.253 (0.0878)	0.298 (0.101)	0.356 (0.211)
Rel. PF iso (EA) <	0.0588 (0.0571)	0.0695 (0.0821)	0.0994 (0.107)	0.175 (0.159)
$\lvert 1/E - 1/p\rvert$ <	0.0129 (0.0129)	0.134 (0.13)	0.241 (0.14)	0.299 (0.15)
Missing hits <	1 (1)	1 (1)	1 (1)	2 (3)
pass conversion veto	yes (yes)	yes (yes)	yes (yes)	yes (yes)

Table 5.1.: Electron identification criteria [81] for all four working points for the barrel (endcap) region.

where $p_T^{\text{charged had.}}$, $p_T^{\text{neutral had.}}$, and p_T^{γ} are charged hadron, neutral hadron and photon candidates reconstructed by the PF algorithm within the isolation cone of the electron, ρ is the average energy density of the event, and A_{eff} is the effective area as a function of η and ϕ. An electron passes this selection criterion if the isolation value is smaller than the selection value from Tab. 5.1. Fig. 5.1 shows the electron identification efficiency for the loose and tight WP as a function of the electron p_T measured in W′ simulation events with a mass of 2.5 TeV for electrons that arise from the W decay. The higher efficiency for the loose WP is visible and both IDs reach their plateau at $p_T^e >$ 100 GeV. In this analysis, electrons can arise from W decays and $V \to \tau_e \tau_h$ (V = Z, h) decays. Since the electrons from the W decay are expected to have a high quality, they have to pass the tight ID requirement. The electrons from the V decay might suffer from efficiency losses due to collimated hadronic tau leptons. They have to pass the loose ID with modified isolation which will be described in section 5.5. The tight electron is required to have a tranverse momentum above 55 GeV as it needs to satisfy the trigger requirements while the loose electron only needs to have a p_T above 10 GeV. The pseudorapidity $|\eta|$ for both has to be smaller than 2.5, excluding the barrel-endcap overlap region between $1.4442 < |\eta| < 1.556$.

5.3. Muons

5.3.1. Reconstruction

The reconstruction of muons is based on [60, 83]. Muon tracks are reconstructed based on hits in the tracker and the muon system or, more precisely, in the three muon subdetectors DT, CSC and RPC. These hits are used to produce two kinds of tracks, namely the tracker-only track, entirely based on the tracker information, and the standalone-muon track based on the muon system. These two tracks are subsequently combined for a full muon reconstruction. Here, only the muon reconstruction steps that are important for the analysis of dibosons are discussed. Descriptions of other reconstruction algorithms, as they are used for example for very high-p_T muons, can be found in [60, 83].

Tracker-only Track

Tracker-only tracks rely completely on the information of the silicon tracker. Based on an iterative approach, several tracking algorithms with slightly changing logic are running and hits that are used in one iteration are removed before the next algorithm starts.

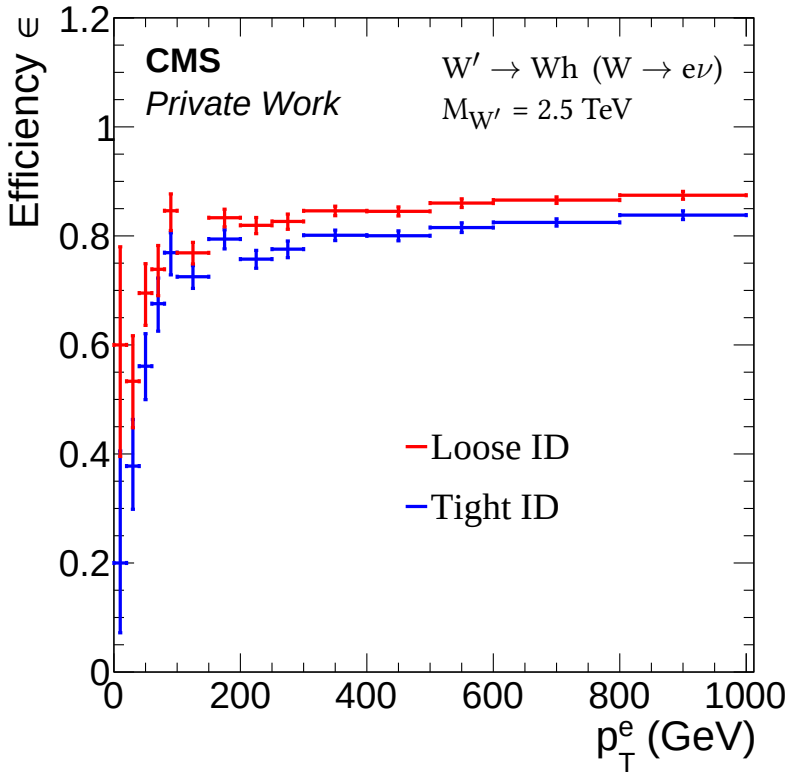

Figure 5.1.: Electron identification efficiency for tight and loose electrons as defined in Tab. 5.1 from the W decay w.r.t. the transverse momentum on generator level for a W′ mass of 2.5 TeV.

.

Standalone-muon Track

Standalone-muon tracks are completely reconstructed from hits in the muon system. Based on starting seeds built out of DT, CSC and RPC segments, the standalone track is reconstructed using a Kalman-filter [79] technique along the muon trajectory.

Tracker Muon

Tracker muons are reconstructed based on an inside-out approach, starting with the tracker-only track and propagating it to the muon system by matching the track to segments in the DTs and CSCs. Since at least one segment in the muon system matching the tracker-only track propagation is enough for a muon to be reconstructed as tracker muon, the tracker muon reconstruction does also have a high efficiency for muons with low transverse momentum (p_T < 6-7 GeV) where no standalone-muon track can be reconstructed.

Global Muon

In contrast to tracker muons, the global muon reconstruction is based on an outside-in approach, matching the standalone-muon tracks with the tracker-only tracks. After propagating pairs of the

two tracks to a common surface, a Kalman-filter is used to produce a combined fit starting from the standalone-muon track. The track with the lowest χ^2 is then used as the global muon. If tracker muons and global muon share the same inner track, they are combined to one candidate. About 99 % of all muons within the geometrical acceptance are reconstructed either as global muon or tracker muon.

Particle-flow Muon

The PF muon reconstruction combines the information from tracker muons and global muons with energy deposits in the calorimeters. This improves the muon reconstruction performance as more information is taken into account.

Muon Momentum

The momentum of muons is estimated using the so called *tune-p* algorithm [60, 83]. It selects the muon momentum based on the best goodness-of-fit information and the resolution from one of the following four tracking fits:

- *Inner-Track fit*: This fit is completely based on the hits in the inner tracker. Its momentum estimation is highly favoured for muons with $p_T < 200$ GeV.
- *Tracker-Plus-First-Muon-Station fit*: A refit of the global muon track is performed based on hits in the inner tracker and the first muon station.
- *Picky fit*: This fit method is optimized for events where muons shower in the muon system, starting again from the global muon track, but in muon stations with a large hit occupancy only hits that are compatible with the estimated muon trajectory are included in the refit [60].
- *Dynamic-Truncation fit*: This refit algorithm is optimized for events with muons that suffer from high energy losses in the muon system and therefore have a significantly stronger bending in the magnetic field.

The PF algorithm includes the information from the *tune-p* algorithm, but adds additional informations, for example from hits in the calorimeters or the missing E_T balance in the event, to estimate the muon p_T.

5.3.2. Identification

Same as for electrons, muons do also have some additional identification criteria applied on top of the reconstruction. The CMS muon object group provides five sets of identification criteria, the loose, medium, tight, soft, and high-p_T ID [84]. Since the soft ID is mainly developed for b-physics at low energies and the high-p_T ID is optimized for muons with $p_T > 200$ GeV, they will not be discussed in the following. This is also the case for the medium ID, as it is a combination of the loose and tight ID. Loose muons have to pass the following criteria [84]:

- The muon has to be reconstructed as a **PF muon** as discussed in Sec. 5.3.
- The muon has to be reconstructed as a **tracker muon or a global muon** as discussed in Sec. 5.3.

Since 99 % of all muons within the acceptance are reconstructed as global or as tracker muon and the PF muon reconstruction has a similar efficiency, the loose ID has its efficiency plateau at about 97-98 %. The tight muon ID has a larger number of selection requirements, these are [84]:

- The muon has to be reconstructed as a **PF muon**.
- The muon has to be reconstructed as a **global muon and tracker muon**.
- The χ^2 **of the global muon track fit has to be smaller than 10**. This requirement reduces the effect of hadronic "punch-throughs" and decays-in-flight.
- At least **one muon chamber needs to be included in the global-muon track fit**. This requirement affects only a small number of muons, as most muon candidates without those hits will not be reconstructed as global muons.
- There have to be **muon segments in at least two muon stations**. This selection suppresses also muon candidates from hadronic "punch-throughs" and decays-in-flight. In addition, this requirement keeps the ID consistent with the muon trigger where the same requirement is applied.
- The **transverse impact parameter of the tracker track with respect to the primary vertex d_{xy} has to be less than 0.2 cm**, reducing the impact of cosmic muons and decays-in-flight.
- The **longitudinal distance with respect to the primary vertex d_z has to be smaller than 0.5 cm**, suppressing the effect of cosmic muons, decays-in-flight and pileup tracks.
- The number of **tracker layers with hits has to be larger than five**. This requirement ensures a good p_T measurement as a large number of hits increases the quality of the track reconstruction.
- **At least one hit in the pixel detector**, reducing the effect of decays-in-flight and increasing the vertex reconstruction quality.

In contrast to electrons where the isolation is part of the ID criteria, for muons, it has to be applied on top of the ID. The relative PF isolation for muons is defined by

$$I_{PF}^{rel} = \left(\sum_{\text{charged had.}} p_T + \max \left[0, \sum_{\text{neutral had.}} p_T + \sum_{\gamma} p_T - 0.5 \cdot \sum_{\text{pileup}} p_T \right] \right) / p_T^{\mu} \tag{5.2}$$

where $0.5 \cdot \sum_{\text{pileup}} p_T$ is the pileup correction term ($\Delta\beta$ correction). There are two working points for the PF muon isolation. In this analysis, the loose WP will be used which is defined as $I_{PF}^{rel} < 0.25$. Fig. 5.2 shows the identification times isolation efficiency for loose and tight muons as a function of the muon momentum for muons that originate from the W decay in a W′ sample with a resonance mass of 2.5 TeV. The muon ID is more efficient than the electron ID, resulting in an efficiency plateau of 97 % for the loose ID and 93 % for the tight ID if the loose PF isolation is applied on top of the ID. Same as for electrons, muons from the W decay are expected to be tight muons and from the V (V = Z, h) decay chain to be loose muons. The tight muons are required to have a transverse momentum of $p_T > 55$ GeV to pass the trigger threshold and the loose muons to have a $p_T > 10$ GeV. Both types of muons have to be in the geometrical acceptance of $|\eta| < 2.4$.

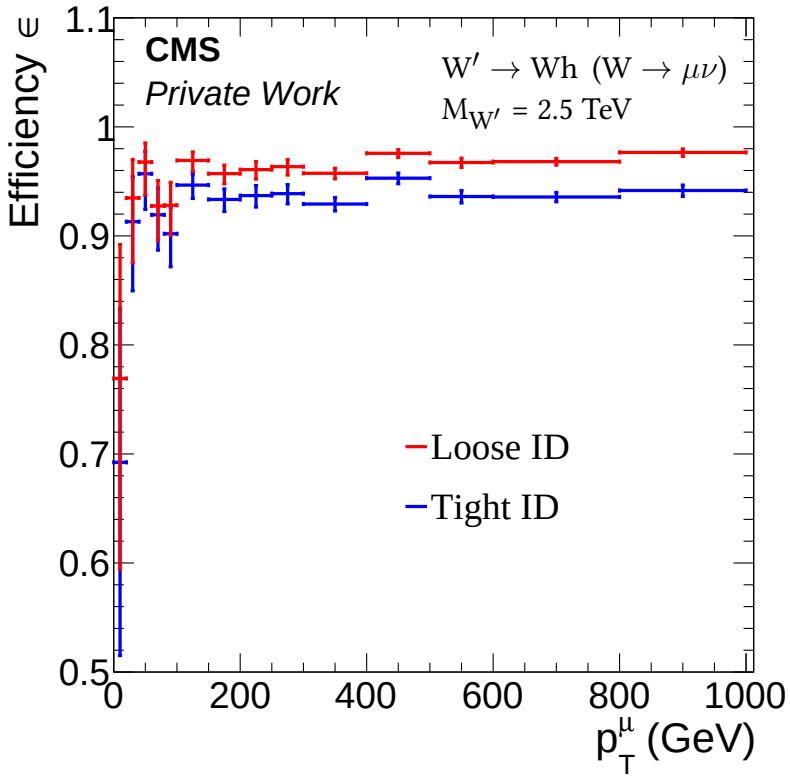

Figure 5.2.: Muon identification efficiency for tight and loose muons from the W decay w.r.t. the transverse momentum on generator level for a W′ mass of 2.5 TeV.

.

5.4. Hadronic Tau Leptons

In this section, the reconstruction and identification of tau leptons will be described, starting with a general introduction to tau leptons and followed by the summary of the hadrons-plus-strips algorithm used for the reconstruction and the isolation requirements. In the end, the special case of nearby taus that is important for a certain phase space will be described.

5.4.1. Properties of the Tau Lepton

The tau lepton has a mass of 1.776 MeV and is therefore the heaviest of all leptons [28]. It can decay to electrons ($\tau^- \rightarrow e^- \bar{\nu}_e \nu_\tau$) and muons ($\tau^- \rightarrow \mu^- \bar{\nu}_\mu \nu_\tau$), but due to its large mass that exceeds the mass of light mesons, it can also to decay to hadrons. In these hadronic decays, charged mesons are produced together with a tau-neutrino and often with additional uncharged mesons. The tau can decay either directly to charged pseudoscalar mesons ($\tau^\pm \rightarrow h^\pm \nu_\tau$), or it can first decay to vector mesons and subsequently to pseudoscalar mesons ($\tau^\pm \rightarrow \rho(770)^\pm \rightarrow h^\pm h^0 \nu_\tau$ or $\tau^\pm \rightarrow a_1(1260)^\pm \rightarrow h^\pm \pi^0 \nu_\tau$ or $h^\pm h^\pm h^\mp \nu_\tau$). A summary of the various tau decay modes and their branching fraction is presented in Tab. 5.2. It is visible that the hadronic decays are dominant and make up about 65 % of all tau decays while the leptonic decays sum up to 35 %. About 13 % of the tau decays contain three charged hadrons and most of them have at least one π^0 in the end.
The lifetime of tau leptons is about $2.91 \cdot 10^{-13}$ s and their decay length is 87.03 μm, meaning that

taus do not decay immediately, but (still) between beam pipe and inner pixel if their momentum does not exceed the TeV scale.

Decay Mode	Resonance	B ($\tau \to x\nu_\tau$) (%)
$e^-\bar{\nu}_e\nu_\tau$	-	17.8
$\mu^-\bar{\nu}_\mu\nu_\tau$	-	17.4
$h^\pm\nu_\tau$	-	11.5
$h^\pm\pi^0\nu_\tau$	$\rho(770)$	25.9
$h^\pm\pi^0\pi^0\nu_\tau$	$a_1(1260)$	9.5
$h^\pm h^\pm h^\mp\nu_\tau$	$a_1(1260)$	9.8
$h^\pm h^\pm h^\mp\pi^0\nu_\tau$	-	3.3
Other Hadronic	-	4.8

Table 5.2.: Summary of the possible tau decays, the corresponding meson resonance, and the branching fraction [85]. Here, $h^\pm$ stands for charged hadrons, namely pions $\pi^\pm$ and kaons $K^\pm$.

5.4.2. Separated Tau Leptons

Here, the reconstruction and identification of well isolated hadronic taus will be discussed, including the hadronic-plus-strips algorithm, based on [85–87].

Reconstruction

While the reconstruction of leptonic tau decays relies on the corresponding electron and muon selection described in Sec. 5.2 and 5.3, the reconstruction of hadronic tau decays is more complicated and needs a unique approach. It is based on the hadrons-plus-strips (HPS) algorithm and makes use of the detailed particle knowledge from the PF algorithm. Starting with reconstructed PF jets, the HPS tau algorithm uses the jet constituents - namely the charged hadrons, neutral hadrons and photons - to acquire the hadronic tau decay mode. Neutral pions from the tau decay end up as diphoton pairs with a large probability to convert to electron pairs while travelling through the detector. Therefore, all electron and photon pairs are clustered within a predefined $\Delta\eta \times \Delta\phi$ region to reconstruct the full neutral pion momentum. The resulting combined objects are called "strips". A schmetic overview of the HPS algorithm is presented in Fig. 5.3. To estimate the $\Delta\eta \times \Delta\phi$ region, the following method is used [85], named "dynamic strip reconstruction":

1. The algorithm searches for the electron or photon (e/γ) with the highest $p_T^{e/\gamma}$ within the jet that is not yet part of any strip. This object is used as the initial seed for a new strip, using the spatial variables η and ϕ of this object.

2. Now, following an iterative approach, the e/γ with the next highest energy deposition that lies within the region

$$\begin{aligned} \Delta\eta &= f(p_T^{e/\gamma}) + f(p_T^{strip}) \quad \text{and} \\ \Delta\phi &= g(p_T^{e/\gamma}) + g(p_T^{strip}) \end{aligned} \tag{5.3}$$

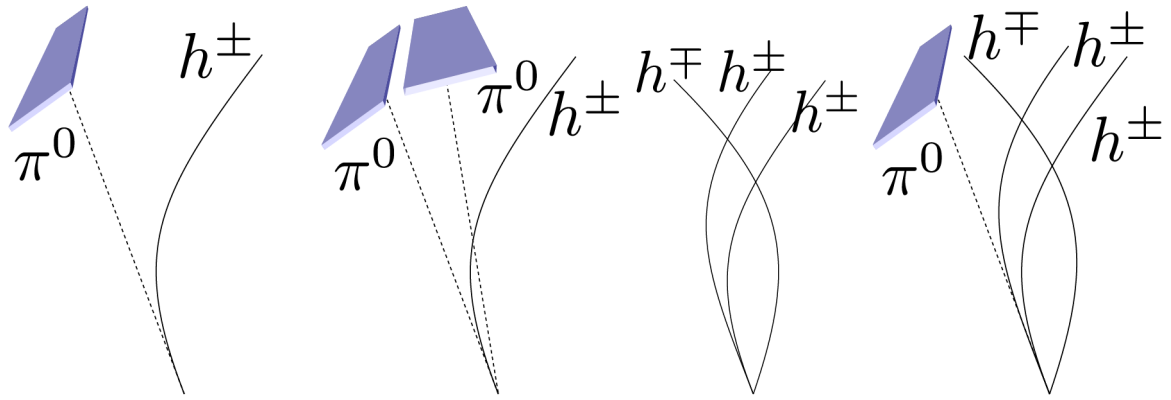

Figure 5.3.: Scetch of the tau reconstruction using the hadron-plus-strips algorithm, taken from [88]. Here, the charged hadrons ($h^{\pm}$) are illustrated as lines and the strips from neutral pions (π^0) as blue planes.

around the strip is merged within the strip. Here, $f(p_T) = 0.20 \left(\frac{p_T}{\text{GeV}}\right)^{-0.66}$ and $g(p_T) = 0.35 \left(\frac{p_T}{\text{GeV}}\right)^{-0.71}$ are dimensionless functions whose values are estimated from simulation. The possible strip size is limited to $0.05 < \Delta\eta < 0.15$ and $0.05 < \Delta\phi < 0.3$.

3. In the next step, the position of the strip is recalculated using the p_T-weighted average of all e/γ in the strip:

$$\begin{aligned} \eta_{\text{strip}} &= \frac{1}{p_T^{\text{strip}}} \sum p_T^{e/\gamma} \eta^{e/\gamma} \quad \text{and} \\ \phi_{\text{strip}} &= \frac{1}{p_T^{\text{strip}}} \sum p_T^{e/\gamma} \phi^{e/\gamma} \end{aligned} \tag{5.4}$$

4. The procedure is repeated starting from (2.) until no other electron or photon candidate is found within $\Delta\eta \times \Delta\phi$. If this happens, a new strip based on the highest e/γ momentum is produced, starting the procedure at (1.).

The used algorithm requires the p_T-weighted center of the strip to lie in the tau signal cone, but some of the strip constituents can exceed the cone size, improving the strip reconstruction w.r.t to a fixed $\Delta\eta \times \Delta\phi$ region.

Charged particles in the HPS algorithm are restricted to have a momentum $p_T > 0.5$ GeV and to originate from the primary vertex of the event, requiring an transverse impact parameter of $d_0 < 0.1$ cm. The charged particles are important for the reconstruction of the charged hadrons arising from the tau decay. The hadronic tau candidate is reconstructed based on the combination of charged particles and strips. To make sure that the combination originates from a hadronic tau, the mass of the hadron-plus-strips combination is expected to lie in the region of the $\rho(770)$ and $a_1(1260)$ resonances. The selected mass windows are optimized for each decay mode to get the highest selection efficiency together with the best jet to tau misidentification rejection.
In addition to the typical decay modes of hadronic taus, new decay modes with two charged hadrons, summing up to a charge of 0, are added in the CMS tau reconstruction. These new decay modes are

used to improve the efficiency of high-p_T taus decaying to three hadrons. Due to the large p_T, the two same sign charged hadrons of these decays are overlapping and might be reconstructed as only one charged particle. Thus, these tau candidates can fail the decay mode reconstruction. With the additional decay modes, the lost efficiency can be recovered. However, they also increase the jet to tau misidentification probability and therefore, they are only used in the high-p_T region where the efficiency loss is high and the jet to tau misidentification probability low.

Identification

For the identification of hadronic tau candidates, three additional criteria on top of the decay mode reconstruction are applied, namely the isolation requirements against jets, electrons and muons. In this analysis, the discriminator against jets is based on a multivariate analysis (MVA) using a large number of input variables. These variables are [85, 87]:

1. The charged hadron and photon isolation sums defined by

$$I_\tau = \sum p_T^{\text{charged}}\,(d_z < 0.2\text{ cm}) + \max\left(0, \sum p_T^{\gamma} - \Delta\beta p_T^{\text{charged}}\,(d_z > 0.2\text{ cm})\right) \tag{5.5}$$

   where p_T^{charged} and p_T^{γ} are the transverse momenta of all charged hadron and photon constituents that are not part of the hadronic tau if their distance to the tau is $\Delta R < 0.5$. The charged constituents are required to originate from the tau production vertex with an impact parameter of $d_0 < 0.2$ cm. Charged constituents with an impact parameter above 0.2 cm are removed if they lie within a cone of $\Delta R < 0.8$ using the $\Delta\beta$ correction ($\Delta\beta = 0.2$) to reduce the effect of pileup.

2. The reconstructed tau decay mode as discussed in Sec. 5.4.2.

3. The lifetime information from the impact parameter d_0 of the leading charged track from the hadronic tau and its significance d_0/σ_{d_0}. Here, σ_{d_0} is the corresponding uncertainty.

4. The distance between primary and secondary vertices of the hadronic tau $|\vec{r_{SV}} - \vec{r_{PV}}|$ and their corresponding significance $|\vec{r_{SV}} - \vec{r_{PV}}|/\sigma_{|\vec{r_{SV}} - \vec{r_{PV}}|}$.

5. Additional variables like the p_T-weighted distance ΔR, the pseudorapidity η, $\Delta\phi$ w.r.t. the hadronic tau axis, as well as the variable $p_T^{\text{strip, outer}} = \sum p_T^{e/\gamma}(\Delta R > R_{\text{sig}})$ which represents the summed transverse momenta of all e/γ objects that are part of a strip, but lie outside of the tau signal cone.

6. The photon and electron multiplicity in the signal and isolation cones for $p_T^{e/\gamma} > 0.5$ GeV.

Based on the isolation efficiency of the MVA, six working points are used. The loosest working point, called "byVLooseIsolationMVArun2v1DBoldDMwLT", is defined by an efficiency of 90 %. The tightest isolation requirement, named "byVVTightIsolationMVArun2v1DBoldDMwLT", has an efficiency of 40 %. In this analysis, the tau momenta are in the medium-p_T region where the impact of jet to tau misidentification is reduced, but not negligible. Therefore, the medium isolation requirement with an efficiency of 70 % is used.

On top of the discriminator against jets, isolation requirements for electrons and muons are applied. Since they are not as important as the jet discrimination for this analysis, they will not be discussed in detail. However, a precise description of these discriminators can be found in [85, 87]. The electron discriminator is also based on a MVA. It mainly makes use of variables depending on energy

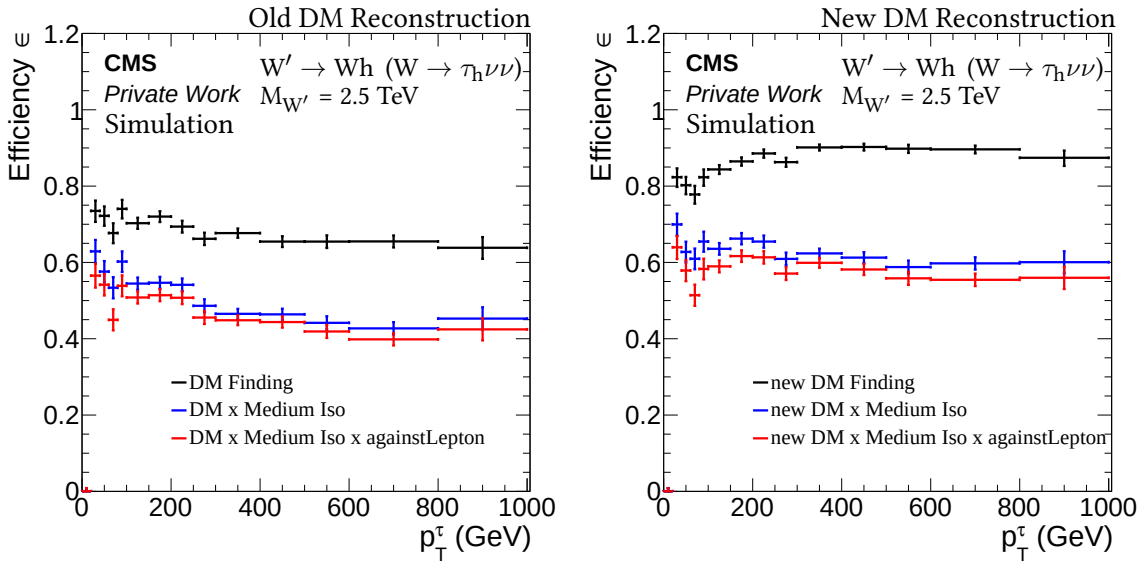

Figure 5.4.: Hadronic tau reconstruction and identification efficiencies as a function of the visible tau momentum for separated taus. The label "(new) DM Finding" refers to the decay mode reconstruction, "Medium Iso" is the medium isolation requirement against jets, and "againstLepton" the discriminator against electron and muons. Left: Old decay mode reconstruction, right: New decay mode reconstruction.

deposits in the ECAL and HCAL, as well as on the tracking of electrons (GSF and Kalman-Filter hits), the electromagnetic shower shape, and the energy deposits used to reconstruct the strips in the HPS algorithm [85]. Here, the loosest requirement, called "againstElectronVLooseMVA6", is used. The discrimination against muons is not based on a MVA. Here, the loose discriminator "againstMuon-Loose3" is used. It vetoes hadronic tau candidates if a track segment with hits in two muon chambers is found within a distance of $\Delta R < 0.3$. In addition, the energy deposit of the leading charged hadron associated with the tau candidate is not allowed to be below 20 % of its track momentum [85].

The hadronic tau leptons in this analyis are required to have a transverse momentum $p_T > 20$ GeV and a pseudorapidity of $|\eta| < 2.3$. They have to pass the normal decay mode finding (referred to as "DM Finding" or "DM" in the follwing figures) which does not include decay modes with two charged hadrons ("new DM Findind" or "new DM"), the medium jet isolation ("Medium Iso"), the very loose electron and the loose muon discriminator (their combination is called "againstLepton") [89]. Fig. 5.4 shows the efficiency of the hadronic tau reconstruction efficiency for normal decay modes (left) and new decay modes (right, including two charged hadrons) as a function of the tau momentum based on the W decay in a 2.5 TeV Wh resonance signal sample. It is visible that the new decay modes have a 10 % higher efficiency at very high transverse momenta. However, the reconstruction of well isolated, separated tau leptons is mainly important for the low-or medium-p_T region in this analysis where the rejection against jets is still important. Therefore, the normal decay mode reconstruction is used for these tau candidates. This is different for the nearby taus, as it will be discussed in Sec. 5.4.3.

5.4.3. Nearby Tau Leptons

In this analysis, the reconstruction of nearby hadronic taus plays an important role to recover efficiency in boosted $h/Z \to \tau\tau$ decays. As discussed in Chap. 4, the tau decay products can overlap for

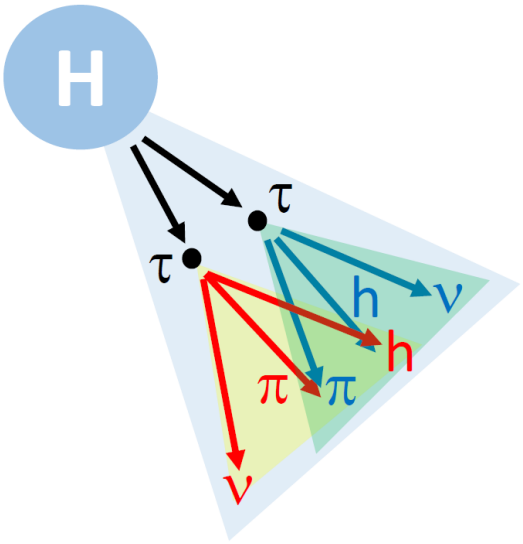

Figure 5.5.: Illustration of the decay of a boosted Higgs boson to two tau leptons with a subsequent fully hadronic decay. Here, π stands for neutral pions π^0 and h refers to charged hadrons $h^{\pm}$ with $h^{\pm} = \pi^{\pm}, K^{\pm}$.

resonance masses above the TeV scale and therefore, they can spoil each others isolation variable. This effect is illustrated in Fig. 5.5. CMS provides a special version of the tau reconstruction for these events, called "BoostedTaus" [85, 90, 91]. The name originates from the boost of the bosons that decay to two taus. As also well separated taus can be boosted (the reason for the new decay modes), it will be referred to "BoostedTaus" as "nearby taus". The reconstruction makes use of the very good description of vertices and tracks using the PF algorithm in CMS. First, the reconstruction of nearby taus will be discussed, followed by their selection requirements and the differences to the separated tau reconstruction.

Not many analyses search in the phase space of nearby taus. In fact, the only known CMS analyses that were performed using nearby taus are a search for SM-like Higgs bosons decaying to a pair of light boson subsequently decaying to tau pairs [92] with 2012 data, searches for $VH \rightarrow qq\tau\tau$ [93] and $HH \rightarrow bb\tau\tau$ [94] resonances and with 2012 data, and a combined search for $VH \rightarrow qq\tau\tau$ and $HH \rightarrow bb\tau\tau$ resonances using 2016 data [26]. All of these searches are based on data collected by CMS. Between Run-I and Run-II, the algorithm was changed and optimized, meaning that only one other analysis [26] utilizes the 2016 version of the nearby tau reconstruction algorithm. This version will be described in the following.

Reconstruction

For events with nearby hadronic taus, the jets used as an input seed for the HPS algorithm are overlapping, resulting an inefficiency in the tau reconstruction. Therefore, a different method needs to be applied. The starting point of the optimized algorithm for nearby taus [85] are so called CA8 jets, jets with large radius ($\Delta R = 0.8$) clustered by the PF algorithm using the Cambridge-Aachen [95] algorithm. The two taus from the boson decay are expected to be subjets within the CA8 jet, if the transverse momentum of the CA8 jet is larger than 100 GeV[1]. If one of the taus decays leptonically,

[1] If a boson decays to two taus, its reconstructed visible momentum is decreased. A momentum of 100 GeV for the reconstructed CA8 jet corresponds to approximately 200 GeV for the decaying boson

the corresponding decay product is also identified as a subjet. To get the initial seeds for the tau reconstruction, the last step of the clustering algorithm is reversed until two subjets sj_1 and sj_2 are found that possibly origin from the tau decays. In order to reduce the impact of jets misidentified as hadronic taus, these subjets have to fulfill the following criteria:

- The transverse momentum of each subjet with respect to the beam axis has to be larger than 10 GeV.
- The mass of the heavier subjet has to be lower than 2/3 of the CA8 jet mass:

$$\frac{\max\left(m_{sj_1},\ m_{sj_2}\right)}{m_{CA8}} < 2/3. \tag{5.6}$$

If the two selected subjets do not satisfy these conditions, they are discarded. Afterwards, a new iteration is started, beginning with the subjet with the highest mass and reversing the clustering algorithm to split it into two new subjets. If it is not possible to find a pair of two subjets satisfying the conditions, the whole CA8 jet is discarded and no tau reconstruction is performed [85]. However, if two subjets are found, they are used as initial seeds in the HPS reconstruction algorithm described in Sec. 5.4.2. In general, leptons from the tau decay are also passed to the HPS algorithm since they are also reconstructed as subjets and therefore, they can also be selected as hadronic tau candidates. Most of these misreconstructions are removed in the analysis by requiring the distance of leptons and hadronic tau to be $\Delta R > 0.1$.

Identification

The identification criteria of nearby taus are calculated in the same way as for separated taus. However, since subjets are used as input for the tau identification, it is more likely that these tau candidates pass the decay mode finding and isolation requirement. On the other hand, due to the increased number of possible other objects as input seeds, the misidentification probability is increased by this procedure. Therefore, the taus passing the nearby tau reconstruction will only be used if another object - electron, muon, or another hadronic tau - is found in a distance of $\Delta R < 0.5$ as expected from the signal for high resonance masses. The nearby tau reconstruction is optimized for events with highly boosted bosons, meaning that the taus itself are also boosted. Therefore, the new decay modes will be used to keep the efficiency high. As the whole reconstruction is only used in a very specific phase space (small ΔR, large p_T^τ), the increased misidentification probability has no negative impact on the analysis result. Since in this phase space a high signal efficiency is crucial, the "byVLooseIsolationMVArun2v1DBnewDMwLT" discriminator will be used. Fig. 5.6 shows a comparison of the nearby and separated tau reconstruction as a function of the momentum based on the W decay of a Wh resonance. For possible comparisons to the previously shown plot with separated taus (see Fig. 5.4), the medium isolation is used here for both tau types. It is visible that for low momenta, the separated reconstruction is much better, and that for high momenta, the two methods are on the same level. The reason is that no CA8 jet can be found to reconstruct hadronic nearby taus in the low-p_T region. With increasing tau momentum, it is possible that the tau itself is identified or part of a CA8 jet, resulting in a possible nearby tau reconstruction. In general, the plot proves that the separated reconstruction is the better choice in these topologies.

In nearby topologies, this changes. Fig. 5.7, 5.8, and 5.9 show the efficiency of the new decay mode finding and very loose isolation requirement for two hadronic taus ($\tau_h\tau_h$), one hadronic tau plus one electron ($\tau_h\tau_e$), and one hadronic tau plus one muon ($\tau_h\tau_\mu$) as a function of the generated boson Higgs boson momentum (left) and distance $\Delta R(\tau,\tau)$ (right). The separated reconstruction is

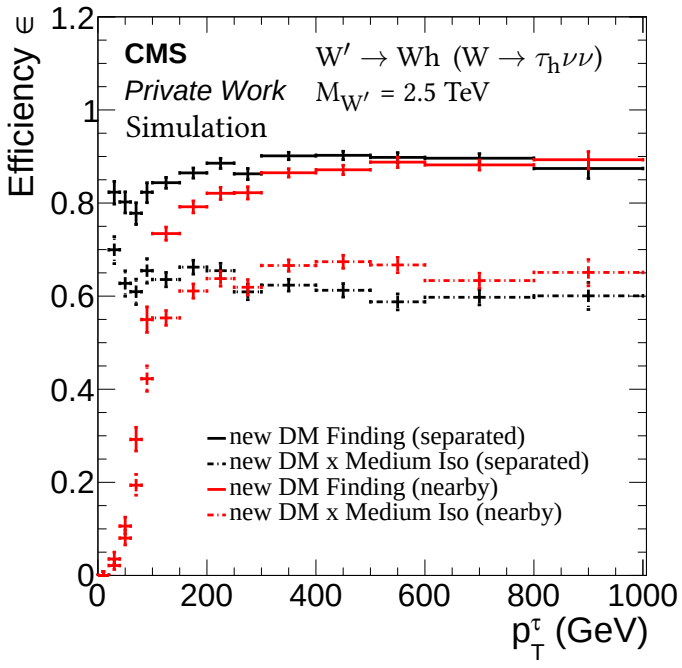

Figure 5.6.: Comparison of the decay mode reconstruction and isolation discriminator efficiency for nearby and separated hadronic taus as a function of the transverse momentum. The label "new DM Finding" refers to the decay mode reconstruction including two charged hadrons and "Medium Iso" is the medium isolation requirement against jets.

better up to boson momenta of 500-600 GeV in all three cases. This is the average threshold where decay products of a Higgs boson decay have a distance of about $\Delta R = 0.5$. For Z boson decays, the threshold is about 20 % lower. Starting from this value, the efficiency of the separated reconstruction decreases while the nearby efficiency still rises. This can be seen better in the ΔR plots where for values below 0.5 the efficiencies drop drastically for separated taus. It is important to note that the effect is much smaller in semileptonic decays, as the important discriminants in these channels are the ones against electrons and muons. In the ΔR plot, the decay mode reconstruction efficiency rises for both tau types for $\Delta R < 0.2$. This rise in efficiency appears from other objects (e.g. the nearby electron or muon) misreconstructed as hadronic taus. However, they are vetoed by the isolation requirement.

In the separated tau selection, the discriminators against leptons are applied on top of tau isolation and decay mode finding. However, this is not done for the nearby taus. The reason is that the lepton discriminators are not affected by the nearby tau reconstruction and their usage still results in an inefficiency. This effect can be seen in Fig. 5.10 showing the efficiency of the two discriminators against leptons for each of the three $\tau\tau$ decay combinations as a function of the distance $\Delta R(\tau, \tau)$. For the fully hadronic decay, no efficiency loss is visible, as no lepton is expected to be close-by. In the semileptonic cases, the efficiency drops to 30 % (electrons) or 5 % (muons). The reason why the "against lepton" discriminators are not really affected by the nearby tau reconstruction lies in their definition. Both of them include variables that are mainly defined by the lepton, but not by the hadronic tau, e.g. the muon discriminator requires hits of track segments in the muon chambers. These hits are not influenced by the tau reconstruction. Due to the low number of expected background events from lepton misidentification in the analysis phase space (they could mainly arise from diboson decays), no discriminators against leptons are applied.

Overall, the nearby tau reconstruction improves the efficiency for two tau pairs from boosted boson decays from 20 % to 70 % for fully hadronic and 50 % to 70 % for semileptonic decays. This improvement in the reconstruction efficiency comes at the cost of an increased misidentification probability. The Tau POG has measured the misidentification rate as a function of the large cone jet momentum in QCD multijet events and found it to increase by about an order of magnitude [85]. However, due to the special phase space used in this analysis, the impact of the increased misidentification rate is small as only a small background is expected. Taus passing the nearby reconstruction are required to fulfill the new decay mode reconstruction and the very loose tau isolation [89]. In addition, have to have a transverse momentum of $p_T^\tau > 20$ GeV and a pseudorapidity of $|\eta| < 2.3$. No discriminators against leptons are applied.

The special nearby tau reconstruction is needed to recover the efficiency. However, it is also interesting to see if the reconstructed decay mode is affected by the nearby topology. Fig. 5.11 shows the decay mode reconstruction efficiency for various generated decay modes for separated taus from the W decay and nearby taus from the Higgs boson decay. For the nearby tau reconstruction, the fully hadronic and the two semileptonic cases are shown. The decay mode reconstruction of well separated taus (red) is used as a benchmark. Reconstructed decay modes with three charged particles are summarized in the category 3p Xπ^0, with two charged particles in the category 2p Xπ^0, and with one charged particle and equal or more than 1π^0 in the category 1p Xπ0. The uncertainties for the three nearby cases show the difference to the separated case and are therefore a measure how much the corresponding decay mode is influenced by the nearby topology. The largest difference can be found in the fully hadronic and in the semileptonic plus electron case where the efficiency for decays with three charged hadrons differs by 4-6 %. These decays are mainly added to decay modes with one charged particle, meaning that two charged particles get lost in these cases. They might be used to reconstruct the other tau or end up within the isolation cone of tau candidates and

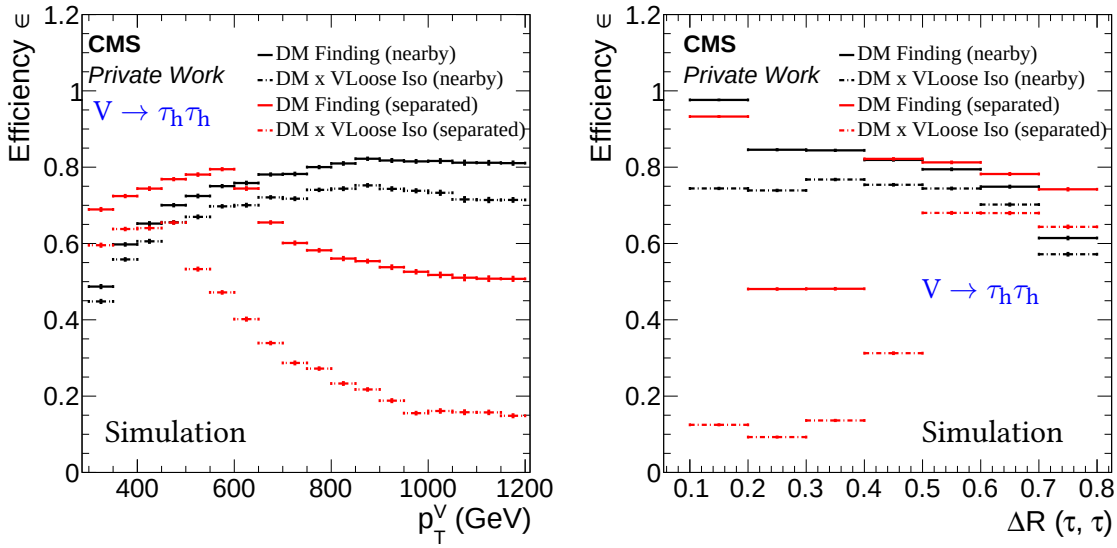

Figure 5.7.: Comparison of the decay mode finding (solid line) and very loose isolation discriminator (dashed line) efficiencies for separated (red) and nearby (black) taus for fully hadronic decays of the vector boson as a function of the transverse boson momentum (left) and the distance $\Delta R(\tau_h, \tau_h)$ (right). The label "DM Finding" refers to the new decay mode reconstruction including two charged hadrons and "VLoose Iso" is the very loose isolation requirement against jets.

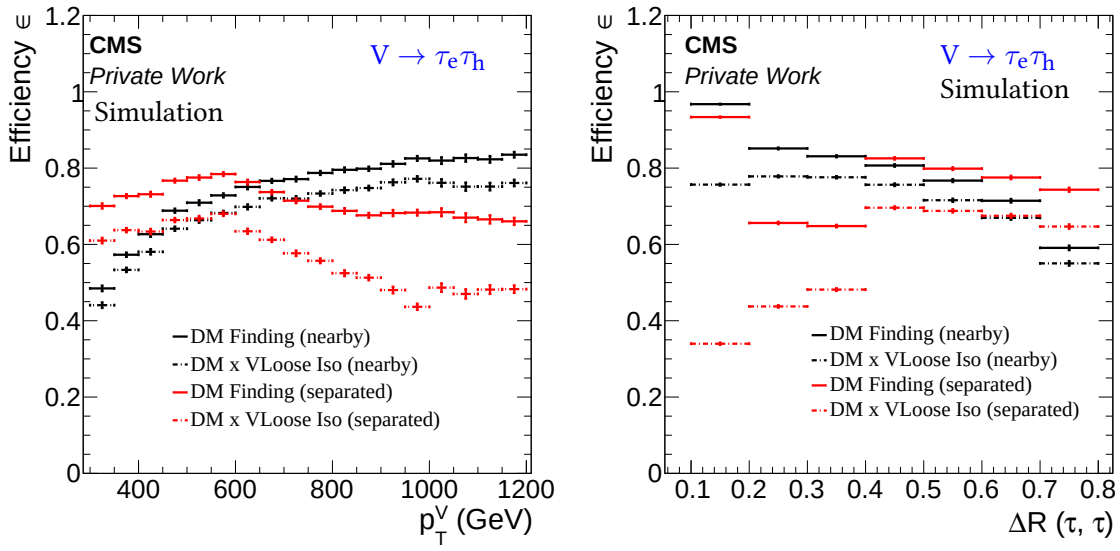

Figure 5.8.: Comparison of the decay mode finding (solid line) and very loose isolation discriminator (dashed line) efficiencies for separated (red) and nearby (black) taus for semileptonic decays of the vector boson including electrons as a function of the transverse boson momentum (top) and the distance $\Delta R(\tau_e, \tau_h)$ (bottom). The label "DM Finding" refers to the new decay mode reconstruction including two charged hadrons and "VLoose Iso" is the very loose isolation requirement against jets.

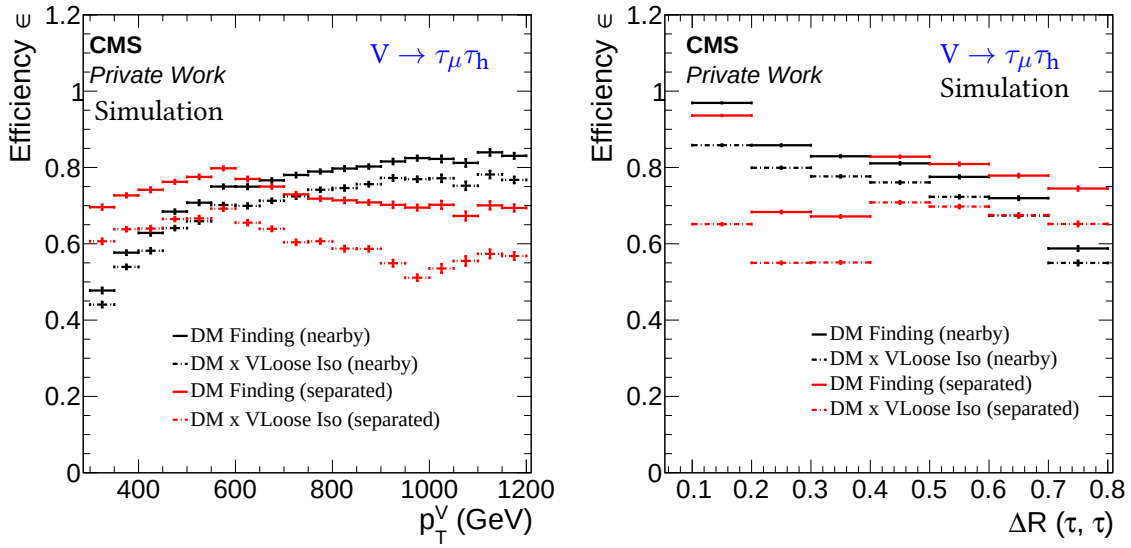

Figure 5.9.: Comparison of the decay mode finding (solid line) and very loose isolation discriminator (dashed line) efficiencies for separated (red) and nearby (black) taus for semileptonic decays of the vector boson including muons as a function of the transverse boson momentum (top) and the distance $\Delta R(\tau_\mu, \tau_h)$ (bottom). The label "DM Finding" refers to the new decay mode reconstruction including two charged hadrons and "VLoose Iso" is the very loose isolation requirement against jets.

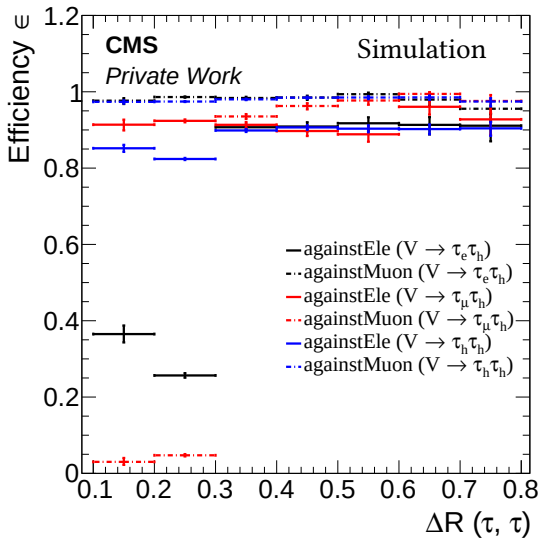

Figure 5.10.: Efficiencies for the discriminators against electrons ("againstElectron", solid line) and muons ("againstMuon", dashed line) for nearby hadronic taus as a function of the distance $\Delta R(\tau, \tau)$ of the two tau decay products for the semileptonic electron (black), semileptonic muon (red), and full hadronic (blue) decay. These discriminators are not applied in the nearby tau selection.

leptons. However, the overall impact of the nearby reconstruction on the decay modes seems to be small and to work nearly as well as for separated taus.

5.5. Correction of the Electron and Muon Isolation

In Sec. 5.2 and 5.3, the reconstruction and identification of electrons and muons in well isolated environments was discussed. However, as shown in Sec. 4, light leptons from the $V \to \tau_\ell \tau_h$ (ℓ = e, μ) decay chain are close to the hadronic tau decay products for resonance masses above the TeV scale. An illustration of this behaviour is shown in Fig. 5.12 for semileptonic tau decays. In these cases, the lepton isolation criteria fail and the signal efficiency drops significantly. To cover this effect, the electron and muon isolation requirements are optimized by removing the charged hadron, neutral hadron and photon constituents that are used to reconstruct the closest well reconstructed hadronic tau if it lies within the lepton isolation cone. The new isolation formula is given by:

$$I_{PF}^{rel} = \left(\sum p_T^{charged} - \sum p_{T,\tau}^{charged} + \max\left[0, \sum p_T^{neutral} - \sum p_{T,\tau}^{neutral} + \sum p_T^{\gamma} - \sum p_{T,\tau}^{\gamma} - p_T^{PU}\right]\right) / p_T^{\ell} \quad (5.7)$$

where p_T^{PU} is the corresponding pileup correction for electrons and muons and $\sum p_{T,\tau}^{charged}$, $\sum p_{T,\tau}^{neutral}$, and $\sum p_{T,\tau}^{\gamma}$ are the summed charged, neutral and photon constituents of the nearby hadronic tau. In this context, the hadronic tau leptons are reconstructed with the nearby tau algorithm that was described in Sec. 5.4.3. Fig 5.13 shows the identification (loose ID) and isolation efficiencies for electrons (left) and muons (right) as a function of the boson momentum (top) and the distance ΔR between the lepton and the hadronic tau on generator level. It is visible that the efficiency of the

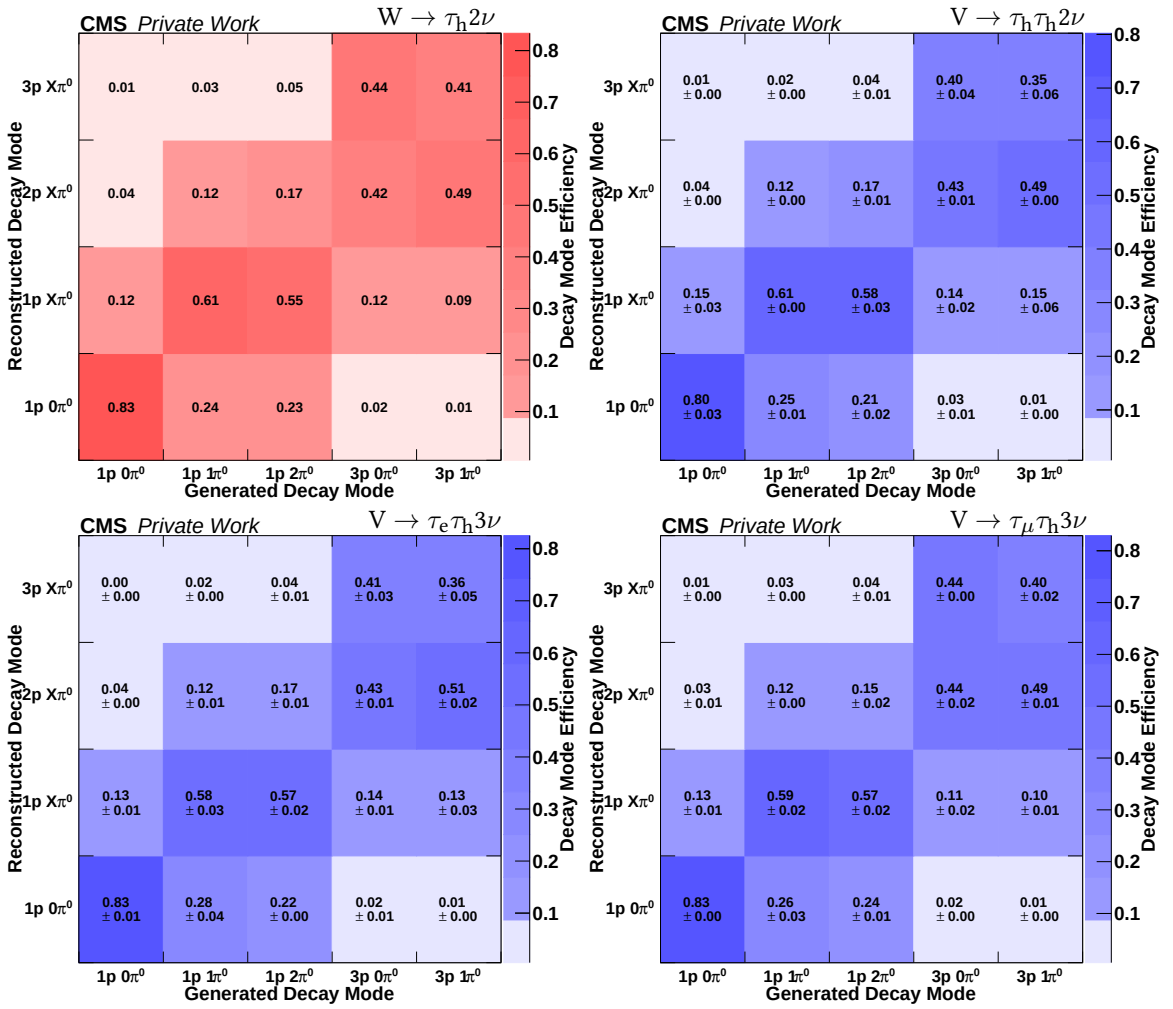

Figure 5.11.: Decay mode reconstruction efficiency for separated taus from the W decay (top left), and nearby taus from the Higgs decay for the fully hadronic (top right), semileptonic plus electron (bottom left), and semileptonic plus muon (bottom right) decays.

reconstruction and identification requirements are not really influenced by the boosted topology. In case of the isolation, the boosted topology of the signal has a great impact. Both lepton isolations suffer from inefficiencies starting with boson momenta above 500-600 GeV ($\Delta R < 0.4$) due to the impact of the hadronic taus on the isolation calculation. After applying the correction by removing the tau constituents, a large amount of efficiency can be recovered, resulting in efficiencies of $\approx$ 60-70 % for muons and 45-55 % for electrons. Since there are still inefficiencies after applying the modified requirements, it will be discussed in the following where they come from.

There are several reasons why it is not possible to recover the full isolation efficiency by removing the contributions of the hadronic tau and why the modified isolation works better for muons than for electrons. These reasons are:

1. Tau reconstruction: The reconstruction of the hadronic tau lepton has a big impact on the modified lepton isolation. In the modified isolation, the contribution of the hadronic tau is only removed if it passes the corresponding tau identification criteria which are the new decay modes based on two charged hadrons and the very loose isolation discriminators for the

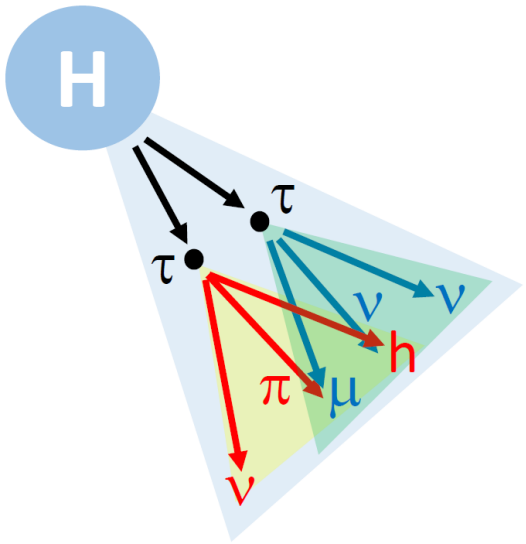

Figure 5.12.: Illustration of the decay of a boosted Higgs boson to two tau leptons with a subsequent semileptonic decay.Here, π stands for neutral pions π^0 and h refers to charged hadrons $h^{\pm}$ with $h^{\pm} = \pi^{\pm}$, $K^{\pm}$.

nearby tau reconstruction. If the hadronic tau in the event is not well reconstructed, it cannot be subtracted from the lepton isolation cone. However, its constituents are still part of the event and therefore, they have an impact on the lepton isolation. It is also possible that a hadronic tau is reconstructed and it passes the discriminators, but it is not completely reconstructed, resulting in some missing information. For example, a hadronic tau decaying to $\pi^{\pm}\pi^0$ might be reconstructed as $\pi^{\pm}$ without π^0. In these cases, it is possible that the missing part spoils the lepton isolation.

2. Lepton misidentification: This effect does mainly impact the electron isolation. It is possible that muons and especially electrons are misidentified as other objects, mostly charged hadrons, by the PF algorithm. If this happens, they artificially increase the isolation value and result in an inefficiency. This happens more likely in busy environments like boosted topologies. Fig. 5.14 shows the relative PF isolation value for electrons (left) and muons (right) for events with $\Delta R(\tau_h, \tau_\ell) < 0.4$ based on a resonance mass of 2.5 TeV. In these histograms, it is required that the nearby hadronic tau has been reconstructed. It is clearly visible that the electron isolation value peaks at zero, but also at one. The peak at one arises from the described effect, the relative isolation value includes the electrons own momentum.

3. Isolation selection value: As one can see in Fig. 5.14, the chosen selection value differs for electrons and muons. While the selection value for electrons is at about 0.1 (see Tab. 5.1), the value for muons is at 0.25. This difference results in an efficiency loss of about 15 % for electrons.

Overall, the modifications to the lepton isolation result in a large improvement of the lepton selection efficiency, although it is not possible to fully recover the lost efficiency.

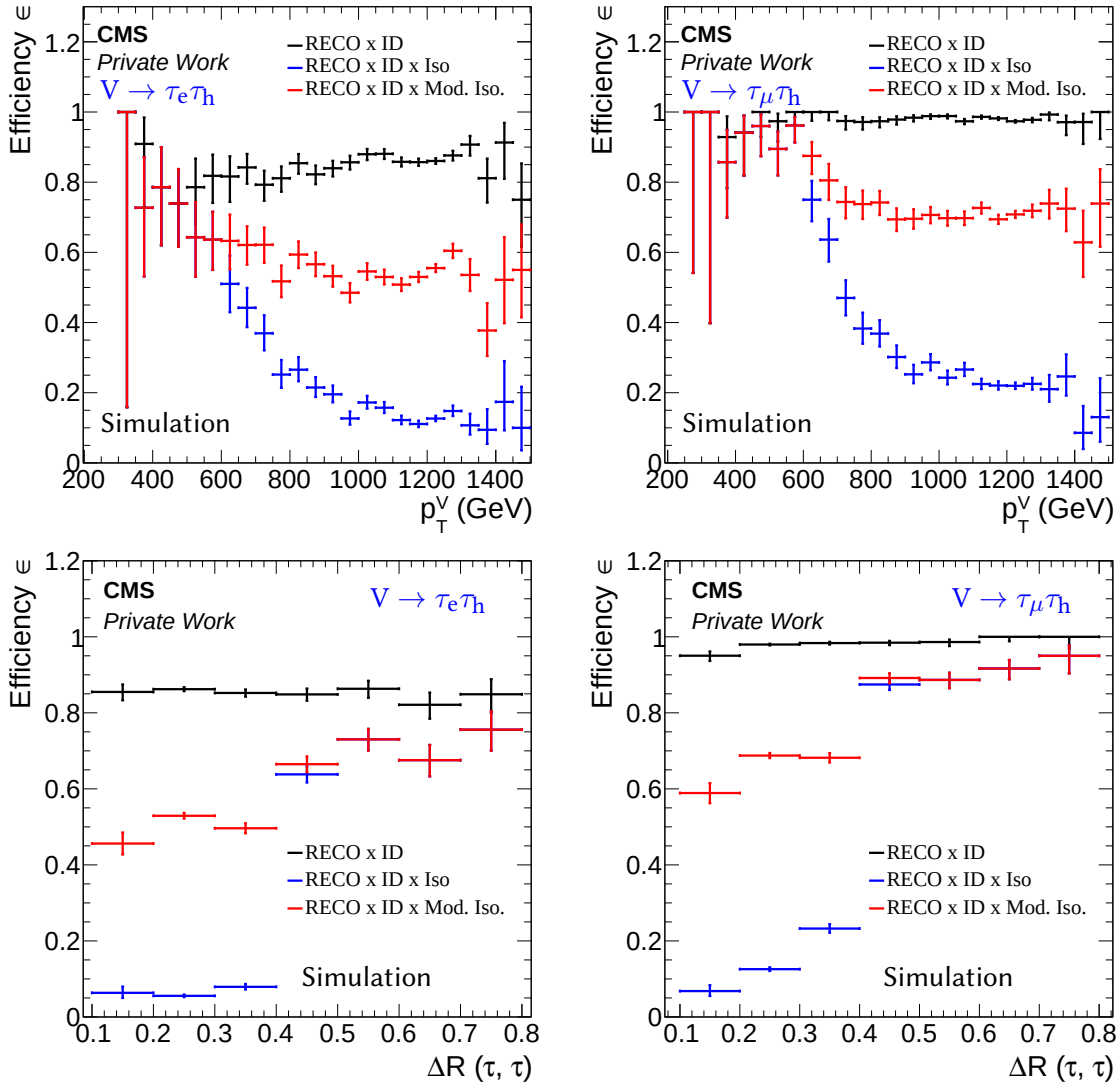

Figure 5.13.: Electron (left) and muon (right) reconstruction, identification and isolation efficiency for leptons from the semileptonic vector boson decay as a function of the transverse momentum of the vector boson (here a Higgs boson) (top) and the distance $\Delta R(\tau_\ell, \tau_h)$ between the visible τ decay products (bottom) on generator level.

5.6. Jets and B-Tagging

In this analysis, the reconstruction of jets is important for two aspects. First, the reconstruction of jets and their energy scale affects the missing E_T measurement (see Sec. 5.7). Second, b-tagged jets are used for additional control regions and they are vetoed in the signal region. In CMS, jets are clustered by the PF algorithm [75, 96], using the information of charged hadrons, neutral hadrons, and photons. Two clustering methods are commonly used, namely the Cambridge-Aachen (CA) and anti-k_T (AK) algorithm. More details about the clustering can be found in [95] and [97]. For well separated jets without boosted topology like they are used for the b-tagging in the following analysis, AK4 jets with a cone size of $\Delta R = 0.4$ are used. To reduce the impact of pileup on the jet energy and substructure reconstruction, the so called charged-hadron subtraction (CHS) [98]

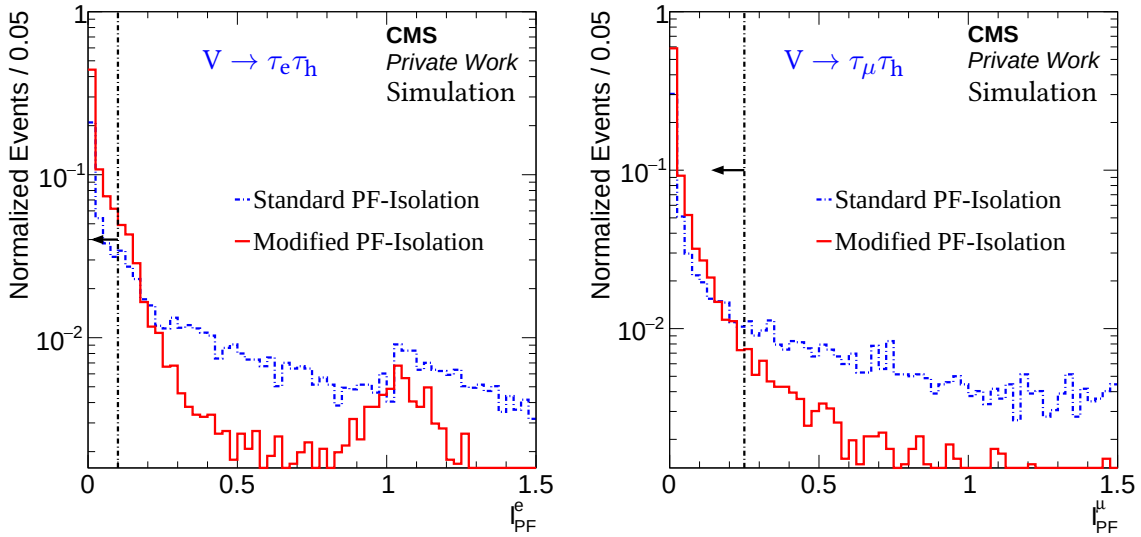

Figure 5.14.: Relative PF isolation value for electrons (left) and muons (right) for a resonance mass of 2.5 TeV if the distance ΔR between the two objects is smaller than 0.4. In general, the shape of the histogram depends on the resonance mass. The mass of 2.5 TeV is only used to illustrate the effect of the modified lepton isolation.

is used, removing charged hadron candidates whose vertices are not compatible with the primary vertex from the event.

A correction is applied to all jets with $p_T^{jet} > 10$ GeV, called jet energy scale correction [99–101]. Three different levels of corrections are applied. The level-1 (L1) pileup correction removes the energy arising from in-time and out-of-time pileup, based on simulated events with and without pileup and their calibration to data. The level-2 (L2) relative η correction calibrates the jet energy based on the balance of dijet simulation events as a function of η^{jet} and p_T^{jet} (the p_T^{jet} dependence is small). The level-3 (L3) absolute scale correction calibrates the jet energy as a function of the jet p_T in the barrel based on a global fit combination of Z+Jets, γ+Jets and multijet samples. While the L1 correction relies on data, the other two corrections are obtained from simulation.

Jets that are selected for the b-tagging procedure are required to have a $p_T^{jet} > 20$ GeV and to be within $|\eta| < 2.4$. They have to pass the loose PF jet identification [102]:

- The charged hadron fraction of the jet energy has to be larger than 0 % of the whole jet energy,
- the charged EM fraction (electrons) has to be smaller than 99 %,
- the neutral EM fraction (photons) has to be smaller than 99 %,
- the neutral hadron fraction has to be smaller than 99 %, and
- the multiplicity of charged particles has to be larger than 0.

To select b-tagged jets[2], the "Combined Secondary Vertex V2" (CSVv2) algorithm [103, 104] is used which combines the information of displaced tracks and secondary vertices. Based on a MVA, several variables considering the vertex and track structure of heavy and light jets are used as an input for

[2]There is a difference between b-jets and b-tagged jets. The first one really appears from b-quark hadronization while the second one is only a jet tagged as a b-jet candidate.

a boosted decision tree, resulting in an output value between 0 and 1. If the value is close to unity, the jet has a high probability to arise from a b-quark. In the analysis, two b-tagging working points are used, namely the loose WP (Discriminator > 0.5426) in semileptonic $\tau\tau$ events and the medium WP (> 0.8484) in fully hadronic $\tau\tau$ events [105]. The decision to use the two loosest WP is based on the good discrimination against the $\bar{t}t$ background without loosing much signal efficiency.

5.7. Missing Transverse Energy

In particle accelerators, the longitudinal energy of the partons that collide is unknown as they carry varying fractions of the proton momentum. However, the energy in the transverse plane is known to be 0 (without inclusion of resolution effects). Thus, the vector sum of all particles produced in the interaction should add up to 0. However, if the collision products contain neutrinos or other particles (like in some BSM models) that travel through the detector without interactions, their momentum cannot be reconstructed and a deficit of energy in the flight direction is observed. To take these energy losses into account, the missing transverse energy (E_T^{miss}) [106] is used, defined by the negative vector sum of all PF candidates in the event:

$$E_T^{miss} = \left| \sum_{\text{PF Cand.}} \vec{p_T} \right| \tag{5.8}$$

If only one neutrino is produced in an event, the E_T^{miss} contains its full transverse momentum information. However, if several neutrinos are within an event and they have a back-to-back signature, the E_T^{miss} of the event is suppressed and does not contain the full energy information. This is the case for a Wh and WZ resonance with leptonic W decays and h/Z decays to two taus. However, as shown in Chap. 4, the event still contains a large amount of E_T^{miss}. Therefore, a selection value of $E_T^{miss} > 50$ GeV is used.

Since all PF objects contribute to the E_T^{miss}, their energy scales influence the measurement. For most objects, these effects are taken into account within the uncertainties. However, for the jet energy corrections described above, they are directly propagated to E_T^{miss} to form the so called type-1 corrected E_T^{miss} [107] using the formula:

$$E_T^{miss}\,(\text{corr}) = E_T^{miss} - \sum_{\text{jet}}^{N_{\text{jets}}} \left(p_{T,\,\text{jet}}^{\text{corr}} - p_T^{\text{jet}} \right) \tag{5.9}$$

where E_T^{miss} (corr) and E_T^{miss} are the corrected and uncorrected missing E_T and $p_{T,\,\text{jet}}^{\text{corr}}$ and $p_{T,\,\text{jet}}$ the corrected and uncorrected jet momenta. To enter the missing E_T correction, the momentum of the corrected jets is required to be above 10 GeV.

CHAPTER 6

Analysis

In this chapter, the details of the analysis chain will be discussed. This includes the selection of the datasets and Monte-Carlo simulation, the event selection, the estimation of the SM background, and the discussion of the systematic uncertainties.

6.1. The 2016 CMS Dataset

The basis of the analysis is the dataset recorded by the CMS experiment in 2016 at a center-of-mass energy of $\sqrt{s}$ = 13 TeV. The data has been collected in eight different run periods, summarized in Tab. 6.1. Overall, the LHC delivered an integrated luminosity of about 40.8 fb^{-1} per interaction region of which 37.8 fb^{-1} have been recorded by the CMS experiment, resulting in a data taking efficiency of 92.5 %. For this analysis, not all of these events are used, but only those where all parts of the detector were working well, corresponding to an integrated luminosity of $\mathscr{L}_{\text{int}}$ = (35.9 $\pm$ 0.9) fb^{-1} [108], collected by electron, photon, muon, or missing transverse energy triggers (see Sec. 6.3.2). A summary of the performance of the LHC and CMS in 2016 is shown in Fig. 6.1.

Dataset Name	Run Range	$\mathscr{L}_{\text{int}}$ (fb^{-1})
Run2016 B	273150 - 275376	5.8
Run2016 C	275656 - 276283	2.6
Run2016 D	276315 - 276811	4.3
Run2016 E	276831 - 277420	4.0
Run2016 F	277932 - 278808	3.1
Run2016 G	278820 - 280385	7.5
Run2016 H-v2	281207 - 284035	8.4
Run2016 H-v3	284036 - 284068	0.2
Full 2016 Data	273150 - 284068	35.9

Table 6.1.: Summary of the various run periods, their CMS run range, and the corresponding luminosity used in this analysis.

6.2. Monte-Carlo Simulation

For the comparison of the observed data to the expected background and for the optimization of the signal selection, Monte-Carlo (MC) simulations are used. The most important characteristics of the MC simulations of SM processes will be discussed in the following.

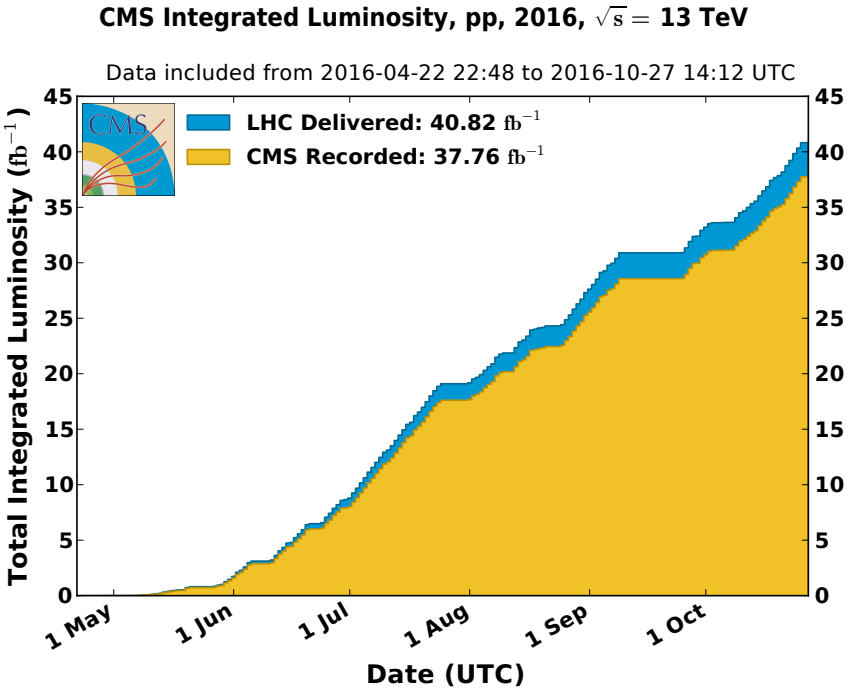

Figure 6.1.: Integrated luminosity as a function of time for the 2016 data taking period [50].

6.2.1. Parton Distribution Functions

In the LHC, bunches of high energy protons are accelerated and collided to obtain a large number of events that can be used for further analyses. Therefore, the composite structure of the protons needs to be taken into account. Protons are built out of partons (valence quarks, sea quarks, and gluons from the strong interaction) that all carry a variable part of the full proton momentum [28]. Therefore, the center-of-mass energy of the proton-proton collision ($\sqrt{s}$ = 13 TeV) differs from the actual center-of-mass energy of the two colliding partons. This energy is given by

$$\sqrt{\hat{s}} = \sqrt{x_1 \cdot x_2}\sqrt{s} \tag{6.1}$$

where $x_{1/2}$ are fractions of the parton momenta with respect to the proton momentum. Since the fraction of the parton momentum varies, it can only be described by a statistical distribution, called parton distribution function (PDF). For each parton, the corresponding PDF describes the probability that it carries the fraction x_i of the proton momentum at a given energy scale μ^2. This can be for example the energy scale of the electroweak interaction, which is approximately $\mu^2 = 10^4$ GeV^2. The PDFs have to be measured experimentally and have been extrapolated to LHC energies based on measurements from previous experiments. There are many different PDF sets, but for the 2016 CMS simulation production, the one mainly used is NNPDF3.0, except for samples generated with Pythia 8 [109, 110] where NNPDF2.3 is used. The PDF sets for NNPDF3.0 at next-to-leading order are presented in Fig. 6.2.

The cross section of a simulated process is given by

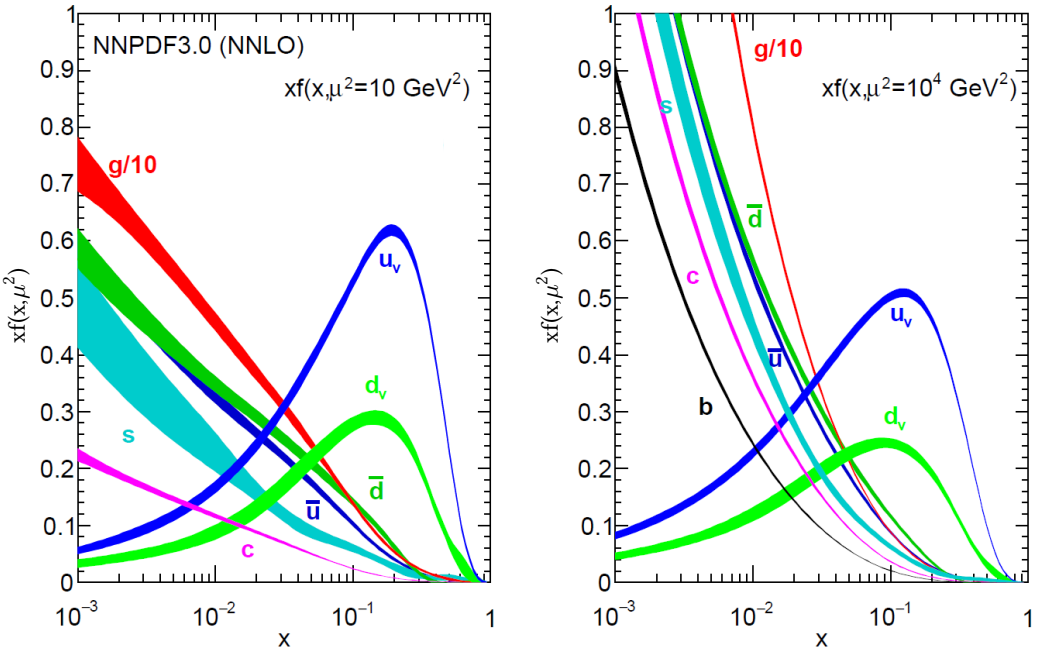

Figure 6.2.: Illustration of next-to-leading order PDF sets NNPDF3.0 for an energy scale μ^2 = 10 GeV^2 (left) and $\mu^2 = 10^4$ GeV^2 (right), adapted from [28]. Here, g/10 corresponds to the PDF of gluons divided by 10. The PDFs are presented in terms of the product xf(x,μ^2) since it can be translated easily to the cross section σ.

$$\sigma = \sum_{i,j} \int_0^1 \int_0^1 dx_1\, dx_2\, f_i\left(x_1, \mu^2\right) f_j\left(x_2, \mu^2\right) \hat{\sigma}_{i,j}(\hat{s}). \tag{6.2}$$

where $\hat{\sigma}_{i,j}(\hat{s})$ is the cross section of the parton-parton collision, $x_{1/2}$ are the momentum fractions of the two partons, and $f_{i/j}$ the corresponding parton distribution functions. Since there are different PDF sets, the theoretical cross section can slightly vary. This variation is taken into account as a systematic uncertainty on the PDFs, as it will be described in Sec. 6.5.

6.2.2. Background Processes

For an accurate description of the expected background, various SM processes are simulated with different generators. The generators used in this analysis are MADGRAPH5_aMC@NLO v2.4.2 [111, 112], POWHEG v2 [113–115], and PYTHIA 8.212 [109,110]. While PYTHIA 8 is a leading order (LO) generator, MADGRAPH5_aMC@NLO and POWHEG can produce events at next-to-leading order (NLO). However, in some cases processes are produced at LO with MADGRAPH5_aMC@NLO to increase the statistics while reducing the computing time. In the following, the generator name MADGRAPH is used for leading order processes and aMC@NLO for next-to-leading order processes if the samples are produces with MADGRAPH5_aMC@NLO. For most background samples, a k-factor is applied to scale the cross section from LO to NLO or NNLO (next-to-next-to-leading order):

$$k = \frac{\sigma_{(N)NLO}}{\sigma_{LO}}. \tag{6.3}$$

Although the general simulation of events is done with different generators, the subsequent showering and hadronization is modelled with PYTHIA 8 using the CUETP8M1 tune [116]. After the events are produced, a pileup scenario (Summer 16 scenario) is implemented to simulate the effect of additional proton-proton interactions per bunch crossing and the events have to pass the full CMS detector simulation implemented in GEANT 4 [117, 118]. Finally, the background samples run through the full analysis chain, including the trigger requirement and the reconstruction and identification of particles.

The SM background processes in this analysis can be split in two categories. The first category includes backgrounds where the hadronic tau arises directly from the corresponding process while the second category describes backgrounds that enter the event selection because of other objects that are misidentified as hadronic taus. Since these processes have a much larger cross section, they end up to be the main contributors to the SM background. In this section, a qualitative discussion of all background processes will be presented. A full list of all SM background samples and the corresponding cross sections can be found in Appendix B.2. If possible, the cross sections are normalised to NNLO. However, for some processes there is no NNLO cross section calculation yet. In these cases, the NLO normalisation will be used.

Prompt Hadronic Tau Backgrounds

- $\underline{q\bar{q}' \to WZ \to 3\ell\nu}$: The production of WZ pairs is the main background process that can directly produce the objects that are selected in the various channels if the W decays leptonically and the Z decays to two tau leptons. If the two bosons are produced back-to-back, this background is completely signal like and cannot be rejected by using additional selection requirements. However, since the lepton momenta are lower than of the signal process, and the cross section of this process is not very high, the impact of WZ production is only the third largest if the backgrounds from hadronic tau misidentification are taken into account. This background is simulated with POWHEG at NLO. The cross section normalisation is also at NLO [119, 120]. Fig 6.3 (left) shows the feynman diagram of the WZ final state decaying to three leptons.

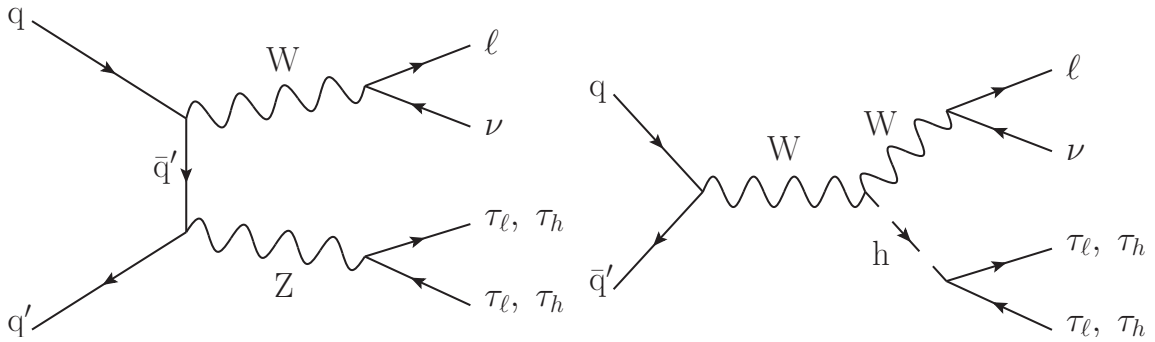

Figure 6.3.: Feynman diagrams of WZ (left) and Wh (right) production and the subsequent decay of the two bosons to the final state objects.

- $\underline{q\bar{q}' \to Wh \to 1\ell 1\nu 2\tau}$: The associated production of a SM Higgs boson together with a W boson can also produce a signal like signature. In general, the description of this background is similar to the WZ process, as it will also only contribute to the final result if the two bosons are back-to-back. The production cross section of Wh pairs is even smaller than the one of

the WZ production, decreasing its impact on the background composition. The corresponding feynman diagram can be found in Fig. 6.3 (right). The process is simulated using POWHEG at NLO. Other Higgs production mechanisms, like $gg \to ZZ$, $t\bar{t}h$ production, and Zh associated production can also contribute to backgrounds including prompt hadronic taus. However, their impact is nearly negligible. Nevertheless, they are included in this analysis with most of the backgrounds being produced with POWHEG, except for the $t\bar{t}h$ production where the aMC@NLO generator is used. For the $t\bar{t}h$ sample, a NLO cross section is used while the other SM Higgs backgrounds use a NNLO normalisation [121, 122].

- ZZ, WWW, WWZ, WZZ, ZZZ: The diboson production of two Z bosons and the triple-boson production of SM vector bosons can also contribute to three lepton events with prompt hadronic taus. However, due to their very low cross section, the impact is very small. While the ZZ background is produced with POWHEG, the triple-boson backgrounds are simulated with aMC@NLO. All of these processes are normalised to NLO [119, 123].

- $t\bar{t}V$, $t\bar{t}t\bar{t}$: Events with two top quarks and one vector boson can contribute if all objects decay leptonically. This is also the case for four top quarks, if at least three of them decay leptonically. Same as for most prompt tau backgrounds, the cross sections of these processes are very small, and therefore their contribution is also small. All of these backgrounds are simulated with aMC@NLO [119, 124].

Backgrounds from Tau Misidentification

- $gg \to t\bar{t} \to 2\ell 2\nu 2b$: The production of two top quarks that subsequently decay to two leptons, neutrinos and bottom quarks can contribute to the SM background, if one of the b-jets is misidentified as a hadronic tau. Because of its large cross section in conjunction with its large number of jets, the $t\bar{t}$ background is the leading background in most channels. In final states where both taus decay hadronically, the semileptonic $t\bar{t}$ decay adds also a small contribution to the background expectation. The $t\bar{t}$ background samples are produced with POWHEG and normalised to NNLO [124–127], including tail samples binned in terms of the dilepton mass which are normalised to NLO. Fig. 6.4 (left) shows the feynman diagram of the $t\bar{t}$ production and its decay to two leptons, including how an additional hadronic tau arises from misidentified b-jets.

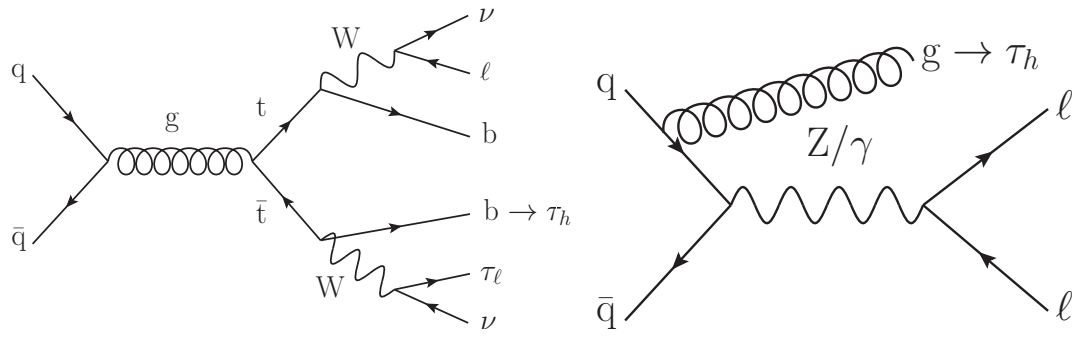

Figure 6.4.: Feynman diagrams of the $t\bar{t}$ production and fully leptonic decay (left) and the Drell-Yan production decaying to leptons (right) with the information how they produce final state particles.

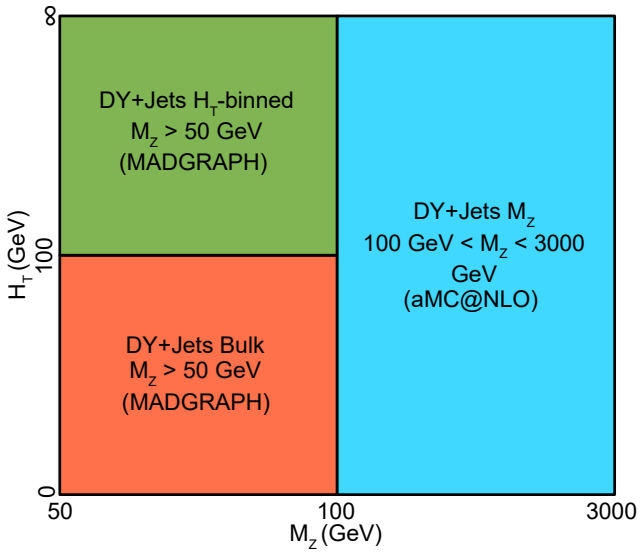

Figure 6.5.: Combination of the various Drell-Yan samples and their cut values in the M_ℓ-H_T plane.

- $q\bar{q} \to Z/\gamma \to \ell\ell$: The Drell-Yan production together with an additional jet is the leading background in the channels with two same flavour leptons. The Z/γ production can result in $\ell\ell\tau_h$ final states if it decays leptonically and an additional jet in the event is misidentified as a hadronic tau. For highly off-shell produced Drell-Yan events ($M_{\ell\ell} \gg 91$ GeV), the two leptons are back-to-back and the signal signature is imitated if the misidentified jet is close to one of the two leptons. To increase the MC statistics of this process, several different simulation samples are combined, as shown in Fig. 6.5. For dilepton masses above 100 GeV, samples binned in terms of the dilepton mass are used, produced with aMC@NLO. Below 100 GeV, a combination of the bulk sample and H_T-binned[1] samples ($H_T > 100$ GeV) is used, both produced with MADGRAPH. The bulk samples are normalised to NNLO while the tail samples are normalised to NLO [119,128]. A feynman diagram that shows how this process can contribute to the background expectation is shown in Fig. 6.4 (right).

- $q\bar{q}' \to W \to \ell\nu$: The production of a W boson can contribute to the fully hadronic channels, if two jets in an event are misidentified as hadronic taus. Since two medium isolated taus reduce the possibility for two misidentifications in one event drastically, the impact of the W production is relatively small, but not negligible. The simulation of these events is done with MADGRAPH with NLO normalisation [119], including H_T-binned samples for $H_T > 100$ GeV.

- $q\bar{q} \to WW \to 2\ell 2\nu$: The WW production process can contribute in a similar way as Drell-Yan, producing two leptons and one hadronic tau from a misidentified jet. The process is simulated with POWHEG with NNLO normalisation [129], including samples binned in terms of the dilepton mass.

- QCD Multijet: QCD multijet events are negligible for the final analysis result, but they play an important role in the data driven method as they contribute to the tight and loose control region. For this background, electromagnetic (EM) and muon enriched samples simulated with PYTHIA 8 at LO are used [119].

[1] H_T corresponds to the sum of transverse hadronic energy within an event and is therefore a measure of the hadronic activity.

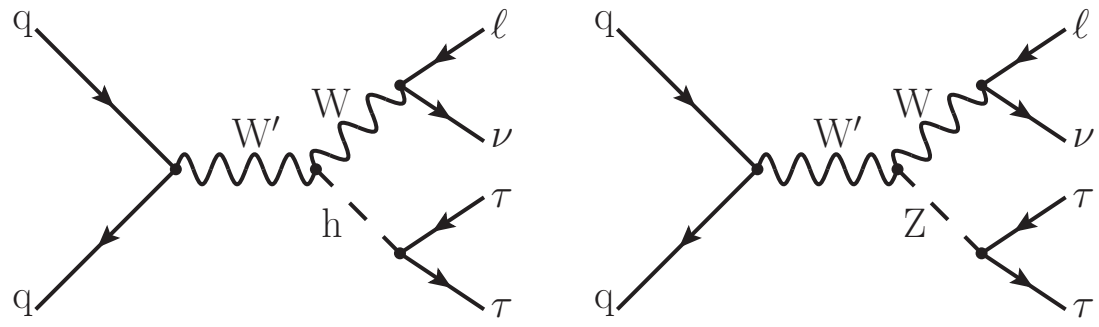

Figure 6.6.: Feynman diagrams of the production of heavy charged particles (W′) decaying to Wh (left) and WZ (right) bosons that subsequently decay to $\ell\nu\tau\tau$.

The various backgrounds will be combined in the histograms. The "V+Jets" background includes the production and decay of single electroweak bosons, namely the $W^{\pm}$ and the Drell-Yan processes, as well as their tail samples. The "$t\bar{t}$, $t\bar{t}V$, t+X" background combines all processes including top-quarks, except for the $t\bar{t}h$ process because it enters the SM Higgs backgrounds. The "VV, VVV" background includes all multiboson processes without Higgs bosons and therefore also the important WZ process, while the "ggH, qqH, VH, $t\bar{t}H$" summarizes the various impacts from the SM Higgs boson production. "QCD" marks all events due to QCD multijet production.

6.2.3. Signal Samples

The signal samples for this analysis have been produced with MADGRAPH [112] at LO based on the HVT model [2] described in Sec. 2.3. In this analysis, two types of signal samples are used, namely the decay of a heavy charged diboson resonance W′ to Wh and to WZ, with both of them subsequently decaying via $W \to \ell\nu$ and $h/Z \to \tau\tau$. Fig. 6.6 shows the feynman diagrams for these processes.

For the Wh decay chain, twelve mass points between $M_{W'}$ = 600 GeV and $M_{W'}$ = 4 000 GeV were produced, each of them with approximately 50 000 events. If the branching fractions are taken into account, this means that each of the two fully hadronic channels has about 7 000 events and each of the four semileptonic channels has about 3 800 events. Tab. 6.2 summarizes the characteristics of the twelve mass points for the $Wh \to \ell\nu\tau\tau$ decay, including the cross section in the HVT model A, HVT model B, and the number of generated events. In case of the WZ decay, the same mass points have been produced. However, the signal samples include also decays of the Z boson to electrons and muons. Since the number of generated events is the same as for the Wh decay, but only 1/3 of these events decay via $Z \to \tau\tau$, the statistics is decreased by a factor of 3. Tab. 6.3 summarizes the characteristics of the twelve mass points for the $WZ \to \ell\nu\tau\tau$ decay. The cross section given here does only include the decay via $Z \to \tau\tau$ for an easier comparison with respect to the Wh decay. No k-factor is applied on the signal cross sections, meaning that also the normalization is at LO.

6.3. Event Selection

After discussing the background composition and the signal processes, the information can now be combined to choose the best event selection to distinguish between the signal and the background.

M'_W (GeV)	Cross section × BR (HVT model A) (pb)	Cross section × BR (HVT model B) (pb)	Events
600	$6.458 \cdot 10^{-2}$	-	50 000
800	$2.158 \cdot 10^{-2}$	$1.763 \cdot 10^{-2}$	50 000
1000	$8.899 \cdot 10^{-3}$	$1.007 \cdot 10^{-2}$	50 000
1200	$4.172 \cdot 10^{-3}$	$5.312 \cdot 10^{-3}$	50 000
1400	$2.134 \cdot 10^{-3}$	$2.892 \cdot 10^{-3}$	50 000
1600	$1.160 \cdot 10^{-3}$	$1.632 \cdot 10^{-3}$	50 000
1800	$6.587 \cdot 10^{-4}$	$9.506 \cdot 10^{-4}$	50 000
2000	$3.866 \cdot 10^{-4}$	$5.678 \cdot 10^{-4}$	37 600
2500	$1.125 \cdot 10^{-4}$	$1.696 \cdot 10^{-4}$	48 400
3000	$3.546 \cdot 10^{-5}$	$5.420 \cdot 10^{-5}$	50 000
3500	$1.162 \cdot 10^{-5}$	$1.791 \cdot 10^{-5}$	50 000
4000	$3.849 \cdot 10^{-6}$	$5.965 \cdot 10^{-5}$	50 000

Table 6.2.: Summary of Monte Carlo signal samples with corresponding cross sections for HVT model A and HVT model B and the number of generated events for Wh resonances.

M'_W (GeV)	Cross section × BR (HVT model A) (pb)	Cross section × BR (HVT model B) (pb)	Events	Events ($\ell\nu\tau\tau$)
600	$4.5 \cdot 10^{-2}$	-	50 000	16 533
800	$1.4 \cdot 10^{-2}$	$7.433 \cdot 10^{-3}$	50 000	16 654
1000	$5.4 \cdot 10^{-3}$	$4.959 \cdot 10^{-3}$	50 000	16 533
1200	$2.4 \cdot 10^{-3}$	$2.734 \cdot 10^{-3}$	50 000	16 583
1400	$1.2 \cdot 10^{-3}$	$1.517 \cdot 10^{-3}$	50 000	16 638
1600	$6.6 \cdot 10^{-4}$	$8.655 \cdot 10^{-4}$	49 200	16 401
1800	$3.7 \cdot 10^{-4}$	$5.073 \cdot 10^{-4}$	50 000	16 704
2000	$2.1 \cdot 10^{-4}$	$3.043 \cdot 10^{-4}$	49 200	16 496
2500	$6.2 \cdot 10^{-5}$	$9.139 \cdot 10^{-5}$	50 000	16 595
3000	$2.0 \cdot 10^{-5}$	$2.929 \cdot 10^{-5}$	50 000	16 702
3500	$6.4 \cdot 10^{-6}$	$9.696 \cdot 10^{-6}$	50 000	16 666
4000	$2.1 \cdot 10^{-6}$	$3.232 \cdot 10^{-6}$	50 000	16 591

Table 6.3.: Summary of Monte Carlo signal samples with corresponding cross sections for HVT model A and HVT model B and the number of generated events for WZ resonances.

First, the categorisation of the channels will be described, followed by the trigger strategy and other event filters, the selection chain and in the end a discussion of the signal efficiencies.

6.3.1. Categorisation of the Channels

A large number of channels is taken into account in this analysis. As already discussed in Sec. 4, these channels are the ones including one well isolated lepton and fully hadronic or semileptonic decays of the di-tau system, resulting in six final states. These six final states can be sorted in three categories:

1. Fully hadronic (HAD): Events in this category include one well isolated electron or muon plus two hadronic taus and missing transverse energy.
2. Semileptonic same lepton flavour (SSLF): Events in this category include one well isolated light lepton (electron or muon) plus one additional lepton of the same flavour, one hadronic tau, and missing transverse energy.
3. Semileptonic different lepton flavour (SDLF): Events in this category include one well isolated light lepton (electron or muon) plus one additional light lepton of another flavour, one hadronic tau, and missing transverse energy.

Within these categories, another separation is done, splitting them into events with separated tau decay products ($\Delta R > 0.5$) and nearby tau decay products ($\Delta R < 0.5$). For events with nearby taus, a different hadronic tau reconstruction and lepton isolation is applied, as discussed in Chap. 5. In some distributions in this section, the separated and nearby categories will be combined, but the final result will be calculated based on the following six distributions: separated HAD, nearby HAD, separated SSLF, nearby SSLF, separated SDLF, and nearby SDLF. The distinction between separated and nearby categories is important since their final background description is different. While the background description of the separated channels is based on a data driven method, the nearby region relies on Monte Carlo. The reasons for that will be discussed in Sec. 6.4.

6.3.2. Trigger Requirement

In CMS, most triggers rely on well described and isolated objects. The signal signature of this analysis consists of several objects, but the only objects that are always well isolated and therefore reliable for the trigger requirement are the leptons that arise from the W decay. As discussed already in Chap. 4, these leptons have a large momentum even for lower W' masses. To get the best possible trigger efficiency, several triggers are combined using their logical "or". For the combined efficiency of N different uncorrelated triggers, the following formula can be used:

$$\epsilon_{\text{Combined}} = 1 - \prod_{i=1}^{N}(1 - \epsilon_i) \tag{6.4}$$

where $\epsilon_{\text{Combined}}$ is the combined trigger efficiency and ϵ_i are the efficiencies of the base triggers.

For analyses where the W decays to electrons, a combination of a single electron and a single photon trigger is applied, namely the HLT_Ele*_WPTight_Gsf (* = 27, 32), the HLT_Ele*_CaloIdVT_GsfTrkIdT (* = 105, 115), and the HLT_Photon_175. The numbers in the trigger name refer to their momentum thresholds. The first trigger combination has a momentum threshold of 27 GeV and 32

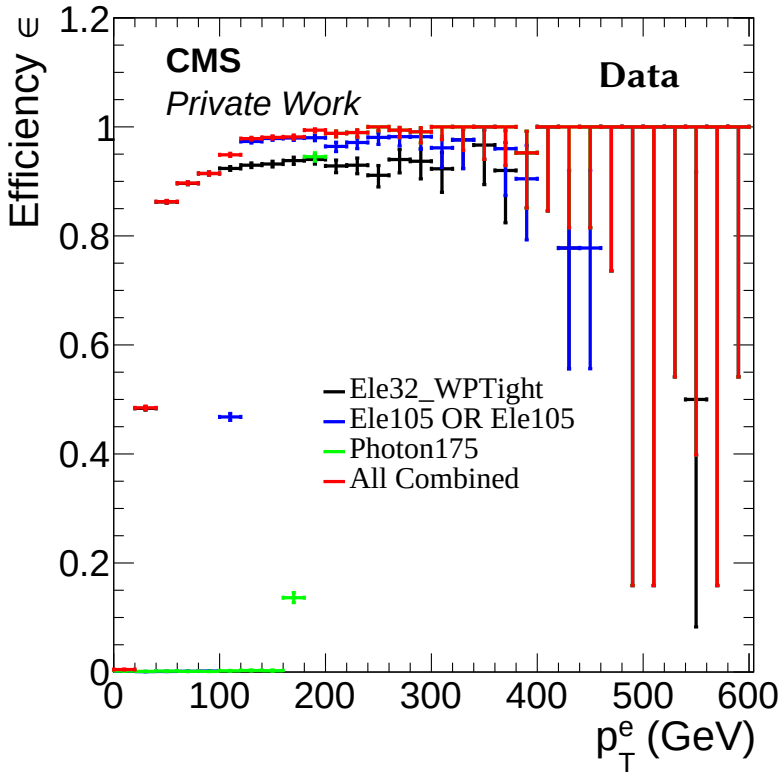

Figure 6.7.: Single electron trigger efficiency as a function of the electron momentum in data measured in single muon triggered events.

GeV. In addition, some tight isolation requirements are applied. Due to its low momentum threshold, it improves the analysis sensitivity for electron momenta below 120 GeV which is important for resonance masses below 1 TeV. The second trigger combination has a momentum threshold of 105 GeV and 115 GeV. Electrons passing these triggers, but not the HLT_Ele*_WPTight_Gsf trigger are required to have a transverse momentum of 120 GeV within the analyses to avoid the trigger turn-on. In case of the HLT_Ele*_CaloIdVT_GsfTrkIdT triggers, the calorimeter trigger is combined with a track, including a very loose isolation requirement. Due to its loose isolation, this trigger has a higher efficiency than the HLT_Ele*_WPTight_Gsf and is therefore important in the medium momentum region. In 2016, it was discovered that the electron trigger has an inefficiency in data for large electron momenta due to the electron trigger isolation. To recover this inefficiency, the HLT_Photon_175 is used in addition to the electron triggers if the electron momentum is above 180 GeV. The single photon trigger does only react to the energy deposit in the electromagnetic calorimeter and therefore does not distinguish between electrons and photons. Fig. 6.7 shows the efficiency for the triggers and their combination as a function of the electron p_T in data if the electron passes the Tight ID and the geometrical acceptance ($|\eta| < 2.5$ without barrel-endcap gap) measured on events collected with single muon triggers. The efficiency is defined by:

$$\epsilon_{\text{Trigger}} = \frac{\text{N}\,(\text{Acceptance} \times \text{Tight ID} \times \text{Trigger})}{\text{N}\,(\text{Acceptance} \times \text{Tight ID})} \tag{6.5}$$

For events where the W decays to muons, a slightly different strategy is used, combining single muon and E_T^{miss} triggers. In case of the single muon triggers, the logical "or" of the HLT_TkMu50

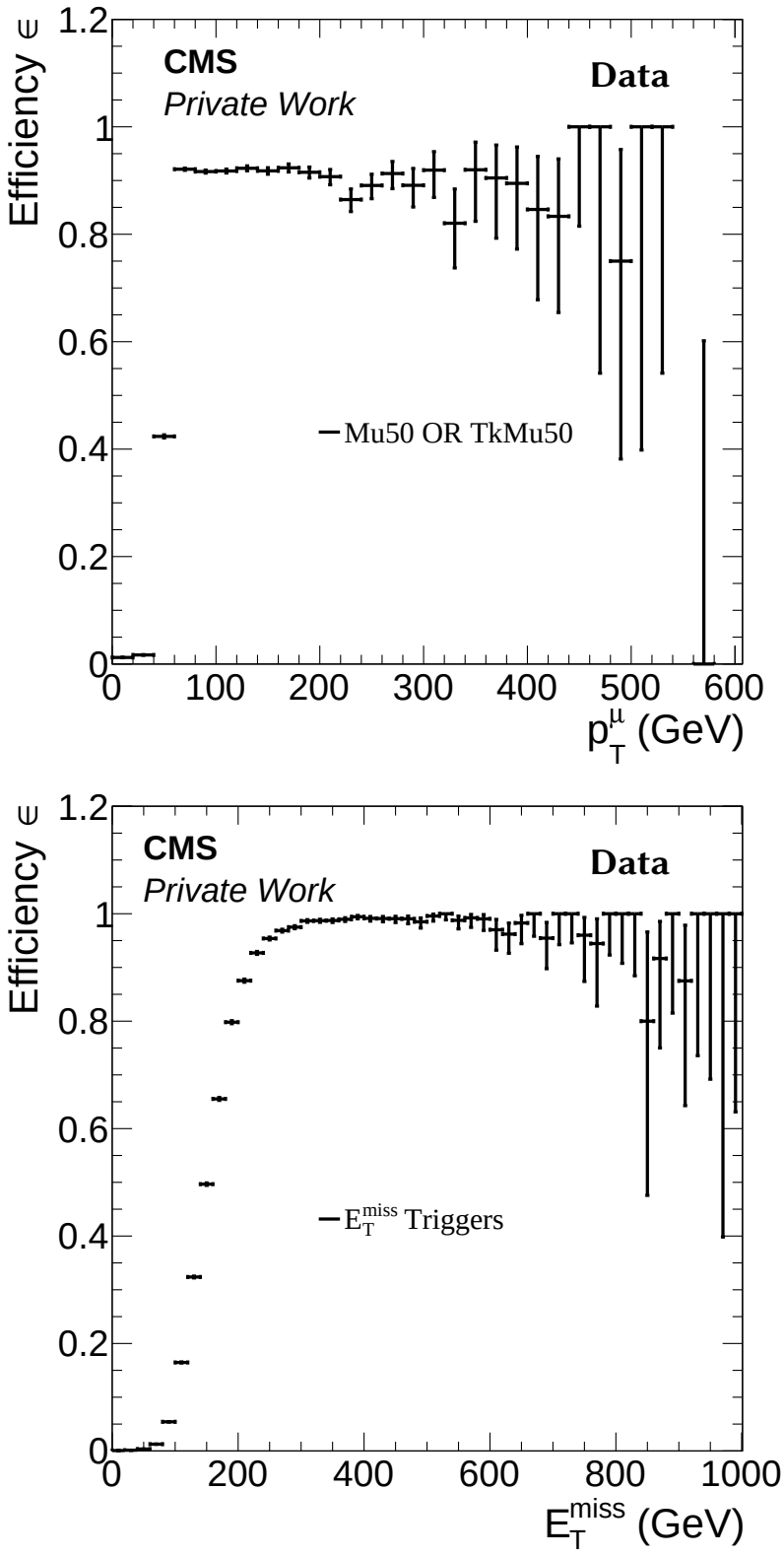

Figure 6.8.: Trigger efficiencies for the single muons triggers (top) as a function of the muon momentum and missing E_T triggers (bottom) as a function of the E_T^{miss} in data measured with single electron triggered events.

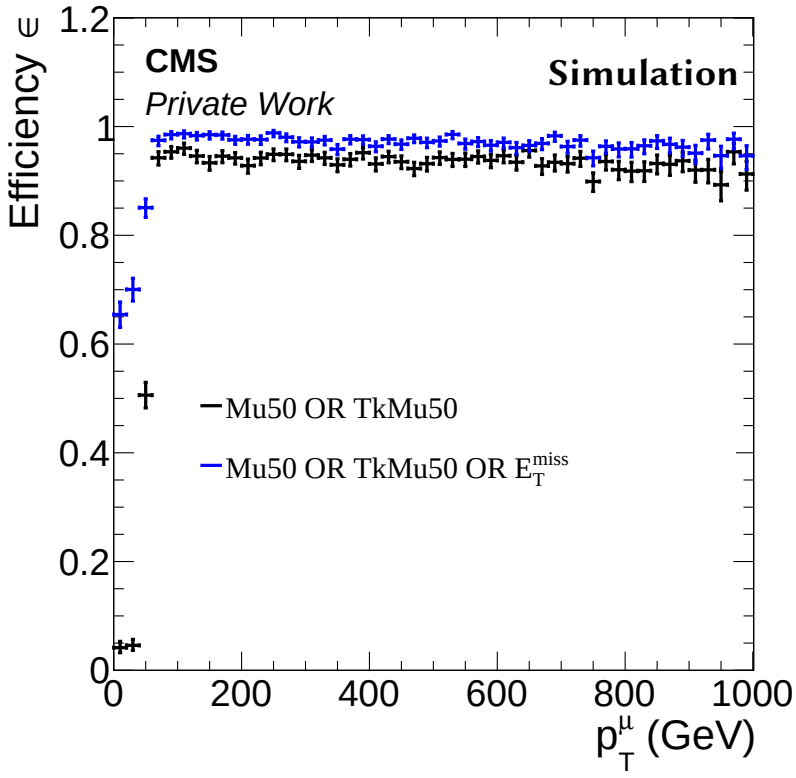

Figure 6.9.: Effect of the combination of single muon triggers and E_T^{miss} triggers on the signal for a resonance mass of 2.5 TeV.

and the HLT_Mu50 is applied. These triggers have a momentum threshold of 50 GeV and no additional isolation requirement. Fig. 6.8 (top) shows the trigger efficiency for the single muon triggers measured in data with events collected by the single electron trigger. It is visible that the single muon trigger reaches its plateau at 95 % and that it stays flat up to high masses. However, it is possible to slightly improve the trigger efficiency for the signal. As discussed in Sec. 4, the average E_T^{miss} increases for high resonance masses, resulting in some events with high E_T^{miss}. This characteristic of the signal can be used to increase the trigger efficiency for high masses. In addition to the single muon triggers, a large number of E_T^{miss} triggers are applied. A list of these triggers can be found in App. C.2. All of them measure the missing E_T^{miss} under slightly different conditions. The HLT_PFMETNoMu*_PFMHTNoMu*_IDTight (* = 90, 110, 120) for example removes good muons from the E_T^{miss} calculation, decreasing the rate of events where muons and E_T^{miss} are back-to-back, but increasing the rate of events where both objects go into the same direction. The E_T^{miss} triggers are used for events with E_T^{miss} > 250 GeV. The corresponding trigger efficiency, measured with single electron events, is shown in Fig. 6.8 (bottom). To estimate the impact of this combination, the trigger efficiency was also measured in signal simulation events. Fig. 6.9 shows the trigger efficiency as a function of the muon momentum for a resonance mass of 2.5 TeV. The application of the E_T^{miss} triggers increases the signal efficiency by 3-4 % for this mass. For lower masses, the effect is smaller, while it increases for higher resonance masses since the E_T^{miss} increases.

6.3.3. Event Filters for E_T^{miss}

The selection of missing transverse energy plays an important role in this analysis. In addition to the physical sources of E_T^{miss}, some detector components can artificially change its value if they are not working properly. To reduce these effects, additional event filters have to be applied in analyses that contain E_T^{miss}. These event filters are [130]:

- **Primary vertex filter**: The event is required to contain at least one well reconstructed primary vertex to suppress events not arising from the hard proton-proton interaction.
- **Tight beam halo filter** [131]: Beam halos are particles produced through the interaction of the proton beams with an external object, e.g. beam-gas or the beam-pipe at high pseudorapidities. These particles can be high energy halo muons that might interact with calorimeters and add a large amount of E_T^{miss} to an event. These events are removed using the timing information of the CSCs.
- **HBHE noise filter** [132]: This filter reduces the number of events with instrumental noise in the HCAL if no additional activity in the event can be found.
- **Isolated HBHE noise filter** [132]: In general this filter has the same effect as the HBHE noise filter, but applied on isolated noises.
- **ECAL dead cell trigger primitive filter** [133]: In CMS, crystals in the ECAL are removed from the readout if they produce an artificial noise. If these crystals are part of a particle reconstruction, their energy is mismeasured which effects the E_T^{miss} reconstruction.
- **ECAL endcap bad supercluster filter**: This filter is only applied on data. It reduces the effect of some 5×5 supercrystals that give anomalously high energies.
- **Bad PF muon filter** [134]: Removes events where badly misreconstructed muons with high-p_T tracks pass the PF muon requirement and enter the E_T^{miss} calculation by comparing the inner track p_T to the candidate p_T based on a ΔR matching.
- **Bad charged hadronic track resolution filter** [134]: If the badly misreconstructed muons fail the PF requirement, they end up as charged hadron candidates and enter again the E_T^{miss} calculation. These events are also removed by comparing the candidates p_T to the inner track p_T based on a ΔR matching.

6.3.4. Preselection

Channel	HAD	SSLF	SDLF
Trigger	Single e (p_T > 27, 32, 105, 115 GeV) or Single γ (p_T > 175 GeV) Single μ (p_T > 45 GeV) or E_T^{miss} (E_T^{miss} > 250 GeV)		
Objects	1 tight e/μ 2 τ_h, p_T > 20 GeV	1 tight e/μ 1 loose e/μ, p_T > 10 GeV 1 τ_h, p_T > 20 GeV	1 tight e/μ 1 loose μ/e, p_T > 10 GeV 1 τ_h, p_T > 10 GeV
E_T^{miss}	> 50 GeV	> 50 GeV	> 50 GeV
$M_{\ell\ell}$	> 20 GeV	> 20 GeV	> 20 GeV
ΔR	Nearby τ: 0.1-0.5, Separated τ: 0.5-∞		

Table 6.4.: Summary of the preselection requirements for each channel.

At the beginning of the analysis, a preselection is performed, only selecting the basic objects and applying basic selection criteria. Additional cuts that reduce the SM background and select the diboson signature are not applied yet.
Each channel that is analysed contains at least one tight lepton, passing the tight electron or muon selection requirements presented in Chap. 5. In case of tight electron events, the combination of single electron and single photon triggered events is used while for tight muon events, the combination of single muon and E_T^{miss} triggered events is used. On top of the tight lepton selection, additional channel dependent objects are required. In fully hadronic channels, two hadronic taus are selected while semileptonic channels include only one hadronic tau and one loose lepton that passes the modified PF isolation. If the ΔR between the hadronic taus or the hadronic tau and loose lepton is below 0.5, the hadronic tau is required to arise from the nearby tau reconstruction, else the separated tau reconstruction is used. In events with more than three selected objects, the combination with the highest invariant mass is used. Although the nearby tau reconstruction is optimized for the ΔR region below 0.5, it has also its limitations. If the ΔR gets smaller than 0.1, the overlap with the electromagnetic shower from the different objects gets too high and the tau reconstruction is not reliable anymore. Therefore, this analysis is restricted to distances of $\Delta R > 0.1$ with a transition region between nearby and separated hadronic taus at $\Delta R = 0.5$. The two taus and the tau plus loose lepton system are expected to reconstruct the visible part of the neutral boson (Z, h).

Background	Event Yield								
	HAD			SSLF			SDLF		
V+Jets	102.6	±	30.4	2417.4	±	50.8	61.9	±	6.9
$t\bar{t}$, $t\bar{t}V$, t+X	182.3	±	3.4	834.7	±	6.0	905.6	±	6.3
VV, VVV	35.4	±	1.8	324.8	±	3.0	97.6	±	3.2
ggH, qqH, VH, $t\bar{t}H$	5.3	±	0.3	12.6	±	0.4	9.6	±	0.4
Total	325.6	±	30.6	3589.5	±	51.2	1074.7	±	9.9
Data	365			3667			1150		

Table 6.5.: Event yields for background and data after preselection for the hadronic, semileptonic same lepton flavour, and semileptonic different lepton flavour channels in the separated tau category. The background expectation is completely estimated from simulation at this stage and the uncertainties correspond to the statistical uncertainties of the Monte-Carlo simulation only.

Additional preselection requirements affect the mass of the visible boson system and the missing transverse energy. The mass of the visible boson system is required to be above 20 GeV to reduce the effect of low mass resonances while the E_T^{miss} has to be larger than 50 GeV, reducing the impact of single vector boson production, but keeping the signal efficiency high, as discussed in Chap. 4. A summary of the preselection requirements is presented in Tab. 6.4 while the comparison between data and simulation is presented in Tab. 6.5 (separated taus) and Tab. 6.6 (nearby taus). The E_T^{miss} distributions for the semileptonic same lepton flavour channel is shown in Fig. 6.10 for the combination of the nearby and separated categories, the other channels can be found in Appendix C.3. The $\sum p_T$-distributions for all three channels after preselection can be found in Fig. 6.11 and Fig. 6.12 for the separated and nearby tau categories. Over all, a good agreement between data and SM background can be observed.

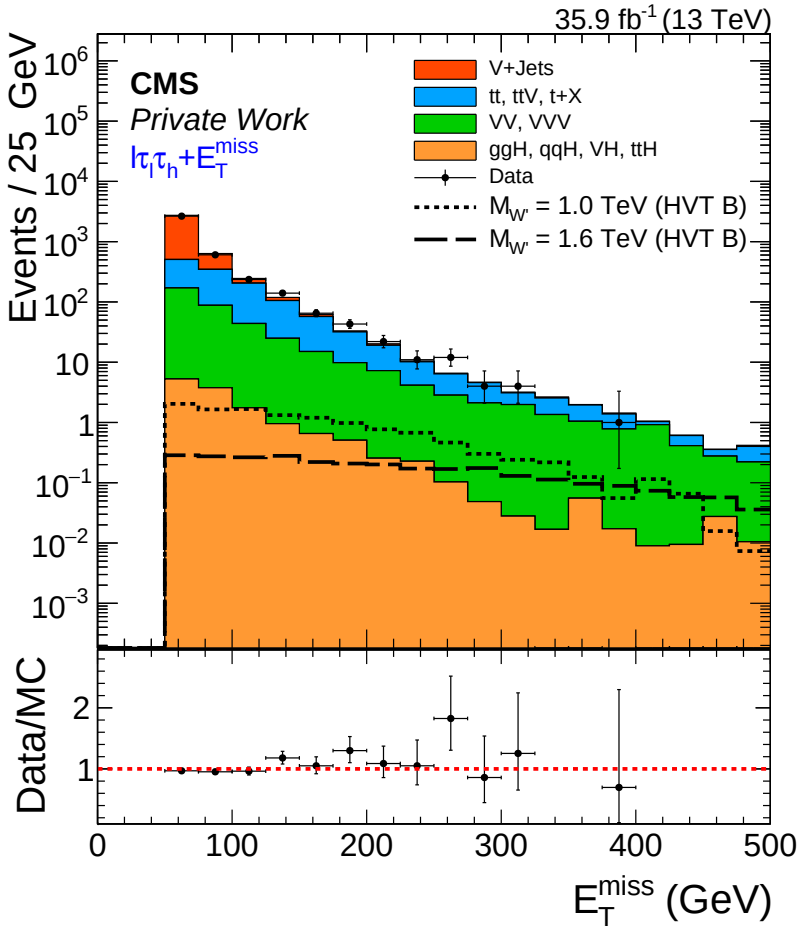

Figure 6.10.: Missing transverse energy distribution of the semileptonic same lepton flavour channel for the combination of the nearby and separated tau categories.

Background	Event Yield		
	HAD	SSLF	SDLF
V+Jets	7.4 ± 1.8	46.4 ± 5.7	3.1 ± 1.3
$t\bar{t}$, $t\bar{t}V$, t+X	18.5 ± 0.9	51.9 ± 1.6	26.2 ± 1.0
VV, VVV	3.1 ± 0.4	14.2 ± 0.8	4.4 ± 0.6
ggH, qqH, VH, $t\bar{t}H$	0.1 ± 0.0	0.3 ± 0.1	0.2 ± 0.0
Total	29.1 ± 2.0	121.1 ± 6.0	33.9 ± 1.7
Data	32	126	30

Table 6.6.: Event yields for background and data after preselection for the hadronic, semileptonic same lepton flavour, and semileptonic different lepton flavour channels in the nearby tau category. The background expectation is completely estimated from simulation at this stage and the uncertainties correspond to the statistical uncertainties of the Monte-Carlo simulation only.

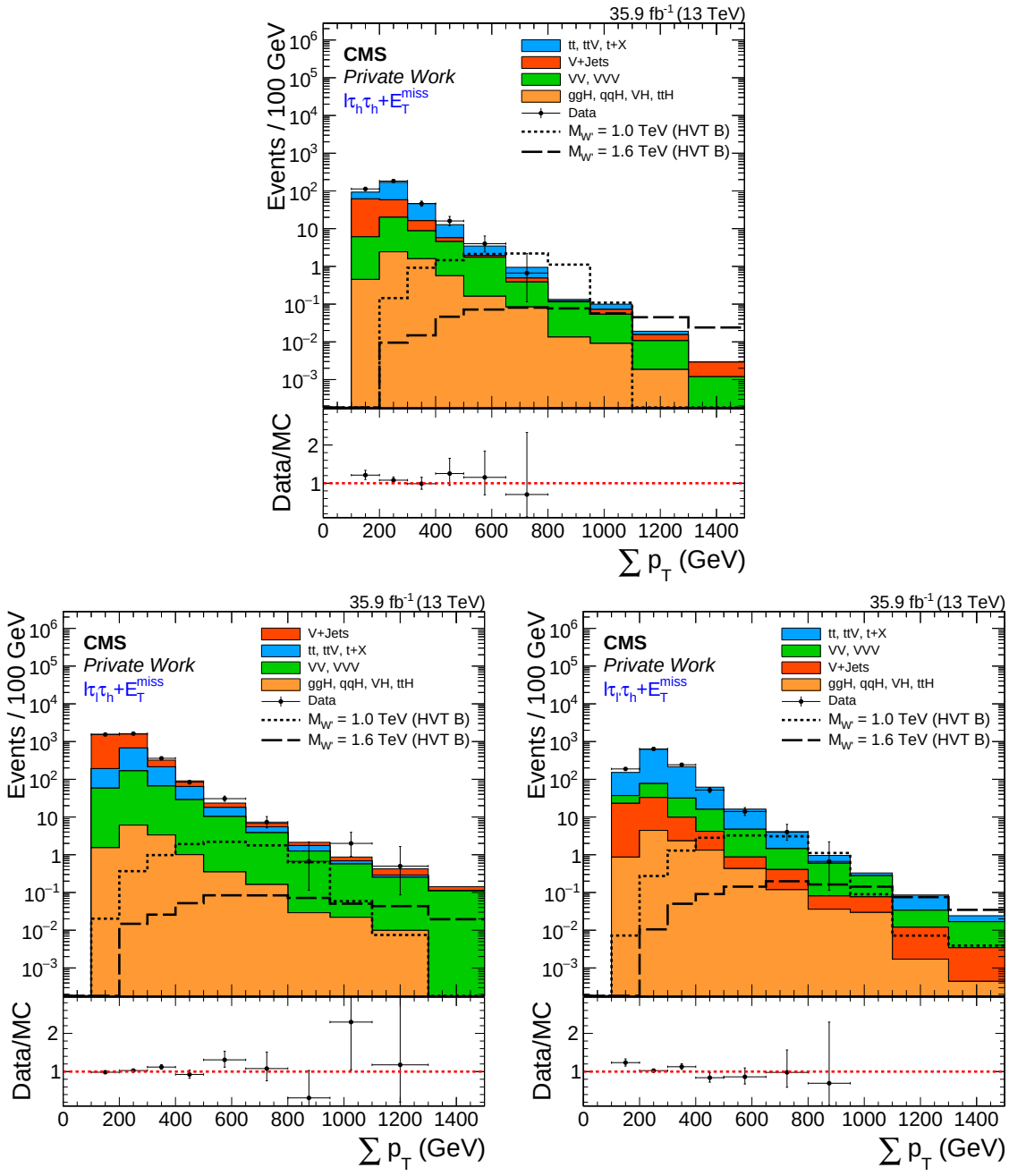

Figure 6.11.: $\sum p_T$ distributions for the hadronic (top), semileptonic same lepton flavour (bottom left) and semileptonic different lepton flavour (bottom right) channels for the separated tau category.

6.3.5. Kinematic Selection

On top of the preselection, additional kinematic selection requirements are applied to separate the signal from the SM background expectation. The selection requirements that are shown in the following part are all applied in the same way in each decay channel and tau category, except for the semileptonic same lepton flavour channels where an additional requirement on the dilepton mass is applied. To decrease the number of histograms, the separated and nearby category will be

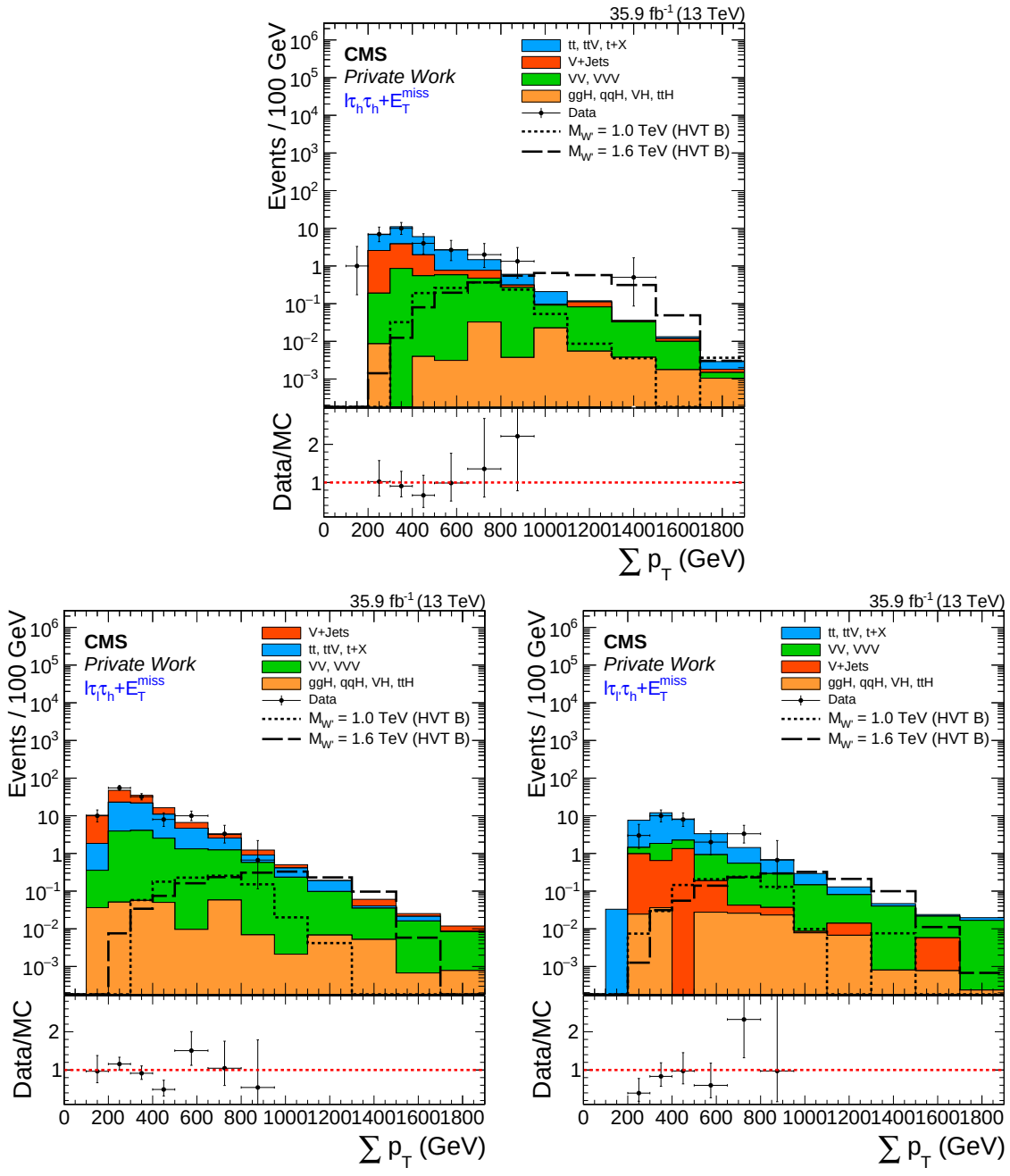

Figure 6.12.: $\sum p_T$ distributions for the hadronic (top), semileptonic same lepton flavour (bottom left) and semileptonic different lepton flavour (bottom right) channels for the nearby tau category. The data point at $\sum p_T \approx 1400$ GeV in the fully hadronic channel does not appear in the ratio plots as its ratio value is above 3.

combined. In addition, only one channel will be shown, the other control histograms are summarized in Appendix C.3. Instead of showing N-1 histograms where all selection criteria are applied except for the discussed one, all histograms are produced after the preselection step and before applying the additional kinematic selection requirements. This is done to keep the background efficiency high, as many of the criteria are very efficient and the N-1 histograms could therefore suffer from low background statistics. The signal in these distributions arises from the Wh resonance simulation

and the cross section is scaled according to the HVT model B. The selection criteria that are applied on top of the preselection are:

1. $\Delta R(\tau_{\mathbf{vis}}, \tau_{\mathbf{vis}}) < 1.5$**:** In Sec. 4, it was discussed that the distance in the detector between the two decay products from the boson decay decreases for increasing resonance masses. In this analysis, masses above 600 GeV are taken into account. For all these mass points, the largest number of signal events is expected to have a distance of $\Delta R(\tau_{\text{vis}}, \tau_{\text{vis}}) < 1.5$. Signal events above this threshold are expected to arise from double counting since an event from the decay chain $W' \rightarrow Wh/WZ \rightarrow \mu\tau_e\tau_h + E_T^{\text{miss}}$ could also be reconstructed as an event from the $W' \rightarrow Wh/WZ \rightarrow e\tau_\mu\tau_h + E_T^{\text{miss}}$ decay chain. This possible source of double counting is removed by this selection criterion since only the channel with the smallest distance between lepton and hadronic tau is kept, as suggested by the signal signature. Events that are still counted twice after this criterion are cleaned in the last step of the event selection. The requirement that each event is counted only once simplifies the final statistical analysis as no unnecessary additional correlations between the various categories need to be taken into account. Since there is a large amount of background above the chosen threshold, it can be easily suppressed by this selection criterion. Fig. 6.13 (left) shows the ΔR distribution for the semileptonic different lepton flavour channel as an example for all channels. The double counting region that is removed by this selection requirement is clearly visible at $\Delta R \approx \pi$. A different aspect that is interesting in this distribution is the transition region between the separated and nearby tau selection that is visible at $\Delta R = 0.5$. Below this region, the background expectation increases again because of the increased misidentification probability for the nearby tau selection. It shows well why the nearby tau selection is only applied in the region where it is necessary to keep the signal efficiency high.

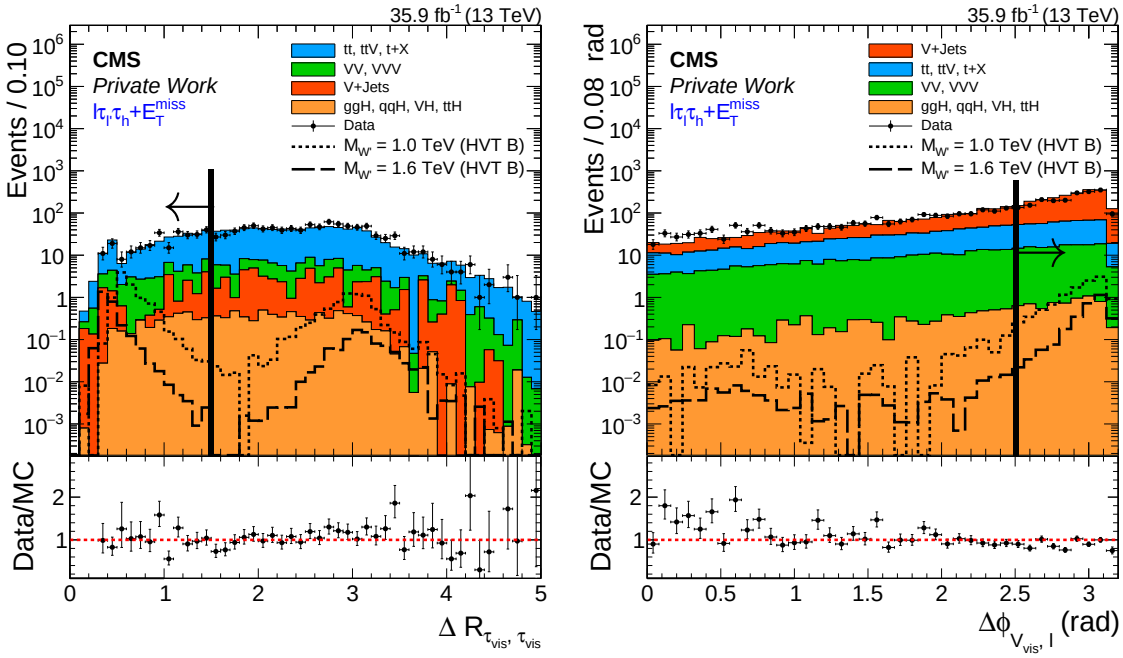

Figure 6.13.: $\Delta R(\tau_{\text{vis}}, \tau_{\text{vis}})$ distribution of the semileptonic different lepton flavour channel (left) and $\Delta\phi(V_{\text{vis}}, \ell)$ distribution of the semileptonic same lepton flavour channel (right) as an example for the corresponding selection criterion.

2. $\Delta\phi(V_{\mathbf{vis}}, \ell) > 2.5$**:** The second selection criterion that is applied uses the back-to-back signature of the heavy charged resonance. The $\Delta\phi$ between the reconstructed visible part of

the boson and the lepton from the W decay is expected to be larger than 2.5. This selection criterion removes backgrounds that do not have a resonant signature, however, it is not as efficient as the ΔR criterion. Fig 6.13 (right) shows the $\Delta\phi$ distribution for the semileptonic same lepton flavour channel. A selection criterion on the angle between the E_T^{miss} and the reconstructed visible objects is not applied since the direction of the E_T^{miss} can either be the same as the one of the boson or the lepton. This effect makes this potential criterion inefficient.

3. $\mathbf{p_T^{V_{vis}}}$ **> 100 GeV:** The next criterion makes also use of the resonance signature or more precisely of the large boson momentum because of the high resonance masses. The visible transverse momentum of the boson is expected to be above 100 GeV, removing the bulk of all SM backgrounds. Fig. 6.14 shows the visible p_T distribution for the hadronic (left) and the semileptonic different lepton flavour (right) channels. It can be seen that in both channels the chosen value discriminates fine against the background. However, it is also visible that the effect in the hadronic channel is much better. There are two reasons for that effect: In Chap. 4, it was shown that the visible momentum of the boson is higher in the hadronic channels than in the semileptonic channels. This results in more events above the selection threshold in the hadronic channel. The second reason can be found in the way the background processes contribute to this distribution. The two main backgrounds in this analysis are Z+Jets and $t\bar{t}$. In most cases, the selected events from these backgrounds consist of two prompt objects and one hadronic tau that arises from misidentified jets. While the effect from the misidentified jet is the same in the hadronic and semileptonic cases, the production mechanism of the second part of the visible boson momentum differs. In the semileptonic channels, the lepton directly arises from the decay of the Z boson or one top quark. In case of the hadronic channels, the hadronic tau arises from an additional decay, lowering its average momentum. Because of the lower energy of the second particle in the hadronic channels, the distribution of the background is shifted to lower momenta and the selection criterion is more efficient in these channels.

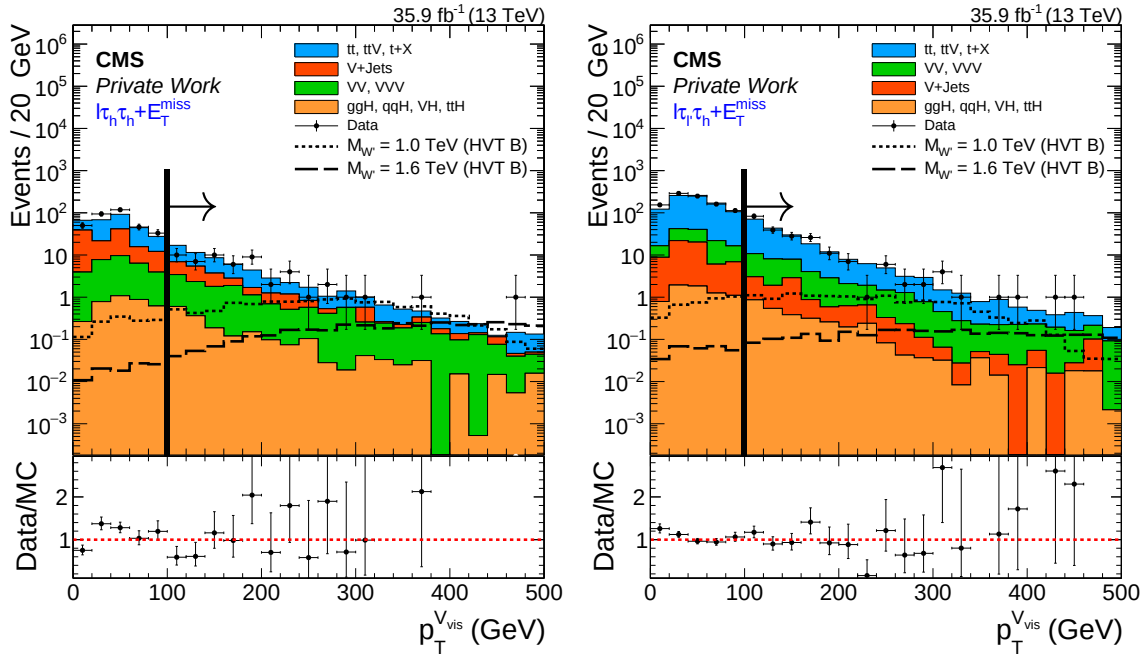

Figure 6.14.: Visible transverse momentum of the reconstructed boson for the hadronic channel (left) and the semileptonic different lepton flavour channel (right) as an example for the corresponding selection criterion.

4. $\mathbf{N_{b\text{-}tagged} = 0}$**:** The only significant reducible background that impacts all channels and categories is the production of two top quarks that subsequently decay leptonically while one of the b-jets from the decay chain is misidentified as a hadronic tau. Since the $t\bar{t}$ background is the only one that contains real b-jets, it can be discriminated easily by applying a veto on b-tagged jets. Therefore, no b-tagged jet is expected in the signal region. In case of the hadronic channel, a veto against medium b-tagged jets is applied while the semileptonic channels rely on a veto against loose b-tagged jets. This decision arose from the larger background expectation in the semileptonic channels. If this criterion is inverted, it results in a very good control region for the background from $t\bar{t}$ that will be used in the later analysis. Fig. 6.15 (left) shows the distribution of b-tagged jets for the hadronic channel. It is visible that most of the $t\bar{t}$ background can be found in the region with at least one b-tagged jet. Since b-tagged jets are only taken into account if there is no hadronic tau or lepton within $\Delta R < 0.5$ and since it is expected that one of the two b-jets in the event is misidentified as a hadronic tau, there is typically only one b-jet left that can pass the tagging criterion. This reduces slightly the discrimination power of the b-tag veto.

5. $\mathbf{M_{vis}^{\ell,\tau} > 106}$ **GeV (Z Veto):** In the semileptonic same lepton flavour channels, the decay of a Z boson to two leptons is the main background in the low energy region. To veto against these events, a Z veto is applied by restricting the combined invariant mass of the two leptons in this channel to be above 106 GeV. This selection criterion removes the largest part of the Z+Jets background, but also the WZ, ZZ and triple boson background. Fig. 6.15 (right) shows the corresponding invariant mass distribution of the two leptons. Since the semileptonic same lepton flavour background is the only background where fully reconstructed Z bosons can be expected, the selection criterion is only applied in this channel.

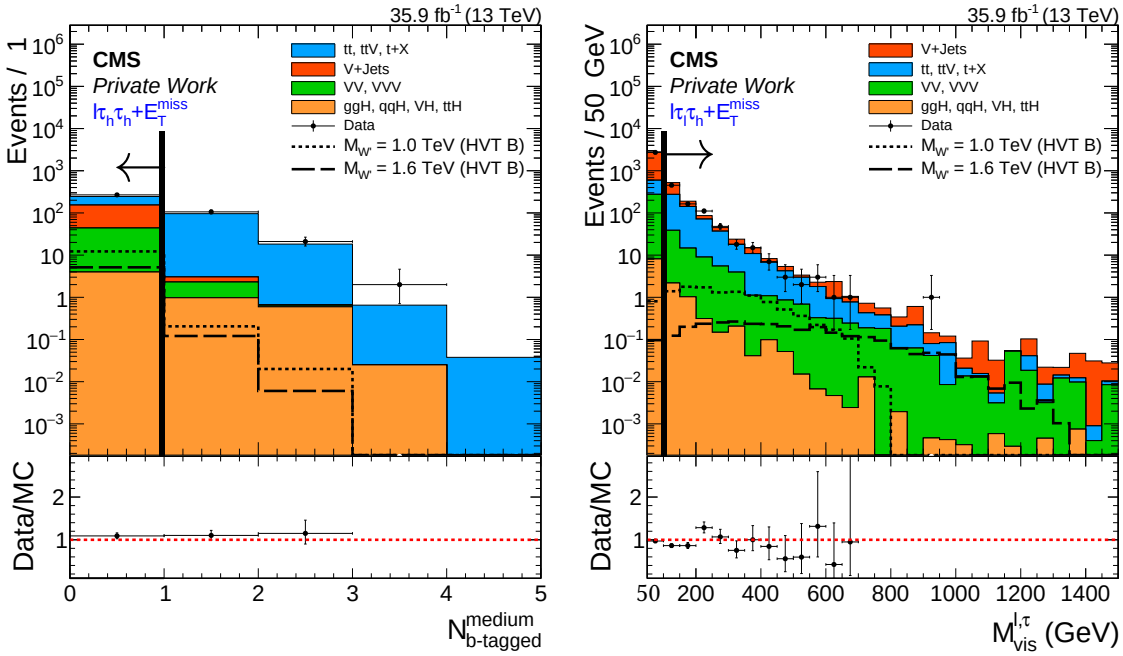

Figure 6.15.: Number of loose b-tagged jets distribution for the hadronic channel (left) as an example for the corresponding selection criterion, and the visible mass of the two leptons in the semileptonic same lepton flavour channel (right). The data point at $M_{vis}^{\ell,\tau} \approx 900$ GeV does not appear in the ratio plots as its ratio value is above 3

6. **Cleaning between categories:** As discussed earlier, there might be some double counting

that needs to be taken into account. There can be two sources for that: First, in the semileptonic different lepton flavour channels, each event can naturally end up twice in the event selection. Although the ΔR selection removes a large amount of this double counting, there might still be some events that pass the selection in both channels. The other source arises from lepton to tau misidentification. It is possible that leptons are misidentified as hadronic taus, especially in the nearby region where no lepton vetoes are applied. If this happens, events from semileptonic channels can also end up in hadronic channels. Therefore, it is restricted that all events are counted only once. If an event ends up in more than one category, it is removed from all categories except for one. In this analysis, the hadronic channels are always preferred as they have the highest sensitivity, followed by the semileptonic different flavour channels and the semileptonic same flavour channels. In case of the trigger, muon triggered events are preferred, resulting in the following order of channels to clean for double counting:

$$\mu\tau_h\tau_h > e\tau_h\tau_h > \mu\tau_e\tau_h > e\tau_\mu\tau_h > \mu\tau_\mu\tau_h > e\tau_e\tau_h.$$

The effect of the cleaning mechanism is small, less than 1 % of a 2 TeV W′ signal are removed.

Tab. 6.7 summarizes all selection criteria applied on top of the preselection. After the full selection chain, the background expectation is drastically reduced to less than 50 events per channel and tau category, as it will be shown in Sec. 6.6.

Channel	HAD	SSLF	SDLF
$\Delta R(\tau_{vis}, \tau_{vis})$	0.1< $\Delta R(\tau_{vis}, \tau_{vis})$ < 1.5		
$\Delta\phi$ (h_{vis}, ℓ_{tight})	> 2.5		
$p_T^{h_{vis}}$	> 100 GeV		
$N_{b\text{-tagged}}$ Jets	**no** medium	**no** loose	
$M_{vis}^{\ell,\tau}$ (Z veto)	-	> 106 GeV	-
Event Cleaning	Yes		

Table 6.7.: Summary of the event selection criteria applied on top of the preselection for all three categories.

6.3.6. Signal Efficiencies

After applying all selection criteria, their effect on the signal selection efficiencies can be discussed. Fig. 6.16 shows the product acceptance times efficiency for Wh (left) and WZ (right) resonance signals as a function of the generated resonance mass. The upper plots demonstrate the efficiency based on the three different channels, while the lower plots show the impact of the nearby and boosted category. The efficiencies are calculated with respect to the number of generated events that decay to $\ell\tau\tau + E_T^{miss}$ final states, also including fully leptonic $\tau\tau$ decays and (ℓ = e, μ, τ). The small spiky behaviour for WZ resonances arises from the three times smaller number of generated events ($\approx$ 16 600). It is visible that there are differences in the signal acceptance and efficiency of Wh and WZ resonances. These differences arise from the different masses of the Higgs and Z boson and the resulting effect on the ΔR of the two decay products, as

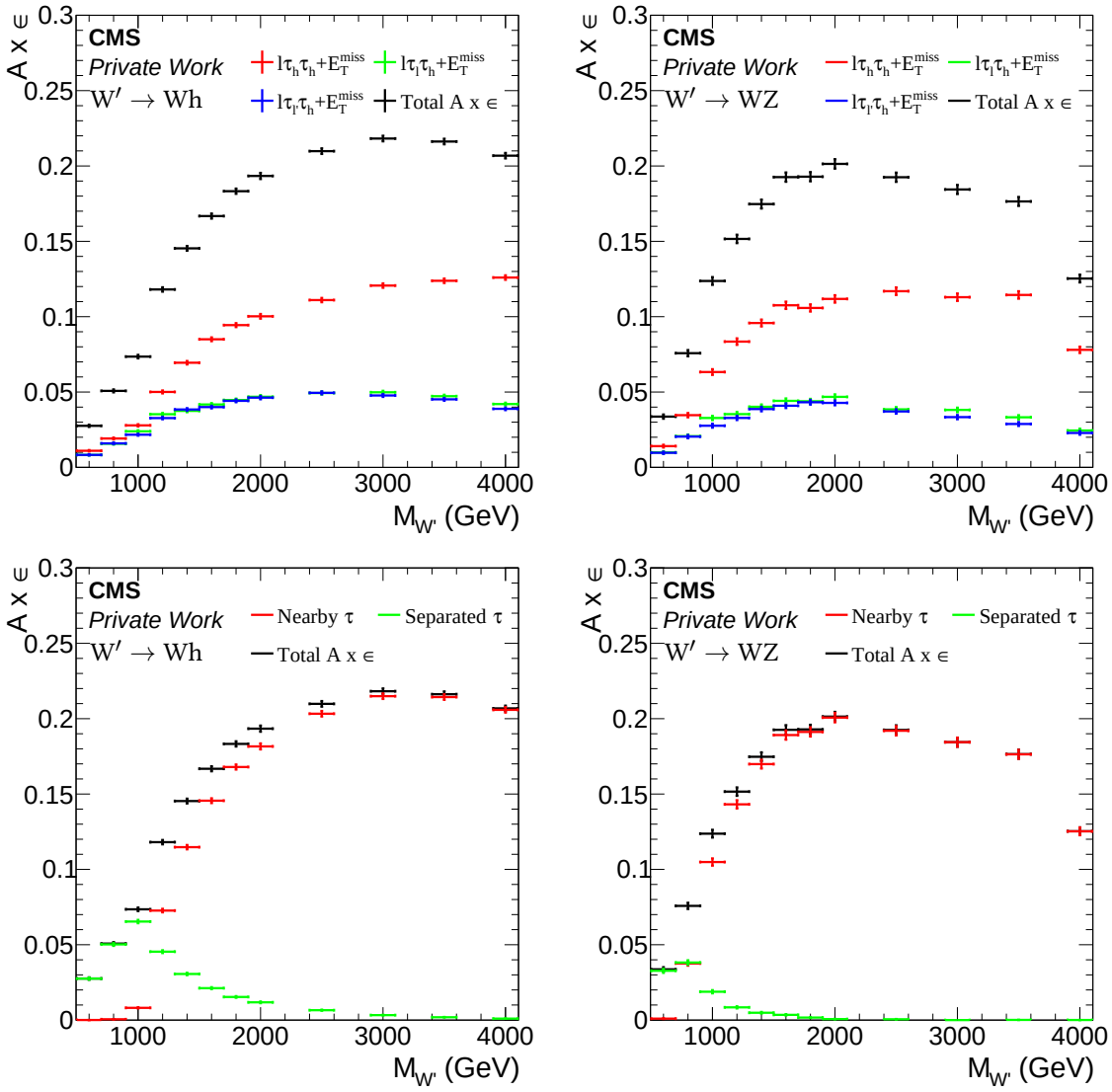

Figure 6.16.: Acceptance × Efficiency for Wh (left) and WZ (right) resonances split in the three subchannels (top) and the two tau reconstruction algorithms (bottom).

$$\Delta R \approx \frac{2 \cdot M_V}{p_T^V} \tag{6.6}$$

where V = Z, h (see Chap. 4). There are two consequences: First, the WZ resonance enters the nearby tau region already for resonance masses of 800 GeV while the Wh resonance reaches it at 1200 GeV. Second, for masses above 3500 GeV, the distance between the decay products of WZ resonances gets smaller than 0.1 and therefore, the efficiency decreases due to the $\Delta R > 0.1$ requirement. This is not the case for Wh resonances where masses above 4500 GeV are needed to enter this region. In general, the WZ resonance reaches its maximum earlier, but the efficiency starts also to decrease earlier. However, both decay channels have a maximum efficiency of 20-22 % which is a high value if the various selection criteria and the complicated object reconstruction in the nearby region is taken into account. It is visible that the efficiency starts decreasing in both channels before the selection value $\Delta R > 0.1$ is passed. This effect arises from the lepton isolation in the semileptonic channels. In

Sec. 5.5 it was shown that the modified lepton isolation does not recover the full efficiency, especially in $e\tau_h$ channels. This is the reason why the efficiency starts decreasing for high resonance masses and it also describes the difference between hadronic and semileptonic final states which is larger than the factor two expected from the different tau decay branching fractions.

6.4. Standard Model Background Estimation

After the discussion of the selection criteria and their influence on the signal, the next step is to estimate the SM background. Here, two different approaches are used for the separated and the nearby analysis. The reasons will be discussed below. The background description is split in three subsections. First, the V+Jets control region in the semileptonic same lepton flavour channel after applying an inverse Z veto will be shown, followed by the top enriched control region where the b-tag requirement is inverted for all channels. In the end, the background estimation for misidentified taus will be described, replacing several backgrounds in the separated tau category.

6.4.1. V+Jets and $t\bar{t}$ Control Regions

To compare the simulation to the observed data, two control regions are used. The first control region is defined by selecting semileptonic same lepton flavour events where the two leptons have an invariant mass below 106 GeV after the preselection requirement. To decrease the amount of top events in this region, the veto against loose b-tagged jets is also applied. This control region is completely dominated by Drell-Yan events, but it also includes the largest part of WZ events. Therefore, it is a good measure for the background description of these two processes. Fig. 6.17 shows the $\sum p_T$ distribution for both tau categories. The agreement between data and simulation in this region is good within the uncertainties for both categories.

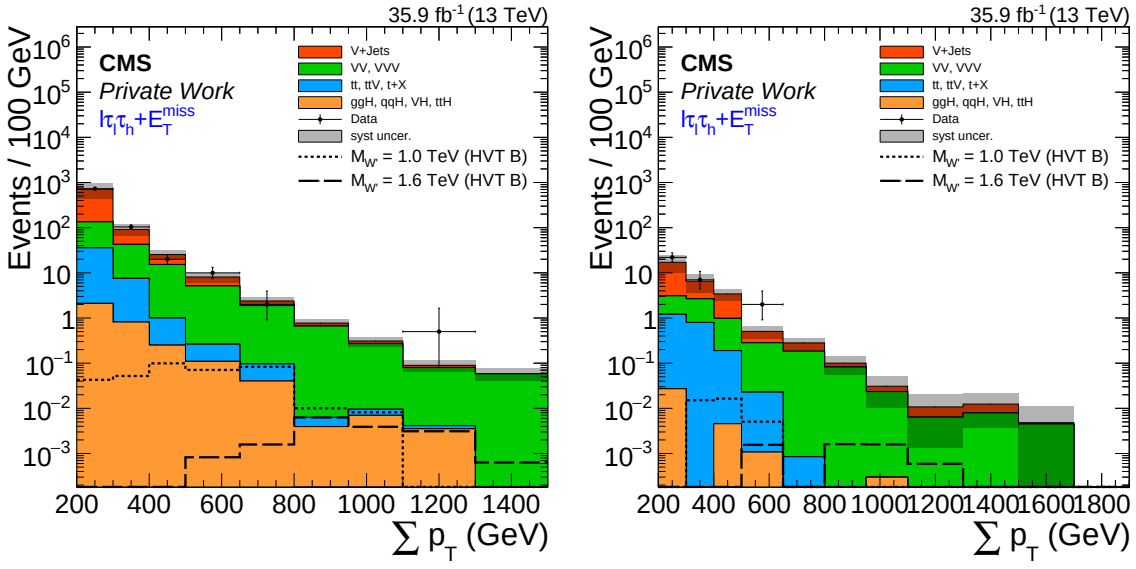

Figure 6.17.: V+Jets control region in the semileptonic same lepton flavour channels for the separated tau category (left) and the nearby tau category (right).

In addition to the V+Jets control region in the semileptonic same lepton flavour channel, a top-enriched region is defined by applying an inverted b-tag requirement on top of the preselection.

Additionally, the Z veto is used in the semileptonic same lepton flavour channel to reduce the impact of V+Jets and WZ events. Fig. 6.18 shows the corresponding $\sum p_T$-distribution in all three channels and the two tau categories. As expected, the different regions are all dominated by processes containing at least one top quark. In the semileptonic same lepton flavour categories, the impact of other processes is the largest, summing up to about 15 %. In the other channels and categories, the contribution of other backgrounds is below 5 %. The simulation describes the data well within the uncertainties, adding confidence in the simulation based background estimation. The only region with a small deficit of data is the semileptonic different lepton flavour region with nearby tau reconstruction.

6.4.2. Corrections to the SM Background

Although the simulation of the CMS detector works well, there are still some small differences in the reconstruction of physic objects in data and MC simulation. To take these differences into account, several corrections are applied to the simulation.

Pileup Reweighting

In the LHC, bunches with about 100 billion protons are collided every 25 ns. In most cases, each collision contains one hard proton-proton interaction. However, with the large number of protons in each bunch additional proton-proton interactions happen and their products also end up in the detector. Theses additional interactions are called "pileup" and they influence the measurement of the interesting hard interactions. There are two types of pileup: The in-time pileup that is produced in the same bunch crossing as the inelastic interaction and the out-of-time pileup which arises from earlier bunch crossings due to large response times of some detector components. While the in-time pileup can have a huge impact on the measurement, the influence of the out-of-time pileup is very small.

The pileup distributions in data are based on a poisson distribution that depends on the instantaneous luminosity and the minimum bias cross section σ_{mb} which includes all proton-proton collision events that are triggered and lie within the detector acceptance. In 2016, σ_{mb} = 69.2 mb is used for the estimation of pileup in data, with a systematic uncertainty of $\pm$ 4.6 % [135]. This value is based on the best fit between data and simulation. Since pileup is important for the event reconstruction, an estimation for the corresponding data taking period is included in simulation. Fig. 6.19 shows the normalized pileup distributions for simulation and data together with the uncertainty distributions based on the $\pm$ 4.6 % shift of σ_{mb}. It is visible that the two distributions look similar, however, there are still differences. To take these differences into account, the simulated events are weighted according to the ratio of these distributions. Since the number of vertices distribution is very sensitive to pileup, it is shown in Fig. 6.20 for the semileptonic same lepton flavour category after preselection before and after applying the pileup reweighting. The systematic uncertainties correspond only to the pileup uncertainties. It can be seen that the description of the background is much better using the reweighting method, but there is still a systematic effect visible. Except for the bump at about 10 vertices, this effect is covered by the systematics uncertainties.

Electron Efficiencies

Differences in the reconstruction of electrons are corrected by applying scale factors based on the identification requirements and efficiencies in data and simulation. These scale factors have been

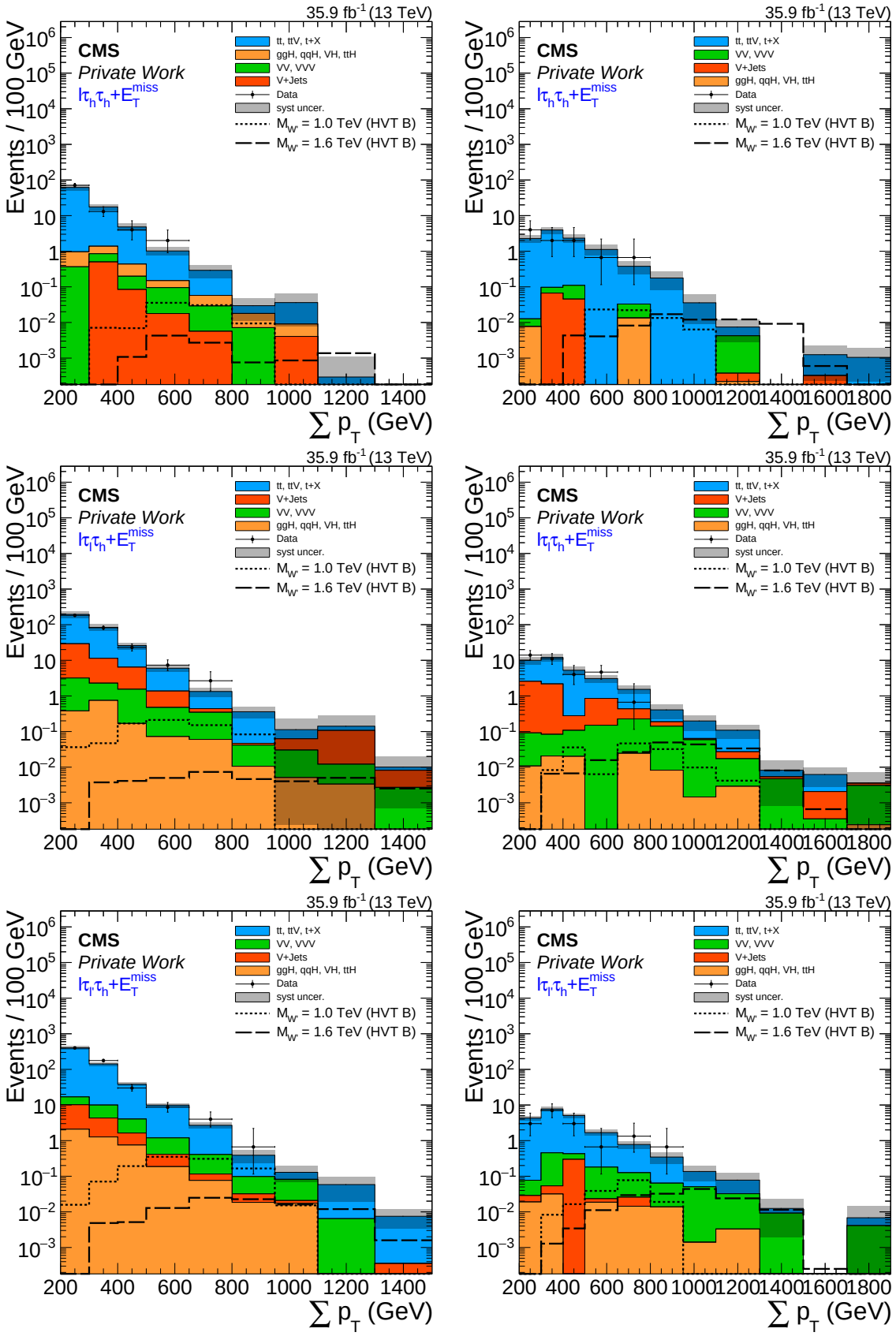

Figure 6.18.: Top-enriched control region for the hadronic (top), semileptonic same lepton flavour (middle), and semileptonic different lepton flavour (bottom) channels in the separated (left) and nearby (right) tau category.

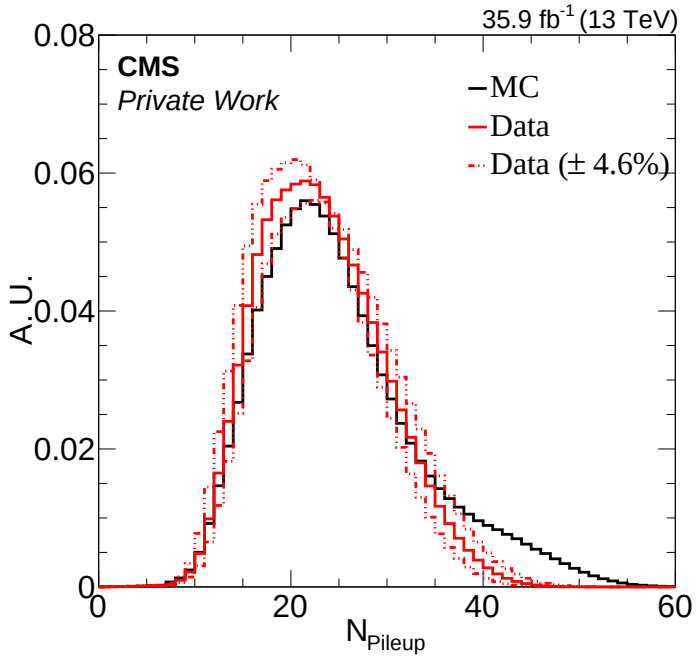

Figure 6.19.: Pileup interactions in simulation (black) and 2016 CMS data (red). The dashed lines correspond to a shift in the minimum bias cross section by ± 4.6 %.

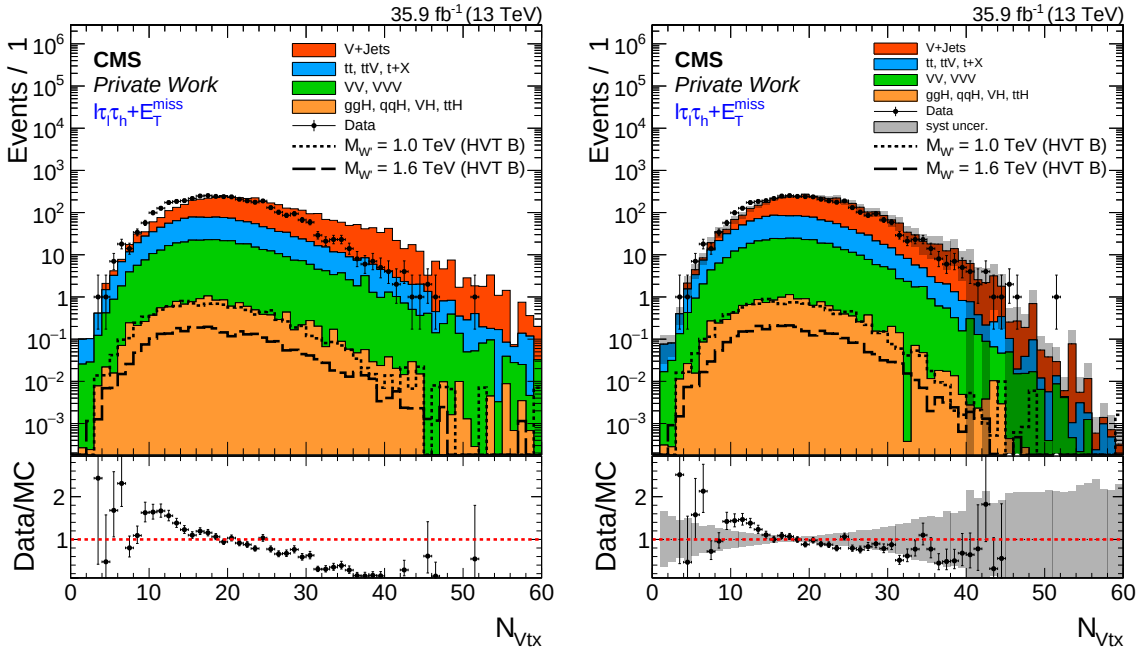

Figure 6.20.: Number of vertices distribution after preselection in the semileptonic same flavour channel before (left) and after (right) pileup reweighting.

calculated by the EGamma Physics Object Group (POG) [136] of CMS using the Tag-and-Probe [137] method and are binned in term of the pseudorapidity $|\eta|$ and the transverse momentum p_T^e. For the loose ID, the scale factors range from 0.95 to 0.98 in the barrel and 0.95 to 1 in the endcaps

for transverse momenta above 20 GeV. Below 20 GeV and if the electrons are close to the overlap region, the scale factors can be below 0.9. In case of the tight ID, the scale factors are slightly smaller, ranging from 0.92 to 0.95 in the barrel and 0.88 to 0.95 in the endcaps for $p_T^e > 20$ GeV. Same as for the loose ID, the scale factors decrease in the overlap region and for lower momenta.

On top of the scale factors for the electron identification, reconstruction scale factors are applied independently from the identification requirements. These tracking scale factors are binned in terms of $|\eta|$ and range from 0.99 in the endcaps to 0.96 in the barrel. However, for the outermost part of the endcaps ($|\eta| > 2.4$), the tracking scale factors differ and are 1.17 (EB-) and 0.88 (EB+).

Muon Efficiencies

For muons, the application of scale factors slightly differs w.r.t. electrons, as the muon isolation requirement has its own scale factors which need to be applied on top of the muon ID. These scale factors depend on the ID requirement used in combination with the isolation. All scale factors have been estimated by the Muon POG [138] using the Tag-and-Probe [139] method. For the loose ID, the scale factors range from 0.99 to 1 in the full $|\eta|$ and p_T range. The scale factors for the tight ID lie between 0.97 and 0.99. For the isolation the scale factors are compatible with unity if the isolation is applied on top of the loose ID as well as on top of the tight ID.

Same as for electrons, tracking scale factors are applied. These are binned in terms of the pseudorapidity $|\eta|$. The tracking scale factors start at 0.995 in the center barrel and decrease with increasing pseudorapidity down to 0.95 in the endcaps.

Tau Efficiencies

The scale factors for the tau efficiencies have been calculated by the Tau POG using the tag-and-probe method [85,89]. In case of the separated scenario where the medium tau isolation requirement is used, the scale factor is estimated to be flat in η and p_T with a value of 0.97. A shape based uncertainty will later be applied on the tau identification, shifting the tau scale factor up by $5\ \% \cdot p_T^\tau/\text{TeV}$ and down by $35\ \% \cdot p_T^\tau/\text{TeV}$ [89].

The efficiencies for nearby taus were also estimated by the Tau POG in events collected with single lepton triggers [85]. The scale factor was calculated in the region $0.4 < \Delta R(\ell, \tau_h) < 0.8$ and was found to be 0.97 for the very loose isolation requirement. The same uncertainties as for the separated tau reconstruction will be applied.

B-tagging Efficiencies

Same as for the other physics objects, the identification efficiency of b-tagged jets differs in data and simulation. Therefore, scale factors SF for the b-tagging efficiency need to be applied. The BTV POG (b-tagging and vertex) has measured scale factors for the b-tagging of light- and b-flavoured jets as a function of $|\eta|$ and p_T [105]. For c-flavoured jets, it is recommended to use the scale factors for b-jets. In contrast to the other objects where the scale factors are applied on events passing the selection, the event weight for b-tagging depends on the exact configuration of light-, c-, and b-jets in the simulation. The probability for a certain configuration of jets in simulation and data is given by [140]

$$\begin{aligned} P\,(MC) &= \prod_{i=\text{tagged}} \epsilon_i \prod_{j=\text{not tagged}} \left(1 - \epsilon_j\right) \quad \text{and} \\ P\,(DATA) &= \prod_{i=\text{tagged}} SF_i\,\epsilon_i \prod_{j=\text{not tagged}} \left(1 - SF_j\,\epsilon_j\right). \end{aligned} \tag{6.7}$$

Here, i and j are light-, c- or b-jets, $SF_{i,j}$ is the measured scale factor for the corresponding jet flavour as a function of $|\eta|$ and p_T, and $\epsilon_{i,j}$ is the b-tagging efficiency in simulation measured in semileptonic and fully leptonic $t\bar{t}$ events also as a function of $|\eta|$ and p_T. The event weight applied on the simulation is then given by

$$w = \frac{P(DATA)}{P(MC)} \tag{6.8}$$

In the most cases the event weight is consistent with unity, but for some extreme cases (many b-tagged jets or many not b-tagged jets) the event weight can range from 0.9 to 1.1.

Jet Energy Resolution

Measurements of the jet energy resolution have shown that it is smaller in simulation than in data. Therefore, a correction on the jet resolution is applied by smearing its momentum in simulation so that it fits the one in data [141]. The algorithm makes use of a combination of two methods, the scaling method and the stochastic smearing. In the scaling method, the four-momentum of the jet is rescaled according to the formula

$$c_{JER} = 1 + (SF_{JER} - 1)\,\frac{p_T - p_T^{ptcl}}{p_T} \tag{6.9}$$

where p_T is the transverse momentum of the jet, p_T^{ptcl} is the transverse momentum of the jet clustered from generator-level particles, and SF_{JER} the core resolution scale factor. The scaling method can only be used if the jet can be matched to the generator-level particles according to the requirements

$$\Delta R < R_{cone}/2 \quad \text{and} \quad \left|p_T - p_T^{ptcl}\right| < 3 \cdot \sigma_{JER} \cdot p_T \tag{6.10}$$

where R_{cone} is the cone size of the jet ($R_{cone} = 0.4$ for AK4 jets) and σ_{JER} is the relative jet resolution in simulation. The scaling method is always preferred if a generator-level match can be found. However, if this is not the case, the stochastic smearing will be used. In this approach, the four-momentum is rescaled based on the formula

$$c_{JER} = 1 + N\left(0, \sigma_{JER}\right)\sqrt{\max(SF_{JER}^2 - 1, 0)}. \tag{6.11}$$

Here, $N\left(0, , \sigma_{JER}\right)$ denotes a random number based on the normal distribution with mean value 0 and variance σ_{JER}.

6.4.3. Backgrounds from Tau Misidentification

To rely as little as possible on simulation for the description of the background from hadronic tau misidentification, a data driven background estimation will be used for the separated tau reconstruction, based on a tight-to-loose ratio. The ratio R_{tl} of the number of tight, well-isolated hadronic taus with respect to loose, non-isolated hadronic taus will be measured in regions orthogonal to the signal region of all channels and afterwards applied to the signal region by scaling non-isolated taus with the ratio R_{tl}. This method will not be applied for nearby taus. The main reason is the lack of statistics in the nearby scenario to perform a data driven estimation due to a large number of dependencies and the special, small phase space. While the ratio for separated taus mainly depends on the pseudorapidity η, the transverse momentum p_{T^τ}, and the flavour of the jet misidentified as a tau, the nearby scenario has additional dependencies on the distance ΔR between the misidentified tau and the nearby object (muon, electron, or another hadronic tau) and especially on the nearby lepton flavour itself. This means that the misidentification probability of the nearby scenario depends on η, p_{T^τ}, jet flavour, lepton flavour and ΔR, resulting in too less events to estimate and apply the tight-to-loose ratio. Therefore, the background estimation of the nearby category will only rely on simulation.

Tight-to-loose Ratio Measurement

The tight-to-loose ratio R_{tl} is measured in events collected with the single electron or muon trigger, containing exactly one tight lepton (e, μ), no additional loose lepton, and exactly one loose hadronic tau or exactly one tight hadronic tau. Loose taus have to pass the decay mode finding and the vetoes against leptons while the isolation requirement is skipped. For tight taus, the medium tau isolation is applied on top of the loose tau selection, meaning that the loose selection includes the tight one. The tight-to-loose ratio is then defined by the number of events in the tight region divided by the number of events in the loose region:

$$R_{tl}\left(p_T^\tau, \eta^\tau\right) = \frac{N_\tau^{\text{tight}}}{N_\tau^{\text{loose}}}\left(p_T^\tau, \eta^\tau\right). \tag{6.12}$$

To ensure that the tight-to-loose ratio is measured on taus from misidentified jets, events with prompt, "true" taus are subtracted if the reconstructed hadronic tau can be matched with a generated hadronic tau in simulation. The final ratio is then estimated by using the formula

$$R_{tl}\left(p_T^\tau, \eta^\tau\right) = \frac{N_\tau^{\text{tight}} - N_{\tau,\text{true}}^{\text{tight}}}{N_\tau^{\text{loose}} - N_{\tau,\text{true}}^{\text{loose}}}\left(p_T^\tau, \eta^\tau\right). \tag{6.13}$$

As described earlier, the tight-to-loose ratio depends on the jet flavour. Since hadronic tau decays mainly consist of light mesons built from up-, down-, and strange-quarks, the misidentification probability is expected to be higher in events with light jets (e.g. V+Jets) in comparison to events with heavy jets (e.g. $t\bar{t}$). Therefore, the ratio will be measured in three separated regions, depending on the number of *medium* b-tagged jets:

1. No b-tagged jets: This region is dominated by V+Jets events where a jet recoils against the W or Z boson and is subsequently misidentified as a hadronic tau. The jets in these events are mainly light jets, meaning that this region provides a good estimation for the misidentification probability of light jets.

2. Exactly one b-tagged jet: This region can be described as mixed region. It includes a comparable number of V+Jets and $t\bar{t}$ events. The V+Jets events typically contain two jets of which one is tagged as a b-jet while the other jet is misidentified as a hadronic tau. In case of the $t\bar{t}$ events, one of the two b-jets is not tagged as a b-jet, but as a hadronic tau.

3. Exactly two b-tagged jets: This region is dominated by $t\bar{t}$ and therefore describes the misidentification probability of b-jets.

The three defined regions are split in the tight and loose hadronic tau category and are shown in Fig. 6.21 as a function of the transverse tau momentum. Fig 6.22 shows the measured tight-to-loose ratio for all three b-tag categories as a function of the transverse tau momentum after subtracting prompt, "true" taus. It is visible that the misidentification probability highly depends on the transverse momentum as well as on the jet flavour. If one compares the zero b-tag region to the two b-tag region, it can be seen that light jets have an 80 % higher tight-to-loose ratio. Overall, the misidentification probability for the medium isolation is about 1-2 %, if the tau candidate did already pass the decay mode finding and the lepton isolation. While the ratios shown here are only depending on the transverse momentum, the applied ratios depend also on the pseudorapidity $|\eta|$.

Application of the Tight-to-loose Ratio

After the tight-to-loose ratio has been measured, it needs to be applied on the event selection. The ratio R_{tl} will be used to predict the impact of all backgrounds from jet to tau misidentification like $t\bar{t}$, Drell-Yan, W+Jets, and WW. If the event contains prompt hadronic taus, its prediction is taken from data. For the estimation of the background in the signal region, events with loose hadronic taus have to pass the full analysis chain. To stay orthogonal to the signal region, these loose taus are required to fail the isolation requirement. The events that pass this selection are afterwards scaled with an event weight based on the tight-to-loose measurement. In general, two types of events need to be taken into account, namely single tau misidentification and double tau misidentification. Single tau misidentification events contain one hadronic tau that arises from jet to tau misidentification, e.g. $t\bar{t} \to \ell\tau_h^{\text{true}} + \tau_h^{\text{mis-id}}$, $t\bar{t} \to \ell\ell + \tau_h^{\text{mis-id}}$, DY $\to \ell\tau_h^{\text{true}} + \tau_h^{\text{mis-id}}$, or WW $\to \ell\ell + \tau_h^{\text{mis-id}}$. This category is filled with $\ell\ell\tau_h^{\text{loose}}$ and $\ell\tau_h^{\text{tight}}\tau_h^{\text{loose}}$ events, the event weight is given by

$$w = \frac{R_{tl}\left(p_T^{\tau}, \eta^{\tau}\right)}{1 - R_{tl}\left(p_T^{\tau}, \eta^{\tau}\right)}. \tag{6.14}$$

Double tau misidentification events are only part of the fully hadronic event selection. In these events, two taus arise from jet to tau misidentification. This happens e.g. in W+Jets events or in semileptonic $t\bar{t}$ events. To collect these events, one tight lepton and two loose hadronic taus are required, the event weight is given by

$$w_{12} = \frac{R_{tl}\left(p_T^{\tau_1}, \eta^{\tau_1}\right)}{1 - R_{tl}\left(p_T^{\tau_1}, \eta^{\tau_1}\right)} \cdot \frac{R_{tl}\left(p_T^{\tau_2}, \eta^{\tau_2}\right)}{1 - R_{tl}\left(p_T^{\tau_2}, \eta^{\tau_2}\right)}. \tag{6.15}$$

Typically, one would expect that the estimation of the jet to tau background in the hadronic channel is based one the sum of the single and double misidentification category. However, this is not the case. Since the selection of the two categories relies on reconstructed and not on generated taus, namely on tight and loose taus, the single misidentification category does already include the double misidentification category. The reason is that the tight taus can also arise from misidentification and

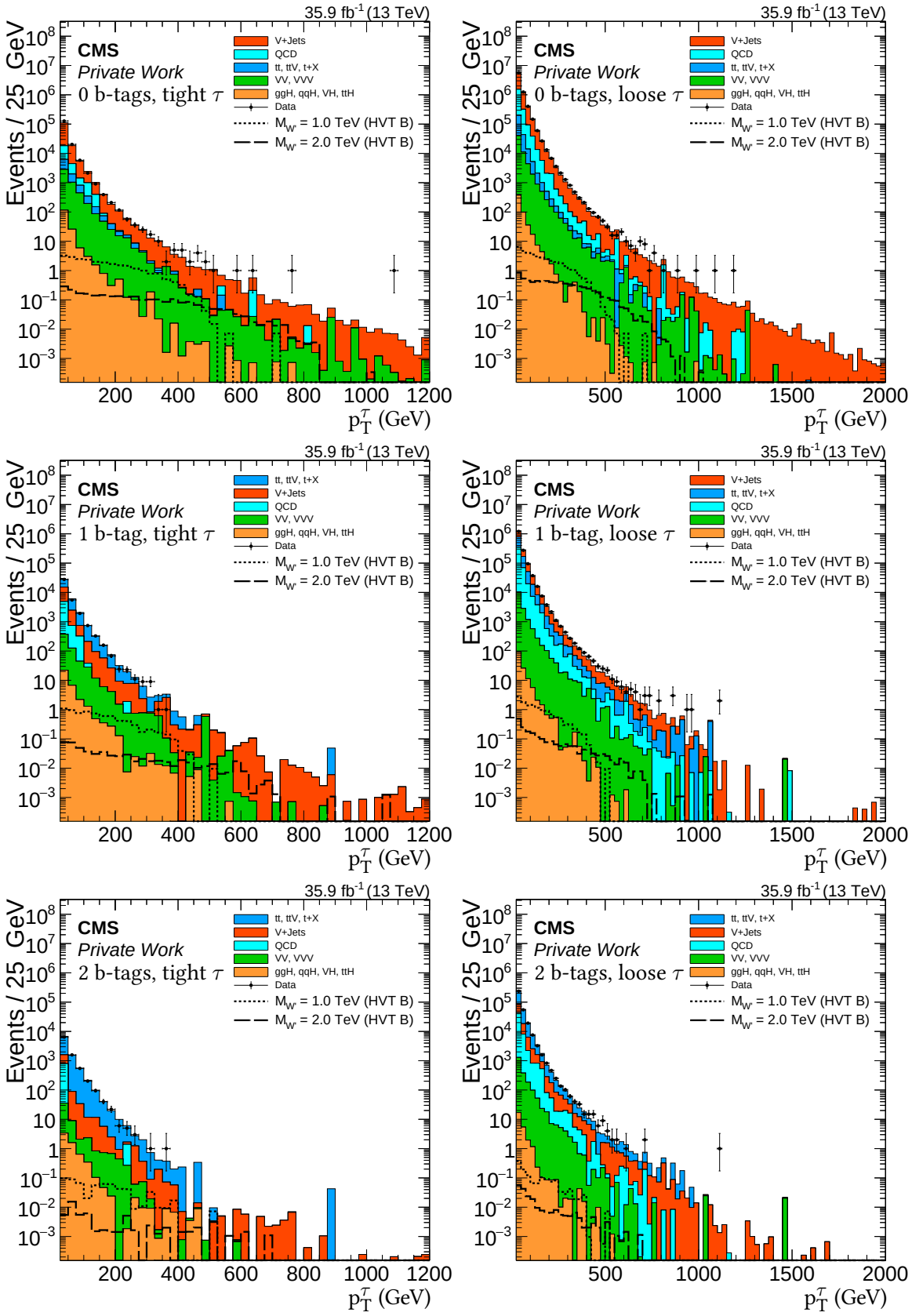

Figure 6.21.: Input histograms for the tight-to-loose ratio in all three b-tag regions as a function of the transverse tau momentum. Top: 0 b-tags, middle: 1 b-Tag, bottom: 2 b-tags, Left: Tight tau selection, right: Loose tau selection.

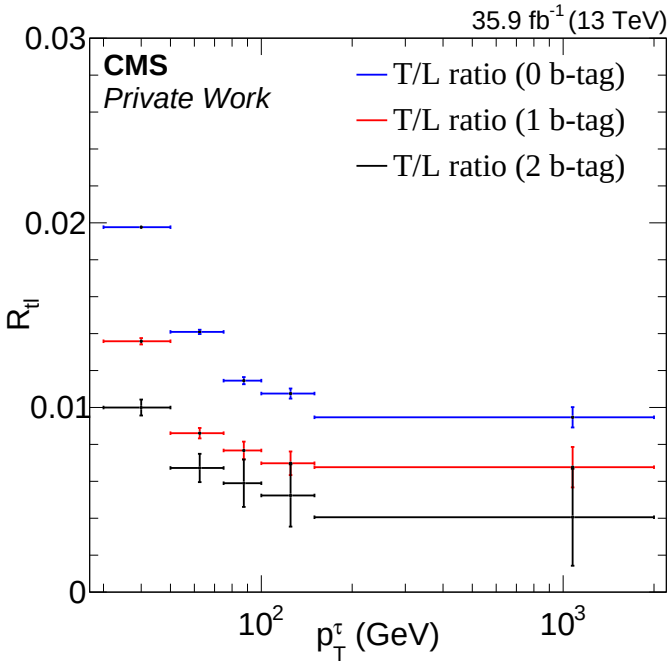

Figure 6.22.: Measured tight-to-loose ratio R_{tl} in data as a function of the transverse tau momentum for the three b-tag regions.

since there are two combinations of tight and loose taus ($\tau_h^{tight}\tau_h^{loose}$ and $\tau_h^{loose}\tau_h^{tight}$), the double misidentification category is already included twice in the single misidentification category. Therefore, the background estimation in the hadronic channels is based on the difference of single and double misidentification category:

$$N = N_{single} - N_{double}. \tag{6.16}$$

To test the quality of the data driven method, a so called closure test on $t\bar{t}$ and Drell-Yan enriched samples has been performed. For the closure test, the tight-to-loose ratio was calculated on simulation and then applied on $t\bar{t}$ and Drell-Yan samples. The result can be found in Fig. 6.23, showing the comparison of the $\sum p_T$-distribution from simulation and using the data driven method (applied on simulation) for the various channels. It is visible that the data driven method describes the background as well as the simulation, but with larger statistics. The effect of the jet flavour is also visible in these distributions. As expected, the ratio with low b-tag multiplicity describes the Drell-Yan background better while the two b-tag ratio gives more consistent results for $t\bar{t}$. However, for $t\bar{t}$, there seems to be still an overestimation of about 25 %. This mainly arises from the tight-to-loose measurement. The selection of a two b-tag region does not ensure that the taus from jet misidentification arise from a b-jet since $t\bar{t}$ events do also contain a large number of light jets. Therefore, the measurement gives no clean b-jet to tau tight-to-loose ratio, but it shows the tendency. The real ratio for b-jets is expected to be slightly lower. Since the final distributions, except for the semileptonic different lepton flavour channel, contain both types of backgrounds - light and b-jets - the ratio measured in the one b-tag region will be used to estimate the background from misidentified taus. In the semileptonic different lepton flavour channel which is dominated by $t\bar{t}$ decays, the ratio estimated from the two b-tag region will be used. A systematic uncertainty is considered based on the differences from the jet flavour. It lies between 30-40 % depending on the tau momentum.

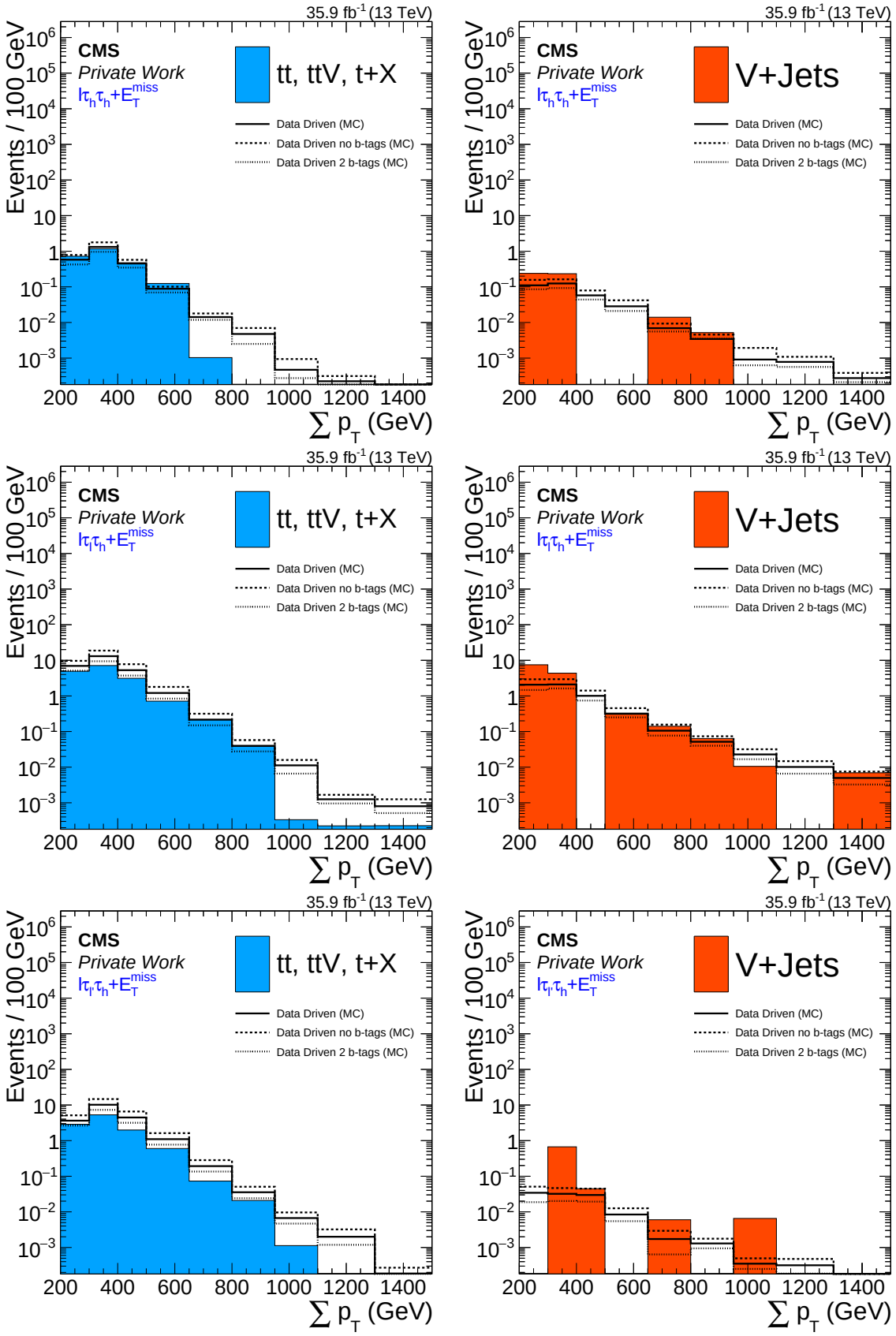

Figure 6.23.: Closure test performed on $t\bar{t}$ (left) and Drell-Yan (right) simulation samples for the hadronic (top), semileptonic same lepton flavour (middle), and semileptonic different lepton flavour (bottom) channel in the separated tau category.

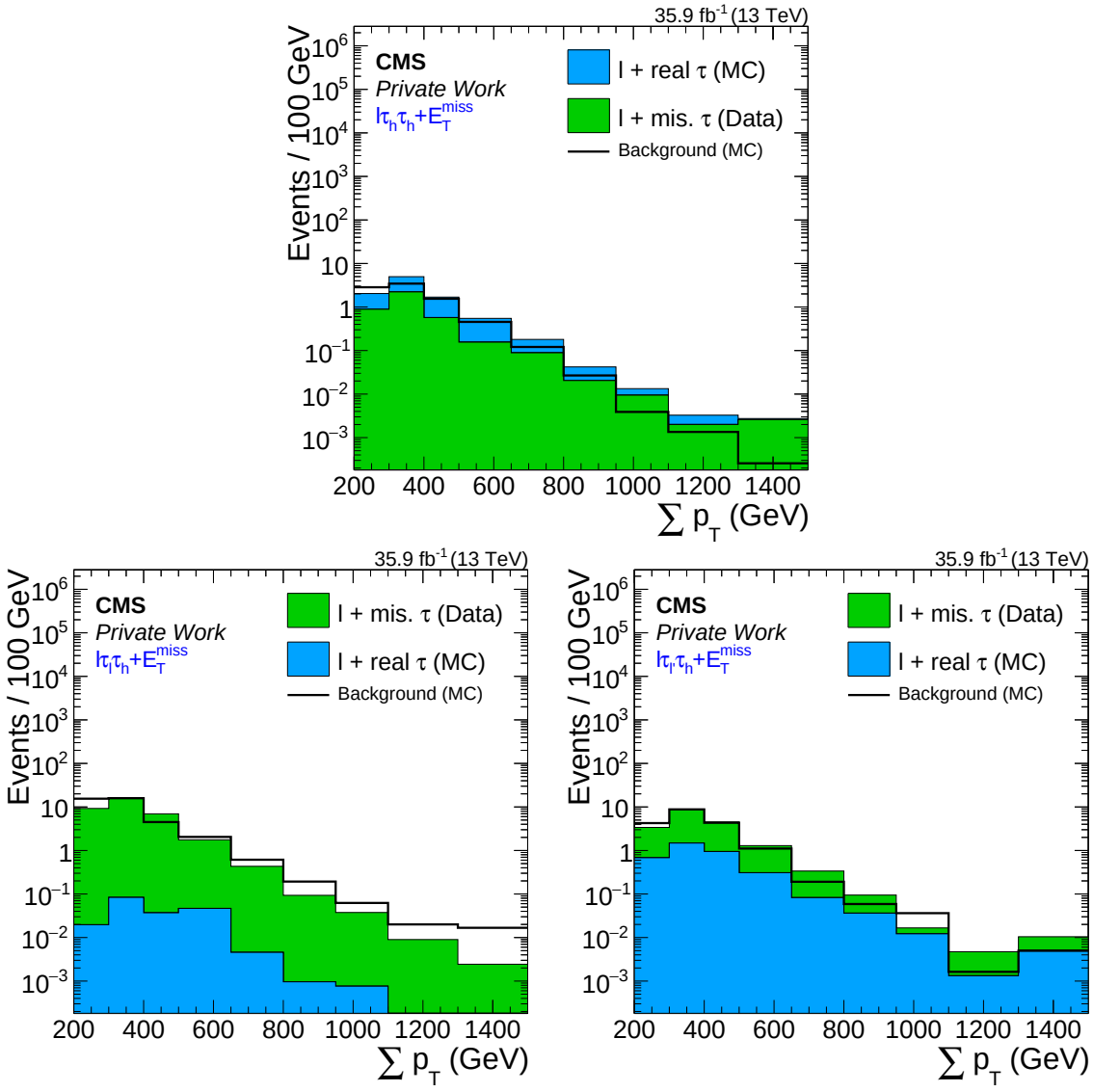

Figure 6.24.: Comparison of the final background estimation from the data driven method with respect to simulation for the hadronic (top), semileptonic same lepton flavour (bottom left), and semileptonic different lepton flavour (bottom right) channel in the separated tau category.

In addition to the closure test, it is also possible to test the data driven method in the V+Jets and the $t\bar{t}$ control region. The corresponding distributions can be found in App. C.4. In a final step, the full background prediction via data driven estimation can be compared to the estimation from simulation. The corresponding plots are shown in Fig. 6.24. For all three channels, the data driven estimation is found to be similar to the simulation based background estimation, adding additional confidence in the data driven method.

6.5. Systematic Uncertainties

Due to the large number of objects in this analysis, several sources of systematic uncertainties need to be considered. There are two types of systematic uncertainties: The first type changes only the normalization of the background and signal, e.g. the uncertainty on the luminosity. The second type does also influence the shape of the final distributions by shifting kinematic variables, e.g. the uncertainty from the lepton energy scale. As many of these uncertainties influence the missing E_T, their impact is propagated accordingly. Except for the data driven uncertainty that is only applied to the data driven background estimation, all uncertainties are applied on the simulated backgrounds and signals. The uncertainties considered in this analysis are:

- *Electron Efficiencies (ID)* [136]: Uncertainties on the electron efficiencies arise from the reconstruction and identification scale factors. For the electron track reconstruction, the statistical uncertainties of the scale factors that are binned in η are applied by shifting the scale factors accordingly. In addition, a systematic uncertainty of 1 % is applied. In case of the identification scale factor, the statistical uncertainties are also applied directly on the scale factor, but depending on $|\eta|$ and p_T. In addition, a 1 % systematic uncertainty per electron is applied on the tag-and-probe method used to estimate the identification scale factors. While the statistical uncertainties have a small impact on the shape, the systematic uncertainties only influence the normalization.

- *Muon Efficiencies (ID)* [138]: The uncertainties on the muon efficiencies arise from the tracking, identification and isolation scale factors. Same as for the electron reconstruction, the statistical uncertainties on the scale factor are applied by shifting it. For muons, no additional systematic uncertainty is applied on the tracking scale factors. Instead, a 0.5 % uncertainty is added in quadrature to the systematic uncertainty on the tag-and-probe method of the identification. The identification scale factors are applied the same way as for electrons with an additional 1 % uncertainty on the tag-and-probe method. Muon isolation scale factor uncertainties do also depend on a mixture of statistical and systematic uncertainties where the systematic uncertainty is 0.5 %.

- *Tau Efficiencies (ID)* [89]: Uncertainties on the tau efficiencies arise only from the tau identification scale factors. These are similar for separated and nearby taus, although their isolation requirement differs. The tau identification has two sources of uncertainties. For low p_T, the uncertainty is estimated to be 5 %. For high-$_T$ taus, an additional, shape based uncertainty is applied, shifting the scale factor by +5 % $\cdot\, p_T^\tau$/TeV and −35 % $\cdot\, p_T^\tau$/TeV.

- *Electron Energy Scale* [142]: A mismeasurement in the electron energy scale can affect the electron energy and therefore the final $\sum p_T$-distribution. To compensate for this source of mismeasurement, a systematic uncertainty on the energy scale needs to be applied. The electron energy scale was measured in $Z \to ee$ events on one electron while the other one is used to tag the event. Based on the residual difference between data and simulation, the electron energy scale uncertainty is estimated to be 0.2 % in the barrel and 0.3 % in the endcaps for low-p_T electrons. For high-p_T electrons, the electron scale was only measured based on energy deposits in the ECAL and validated up to 1-2 % level for energies beyond 500 GeV. The uncertainty is applied by shifting the electron momentum based on these values.

- *Muon Momentum Scale* [143]: Same as for electrons, a mismeasurement of the muon momentum scale affects the $\sum p_T$-distribution. The muon momentum scale was measured using the generalized endpoint method and comparing the data to the simulation. The result is a

two-dimensional η-ϕ-distribution showing shifts in the muon momentum scale and the corresponding uncertainties as presented in Fig. 6.25. The scale uncertainty is estimated by shifting q/p_T^{μ} (q is the charge) according to $q/p_T^{\mu} \rightarrow q/p_T^{\mu}$ + Gauss (k, σ_k) were k is the scale shift and σ_k its uncertainty.

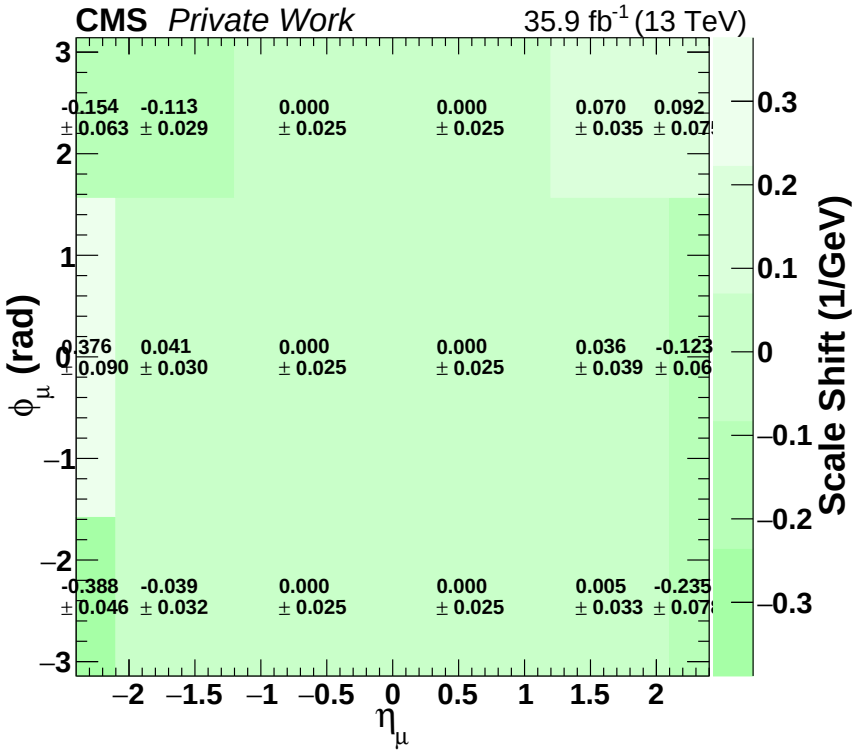

Figure 6.25.: Muon p_T scale shifts and the corresponding uncertainties as a function of η and ϕ measured with the generalized endpoint method, values taken from [144, 145].

- *Muon Momentum Resolution* [143]: For increasing muon momenta, the muon resolution gets worse due to its tracking based measurement. Since this analysis includes medium- and high-p_T muons, an uncertainty on the muon resolution is needed. To estimate the uncertainty on the muon momentum resolution, the p_T is smeared by 0.3 % (p_T < 200 GeV), 0.5 % (p_T < 500 GeV), and 1 % (p_T > 500 GeV) for muons in the barrel. In the endcaps, the uncertainty shifts are doubled.

- *Tau Energy Scale* [89]: Same as for the other objects, the measurement of the hadronic tau energy scale can affect the results. It was measured in $Z \rightarrow \ell\tau_h$ events by comparing data to different simulation templates. It was found that the results of data and simulation are compatible within $\pm$ 3 %. This value is used to estimate the uncertainty on the tau energy scale.

- *Jet Energy Scale* [100]: The procedure of jet energy scale corrections is assigned with a systematic uncertainty. The jet energy correction uncertainty is based on the three levels of measurement and is below 5 % for their combination. The uncertainty does also affect the E_T^{miss} value.

- *Jet Energy Resolution* [141]: The correction of the jet energy resolution is assigned with an uncertainty depending on the pseudorapidity of the jet. This uncertainty ranges from 6 % in the barrel up to 10 % in the endcaps and is applied on the core resolution scale factor, thus its

impact is reduced by the smearing procedure. This uncertainty affects the b-tag requirement and the E_T^{miss} value.

- *b-tagging Efficiencies* [105]: Same as the other object selections, the b-tagging has a systematic uncertainty. It ranges from 1-4 % depending on p_T, η and jet flavour (on generator level).

- *Missing transverse Energy* [107]: All systematic uncertainty sources that shift the momentum of a particle are propagated to the E_T^{miss}. In addition, an uncertainty on the unclustered energy is applied. The unclusterd energy arises from particles that are not clustered in a jet. To estimate this uncertainty, the momenta of all PF objects are shifted within their uncertainty.

- *Pileup Reweighting* [135]: As discussed in Sec. 6.4.2, the pileup reweighting method leads to a systematic uncertainty. It is estimated by shifting the minimum bias cross section by $\pm$ 4.6 % and weighting the events according to the new pileup distributions. Since the events have a different pileup weight, it is a shape uncertainty.

- *Luminosity* [50]: The uncertainty on the integrated luminosity was found to be 2.5 % for 2016 CMS data. As the luminosity scales with the expected events from simulation, this uncertainty only affects the normalization.

- *Monte-Carlo Statistics*: The effect of the MC statistics is taken into account by shifting each bin individually according to its statistical uncertainty. Based on these shifts, about 10 additional uncertainties arise, one for each bin. The algorithm used to estimate the statistical uncertainty is implemented in the CMS Higgs Combine Limit Tool [146] and works as follows [147–149]:

  1. The event yield n_i and corresponding uncertainties e_i of each background process i in the bin are combined to get the total event yield n_{tot} and uncertainty e_{tot}, defined as

  $$\begin{aligned} n_{tot} &= \sum_i n_i \\ e_{tot} &= \sqrt{\sum_i e_i^2}. \end{aligned} \tag{6.17}$$

  2. If the total background uncertainty in the bin is $e_{tot} = 0$, the bin is skipped and no parameters will be created for this bin.

  3. If the effective number of events $n_{tot}^{eff} = n_{tot}^2/e_{tot}^2$ is smaller or equal a given threshold $n^{threshold}$, separate uncertainties for each process are calculated, using a Poisson constrained parameter if the number of effective events of the process $n_{i,tot}^{eff}$ is below the threshold and a Gaussian-constrained parameter if it is above the threshold.

  4. If n_{tot}^{eff} is above the threshold, a single Gaussian-constrained Barlow-Beeston-lite parameter x [149] will be created and applied by scaling the total event yield n, based on the total uncertainty e_{tot}, according to $n_{tot} + x \cdot e_{tot}$ in the bin. Since this analysis has only a low number of expected events, the threshold is set to $n^{threshold} = 0$, meaning that all statistical bin uncertainties are combined and estimated with a Gaussian constrained.

  5. While the Poisson constrained parameter x works as a multiplier for the event yield ($n_{tot} \cdot x$) with nominal value 1, the Gaussian constrained parameter is used to scale the event yield according to $n_{tot} + x \cdot e_{tot}$ and has a mean value of 0.

- *PDF Uncertainties*: The estimation of PDF uncertainties is based on the recommendation of PDF4LHC for the LHC Run 2 [150]. In addition to the pdf set used for the production of the simulation, 100 sets are used to create 100 additional final distributions. The PDF uncertainty histogram is then calculated based on these 100 distributions by using the standard deviation of each bin. In case of the signal simulation, the pdf uncertainties are calculated in a different way, only taking into account the effect on the acceptance. The effect on the normalization of the signal from PDF uncertainties is later demonstrated in the cross section limit plot as an uncertainty on the theory curve.

- *Tau Misidentification*: The uncertainty on the tau misidentification corresponds to the uncertainties of the data driven method and is therefore only applied on this background. There are two sources of uncertainties: The statistical uncertainty, arising from the tight-to-loose measurement and a systematic uncertainty from the different misidentification probabilities for light- and b-jets. The statistical uncertainty varies depending on the tau momentum and jet flavour between 1 % (low-p_T, no b-tag) and 50 % (high-p_T, 2 b-tags). The uncertainty on the jet flavour corresponds to the relative difference of the measurements and lies between 30-40 %.

The combined impact of the uncertainties on the background shape is shown in Fig. 6.26 for all channels and tau categories while the impact on the integral of background and signal ($W' \rightarrow Wh$) can be found in Tab. 6.8 for separated taus and in Tab. 6.9 for nearby taus. For separated taus, a signal mass of 1 TeV and for nearby taus, a mass of 2 TeV is used to take the differences in the sensitivity of tau the reconstruction methods into account. For the separated tau category, the uncertainty is dominated by the data driven background estimation, especially the uncertainty based on the jet

Uncertainty (%)	HAD		SSLF		SDLF	
	Backgr.	Signal	Backgr.	Signal	Backgr.	Signal
Electron Eff.	0.9	1.4	< 0.1	2.8	0.6	3.1
Muon Eff.	1.1	1.8	< 0.1	3.8	0.7	3.4
Tau Eff.	9.4	19.3	< 0.1	10.0	1.8	10.0
Electron Scale	0.4	0.1	< 0.1	1.0	0.2	1.0
Muon Resolution	1.6	0.1	< 0.1	0.9	0.3	0.8
Muon Scale	1.2	0.2	< 0.1	1.0	0.7	1.1
Tau Scale	2.6	1.0	< 0.1	2.0	0.6	1.4
Jet Scale	0.5	0.3	< 0.1	1.1	0.6	1.5
Jet Resolution	1.9	0.3	< 0.1	1.9	2.1	1.6
b-tagging Eff.	0.2	0.1	< 0.1	0.9	0.3	0.9
Missing E_T	1.7	1.3	< 0.1	2.8	1.2	1.8
Pileup	1.8	1.7	< 0.1	2.1	0.4	2.0
Luminosity	1.3	2.5	< 0.1	2.5	0.5	2.5
PDF uncertainties	1.1	0.1	< 0.1	0.1	0.7	0.2
Tau misidentification	14.2	-	35.1	-	31.9	-
Systematic	17.7	19.9	35.1	12.4	32.1	12.0
MC Statistics	7.7	2.9	0.3	3.1	3.1	3.3
Combined	19.3	20.1	35.1	12.8	32.2	12.4

Table 6.8.: Summary of the impact of systematic uncertainties on the background signal event yield for a 1 TeV Wh resonance in the separated tau category.

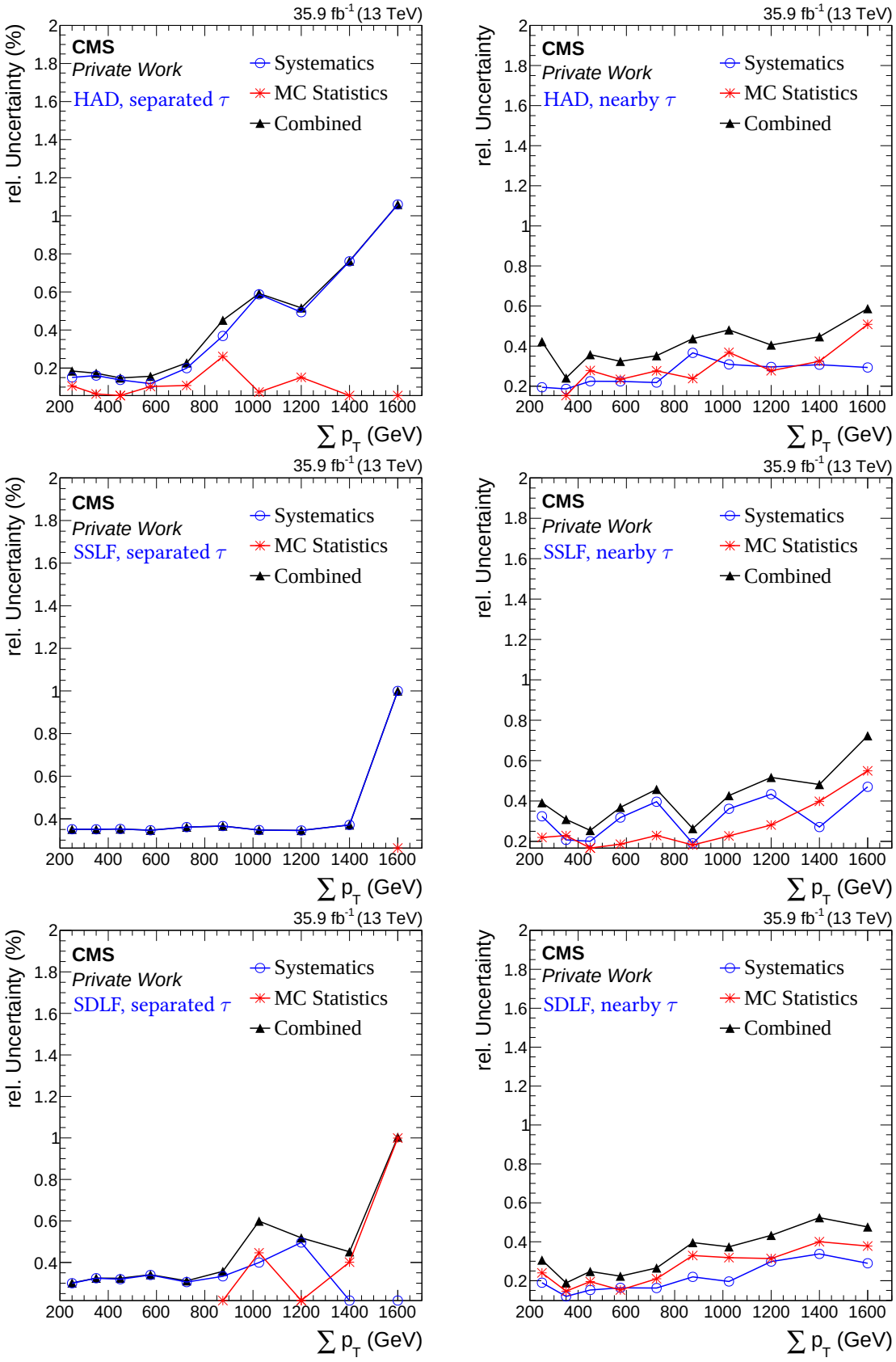

Figure 6.26.: Relative systematic uncertainties for the various channels. Left: Separated tau reconstruction, right: Nearby tau reconstruction. Top: hadronic, middle: semileptonic same lepton flavour, bottom: semileptonic different lepton flavour.

Uncertainty (%)	HAD		SSLF		SDLF	
	Backgr.	Signal	Backgr.	Signal	Backgr.	Signal
Electron Eff.	1.5	1.4	2.1	2.6	3.0	3.0
Muon Eff.	1.8	1.8	4.6	4.0	3.4	3.4
Tau Eff.	16.8	27.7	7.7	14.1	8.4	14.2
Electron Scale	1.9	0.1	3.4	1.1	2.4	1.1
Muon Resolution	2.7	0.2	7.3	0.9	2.9	1.1
Muon Scale	2.2	0.4	4.7	1.3	2.8	1.1
Tau Scale	5.6	0.7	2.6	1.4	2.9	1.3
Jet Scale	3.4	0.1	4.5	1.2	3.2	1.3
Jet Resolution	5.5	0.1	9.1	1.5	4.0	1.0
b-tagging Eff.	0.8	0.2	2.0	1.1	2.5	1.1
Missing E_T	3.9	0.9	8.1	1.9	3.8	1.7
Pileup	5.1	1.6	2.4	2.2	3.0	2.2
Luminosity	2.5	2.5	2.5	2.5	2.5	2.5
PDF uncertainties	5.1	0.1	2.4	0.1	3.0	0.1
Systematic	21.2	28.0	19.2	15.7	13.9	15.8
MC Statistics	11.0	1.7	20.1	2.6	8.4	2.6
Combined	23.9	28.1	27.8	15.9	16.2	16.0

Table 6.9.: Summary of the impact of systematic uncertainties on the background signal event yield for a 2 TeV Wh resonance in the nearby tau category.

flavour dependency. As in the semileptonic channels the data driven background is dominant, the impact of simulation based uncertainties is very low here. In the hadronic channel where the irreducible WZ background has a large contribution, the uncertainty on the tau efficiency plays an important role in addition to the data driven uncertainty. This is not surprising, as the uncertainty shifts are large and the event contains two hadronic taus.
In the nearby tau channels, the background is completely taken from simulation. Therefore, the dominant systematic uncertainty is the tau efficiency with uncertainties on the integral up to 17 %. However, due to the limited statistics of some background processes in this special phase space, the statistical uncertainties on the simulation are relatively high in the nearby category, resulting in uncertainties of about 20 %.
For the signal, the uncertainties on the tau efficiency play an even more important role. Since the uncertainty is estimated with respect to the tau momentum, its impact increases for high tau momenta. The tau momentum increases with the signal mass and therefore, the uncertainty increases for higher masses. A W' with a mass of 1 TeV has tau efficiency uncertainties of about 19 % in the hadronic and 10 % in the semileptonic channels. For a 2 TeV mass, the uncertainty is increased by about 40 %. While the impact of the tau efficiency uncertainty is large, the other uncertainties have a small effect, resulting in about 5-6 % uncertainty.

6.6. Final Distributions

After the important steps of the event selection and background estimation have been discussed, everything is cumulated in the final distributions of the various channel. The final distributions for the separated tau category are shown in Fig. 6.27 while the corresponding summary of event

numbers of background expectation and data can be found in Tab. 6.10. The "real τ" background is estimated from simulation and the "mis. τ" background arises from the data driven method. For the hadronic channel, a good agreement between data and simulation can be observed, with 9.9 ± 1.9 events expected and 7 events observed. Although the number of events is quite low, the observation follows the shape of the expectation, showing no evidence for new physics. The signal can be well distinguished from the background for 500 GeV < $\sum p_T$ < 1000 GeV for a resonance mass of 1 TeV. In case of the semileptonic same lepton flavour channel, the agreement between expectation and data is worse, but it is still covered by the uncertainties. Overall, 36.3 ± 12.7 events are expected and 52 events are observed. In contrast to the hadronic channel where one could distinguish the signal well from the background, the signal in this channel only exceeds the background for 650 GeV < $\sum p_T$ < 1000 GeV for a mass of 1 TeV. This difference arises from a higher branching fraction and from a lower background expectation in the hadronic channel, mainly because of the additional Drell-Yan background in the semileptonic same lepton flavour channel. Therefore, the hadronic channel will have the largest impact on the final result.
The semileptonic different lepton flavour channel shows a good agreement between data and background expectation, with 19.5 ± 6.3 events expected and 17 events observed. Although the background is smaller than in the semileptonic same lepton flavour channel, the impact of the signal is comparable since the difference in the background expectation mainly appears in the low-$\sum p_T$ region. Overall, the separated tau channels show a good agreement between data and background and provide a good distinction w.r.t the signal for a resonance mass of 1 TeV.

Background	HAD	SSLF	SDLF
Real τ	5.7 ± 1.3	0.2 ± 0.0	3.8 ± 0.5
Misid. τ	4.2 ± 1.4	36.1 ± 12.7	15.7 ± 6.3
Combined	9.9 ± 1.9	36.3 ± 12.7	19.5 ± 6.3
Data	7	52	17

Table 6.10.: Summary of the data and background event numbers for the separated tau category for the various channels including the systematic uncertainties on the background expectation.

Background	HAD	SSLF	SDLF
V+Jets	2.8 ± 0.9	4.8 ± 1.4	0.5 ± 0.2
$t\bar{t}$, $t\bar{t}V$, t+X	6.1 ± 0.6	8.5 ± 1.0	5.9 ± 0.6
VV, VVV	1.6 ± 0.5	3.0 ± 0.6	1.8 ± 0.3
ggH, qqH, VH, $t\bar{t}H$	0.1 ± 0.0	0.1 ± 0.0	0.1 ± 0.0
Combined	10.6 ± 1.2	16.4 ± 3.3	8.3 ± 0.7
Combined (with Systematics)	10.6 ± 2.5	16.4 ± 4.6	8.3 ± 1.3
Data	16	9	9

Table 6.11.: Summary of the data and background event numbers for the nearby tau category for the various channels including the systematic uncertainties on the background expectation. The uncertainty of the four background processes corresponds to the uncertainty from MC statistics only.

For the nearby tau category, the background estimation is completely driven by simulation as the statistics is too limited for a data driven approach due to the small phase space of the analysis. The corresponding histograms and event tables can be found in Fig. 6.28 and Tab. 6.11. Overall, all three

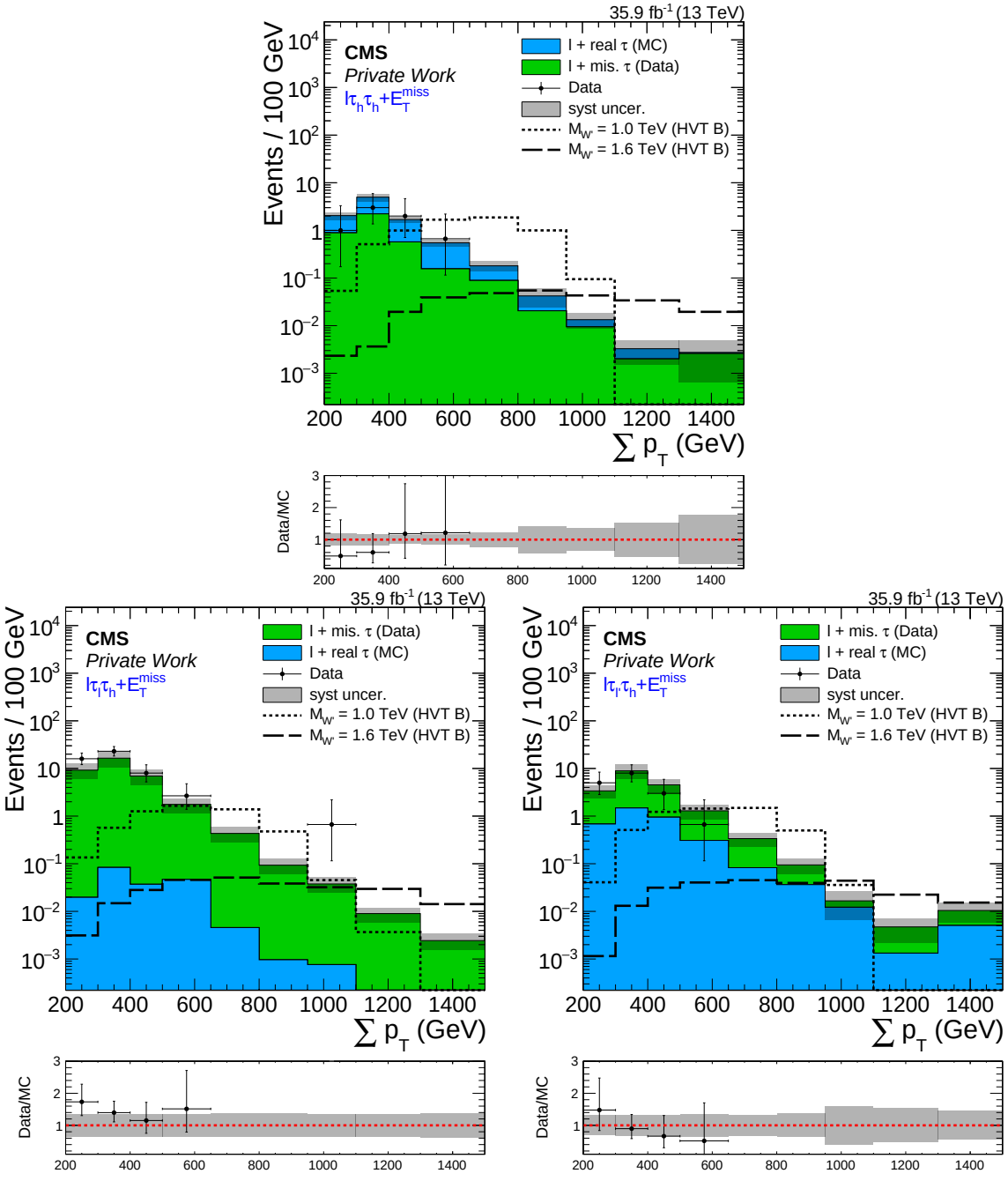

Figure 6.27.: Final distributions for the separated tau category in the hadronic (top), semileptonic same lepton flavour (bottom left), and semileptonic different lepton flavour flavour (bottom right) channel. Data points missing in the ratio plots have ratio values above 3.

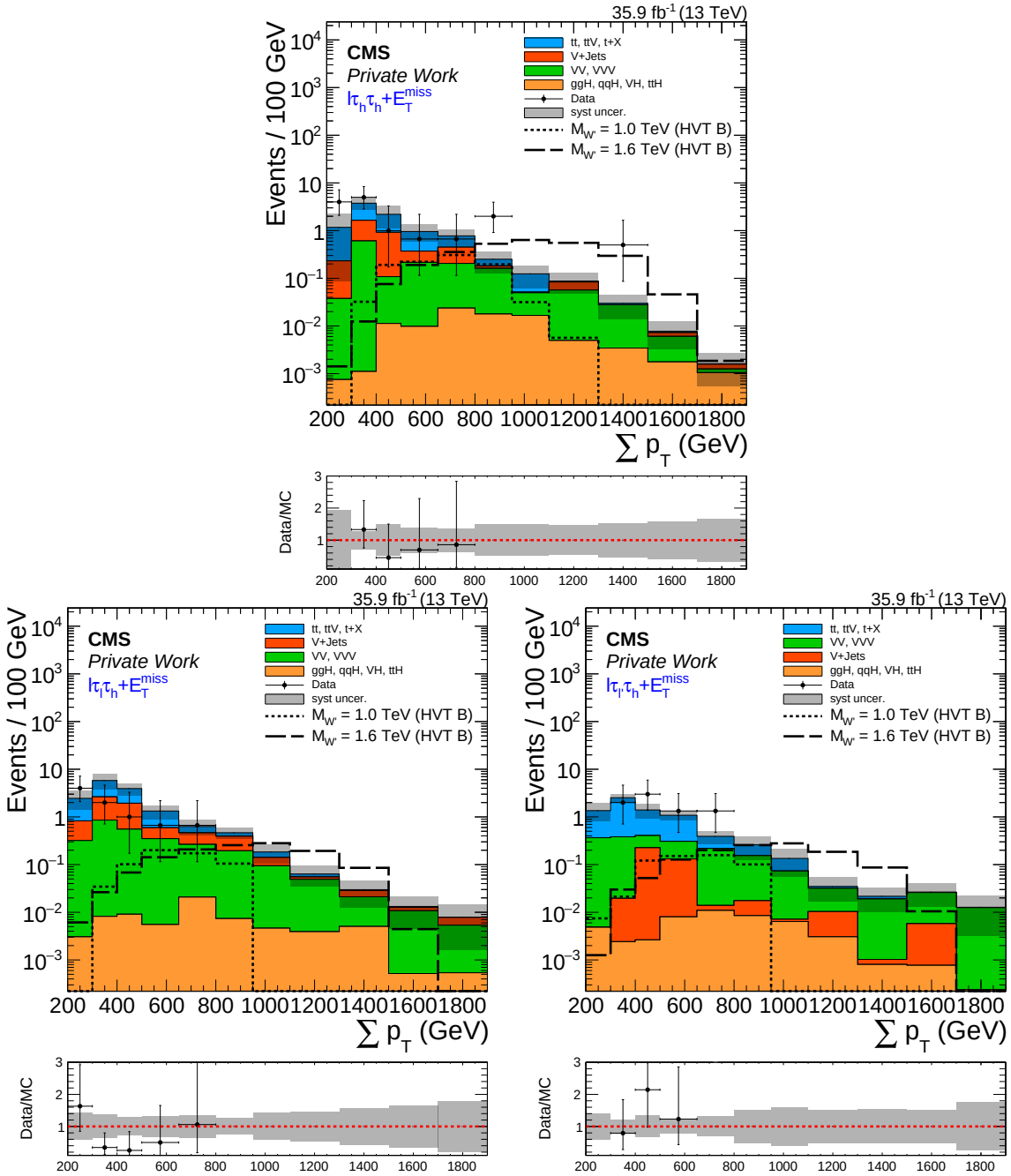

Figure 6.28.: Final distributions for the nearby tau category in the hadronic (top), semileptonic same lepton flavour (bottom left), and semileptonic different lepton flavour flavour (bottom right) channel. Data points missing in the ratio plots have ratio values above 3.

channels have a reasonable agreement between data and background. In the hadronic channel, a small excess around 900 GeV is observed in the $\sum p_T$ distribution. Here, 3 events are observed while only around 0.4 events are expected, resulting in a significance of about 1.6σ. A more detailed discussion of the significances will be presented in Sec. 7.2. For the whole distribution, 10.6 ± 2.5 events are expected and 16 events are observed.
The semileptonic same lepton flavour channel does not show a comparable deviation as the hadronic channel. Here, the observed data lies slightly below the background expectation, showing no evidence for new physics in this distribution. In this channel, 16.4 ± 4.6 events are expected and 9 events are observed, resulting in a deviation slightly above 1σ. In the semileptonic different lepton flavour channel, also no sign for new physics can be detected. The data agrees with the expectation as 8.3 ± 1.3 events are expected and 9 events are observed. After showing the various final distributions, the statistical interpretation and discussion of results follows in the next chapter.

A full list of all data events passing the full analysis chain can be found in App. C.1. Fig. 6.29 shows the display of the event with the highest $\sum p_T$ ($\approx$ 1346 GeV) value in the x-y (top) and η-r (bottom) plane. A zoomed version can be found in Fig 6.30. The event is part of the single muon stream and contains one muon (p_T^{μ} = 613 GeV), two hadronic taus ($p_T^{\tau_1}$ = 418 GeV and $p_T^{\tau_1}$ = 141 GeV) and 174 GeV of missing E_T. In the x-y plane, the muon is back-to-back to the two hadronic taus as expected from the event selection. The tau leptons are not separated in ϕ, but they have a small separation in η, resulting in a ΔR of 0.34. All objects are produced in the central region of the detector and therefore in the region with the best possible reconstruction. The visible mass of the two tau candidates is about M_{vis} = 82 GeV, an expectable value for two products arising from $h \rightarrow \tau\tau$ decays. The largest part of the energy of τ_1 is reconstructed in the ECAL. This means that either the energy from the neutral meson decay is large, or more likely, that the candidate arises from an electron misidentified as hadronic tau.

Altogether, no significant deviation is seen in the various channels and categories, thus exclusion limits for Wh resonances, WZ resonances, and their combination (WZ+Wh) will be calculated in the next chapter.

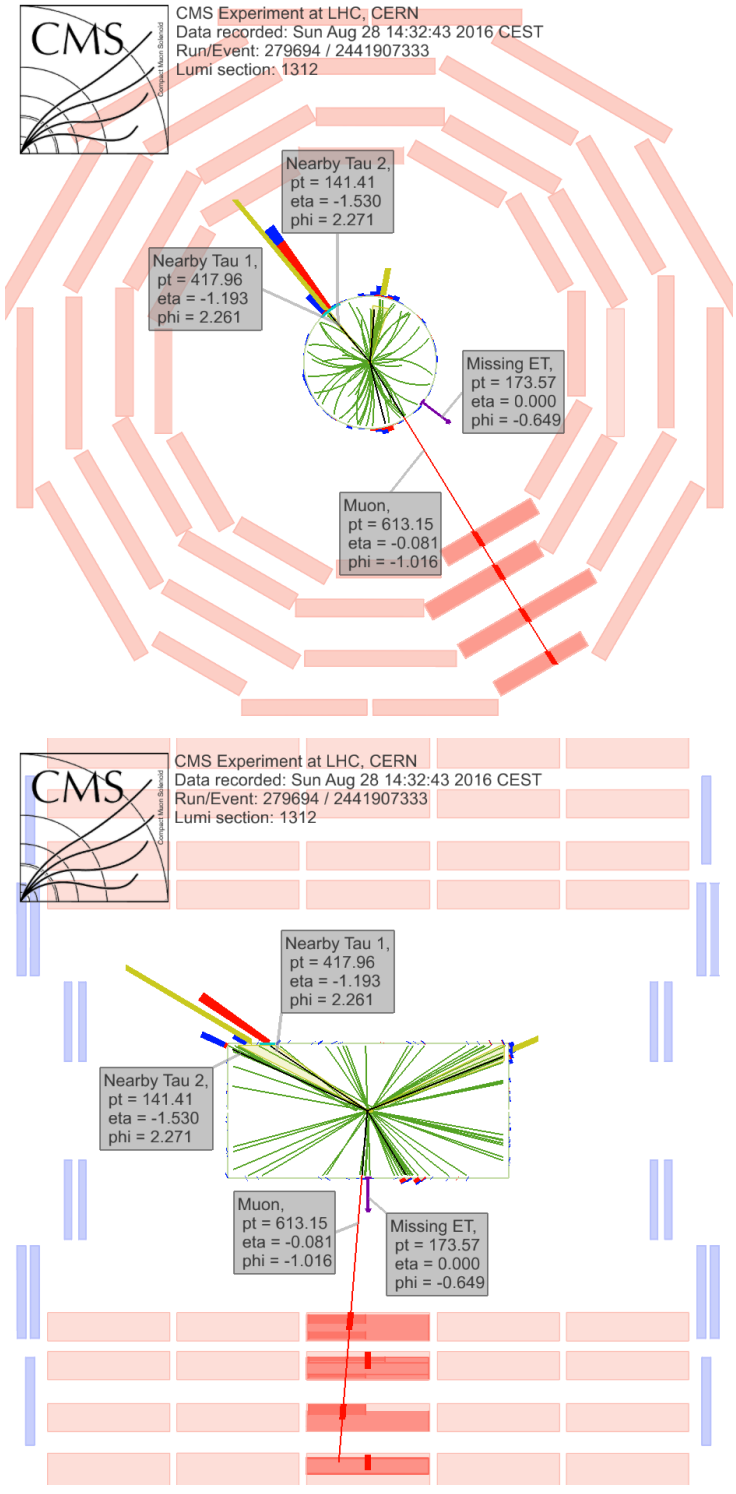

Figure 6.29.: Event display of the highest $\sum p_T$ event ($\sum p_T \approx 1346$ GeV). This CMS event was found in the $\mu\tau_h\tau_h + E_T^{miss}$ channel and is part of the nearby tau category. The red lines represent muon candidates, the black lines nearby tau candidates, and the purple arrow the direction of the missing E_T. The information of the objects finally selected in the event are added in the gray boxes.

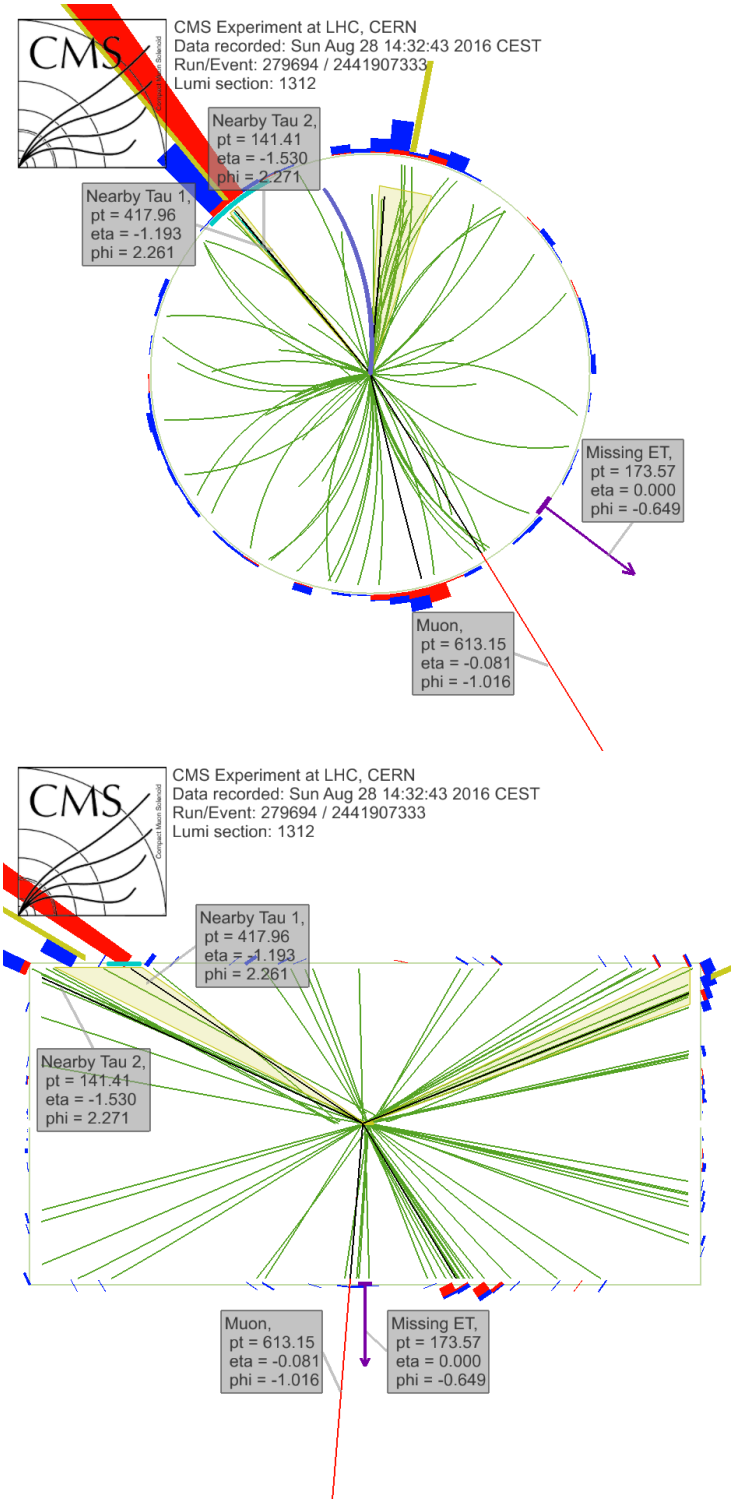

Figure 6.30.: Zoomed event display of the highest $\sum p_T$ event ($\sum p_T \approx 1346$ GeV). This CMS event was found in the $\mu\tau_h\tau_h + E_T^{miss}$ channel and is part of the nearby tau category. The red lines represent muon candidates, the black lines nearby tau candidates, and the purple arrow the direction of the missing E_T. The information of the objects finally selected in the event are added in the gray boxes.

CHAPTER 7

Statistical Interpretation

In order to obtain final results, namely the observed significance or exclusion limits on the cross section and model parameters, the final distributions from Sec. 6.6 need to be interpreted based on a statistical analysis. At the beginning, the foundations of Bayesian statistics will be described, followed by consistency checks based on a maximum likelihood fit, the significance evaluation and the calculation of cross section limits. The final result will then be a limit on the coupling parameters of the HVT model. All results will be calculated for three resonance hypotheses, namely Wh resonances, WZ resonances, and their combination where their contributions are summed up, referred to as WZ+Wh.

In particle physics, two main exclusion limit setting methods are used, the bayesian and the frequentist approach [28]. Both approaches are consistent in several regions of the phase space and give comparable results. Since most W′ analyses in CMS utilize the bayesian limit setting method, it will also be used in this analysis. The limits are obtained using the Higgs Combine Tool [146, 151] from CMS which is based on RooStats [152].

7.1. Bayesian Statistics

The bayesian limit setting method [28, 153] is based on Bayes' Theorem stating

$$\mathrm{P}(\mathrm{B}|\mathrm{A}) = \frac{\mathrm{P}(\mathrm{A}|\mathrm{B}) \cdot \mathrm{P}(\mathrm{B})}{\mathrm{P}(\mathrm{A})}, \tag{7.1}$$

meaning that the probability for event B to occure under the condition that event A is true is given by the probability that event A occures under the condition that B is true multiplied with the probability of an independent observation of event B divided by the independent probability that event A happens. For the case of an experiment where an unknown parameter of interest θ should be determined, the Bayes' Theorem translates to

$$\mathrm{p}(\theta|\vec{\mathrm{x}}) = \frac{\mathrm{L}(\vec{\mathrm{x}}|\theta) \cdot \pi(\theta)}{\int \mathrm{L}(\vec{\mathrm{x}}|\theta) \cdot \pi(\theta)\, \mathrm{d}\theta} \tag{7.2}$$

where $\vec{\mathrm{x}}$ is a vector of data that characterizes the outcome of the experiment, $\mathrm{p}(\theta|\vec{\mathrm{x}})$ is the posterior probability density function (p.d.f.) of θ depending on the data $\vec{\mathrm{x}}$, $\mathrm{L}(\vec{\mathrm{x}}, \theta)$ is the likelihood function of the data depending on θ, and $\pi(\theta)$ is the prior p.d.f. of the parameter θ. As discussed in Sec. 6.5, the model parameters are assigned with several systematic uncertainties. These are taken into account in the posterior p.d.f as nuisance parameters with an additional prior $\pi(\vec{\nu})$, mostly modeled based on a log-normal distribution, except for the uncertainties from MC statistics. Each element of the vector $\vec{\nu}$ corresponds to one uncertainty. The nuisance parameters lead to a smearing of the

Likelihood function based on their value and shape and can therefore have a large impact on the result. The posterior p.d.f. including the nuisance parameters is given by

$$p(\theta|\vec{x}) = \frac{L(\vec{x}|\theta) \cdot \pi(\theta) \cdot \pi(\vec{\nu})}{\int\int L(\vec{x}|\theta) \cdot \pi(\theta) \cdot \pi(\vec{\nu})\, d\theta\, d\vec{\nu}}. \tag{7.3}$$

Using this distribution, a limit on the unknown model parameter θ can be set by integrating the posterior p.d.f. to a certain confidence level (CL):

$$1 - \alpha = CL = \int_{\theta_{down}}^{\theta_{up}} p(\theta|\vec{x})\, d\theta. \tag{7.4}$$

Here, the CL is set to 95 % which corresponds to two standard deviations, meaning that $\alpha = 0.05$. In addition, we are only interested in the upper limit, setting $\theta_{down} = 0$. The parameter of interest (POI) in this thesis is the cross section σ, resulting in the definition of the upper cross section limit with 95 % CL:

$$0.95 = \int_{0}^{\sigma_{up}} p(\sigma|\vec{x})\, d\sigma. \tag{7.5}$$

The cross section limit is calculated for the combination of nearby and separated tau categories, as well as for the full combination of all channels. Subsequently, it will be reinterpreted in terms of the coupling parameters of the HVT model.

7.2. Maximum Likelihood Fit, Uncertainty Impacts and Significances

To test the consistency of the expectation and its uncertainties with the observed data, a maximum likelihood fit of the expectation with respect to the data is performed for each of the final distributions, namely the $\sum p_T$-distributions. The fit is done based on the background only and on the background plus signal hypothesis with a floating signal strength. In case of the signal plus background hypothesis, a 2 TeV Wh resonance signal is used. The fit is performed by maximizing the likelihood function of the hypothesis to describe to observed data. The nuisance parameters of the hypothesis are varied within the fit and optimized to the value that results in the best description of the data. As the nuisance parameters are required to be compatible to the observed data, their values, namely their mean value and their uncertainty, get changed by the fit. For example, if the mean value of a nuisance parameter does not describe the data well, but its uncertainty covers the data, the parameter will be pulled and its uncertainty will be constrained. On the other hand, if the nuisance parameter describes the data well, it will not be pulled, but its uncertainty will be constrained if it is overestimated. The maximum likelihood fit shows how the expectation is influenced by the various uncertainties and how these uncertainties are pulled, constrained or stretched in the presence of data. Based on the results from the fit, the final distributions before (called "prefit") and after (called "postfit") the fit can be produced and compared to see if all parameters behave as expected. For a final conclusion about the agreement of data and background, the postfit distributions will be used as they include more information. Figs. 7.1 and 7.2 show the comparison of the prefit and background only postfit $\sum p_T$-distributions for each channel - hadronic (HAD), semileptonic same lepton flavour (SSLF), and semileptonic different lepton flavour (SDLF) - and tau reconstruction category (separated and nearby) as well as the corresponding total uncertainties. The signal used here corresponds to a 2 TeV Wh resonance. It is visible that for the most channels the postfit distribution

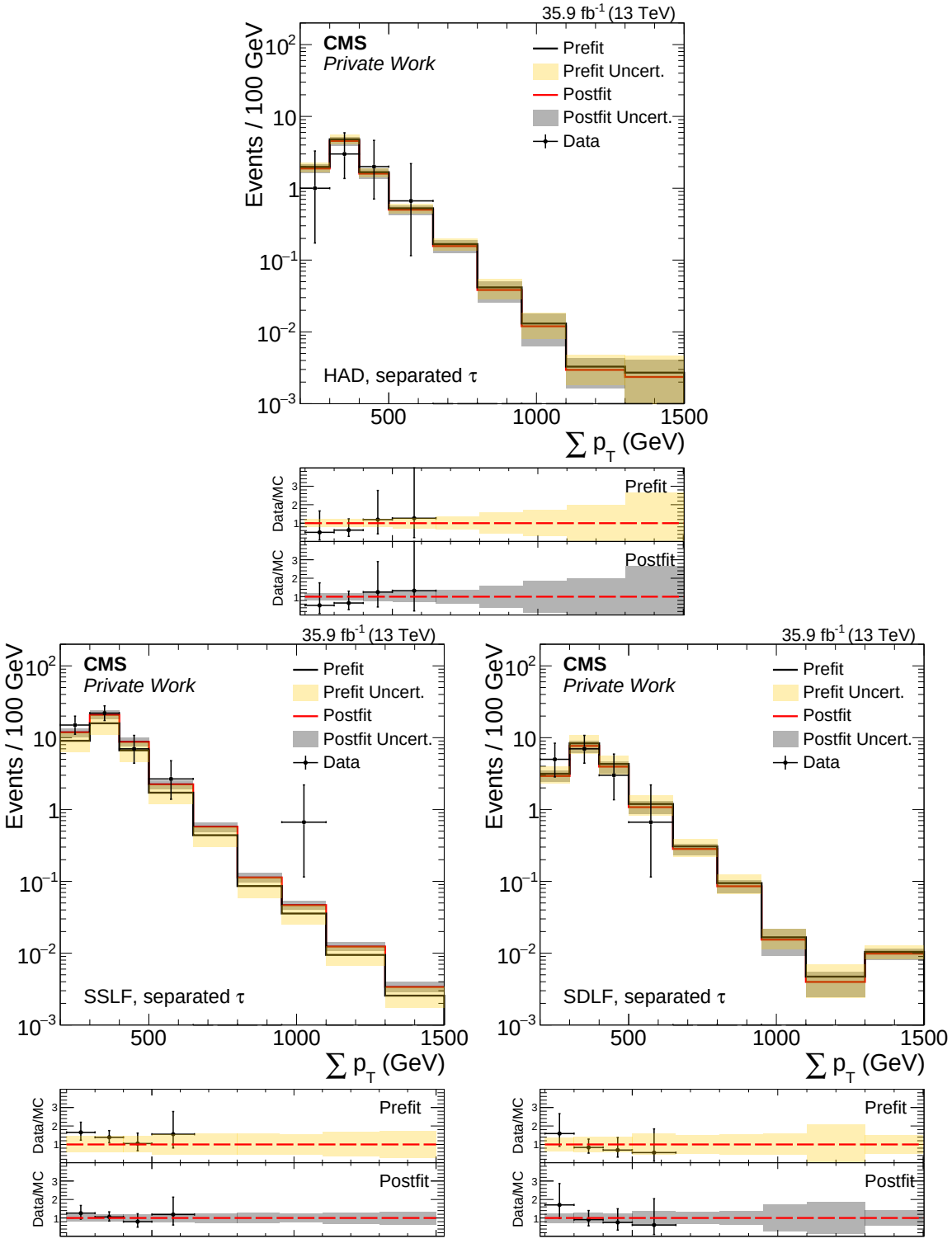

Figure 7.1.: Comparison of the distributions and uncertainties before and after the maximum likelihood fit for separated taus. Top: hadronic channel, bottom left: semileptonic same lepton flavour channel, bottom right: semileptonic different lepton flavour channel. Data points that are not visible in the ratio plot have a value larger than 3.

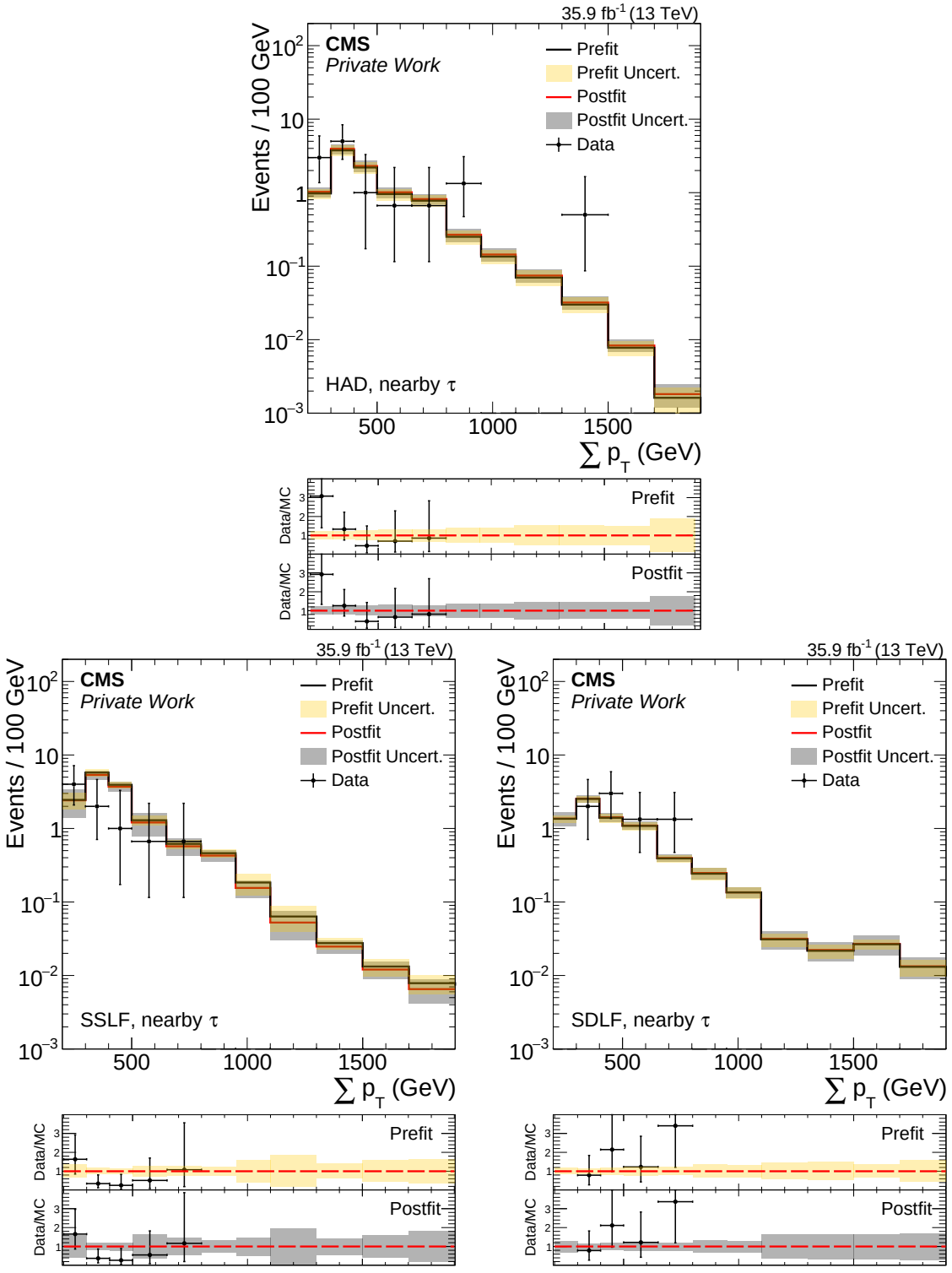

Figure 7.2.: Comparison of the distributions and uncertainties before and after the maximum likelihood fit for nearby taus. Top: hadronic channel, bottom left: semileptonic same lepton flavour channel, bottom right: semileptonic different lepton flavour channel. Data points that are not visible in the ratio plot have a value larger than 3.

and uncertainties do not differ much with respect to the prefit, indicating that the prefit expectation and uncertainties model the data and its shape already well. The only exception can be seen in the semileptonic same lepton flavour channel with separated taus (see Fig. 7.1, bottom left). Here, the difference of prefit and postfit distribution is comparatively high. This effect arises from the excess in data in the first three bins that is covered by the prefit uncertainties, mainly the uncertainty from the jet flavour in the data driven method. After performing the fit, the agreement between data and background is very good in this channel and the uncertainties are highly constrained, resulting in postfit uncertainties of about 13 % instead of 35 % prefit uncertainty.

The maximum likelihood fit can also be used to show its influence on each nuisance parameter in the postfit distributions, e.g. if the corresponding uncertainties have been pulled up or down or if they have been stretched or constrained. The pull distributions of the various channels can be found in Fig. 7.3 for the background only fit (blue) and the signal plus background fit (red) using a 2 TeV Wh resonance signal with floating signal strength. The signal strength that maximizes the likelihood function used in the signal plus background fit is taken for the pull distribution. If a signal is found in data, this method can also be used to extract the signal strength. The gray band in the pull distributions indicates the $\pm 1\sigma$ and the green dashed line the $\pm 2\sigma$ prefit uncertainty. Here, the labels Ele ID, Muon ID, and Tau ID stand for the corresponding object efficiency uncertainties, T/L Jet flavour and T/L Stat. represent the two uncertainties on the data driven method, and Stat_binX ($0 \leq X \leq 11$) are the statistical uncertainties for each bin of the $\sum p_T$-distribution. The results for background-only and signal plus background fit are very similar. The reason is that the signal is based on a resonance and its effect on the signal plus background fit is therefore very small if no corresponding deviation is found in the data. In the separated tau category, most nuisance parameters are neither pulled nor constrained. The reason is that except for the hadronic channel which consists of similar background contributions from real and misidentified taus, the background is completely dominated by the tau misidentification contribution from the data driven method and its uncertainty, and therefore it is the only uncertainty influenced by the maximum likelihood fit. This is especially visible in the semileptonic same lepton flavour channel (Fig. 7.3, middle left) where the effect of the data driven uncertainty from jet flavour on the fit can be clearly seen. The fit to the background affects the corresponding uncertainty by pulling it down and constraining it, which is what one would expect in this case. In the hadronic channel, most uncertainties have very small pulls, except for the jet flavour and tau ID uncertainty as they are the dominant uncertainties. For the nearby category, the nuisance parameters are slightly pulled up or down and their uncertainty is slightly constrained, and thus they all behave as expected. Overall, the input parameters behave pretty well and the maximum likelihood fit produces consistent results.

An additional test was done for each channel to determine the impact of the nuisance parameters on the POI. The corresponding plots are shown in Fig. 7.4, 7.5, and 7.6 and are based on a 1 TeV Wh resonance signal for the separated tau categories and 2 TeV Wh resonance signal for the nearby tau categories with signal strength set to 1. The distributions show the impact of each uncertainty, split in up- and down-shift impacts, and were produced using the CMS CombineHarvester [154, 155] by fixing the nuisance parameter of interest to its $\pm 1\,\sigma$ prefit value before performing the fit. In the distributions, $\hat{\mu}$ is the POI which corresponds to the signal strength r, $\Delta\hat{\mu}$ is the difference with respect to the POI arising from the uncertainties, and $\left(\hat{\theta} - \theta_0\right)/\Delta\theta$ are the pull distributions of the nuisance parameters. The nuisance parameters that have the largest impact on the POI are the tau efficiency uncertainty, labelled as "Tau ID" and the data driven background uncertainties, labelled as "T/L Jet flavour" and "T/L Stat.". The impact of the tau ID uncertainty is very asymmetric, showing that the influence of the down-shift is much larger and that it can affect the value of the POI by 20-30 %. This effect arises from the p_T dependent uncertainty of 35 % per TeV for the down-shift, but only 5 % per TeV for the up-shift. In the separated tau categories, the data driven uncertainties

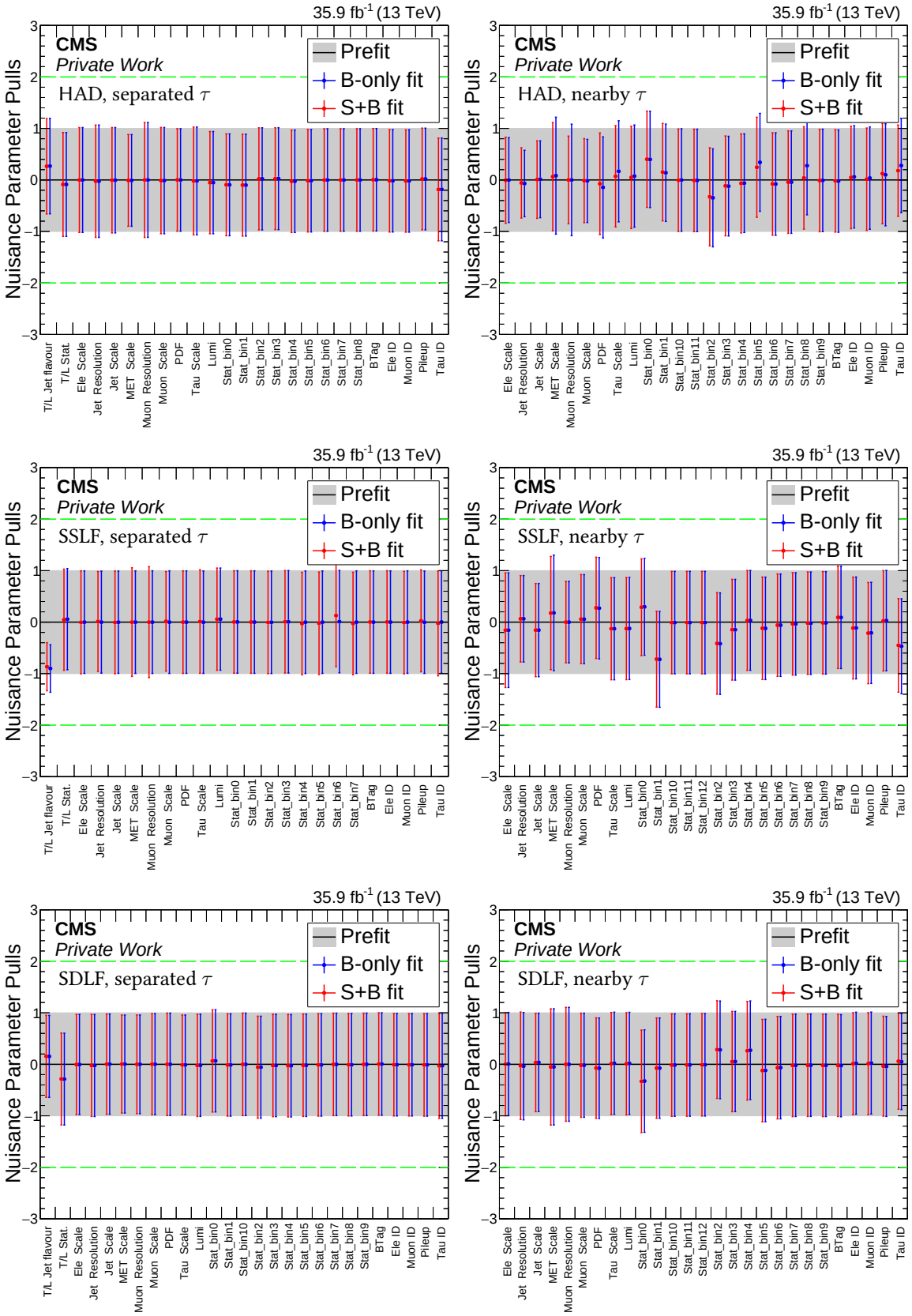

Figure 7.3.: Pull distribution of the nuisance parameters after performing the maximum likelihood fit. Left: Separated taus, right: Nearby taus, top: hadronic channel, middle: semileptonic same lepton flavour channel, bottom: semileptonic different lepton flavour channel

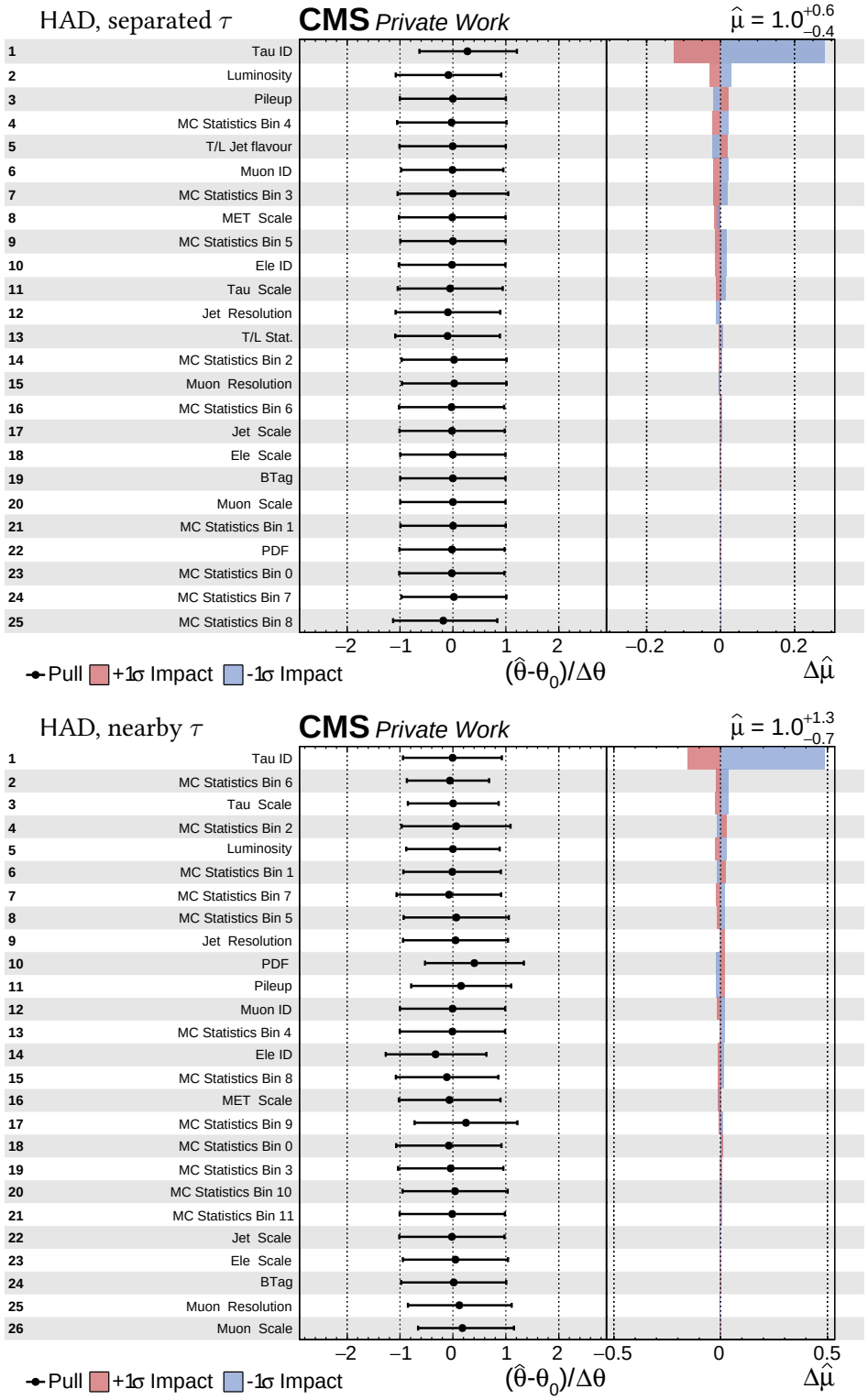

Figure 7.4.: Impact of the nuisance parameters on the calculated limit for the hadronic channels and a Wh resonance mass of 2 TeV. Top: Separated taus, bottom: nearby taus.

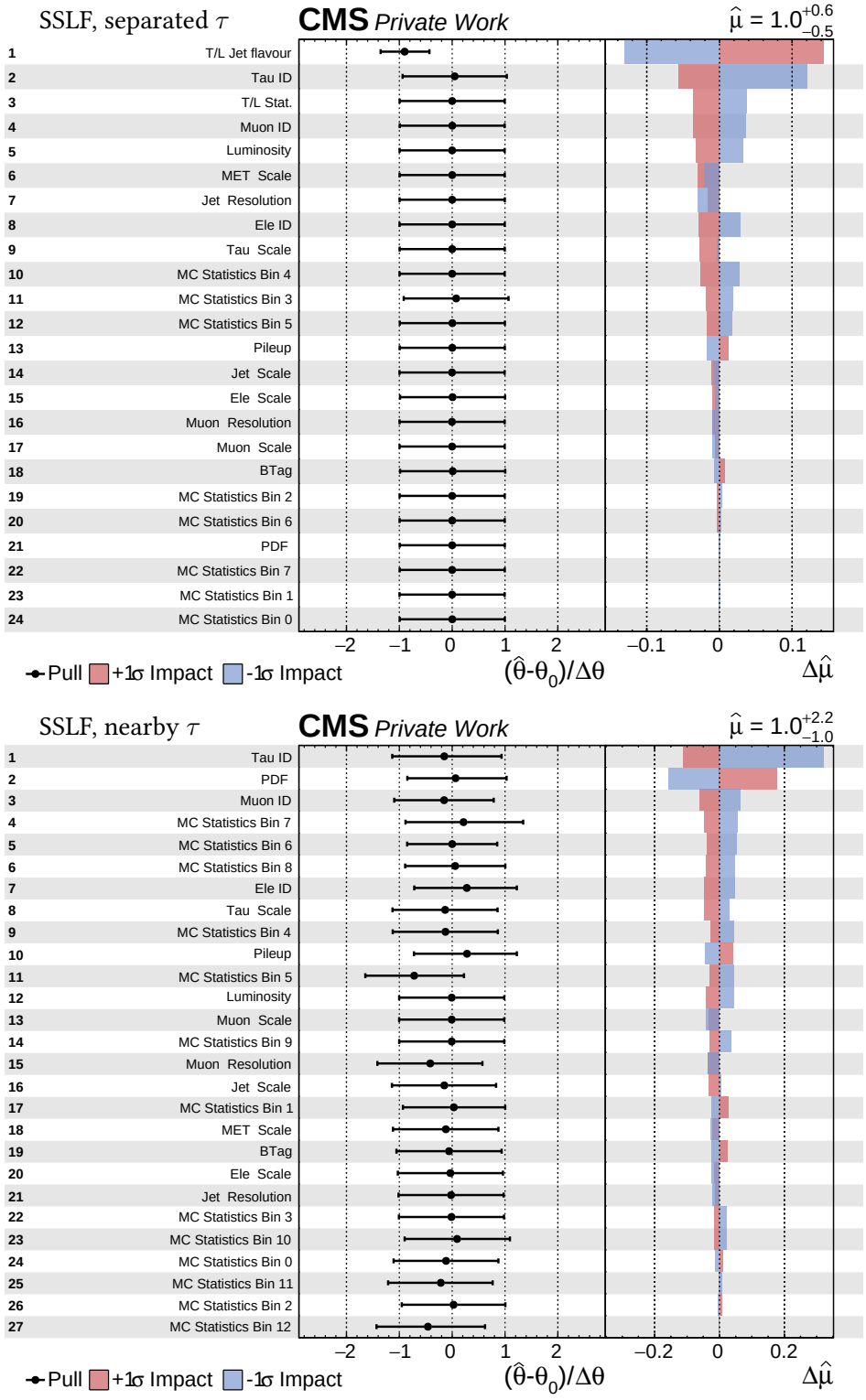

Figure 7.5.: Impact of the nuisance parameters on the calculated limit for the semileptonic same lepton flavour channels and a Wh resonance mass of 2 TeV. Top: Separated taus, bottom: nearby taus.

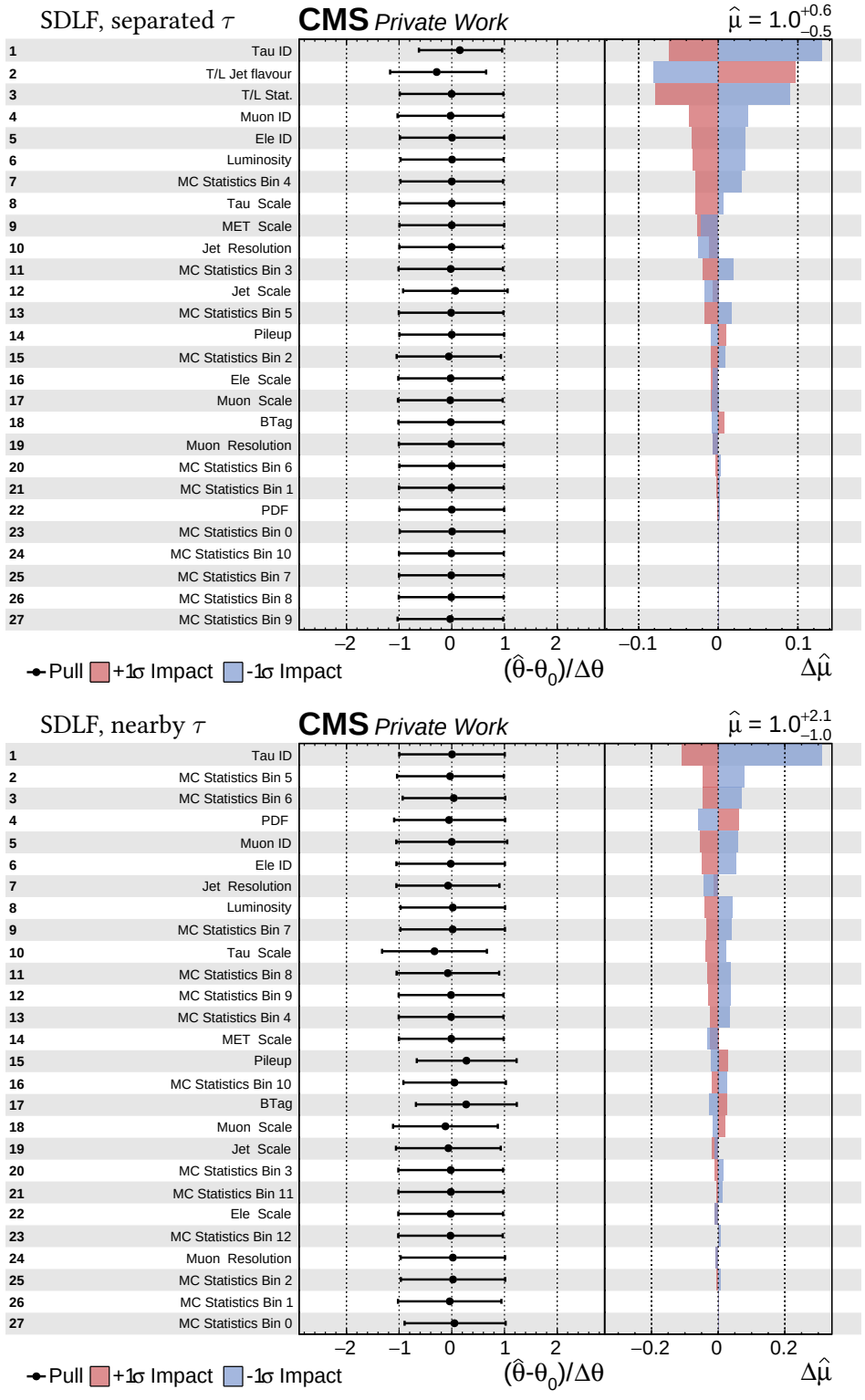

Figure 7.6.: Impact of the nuisance parameters on the calculated limit for the semileptonic different lepton flavour channels and a Wh resonance mass of 2 TeV. Top: Separated taus, bottom: nearby taus.

are dominant, except for the hadronic channel where a large part of the background is modeled by simulation. This is expected, as the data driven background and its uncertainties are dominating in the semileptonic channels. However, since the tau ID uncertainty plays an important role for the signal expectation, it still has a non-negligible impact on the POI value. The other uncertainties show a smaller impact on the result, especially in the separated tau category where their influence is nearly negligible w.r.t. the data driven and tau ID uncertainty. However, they still have some impact in the nearby tau category.

The consistency checks performed based on the maximum likelihood fit give additional confidence in the modeling of the background, signal, and their uncertainties and therefore, in the statistical analysis itself. This statistical analysis will be started with the estimation of the observed significance. Significances and the corresponding p-values [156] have been calculated for all three resonance hypotheses, namely Wh, WZ and WZ+Wh, as well as for each channel and their combination. For the combination, an expected a-posteriori (after maximum likelihood fit) significance has been calculated for each hypothesis. To estimate the significance, the profiled likelihood ratio of two likelihoods is used. The likelihood of the nominator is based on the background only hypothesis with signal strength set to 0 only taking into account the nuisance parameters of the background while the likelihood of the denominator is based on the signal plus background fit with freely floating signal strength including also the signal nuisance parameters. The test statistics, referred to as log-likelihood ratio, is given by

$$q_0 = -2 \ln \left[\mathcal{L}\left(\text{data}|r = 0, \hat{\theta}_0\right) / \mathcal{L}\left(\text{data}|r = \hat{r}, \hat{\theta}\right) \right] \tag{7.6}$$

where $\mathcal{L}$ are the profiled likelihood functions, r is the signal strength and θ are the nuisance parameters that are profiled differently for freely floating signal strengths $r = \hat{r}$ and $r = 0$. The likelihoods are defined by the product of the Poisson probabilities multiplied with the product of nuisance parameter constrain functions of each bin [153, 157]:

$$\mathcal{L} = \prod_{i=1}^{N_{bins}} \left(\frac{(r\, s_i(\theta) + b_i(\theta))^{n_i}}{n_i!} e^{-r\, s_i(\theta) - b_i(\theta)} \cdot \prod_{j\, \epsilon\, nui} C\left(\theta_j\right) \right) \tag{7.7}$$

where r is the signal strength, s_j, b_j, and n_j are the number of signal, background and observed data events in one bin, and $C(\theta_j)$ are the constrain functions for the various nuisance parameters. The results of the significance scans are presented in Fig. 7.7 for all three signal hypotheses, based on the HVT model B. Since the signal strength is freely floating and the signal shapes of the Wh and WZ resonances look similar, the observed significances are comparable. The expected significances for HVT model B are illustrated by the dashed black line. If a signal is found in data which corresponds to HVT model B, the expected and observed significance would obtain approximately the same value for the corresponding resonance mass. Since this is not the case, the observed significances are much lower than the expected significances. Expected significances are also a good measure for the sensitivity of an analysis. If it lies above $3\,\sigma$, the analysis is sensitive for an evidence of the corresponding model in data. Here, WZ+Wh resonances are sensitive for masses below 2 TeV, Wh resonances for masses below 1.5 TeV, and WZ resonances only for masses of 1 TeV if HVT model B is taken into account. For the WZ significances, the expected significance decreases for masses below 1 TeV due to the increasing background. This feature exists also for the other two hypothesis, but it lies outside of the plotting range.
As expected, the largest significance is observed in the hadronic channel with nearby taus, where one bin in the $\sum p_T$-distribution between 800 GeV and 950 GeV contains three data events, but only

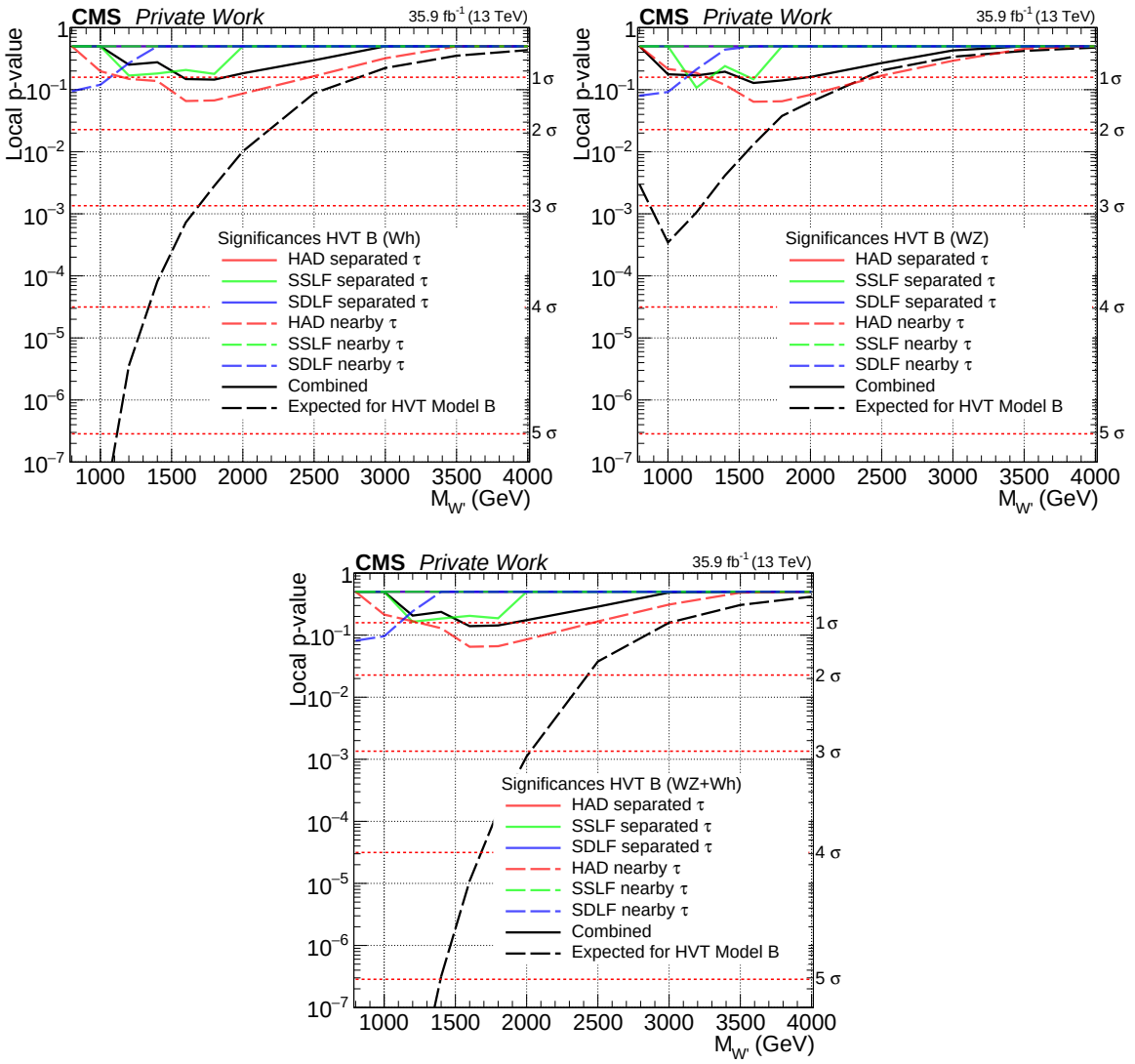

Figure 7.7.: Observed significance for each channel and category and combined observed and expected significance for a Wh (top left), WZ (top right) and WZ+Wh (bottom) signal hypothesis using HVT model B. If a signal of HVT model B is found in data, the observed and expected significances should obtain the same values at the given mass point, otherwise their values should differ.

0.4 background events are expected. The significance is maximized for a resonance mass of 1.6 TeV and corresponds to a local value of 1.6 σ. Since this deviation is not confirmed in the other search regions, the combined significance is smaller, resulting in a maximum of 1.1 σ. The only differences between HVT model A and model B that are relevant for this analysis are the branching fractions and the cross sections. Therefore, as the signal strength is floating, the same observed significances for HVT model A can be expected as the signal shape is the same. However, the expected significances of model A will differ with respect to model B since the branching fractions and the cross section differ. If a signal strength of r = 1 is assumed for HVT model A, the expected significances should be lower for masses above 1 TeV in comparison to HVT model B (with r = 1) as the cross section is lower. However, the differences are small and therefore, only the expected significance for HVT

model B is cited in Fig. 7.7. Since no significant deviation can be found, it can be proceeded to calculate cross section and model parameter limits.

7.3. Exclusion Limits

No significant deviation was found in the analysis and therefore, exclusion limits can be set. Two types of exclusion limits are calculated, namely limits on the cross section times branching fraction ($\sigma \times \mathrm{B}$) and limits on the couplings of the HVT model. The limits are calculated for three signal hypotheses: Charged resonance decays to WZ, Wh, and WZ as well as Wh (WZ+Wh). All limits are obtained using the Bayesian method described in Sec. 7.1 with a confidence level (CL) of 95 %. Instead of calculating a single bin limit where only one part of the distribution is used to compare the number of observed data events to the background and signal expectation, the shape based approach is used which includes information about the data, background, and signal shape. Using this approach, every bin of the distribution is taken into account and therefore, shape based limits are very sensitive to differences in the data/background and signal shape. It is especially useful in resonance searches where the signal shape differs from the background shape and gives better results in regions with a large background contamination. In regions with small background, the single bin approach provides comparable results.

7.3.1. Cross Section Limits

Using all the information of the analysis and the limit setting method described in Sec. 7.1, exclusion limits on $\sigma \times \mathrm{B}$ are obtained. Although this analysis is based on the decay of a diboson resonance to $\ell\tau\tau + \mathrm{E_T^{miss}}$, the limits will not be quoted with respect to $\mathrm{B}\left(\mathrm{W'} \to \mathrm{WV} \to \ell\tau\tau + \mathrm{E_T^{miss}}\right)$ (V = h, Z), but with respect to the branching fraction of the diboson system $\sigma\left(\mathrm{W'}\right) \times \mathrm{B}\left(\mathrm{W'} \to \mathrm{WV}\right)$, changing only the scale of the limit output. Details about the branching fractions in HVT model A and model B can be found in Fig. 2.6 and 2.7 of Sec. 2.3. The advantages of this method are that the results are more easy to compare to other diboson resonance searches and that the results can be reinterpreted easier. The two cross section limits for Wh and WZ are calculated under the assumption that the other decay mode is set to zero. A combination of both possible decays will be presented afterwards. Fig. 7.8 shows the $\sigma\left(\mathrm{W'}\right) \times \mathrm{B}\left(\mathrm{W'} \to \mathrm{WV}\right)$ cross section limit as a function of the heavy charged resonance W′ while Tab. 7.1 and Tab. 7.2 summarize the cross section limit results of the Wh and WZ decay and compare it to the theory cross section. The exclusion limit is based on the combination of all three channels and two tau categories while the red lines correspond to the observed limits of the three subchannels, separated and nearby category combined. The limit plots for these subchannels are shown in App. C.5. The uncertainty bands of the theory curves represent the impact of the PDF normalization uncertainties on the signal. The intersection of the theory curves with the cross section limit lines gives the mass limit on the theory. For Wh resonances, the mass limits on the HVT model can be set to

$$\mathbf{M_{W' \to Wh} > 1.40\ TeV} \quad \textbf{for} \quad \textbf{HVT model A @ 95 \% CL and}$$
$$\mathbf{M_{W' \to Wh} > 1.60\ TeV} \quad \textbf{for} \quad \textbf{HVT model B @ 95 \% CL}$$

The cross section limit of Wh resonances behaves as expected. Since the background decreases while the signal efficiency increases for higher masses, the limit improves. Overall, the limit is highly dominated by the hadronic channel due to its large efficiency and branching fraction. For the observed limit, a small excess of 1 σ is found. This excess arises from the deviation in the nearby

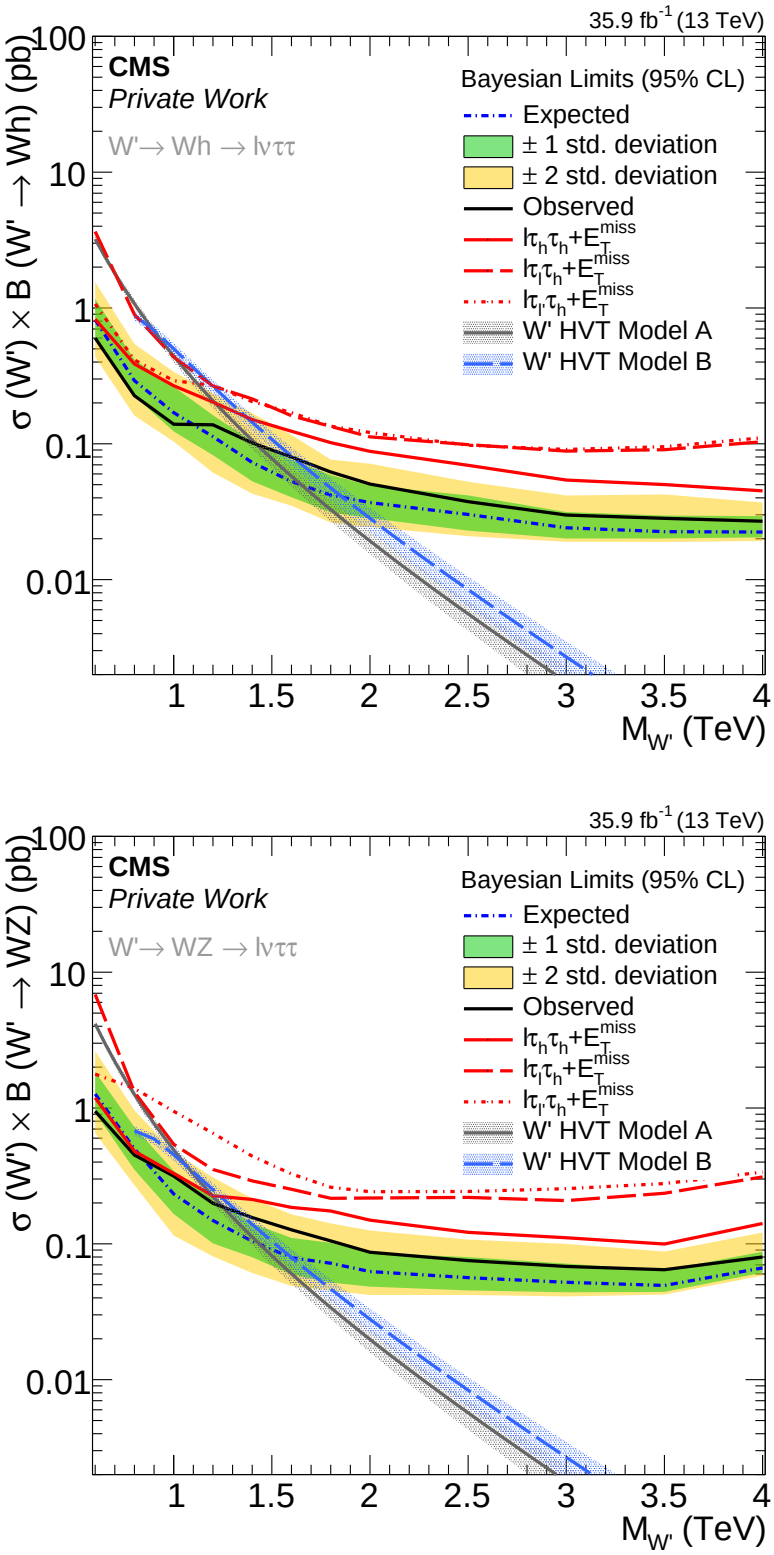

Figure 7.8.: Limits on the cross section times branching ratio for charged high mass resonances decaying to Wh $\left(\sigma\left(\mathrm{W}'\right) \times \mathrm{B}\left(\mathrm{W}' \rightarrow \mathrm{Wh}\right)\right)$ (top) and to WZ $\left(\sigma\left(\mathrm{W}'\right) \times \mathrm{B}\left(\mathrm{W}' \rightarrow \mathrm{WZ}\right)\right)$ (bottom).

hadronic category between 800 and 950 GeV. As discussed earlier, it is not significant.
For WZ resonances, the mass limits on the HVT model are given by

$$\mathbf{M_{W'\to WZ} > 1.25\ TeV \quad for \quad HVT\ model\ A\ @\ 95\ \%\ CL\ and}$$
$$\mathbf{M_{W'\to WZ} > 1.30\ TeV \quad for \quad HVT\ model\ B\ @\ 95\ \%\ CL}$$

The limits for WZ are slightly worse than for Wh resonances because of the lower SM branching fraction of $Z \to \tau\tau$ (3.4 %) w.r.t $h \to \tau\tau$ (6.2 %) [28]. However, the general shape is comparable. Since the branching fractions of Wh and WZ are comparable in the HVT model, their branching fractions to two tau leptons translate directly to the mass limits. While the Wh limit improves up to high masses, the WZ limit starts getting worse for masses beyond 3.5 TeV. This is due to the decreasing efficiency of the nearby tau channels for high masses as discussed in detail in Sec. 6.3.6.
As expected, the cross section limits in this particular diboson decay mode are strong in the low mass region because of the background rejection, while in the high mass region many other channels are more sensitive due to their enhanced branching fraction. For resonance masses below 1 TeV, the limits of this analysis are only exceeded by the $\ell\nu$bb channel for Wh resonances where a limit of 0.2 pb is set [24, 25] (see Sec. 2.3.4) in comparison to 0.6 pb from the $\ell\nu\tau\tau$ channel for resonance masses of 0.6 TeV. For WZ resonances, a larger number of leptonic final states are possible and therefore, the limit is beaten by three other analyses at low masses, namely $\ell\nu\ell\ell$, qq$\ell\ell$, and $\ell\nu$qq. However, the relative difference to these limits is smaller than one would expect if only the branching ratio is taken into account. This decreasing difference hints to a possible interesting phase space of the $\ell\nu\tau\tau$ channel for masses between 0.2 and 0.6 TeV. To reach this phase space, the analysis strategy for separated tau channels needs to be changed slightly by loosening the criteria on the distance $\Delta R(\tau_{vis}, \tau_{vis})$, the angle $\Delta\phi(V_{vis}, \ell)$, and the visible boson momentum $p_T^{V_{vis}}$. An increased number of background could be suppressed by adding a same sign charge category. These optimizations would be interesting for future analysis iterations.

Following the separated results of the two diboson decay modes, they can now be combined in one result. Since the selection is exactly the same for both of them, the background and data stays the same and the two signal contributions add up. In contrast to the Wh and WZ limits where one cross section limit could be interpreted by different theories, this is not the case for their combination. The reason is that the relative branching fraction of Wh and WZ with respect to each other changes the cross section limit, meaning that the cross section limit depends on the ratio

$$c = \frac{B\left(W' \to Wh\right)}{B\left(W' \to Wh\right) + B\left(W' \to WZ\right)}. \tag{7.8}$$

The two extreme cases are given by $B\left(W' \to WZ\right) = 0$ (only Wh decays) and $B\left(W' \to Wh\right) = 0$ (only WZ decays) and correspond to the results discussed above. In the HVT models A and B, the relative branching fraction between Wh and WZ decays are approximately the same for high masses, but it differs for low masses. While for model A the WZ decay has a higher branching fraction ($\approx$ 25 %), it is the opposite for model B (see Fig. 2.6 and 2.7 in Sec. 2.3). Therefore, two cross section limits for the combination of Wh and WZ decays are shown in Fig. 7.9, one for model A (top) and one for model B (bottom). It is visible that the differences are mainly in the low mass region where the WZ decay has a larger impact in model A on the result. Here, the limit gets worse due to the lower branching fraction of $Z \to \tau\tau$ compared to $h \to \tau\tau$. In the high mass region, the limits are compatible because the relative branching fraction is 50 % in both models. Since the HVT model B is theoretically excluded for masses below 0.8 TeV [2], the range of the x-axis is different w.r.t the

$M_{W' \to Wh}$ (TeV)	$\sigma_{HVT\ A}$ (pb)	$\sigma_{HVT\ B}$ (pb)	Exp. Limit $\pm 1\sigma \pm 2\sigma$ (pb)	Obs. Limit (pb)
0.6	3.22	-	$0.82^{+0.35+0.74}_{-0.23-0.38}$	0.60
0.8	1.074	0.879	$0.29^{+0.13+0.25}_{-0.07-0.13}$	0.23
1.0	0.443	0.501	$0.17^{+0.09+0.17}_{-0.05-0.07}$	0.14
1.2	0.208	0.264	$0.11^{+0.05+0.12}_{-0.03-0.05}$	0.14
1.4	0.106	0.144	$0.07^{+0.03+0.10}_{-0.02-0.03}$	0.10
1.6	0.058	0.081	$0.05^{+0.02+0.06}_{-0.01-0.02}$	0.08
1.8	0.033	0.047	$0.04^{+0.02+0.04}_{-0.01-0.02}$	0.06
2.0	0.019	0.028	$0.04^{+0.01+0.03}_{-0.01-0.01}$	0.05
2.5	0.006	0.008	$0.030^{+0.012+0.022}_{-0.007-0.009}$	0.038
3.0	0.002	0.003	$0.024^{+0.007+0.018}_{-0.004-0.005}$	0.030
3.5	$6 \cdot 10^{-4}$	$9 \cdot 10^{-4}$	$0.023^{+0.007+0.020}_{-0.002-0.004}$	0.028
4.0	$2 \cdot 10^{-4}$	$3 \cdot 10^{-4}$	$0.022^{+0.007+0.015}_{-0.002-0.003}$	0.027

Table 7.1.: Comparison of theory cross section and cross section limit for various W′ masses for decays to Wh.

earlier limit plots. For the combination of Wh and WZ decays, the mass limits on the HVT model are given by

$M_{W'}$ > 1.70 TeV for HVT model A → Wh+WZ @ 95 % CL and
$M_{W'}$ > 1.90 TeV for HVT model B → Wh+WZ @ 95 % CL

This is an improvement of about 15-20 % in the mass limit w.r.t. the Wh decay. In the combined limits plots, it is visible that the limit worsens for masses beyond 3.5 TeV due to the efficiency loss in the WZ decay. However, the effect is much smaller than before because of the additional Wh decay. The excess in the nearby hadronic channel is also visible in these distributions and corresponds again to a 1 σ deviation.

$M_{W' \to WZ}$ (TeV)	$\sigma_{\text{HVT A}}$ (pb)	$\sigma_{\text{HVT B}}$ (pb)	Exp. Limit $\pm 1\sigma \pm 2\sigma$ (pb)	Obs. Limit (pb)
0.6	4.170	-	$1.27^{+0.56+1.35}_{-0.35-0.62}$	0.95
0.8	1.258	0.681	$0.50^{+0.22+0.46}_{-0.15-0.23}$	0.45
1.0	0.492	0.454	$0.23^{+0.11+0.24}_{-0.07-0.12}$	0.32
1.2	0.224	0.250	$0.15^{+0.07+0.16}_{-0.05-0.07}$	0.20
1.4	0.112	0.139	$0.11^{+0.04+0.11}_{-0.03-0.04}$	0.16
1.6	0.060	0.079	$0.08^{+0.03+0.09}_{-0.02-0.03}$	0.13
1.8	0.034	0.046	$0.07^{+0.03+0.07}_{-0.02-0.03}$	0.11
2.0	0.020	0.028	$0.06^{+0.02+0.06}_{-0.01-0.02}$	0.09
2.5	0.006	0.008	$0.056^{+0.023+0.051}_{-0.011-0.014}$	0.075
3.0	0.002	0.003	$0.052^{+0.019+0.048}_{-0.008-0.011}$	0.068
3.5	$6 \cdot 10^{-4}$	$9 \cdot 10^{-4}$	$0.049^{+0.014+0.038}_{-0.005-0.007}$	0.064
4.0	$2 \cdot 10^{-4}$	$3 \cdot 10^{-4}$	$0.066^{+0.021+0.055}_{-0.005-0.008}$	0.080

Table 7.2.: Comparison of theory cross section and cross section limit for various W′ masses for decays to WZ.

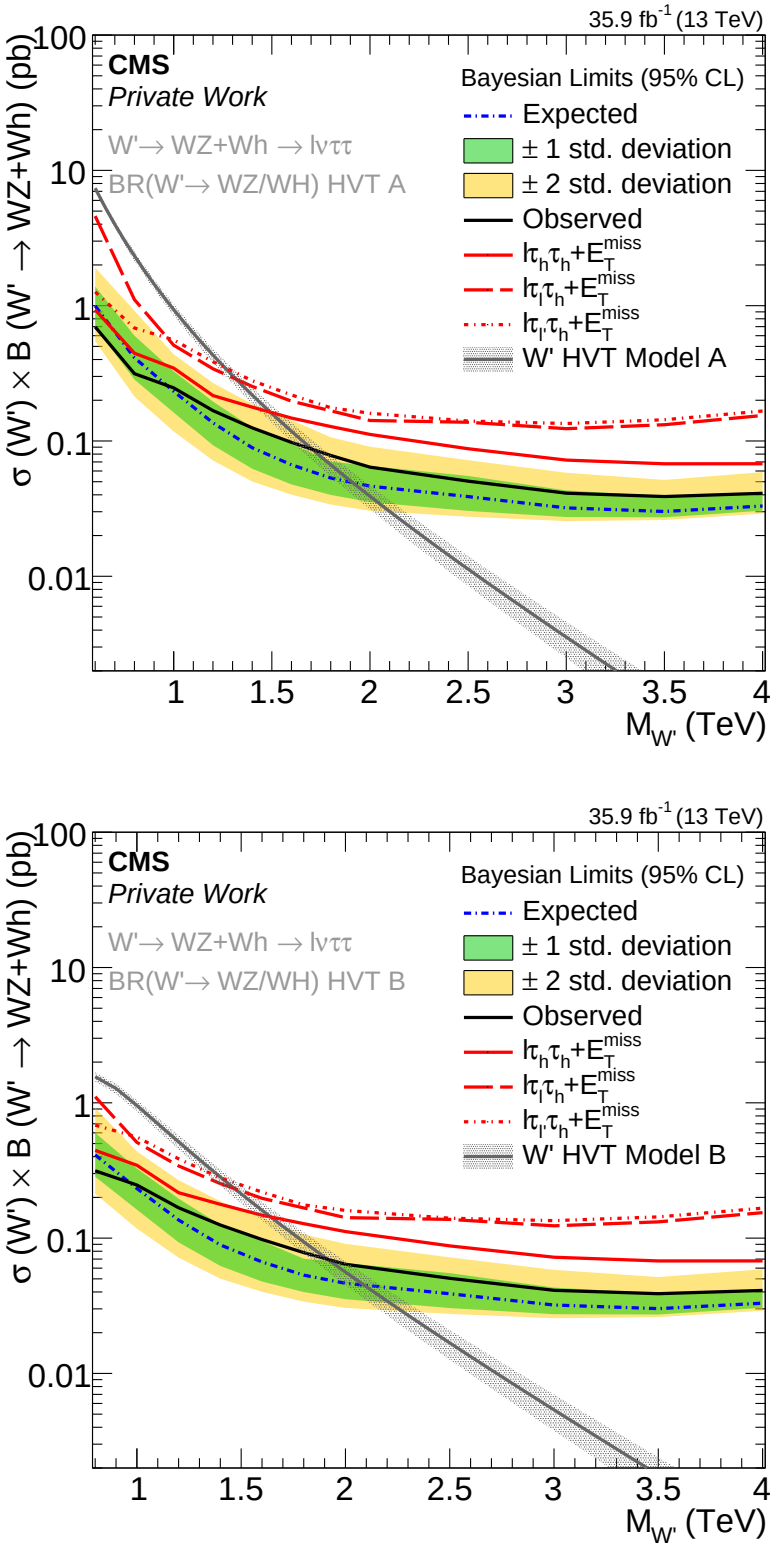

Figure 7.9.: Limits on the cross section times branching ratio for charged high mass resonances decaying to WZ+Wh $\left(\sigma\left(\mathrm{W}'\right) \times \mathrm{B}\left(\mathrm{W}' \rightarrow \mathrm{WZ{+}Wh}\right)\right)$ for HVT model A (top) and HVT model B (bottom) as a function of the resonance mass.

7.3.2. Limits on the Model Parameters

The calculated cross section limits can be reinterpreted in limits on the parameters in the HVT model. As discussed in Sec. 2.3, the HVT model can be described by three parameter combinations, namely the resonance mass M_V, the coupling to the bosons $g_V c_H$, and the coupling to the fermions $g^2 c_F / g_V$. The production process is dominated by $q\bar{q}$ and its parametrisation depends mainly on the decay width to fermions for a given resonance mass. Based on these information, two-dimensional limits on the model parameters $g_V c_H$ and $g^2 c_F / g_V$ can be estimated for given resonance masses. These limits are shown in Fig. 7.10 for Wh only and WZ only decays. The gray area corresponds to a full relative decay width of 7 % estimated based on the $\sum p_T$-resolution that lies at about 10 %. This value was estimated using a 2 TeV Wh resonance signal. This gray area is important as the resonance width depends on the coupling parameters and therefore, the narrow width approximation does not work here, resulting in unreliable coupling limits. The decay width depends on the square of the coupling parameters which leads to four regions with the same limits on the coupling parameters. Parameter combinations that lie in the shaded area are excluded. For the Wh as well as for the WZ decay, the HVT models A and B can be excluded for a resonance mass of 1 TeV, but not for 2 TeV, as one would expect based on the cross section limits. While for the WZ decay no coupling limit for $M_{W'} = 3$ TeV can be set, it is possible for Wh decays in a very small region of the parameter space.

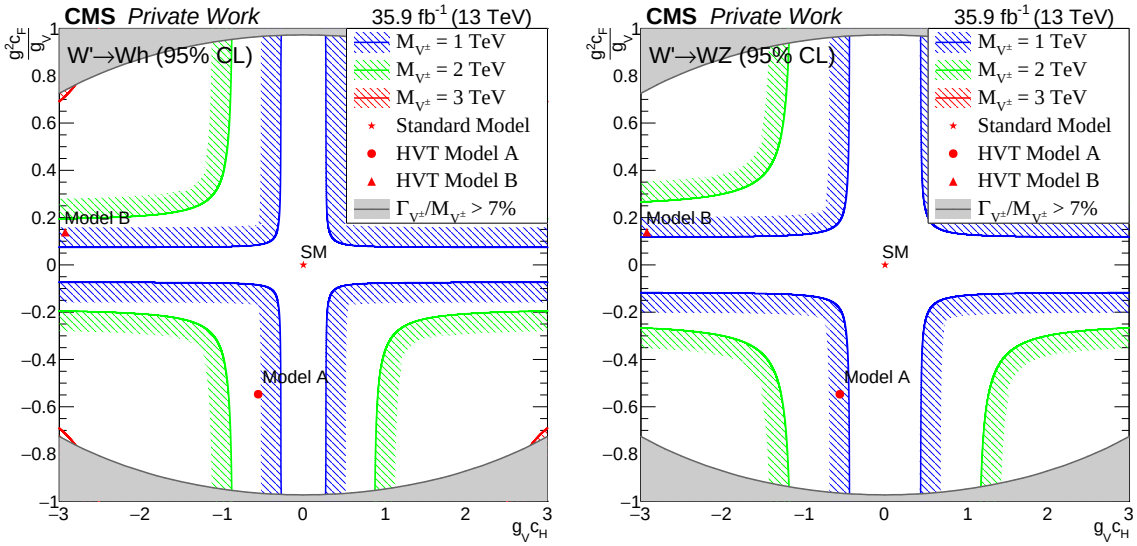

Figure 7.10.: Limits on the HVT model coupling parameters $g_V c_H$ and $g^2 c_F / g_V$ for $M_{W'} = 1$ TeV, 2 TeV and 3 TeV. Left: Wh decay, right, WZ decay.

The same procedure can also be applied to the combination of Wh and WZ. For the calculation of the HVT limit plane, the combined limit from the HVT model B is used. The differences in the branching ratio between Wh and WZ are taken into account within the parameter transformation. Fig. 7.11 shows the limit on the coupling parameter for the combination of Wh and WZ decays. As seen in the cross section limits, model B cannot be excluded for a 2 TeV signal. However, the parameter space that can be excluded is much larger in comparison to the Wh and WZ only decays, including a larger part for $M_{W'} = 3$ TeV.

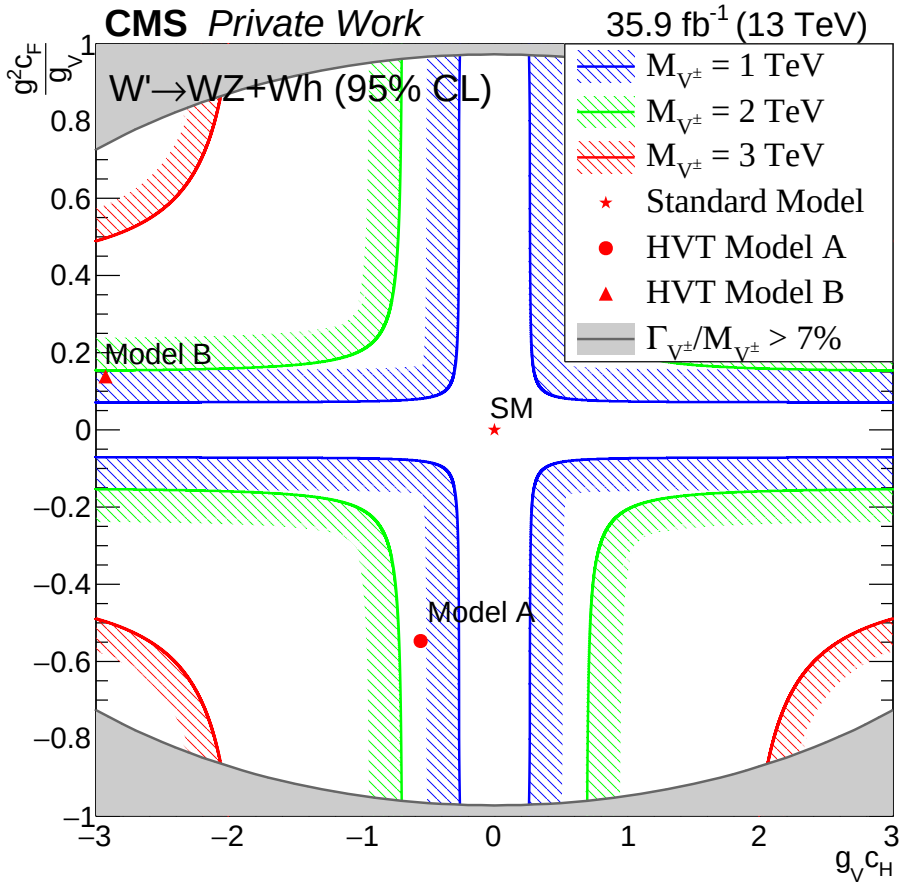

Figure 7.11.: Limits on the HVT model coupling parameters $g_V c_H$ and $g^2 c_F / g_V$ for $M_{W'}$ = 1 TeV, 2 TeV and 3 TeV based on the combination of Wh and WZ decay.

CHAPTER 8

Conclusion

In this thesis, a search for heavy charged diboson resonances in the decay channel $\ell\nu\tau\tau$ was presented, using fully hadronic and semileptonic $\tau\tau$ decays. The analysis was based on the 2016 dataset collected from proton-proton collisions by the CMS experiment corresponding to an integrated luminostiy of 35.9 fb^{-1} at a center-of-mass energy of $\sqrt{s}$ = 13 TeV. The resonances considered here are produced via quark-quark annihilation and decay to Wh and WZ bosons. The signal selection efficiency was kept high by using special reconstruction techniques for the lepton isolation and the identification of nearby taus in a boosted topology. These methods were proven to work well. A good separation between signal and background expectation was achieved by making use of the special kinematics of the signal. For the case of well separated hadronic taus, a data driven background estimation relying on a tight-to-loose ratio was developed and applied. The background estimation of nearby tau channels relies completely on simulation. However, its consistency was checked in control regions for the V+Jets and $t\bar{t}$ background. In all three channels and the corresponding two tau categories, no evidence for new physics could be found.

	Channel	HVT model A Limit (95 % CL)		HVT model B Limit (95 % CL)	
		Expected (TeV)	Observed (TeV)	Expected (TeV)	Observed (TeV)
Wh	HAD	1.45	1.20	1.65	1.35
	SSLF	-	-	-	-
	SDLF	0.90	1.15	-	1.20
	Combined	1.65	1.40	1.85	1.60
WZ	HAD	1.30	1.20	1.40	1.25
	SSLF	-	-	-	-
	SDLF	-	0.80	-	-
	Combined	1.40	1.25	1.60	1.30
WZ+Wh	HAD	1.70	1.50	1.95	1.65
	SSLF	1.25	1.30	1.40	1.45
	SDLF	1.25	1.25	1.45	1.45
	Combined	1.90	1.70	2.10	1.90

Table 8.1.: Limits on the W′ mass in the HVT model A and B for Wh, WZ and Wh+WZ decays at 95 % confidence level (CL).

Since no significant sign for new physics was found, cross section limits as a function of the resonance mass have been calculated. However, before that was done, the impact of the systematic uncertainties on the result was tested. The cross section limits were obtained using the bayesian limit setting method. They are quoted in term of the cross section times branching fraction to diboson decays and were calculated for Wh, WZ, and combined Wh+WZ resonances. An interpretation

was done using the Heavy Vector Triplet (HVT) model. The two used parameter sets, mimicking extended gauge symmetries with weak interactions (model A) and composite Higgs models with strong interactions (model B) could be excluded for masses up to $M\left(W'_{\mathrm{HVT\,A}}\right) > 1.7$ TeV and $M\left(W'_{\mathrm{HVT\,B}}\right) > 1.9$ TeV. A detailed list of the obtained mass limits is shown in Tab. 8.1. These are the first known limits in this particular channel for diboson resonances above the TeV scale.

Since this was the first diboson resonance search in the $\ell\nu\tau\tau$ channel, there is still some room for improvements. One possibility would be to follow a more model independent approach in the separated tau category. The analysis selection was optimized for Wh/WZ resonances at the TeV scale, especially regarding the angular requirements ($\Delta\phi$ and ΔR) and the visible boson momentum. Removing or loosening these requirements in the separated tau category could result in an increased sensitivity for low mass resonances (200 GeV $< M_{V^\pm} <$ 600 GeV) which might be interesting for some additional theories, for example heavy charged Higgs production in some two-Higgs-doublet models (2HDM) decaying to Wh or WZ [158, 159]. However, this would also lead to a lower sensitivity in the medium mass region 600 GeV $< M_{V^\pm} <$ 1200 GeV since the SM background would increase. The high mass region should be unaffected.

Another possibility is the implementation of b-tagged and jet-tagged regions as additional signal regions. The requirement of additional jets in an event could result in a good sensitivity for charged resonances produced via vector boson fusion (VBF). The inclusion of this model would be the next step of this analysis as it opens a new theory phase space. B-tagged regions could give rise to sensitivities on resonance decays including b-jets, e.g. from heavy vector like quarks like $T'b \rightarrow htb \rightarrow Whbb \rightarrow \ell\tau\tau + 2b + E_T^{\mathrm{miss}}$. Of course, this approach would make the background estimation more complicated as some important control regions are replaced by signal regions. In conclusion, an analysis in a complicated phase space was presented in this thesis. As no deviation from the Standard Model expectation was found, exclusion limits on the cross section times branching fraction and the HVT model parameters were set, resulting in observed mass limits of 1.7 TeV (model A) and 1.9 TeV (model B) for charged resonances produced via $q\bar{q}'$ annihilation at 95 % confidence level.

APPENDIX A

Derivation of Formula $\Delta R \approx 2\,M_V/p_T^V$

In Sec. 4 it is discussed that the distance ΔR of two light particles arising from a boosted boson decay can be estimated using the formula $\Delta R \approx 2M_V/p_T^V$. Here, the derivation of this formula will be shown. Starting from the relation of the boson to its decay products in the labor system

$$\begin{pmatrix} E_V \\ \vec{p}_V \end{pmatrix} = \begin{pmatrix} E_1 \\ \vec{p}_1 \end{pmatrix} + \begin{pmatrix} E_2 \\ \vec{p}_2 \end{pmatrix} \tag{A.1}$$

one obtains the invariant mass of the boson via

$$\begin{aligned} M_V^2 &= (E_1 + E_2)^2 - \left(\vec{p}_1 + \vec{p}_2\right)^2 \\ &= E_1^2 + E_2^2 + 2\,E_1\,E_2 - \vec{p}_1^{\,2} - \vec{p}_2^{\,2} - 2\,|\vec{p}_1|\,|\vec{p}_2|\cos\alpha \\ &= m_1^2 + m_2^2 + 2\left(E_1\,E_2 - |\vec{p}_1|\,|\vec{p}_2|\cos\alpha\right) \end{aligned} \tag{A.2}$$

where α is the opening angle between the two decay products. The masses of the two decay products m_1 and m_2 are negligible with respect to the other energies and momenta, especially in comparison to the bosons mass and momentum. As a consequence, it can also be assumed that $E_1 \approx |\vec{p}_1|$, $E_2 \approx |\vec{p}_2|$, $E_1 = E_2 = E_V/2$, and $|\vec{p}_1| = |\vec{p}_2| = |\vec{p}_V|/2$, resulting in the expressions $E_1\,E_2 = E_V/4$ and $|\vec{p}_1|\,|\vec{p}_2| = |\vec{p}_V|/4$. Using these approximations, one obtains

$$M_V^2 = 2\left(\frac{1}{4}\,E_V^2 - \frac{1}{4}\,|\vec{p}_V|^2\cos\alpha\right) \Leftrightarrow \cos\alpha = \frac{E_V^2 - 2\,M_V^2}{|\vec{p}_V^{\,2}|}. \tag{A.3}$$

Now, one can use the Taylor approximation for $\cos\alpha$, given by $\cos\alpha \approx 1 - \alpha^2/2$. Since this approximation is only valid for small opening angles, it is also required that the energy of the boson E_V is dominated by its momentum $\vec{p}_V$ and thus, it is assumed that $E_V^2 = |\vec{p}_V^{\,2}|$ resulting in the formula

$$1 - \frac{\alpha^2}{2} \approx \frac{|\vec{p}_V^{\,2}| - 2\,M_V^2}{|\vec{p}_V^{\,2}|} \Leftrightarrow \alpha^2 = \frac{4\,M_V^2}{|\vec{p}_V^{\,2}|} \Leftrightarrow \alpha = \frac{2\,M_V}{|\vec{p}_V|} \tag{A.4}$$

If this formula is transferred to the distance ΔR and it is taken into account that the momentum is highly dominated by its transverse component, one obtains the formula

$$\Delta R \approx \frac{2\,M_V}{p_T^V}. \tag{A.5}$$

APPENDIX B

Dataset and Background Samples

B.1. The 2016 CMS Datasets

Dataset Name	Luminosity $\mathscr{L}_{\text{int}}$ (fb^{-1})
/SinglePhoton/Run2016B-03Feb2017_ver2-v2/MINIAOD /SingleMuon/Run2016B-03Feb2017_ver2-v2/MINIAOD /SinglePhoton/Run2016B-03Feb2017_ver2-v2/MINIAOD /MET/Run2016B-03Feb2017_ver2-v2/MINIAOD	5.8
/SinglePhoton/Run2016C-03Feb2017-v1/MINIAOD /SingleMuon/Run2016C-03Feb2017-v1/MINIAOD /SinglePhoton/Run2016C-03Feb2017-v1/MINIAOD /MET/Run2016C-03Feb2017-v1/MINIAOD	2.6
/SinglePhoton/Run2016D-03Feb2017-v1/MINIAOD /SingleMuon/Run2016D-03Feb2017-v1/MINIAOD /SinglePhoton/Run2016D-03Feb2017-v1/MINIAOD /MET/Run2016D-03Feb2017-v1/MINIAOD	4.3
/SinglePhoton/Run2016E-03Feb2017-v1/MINIAOD /SingleMuon/Run2016E-03Feb2017-v1/MINIAOD /SinglePhoton/Run2016E-03Feb2017-v1/MINIAOD /MET/Run2016E-03Feb2017-v1/MINIAOD	4.0
/SinglePhoton/Run2016F-03Feb2017-v1/MINIAOD /SingleMuon/Run2016F-03Feb2017-v1/MINIAOD /SinglePhoton/Run2016F-03Feb2017-v1/MINIAOD /MET/Run2016F-03Feb2017-v1/MINIAOD	3.1
/SinglePhoton/Run2016G-03Feb2017-v1/MINIAOD /SingleMuon/Run2016G-03Feb2017-v1/MINIAOD /SinglePhoton/Run2016G-03Feb2017-v1/MINIAOD /MET/Run2016G-03Feb2017-v1/MINIAOD	7.5
/SinglePhoton/Run2016H-03Feb2017_ver2-v1/MINIAOD /SingleMuon/Run2016H-03Feb2017_ver2-v1/MINIAOD /SinglePhoton/Run2016H-03Feb2017_ver2-v1/MINIAOD /MET/Run2016H-03Feb2017_ver2-v1/MINIAOD	8.4
/SinglePhoton/Run2016H-03Feb2017_ver3-v1/MINIAOD /SingleMuon/Run2016H-03Feb2017_ver3-v1/MINIAOD /SinglePhoton/Run2016H-03Feb2017_ver3-v1/MINIAOD /MET/Run2016H-03Feb2017_ver3-v1/MINIAOD	0.2
Full CMS 2016 Data	35.9

Table B.1.: Summary of the data samples used for this analysis.

B.2. Background Samples and Cross Sections

Process	Generator	Cross section (pb)	k-factor / weight
$W \to \ell\nu$	Madgraph	61526.7	1.
$W \to \ell\nu$ $(100 < H_T < 200)$	Madgraph	1345.	1.21
$W \to \ell\nu$ $(200 < H_T < 400)$	Madgraph	359.7	1.21
$W \to \ell\nu$ $(400 < H_T < 600)$	Madgraph	48.91	1.21
$W \to \ell\nu$ $(600 < H_T < 800)$	Madgraph	12.05	1.21
$W \to \ell\nu$ $(800 < H_T < 1200)$	Madgraph	5.501	1.21
$W \to \ell\nu$ $(1200 < H_T < 2500)$	Madgraph	1.329	1.21
$W \to \ell\nu$ $(2500 < H_T < \infty)$	Madgraph	0.03216	1.21
$Z/\gamma \to \ell\ell$ $(M_{\ell\ell} > 50)$	Madgraph	5765.4	1.
$Z/\gamma \to \ell\ell$ $(M_{\ell\ell} > 50, 100 < H_T < 200)$	Madgraph	147.4	1.23
$Z/\gamma \to \ell\ell$ $(M_{\ell\ell} > 50, 200 < H_T < 400)$	Madgraph	40.99	1.23
$Z/\gamma \to \ell\ell$ $(M_{\ell\ell} > 50, 400 < H_T < 600)$	Madgraph	5.678	1.23
$Z/\gamma \to \ell\ell$ $(M_{\ell\ell} > 50, 600 < H_T < 800)$	Madgraph	1.367	1.23
$Z/\gamma \to \ell\ell$ $(M_{\ell\ell} > 50, 800 < H_T < 1200)$	Madgraph	0.6304	1.23
$Z/\gamma \to \ell\ell$ $(M_{\ell\ell} > 50, 1200 < H_T < 2500)$	Madgraph	0.1514	1.23
$Z/\gamma \to \ell\ell$ $(M_{\ell\ell} > 50, 2500 < H_T < \infty)$	Madgraph	0.003565	1.23
$Z/\gamma \to \ell\ell$ $(100 < M_{\ell\ell} < 200)$	aMC@NLO	226	1
$Z/\gamma \to \ell\ell$ $(200 < M_{\ell\ell} < 400)$	aMC@NLO	7.67	1
$Z/\gamma \to \ell\ell$ $(400 < M_{\ell\ell} < 500)$	aMC@NLO	0.423	1
$Z/\gamma \to \ell\ell$ $(500 < M_{\ell\ell} < 700)$	aMC@NLO	0.24	1
$Z/\gamma \to \ell\ell$ $(700 < M_{\ell\ell} < 800)$	aMC@NLO	0.035	1
$Z/\gamma \to \ell\ell$ $(800 < M_{\ell\ell} < 1000)$	aMC@NLO	0.03	1
$Z/\gamma \to \ell\ell$ $(1000 < M_{\ell\ell} < 1500)$	aMC@NLO	0.016	1
$Z/\gamma \to \ell\ell$ $(1500 < M_{\ell\ell} < 2000)$	aMC@NLO	0.002	1
$Z/\gamma \to \ell\ell$ $(2000 < M_{\ell\ell} < 3000)$	aMC@NLO	0.00054	1
$t\bar{t} \to 2\ell\ 2\nu\ 2b$	Powheg	87.31	1.
$t\bar{t} \to 2\ell\ 2\nu\ 2b$ $(500 < M_{\ell\ell} < 800)$	Powheg	87.31	0.003733
$t\bar{t} \to 2\ell\ 2\nu\ 2b$ $(800 < M_{\ell\ell} < 1200)$	Powheg	87.31	0.0003737
$t\bar{t} \to 2\ell\ 2\nu\ 2b$ $(1200 < M_{\ell\ell} < 1800)$	Powheg	87.31	0.00003494
$t\bar{t} \to 2\ell\ 2\nu\ 2b$ $(1800 < M_{\ell\ell} < \infty)$	Powheg	87.31	0.000002001
$t\bar{t} \to 1\ell\ 1\nu\ 2q\ 2b$	Powheg	365.345	1.
ST_s-channel_4f_leptonDecays	aMC@NLO	3.36	1.
ST_t-channel_top_4f_inclusiveDecays	aMC@NLO	41.90	1.
ST_t-channel_antitop_4f_inclusiveDecays	aMC@NLO	25.30	1.
ST_tW_top_5f_NoFullyHadronicDecays	aMC@NLO	38.09	1.
ST_tW_antitop_5f_NoFullyHadronicDecays	aMC@NLO	38.09	1.
$t\bar{t} + Z$ $(Z \to \ell\ell/\nu\nu, M_Z > 10)$	aMC@NLO	0.2529	1.
$t\bar{t} + Z$ $(Z \to qq)$	aMC@NLO	0.2529	1.
$t\bar{t} + W$ $(W \to \ell\nu)$	aMC@NLO	0.1829	1.
$WW \to 1\ell 1\nu 2q$	aMC@NLO	45.85	1.0904
$WW \to 2\ell 2\nu$	Powheg	12.179	1.
$WW \to 2\ell 2\nu$ $(200 < M_{\ell\ell} < 600)$	Powheg	12.179	0.113773
$WW \to 2\ell 2\nu$ $(600 < M_{\ell\ell} < 1200)$	Powheg	12.179	0.0046514
$WW \to 2\ell 2\nu$ $(1200 < M_{\ell\ell} < 2500)$	Powheg	12.179	0.00029203
$WW \to 2\ell 2\nu$ $(2500 < M_{\ell\ell} < \infty)$	Powheg	12.179	0.000004431
$WZ \to 3\ell 1\nu$	aMC@NLO	5.26	1.
$WZ \to 2\ell 2q$	aMC@NLO	5.595	1.
$WZ \to 1\ell 3\nu$	aMC@NLO	3.033	1.
$WZ \to 1\ell 1\nu 2q$	aMC@NLO	10.71	1.
$ZZ \to 4\ell$	Powheg	1.212	1.
$ZZ \to 2\ell 2\nu$	Powheg	0.5644	1.
$ZZ \to 2\ell 2q$	aMC@NLO	3.22	1.

WWW_4F	aMC@NLO	0.2086	1.
WWZ	aMC@NLO	0.1651	1.
WZZ	aMC@NLO	0.05565	1.
ZZZ	aMC@NLO	0.01398	1.
QCD μ-Enriched ($15 < p_T < 20$)	Pythia	1273190000	0.003
QCD μ-Enriched ($20 < p_T < 30$)	Pythia	558528000	0.0053
QCD μ-Enriched ($30 < p_T < 50$)	Pythia	139803000	0.01182
QCD μ-Enriched ($50 < p_T < 80$)	Pythia	19222500	0.02276
QCD μ-Enriched ($80 < p_T < 120$)	Pythia	2758420	0.03844
QCD μ-Enriched ($120 < p_T < 170$)	Pythia	469797	0.05362
QCD μ-Enriched ($170 < p_T < 300$)	Pythia	117989	0.07335
QCD μ-Enriched ($300 < p_T < 470$)	Pythia	7820.25	0.10196
QCD μ-Enriched ($470 < p_T < 600$)	Pythia	645.528	0.12242
QCD μ-Enriched ($600 < p_T < 800$)	Pythia	187.109	0.13412
QCD μ-Enriched ($800 < p_T < 1000$)	Pythia	32.3486	0.14552
QCD μ-Enriched ($1000 < p_T < \infty$)	Pythia	10.4305	0.15544
QCD EM-Enriched ($15 < p_T < 20$)	Pythia	1279000000	0.0018
QCD EM-Enriched ($20 < p_T < 30$)	Pythia	557600000	0.0096
QCD EM-Enriched ($30 < p_T < 50$)	Pythia	136000000	0.073
QCD EM-Enriched ($50 < p_T < 80$)	Pythia	19800000	0.146
QCD EM-Enriched ($80 < p_T < 120$)	Pythia	2800000	0.125
QCD EM-Enriched ($120 < p_T < 170$)	Pythia	477000	0.132
QCD EM-Enriched ($170 < p_T < 300$)	Pythia	114000	0.165
QCD EM-Enriched ($300 < p_T < \infty$)	Pythia	9000	0.15
$gg \to h \to \tau\tau$	Powheg	2.744	1
VBF $\to h \to \tau\tau$	Powheg	0.237	1
$t\bar{t}h$ ($h \to \tau\tau$)	aMC@NLO	0.032	1
$qq \to Zh$ ($h \to \tau\tau$	Powheg	0.055	1
$qq \to W^-h$ ($h \to \tau\tau$	Powheg	0.033	1
$qq \to W^+h$ ($h \to \tau\tau$	Powheg	0.052	1

Table B.2.: Summary of the used Monte Carlo background samples with the corresponding cross sections and weights. Here, weights can either be k-factors used to scale the cross sections (if the cited cross sections are not already given at higher order) or they are applied to correct the cross sections for selection efficiencies in the event generation, e.g. for mass tail samples produced with POWHEG

APPENDIX C

Supplementary Tables and Figures

C.1. Candidate Event List

Run	Lumisection	Event	Dataset	Channel	Tautype	$\sum p_T$ (GeV)
273502	292	321400859	SingleMuon	$\mu\tau_\mu\tau_h$	Separated	311.926
273555	168	250139225	SingleElectron	$e\tau_e\tau_h$	Separated	390.427
274161	123	216918568	SingleElectron	$e\tau_\mu\tau_h$	Nearby	498.291
274200	37	53494055	SingleMuon	$\mu\tau_h\tau_h$	Nearby	816.633
274244	450	645142542	SingleElectron	$e\tau_\mu\tau_h$	Separated	251.455
274250	355	706269340	SingleElectron	$e\tau_h\tau_h$	Nearby	278.46
274251	158	247174949	SingleElectron	$e\tau_e\tau_h$	Separated	364.917
274316	269	498807352	SingleElectron	$e\tau_\mu\tau_h$	Separated	256.512
274422	1164	2003993809	SingleMuon	$\mu\tau_\mu\tau_h$	Separated	447.013
274422	1282	2200723870	SingleMuon	$\mu\tau_\mu\tau_h$	Separated	287.032
274999	679	1241872085	SingleMuon	$\mu\tau_\mu\tau_h$	Nearby	378.534
275074	4	2778098	SingleElectron	$e\tau_h\tau_h$	Nearby	324.117
275067	203	374723449	SingleMuon	$\mu\tau_\mu\tau_h$	Nearby	461.775
275068	150	303448745	SingleMuon	$\mu\tau_h\tau_h$	Nearby	268.04
275073	223	405297577	SingleElectron	$e\tau_e\tau_h$	Nearby	294.959
275125	344	656055617	SingleElectron	$e\tau_e\tau_h$	Separated	320.879
275292	52	81174727	SingleMuon	$\mu\tau_e\tau_h$	Separated	386.022
275338	202	339922784	SingleMuon	$\mu\tau_\mu\tau_h$	Separated	293.285
275345	353	708532603	SingleMuon	$\mu\tau_\mu\tau_h$	Separated	281.044
275375	1323	2282574322	SinglePhoton	$e\tau_e\tau_h$	Separated	292.955
275376	782	1303846416	SingleMuon	$\mu\tau_\mu\tau_h$	Nearby	570.085
275774	86	152978043	SingleElectron	$e\tau_e\tau_h$	Separated	377.541
275778	235	414748888	SingleElectron	$e\tau_h\tau_h$	Nearby	246.504
275890	684	1318016281	SingleElectron	$e\tau_e\tau_h$	Separated	268.117
275911	271	386438955	SingleElectron	$e\tau_e\tau_h$	Separated	353.062
275913	249	490498970	SingleElectron	$e\tau_\mu\tau_h$	Nearby	501.24
275913	284	557721195	SingleMuon	$\mu\tau_\mu\tau_h$	Separated	264.705
275918	18	30898901	MET	$\mu\tau_h\tau_h$	Nearby	856.583
276097	382	735553619	SingleMuon	$\mu\tau_\mu\tau_h$	Separated	274.955
276242	926	1780934785	SingleElectron	$e\tau_h\tau_h$	Nearby	396.248
276242	1392	2600364369	SingleElectron	$e\tau_e\tau_h$	Separated	319.49
276244	868	1283405011	SingleMuon	$\mu\tau_\mu\tau_h$	Separated	1013.4
276437	1169	2130197407	SingleMuon	$\mu\tau_e\tau_h$	Separated	457.022
276437	1296	2364499182	SingleElectron	$e\tau_\mu\tau_h$	Separated	308.449
276501	602	971786460	SingleMuon	$\mu\tau_h\tau_h$	Nearby	378.883
276501	1062	1772413214	SingleElectron	$e\tau_\mu\tau_h$	Separated	302.877

276525	1097	1880200148	SingleMuon	$\mu\tau_e\tau_h$	Separated	344.388
276528	29	34203639	SingleMuon	$\mu\tau_h\tau_h$	Nearby	353.3
276831	296	478466656	SingleMuon	$\mu\tau_\mu\tau_h$	Separated	357.66
276831	264	415397463	SingleElectron	$e\tau_\mu\tau_h$	Separated	240.26
276831	804	1431475027	SingleMuon	$\mu\tau_\mu\tau_h$	Separated	376.538
276870	391	613224262	SingleMuon	$\mu\tau_h\tau_h$	Separated	353.521
276870	2702	544390674	SingleElectron	$e\tau_e\tau_h$	Separated	519.332
276870	2840	759659396	SingleMuon	$\mu\tau_e\tau_h$	Separated	400.98
276948	282	547407606	SingleMuon	$\mu\tau_\mu\tau_h$	Separated	417.554
276948	382	724395634	SingleElectron	$e\tau_e\tau_h$	Separated	263.887
276950	751	1385753832	SingleElectron	$e\tau_e\tau_h$	Separated	374.824
277069	123	119624415	SingleMuon	$\mu\tau_\mu\tau_h$	Separated	354.322
277148	185	217861991	SingleElectron	$e\tau_\mu\tau_h$	Separated	302.546
277168	1141	2103163856	SingleMuon	$\mu\tau_\mu\tau_h$	Separated	314.095
277194	690	1138961795	SingleMuon	$\mu\tau_h\tau_h$	Separated	447.178
277305	366	550992682	SingleMuon	$\mu\tau_\mu\tau_h$	Nearby	246.118
277305	517	840901153	SingleElectron	$e\tau_e\tau_h$	Separated	432.64
277992	224	252963122	SingleMuon	$\mu\tau_\mu\tau_h$	Separated	346.631
278018	33	60195039	SingleElectron	$e\tau_h\tau_h$	Separated	280.237
278018	580	1068784555	SingleMuon	$\mu\tau_\mu\tau_h$	Nearby	283.276
278167	132	108278574	SingleMuon	$\mu\tau_e\tau_h$	Separated	496.588
278167	2146	3800524976	SingleElectron	$e\tau_e\tau_h$	Separated	373.587
278239	503	848026311	SingleMuon	$\mu\tau_\mu\tau_h$	Separated	437.184
278345	821	1454605642	SingleMuon	$\mu\tau_\mu\tau_h$	Separated	331.05
278509	1136	1902958454	SingleMuon	$\mu\tau_\mu\tau_h$	Nearby	609.259
278803	46	82706911	SingleMuon	$\mu\tau_h\tau_h$	Separated	400.263
278820	1127	2083706249	SingleElectron	$e\tau_\mu\tau_h$	Nearby	555.424
278820	1239	2287691997	SingleMuon	$\mu\tau_\mu\tau_h$	Separated	279.001
278875	102	197134649	SingleElectron	$e\tau_e\tau_h$	Nearby	331.412
279024	143	156880637	SingleMuon	$\mu\tau_e\tau_h$	Separated	556.612
279694	1312	2441907333	SingleMuon	$\mu\tau_h\tau_h$	Nearby	1346.1
279694	1588	2910929954	SingleMuon	$\mu\tau_h\tau_h$	Nearby	271.818
279715	100	64466116	SingleMuon	$\mu\tau_\mu\tau_h$	Separated	598.286
279715	548	893399873	SingleElectron	$e\tau_e\tau_h$	Separated	274.441
279716	1443	2542116918	SingleMuon	$\mu\tau_\mu\tau_h$	Separated	591.605
279760	604	988879433	SingleElectron	$e\tau_\mu\tau_h$	Separated	386.009
279841	1576	2761020771	SingleMuon	$\mu\tau_e\tau_h$	Separated	302.816
279931	972	1662144611	SingleElectron	$e\tau_h\tau_h$	Nearby	657.545
279931	2940	709032545	SingleMuon	$\mu\tau_h\tau_h$	Nearby	406.265
279966	165	186758879	SingleMuon	$\mu\tau_e\tau_h$	Separated	316.341
280017	173	318248155	SingleMuon	$\mu\tau_\mu\tau_h$	Nearby	220.975
280188	127	227056364	SingleMuon	$\mu\tau_\mu\tau_h$	Separated	325.788
280249	1020	1845674170	SingleElectron	$e\tau_e\tau_h$	Separated	380.094
280249	1353	2387540803	SingleMuon	$\mu\tau_e\tau_h$	Nearby	699.836
280349	38	70577493	SingleMuon	$\mu\tau_\mu\tau_h$	Separated	367.955
280349	459	875461834	SingleElectron	$e\tau_\mu\tau_h$	Nearby	391.959
280364	267	509721823	SingleElectron	$e\tau_e\tau_h$	Separated	251.307
280385	107	198263839	SingleMuon	$\mu\tau_\mu\tau_h$	Separated	226.961
281693	1270	2394893007	SingleMuon	$\mu\tau_\mu\tau_h$	Separated	382.471

281707	882	1411266856	SingleElectron	$e\tau_h\tau_h$	Nearby	330.982
281797	548	758029087	SingleMuon	$\mu\tau_e\tau_h$	Nearby	375.717
281797	896	1413775478	SingleElectron	$e\tau_e\tau_h$	Nearby	352.057
281976	2026	3540312300	SingleMuon	$\mu\tau_\mu\tau_h$	Separated	252.073
282092	1703	2775188492	SingleMuon	$\mu\tau_\mu\tau_h$	Separated	433.339
282807	300	592258417	SingleElectron	$e\tau_h\tau_h$	Nearby	562.553
283270	696	1097474058	SingleMuon	$\mu\tau_\mu\tau_h$	Separated	273.97
283270	1590	2730049140	SingleElectron	$e\tau_e\tau_h$	Separated	477.991
283283	628	1242137253	SingleMuon	$\mu\tau_h\tau_h$	Separated	375.303
283283	1466	2580897831	SingleElectron	$e\tau_\mu\tau_h$	Nearby	401.449
283358	167	299511668	SingleMuon	$\mu\tau_\mu\tau_h$	Separated	568.851
283358	370	684042957	SingleElectron	$e\tau_e\tau_h$	Separated	328.188
283408	2083	3536612356	SingleElectron	$e\tau_h\tau_h$	Separated	357.127
283453	512	759368646	SingleMuon	$\mu\tau_\mu\tau_h$	Separated	294.224
283478	280	371606164	SingleElectron	$e\tau_e\tau_h$	Separated	351.033
283820	1305	2301441644	SingleElectron	$e\tau_\mu\tau_h$	Nearby	420.31
283830	530	942369458	SingleMuon	$\mu\tau_\mu\tau_h$	Separated	240.896
283865	198	344457320	SingleMuon	$\mu\tau_\mu\tau_h$	Separated	426.598
283876	612	972653946	SingleElectron	$e\tau_\mu\tau_h$	Separated	268.589
283876	671	1080837848	SingleMuon	$\mu\tau_\mu\tau_h$	Separated	308.35
283885	775	1415463399	SingleMuon	$\mu\tau_h\tau_h$	Separated	592.129
283885	1572	2720072340	SingleMuon	$\mu\tau_h\tau_h$	Nearby	808.295
283946	132	90439923	SingleMuon	$\mu\tau_\mu\tau_h$	Separated	342.054
283946	215	236275367	SingleElectron	$e\tau_e\tau_h$	Separated	436.728
283946	222	249201759	SingleElectron	$e\tau_e\tau_h$	Nearby	388.99
283946	610	902012950	SingleElectron	$e\tau_e\tau_h$	Nearby	731.693
284014	220	384899110	SingleMuon	$\mu\tau_e\tau_h$	Nearby	784.245
284043	217	317995734	SingleMuon	$\mu\tau_e\tau_h$	Separated	275.118

Table C.1.: List of all candidate events that pass the full event selection. The event with the highest $\sum p_T$ is marked red.

C.2. Missing E_T triggers

Missing E_T HLT Trigger
HLT_PFMETNoMu90_PFMHTNoMu90_IDTight
HLT_PFMETNoMu110_PFMHTNoMu110_IDTight
HLT_PFMETNoMu120_PFMHTNoMu120_IDTight
HLT_PFMETNoMu90_JetIdCleaned_PFMHTNoMu90_IDTight
HLT_PFMETNoMu120_JetIdCleaned_PFMHTNoMu120_IDTight
HLT_PFMET110_PFMHT110_IDTight
HLT_PFMET120_PFMHT120_IDTight
HLT_PFMET170_NoiseCleaned
HLT_PFMET170_HBHECleaned
HLT_PFMET170_HBHE_BeamHaleCleaned

Table C.2.: List of missing E_T^{miss} triggers used in the analysis.

C.3. Data/MC Control Distributions

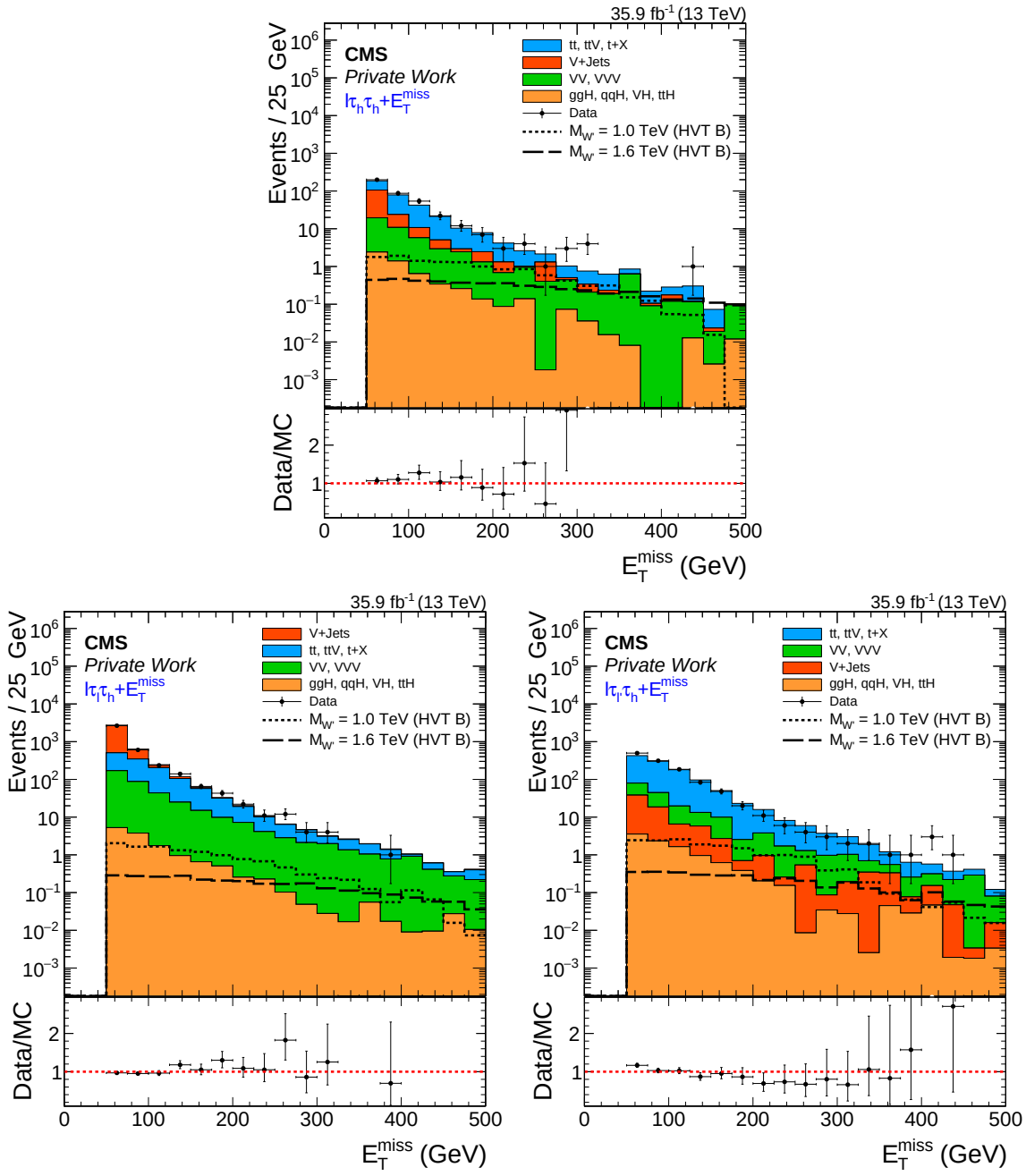

Figure C.1.: Missing transverse energy E_T^{miss} distribution in the hadronic (top), semileptonic same lepton flavour (bottom left) and semileptonic different lepton flavour (bottom right) category.

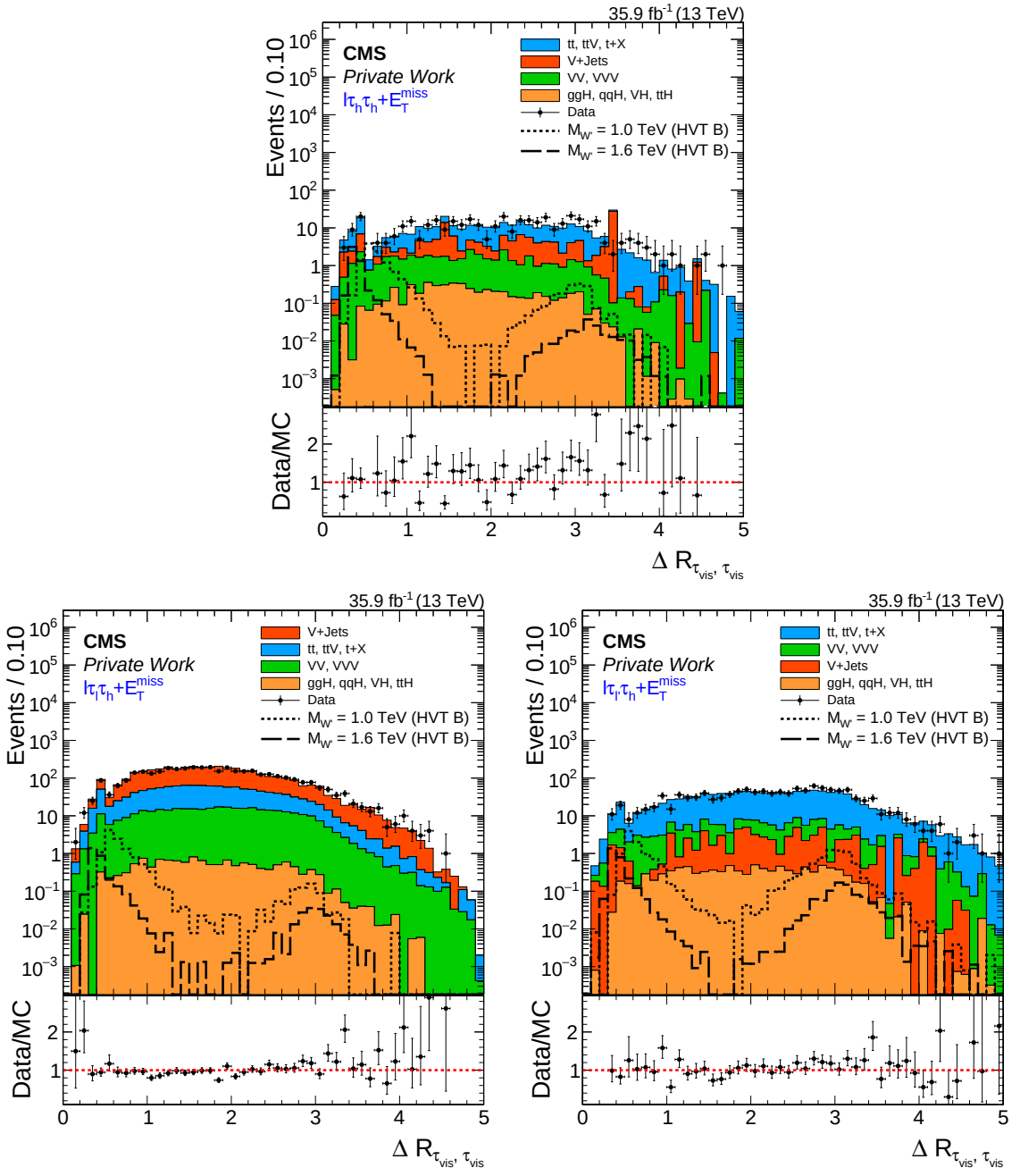

Figure C.2.: $\Delta R(\tau_{vis}, \tau_{vis})$ distribution in the hadronic (top), semileptonic same lepton flavour (bottom left) and semileptonic different lepton flavour (bottom right) category.

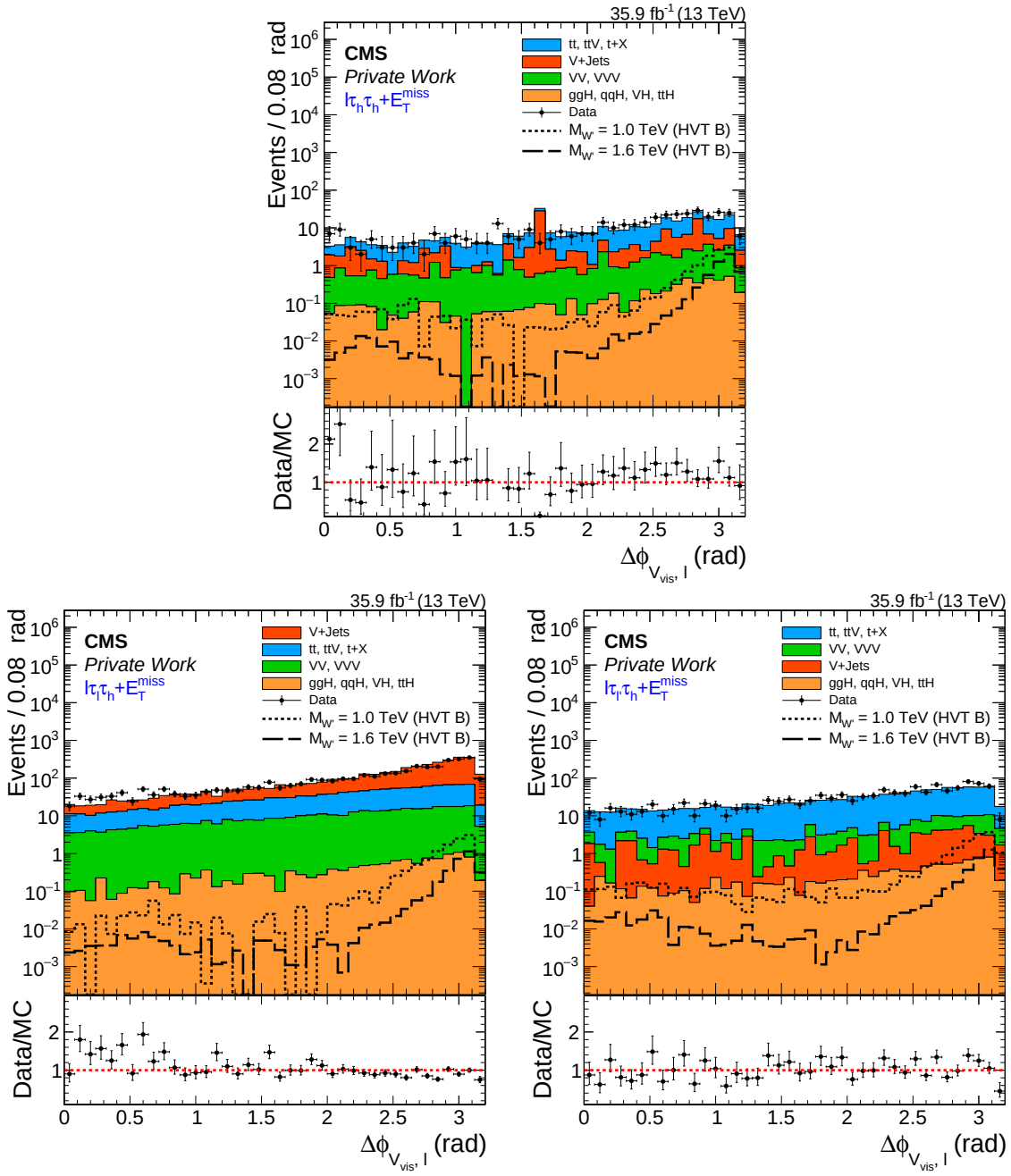

Figure C.3.: $\Delta\phi(V_{vis}, l)$ distribution in the hadronic (top), semileptonic same lepton flavour (bottom left) and semileptonic different lepton flavour (bottom right) category.

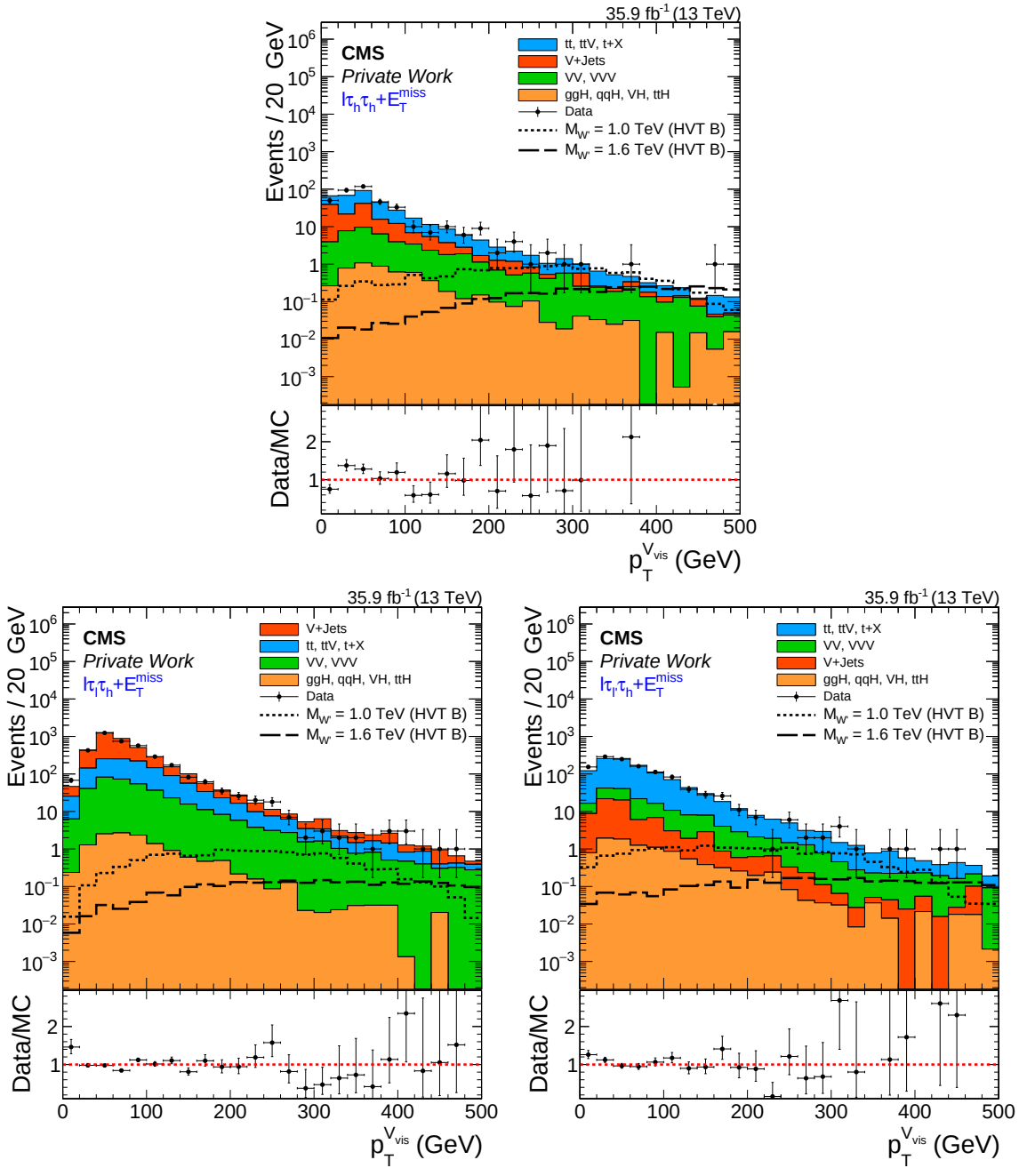

Figure C.4.: Visible boson p_T distribution in the hadronic (top), semileptonic same lepton flavour (bottom left) and semileptonic different lepton flavour (bottom right) category.

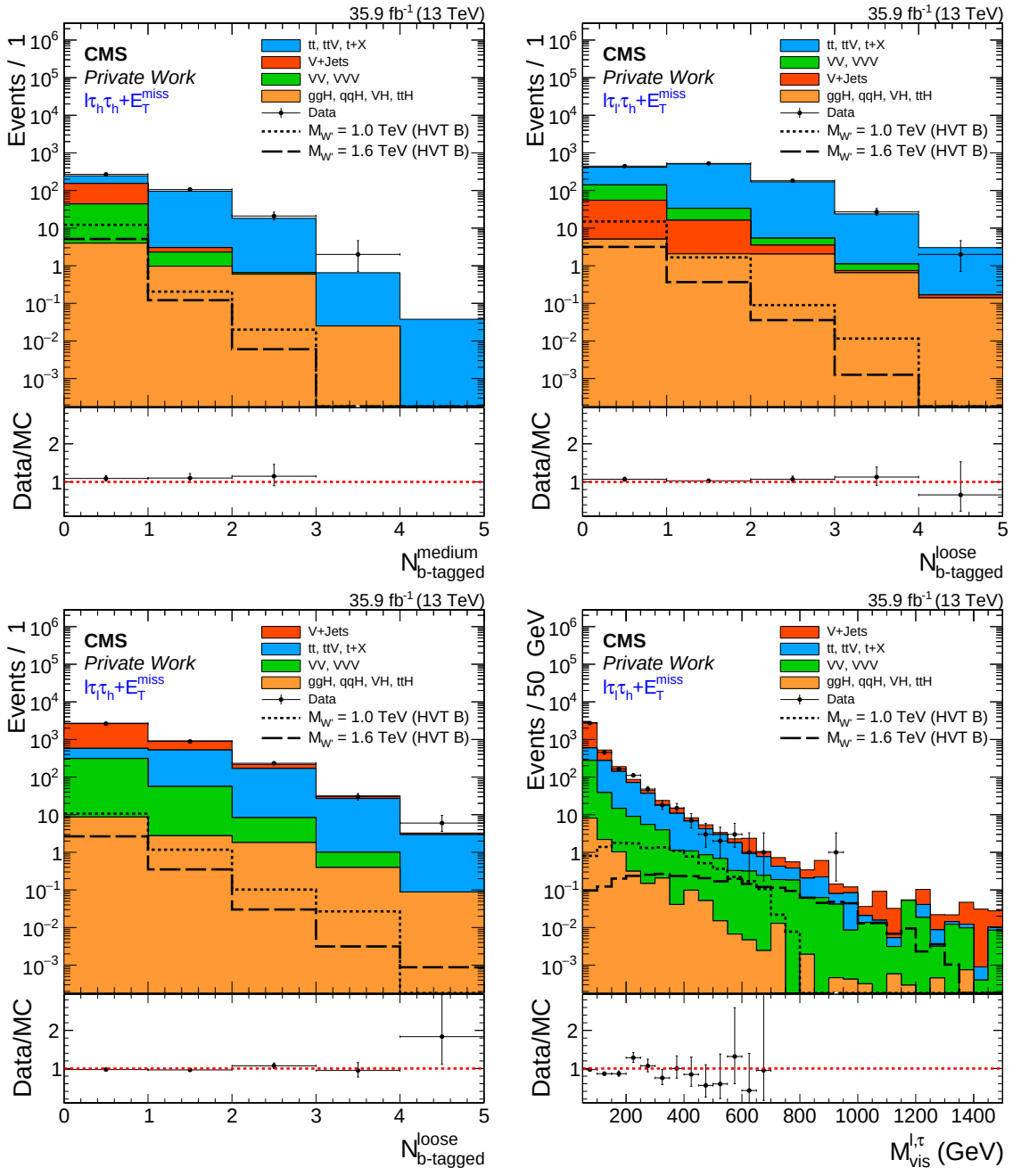

Figure C.5.: Number of b-tagged jets distribution in the hadronic (top left), semileptonic different lepton flavour (top right) and semileptonic same lepton flavour (bottom left) category as well as the visible mass of the two leptons in the semileptonic same lepton flavour channel (bottom right).

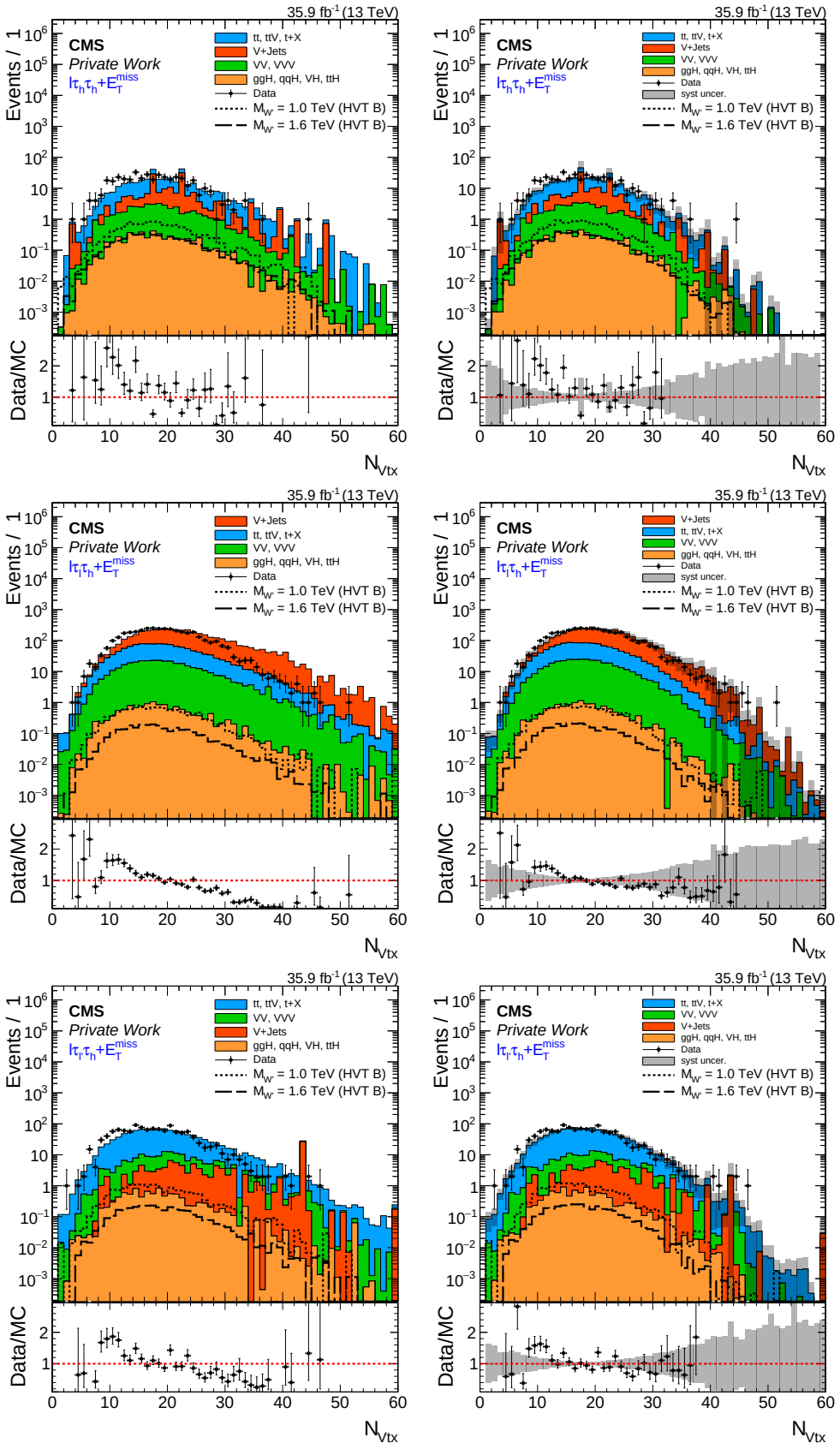

Figure C.6.: Distribution of number of vertices in the hadronic (top), semileptonic same lepton flavour (middle) and semileptonic different lepton flavour (bottom) category before (left) and after (right) pileup reweighting.

C.4. Data Driven Control Distributions

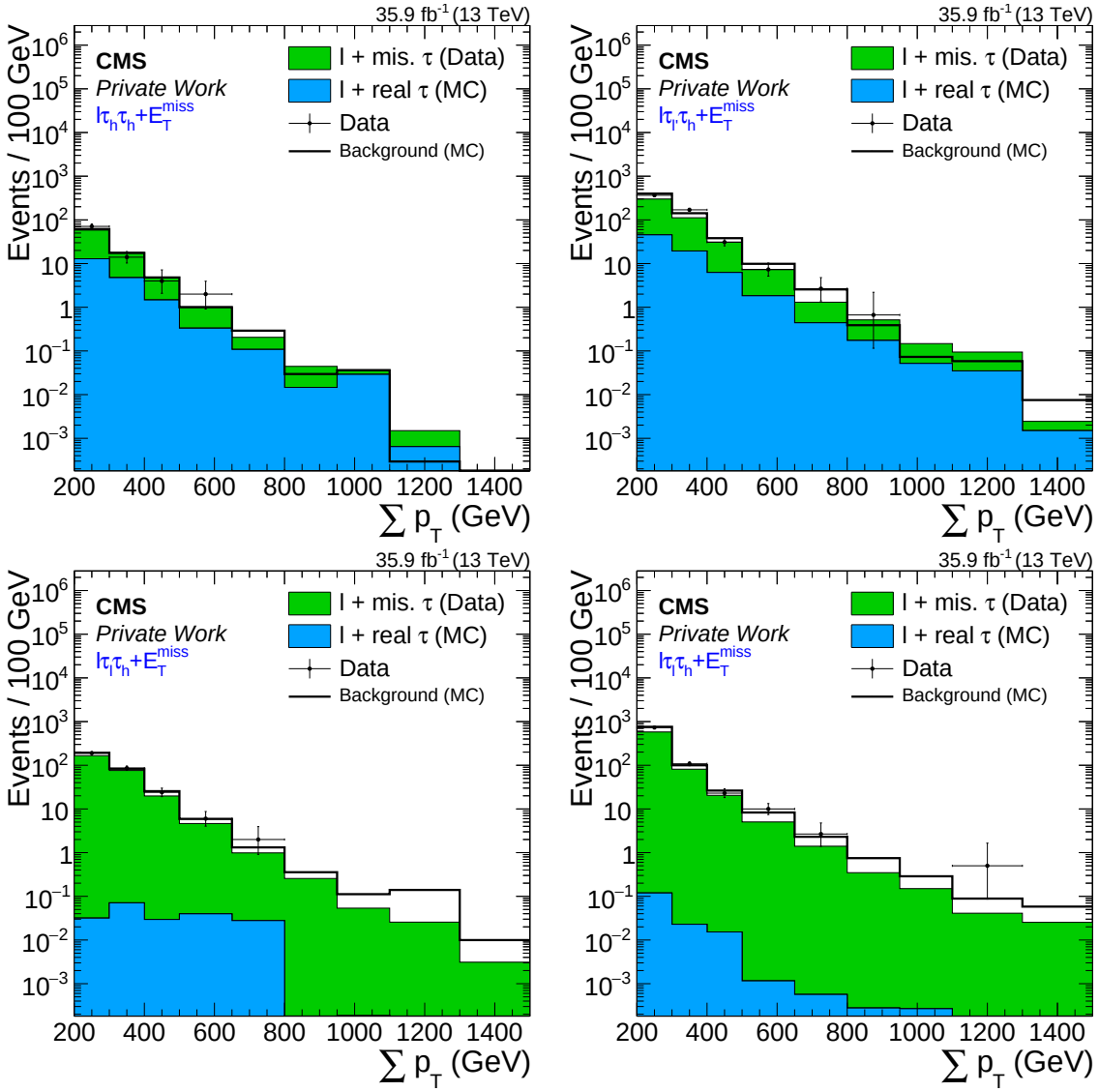

Figure C.7.: Comparison of the data driven estimation with simulation in the $t\bar{t}$ and Z+Jets control region for the hadronic ($t\bar{t}$, top left), semileptonic different lepton flavour ($t\bar{t}$, top right), and semileptonic same lepton flavour ($t\bar{t}$, bottom left and Z+Jets, bottom right) channel.

C.5. Cross Section Limits

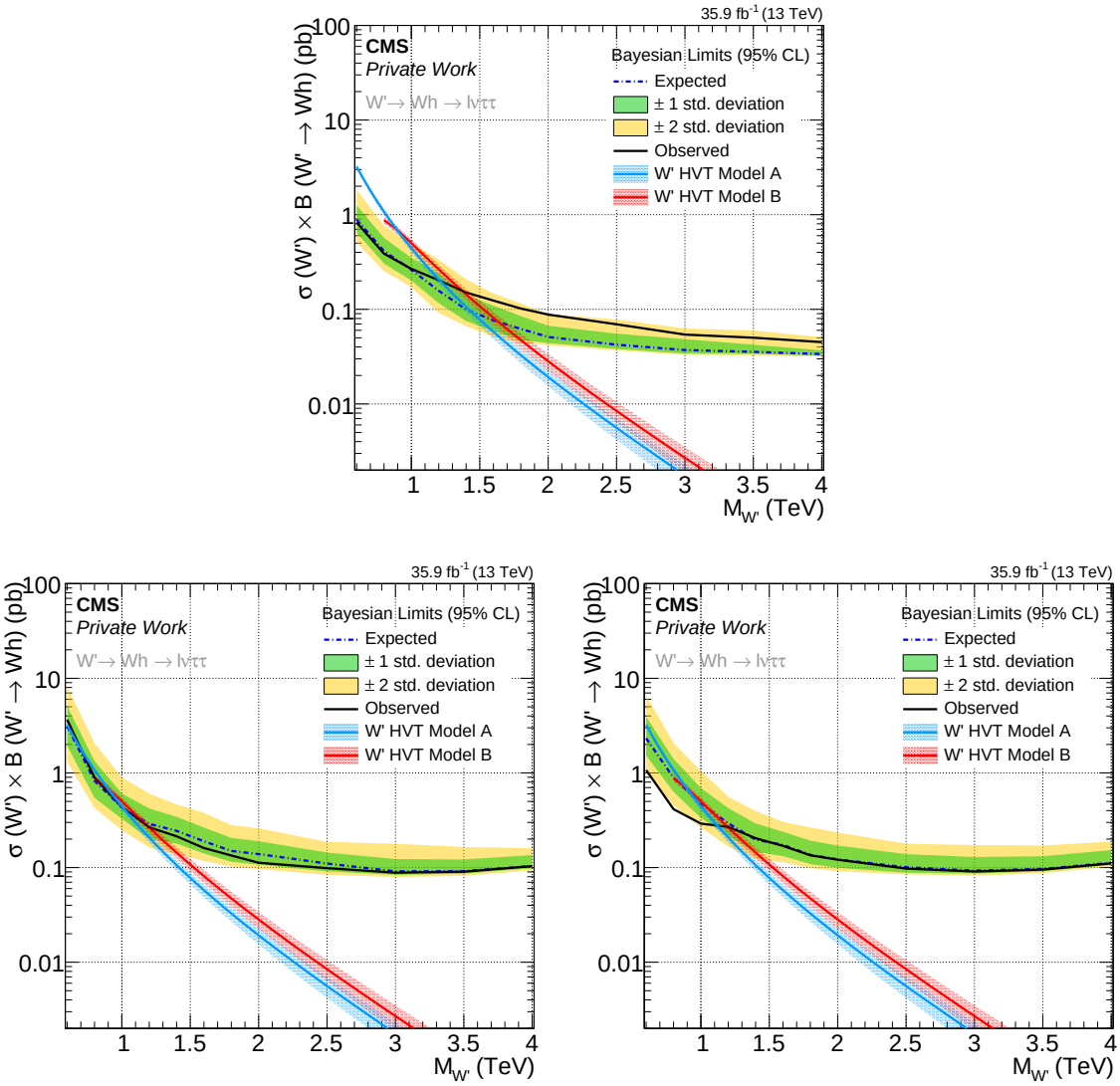

Figure C.8.: Cross section times branching fraction limits for Wh resonances for the hadronic (top), semileptonic same lepton flavour (bottom left), semileptonic different lepton flavour (bottom right) channel as a function of the resonance mass.

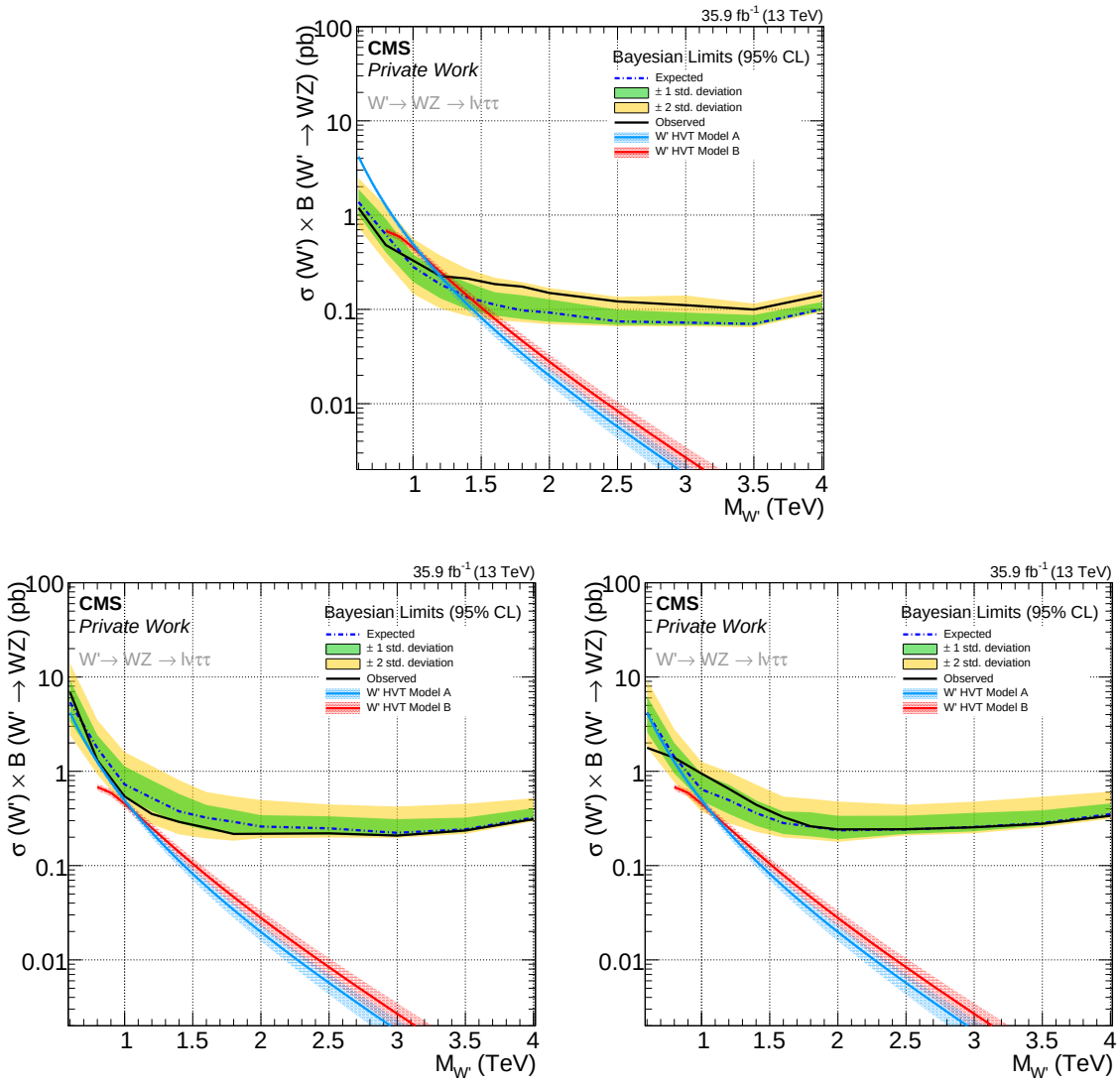

Figure C.9.: Cross section times branching fraction limits for WZ resonances for the hadronic (top), semileptonic same lepton flavour (bottom left), semileptonic different lepton flavour (bottom right) channel as a function of the resonance mass.

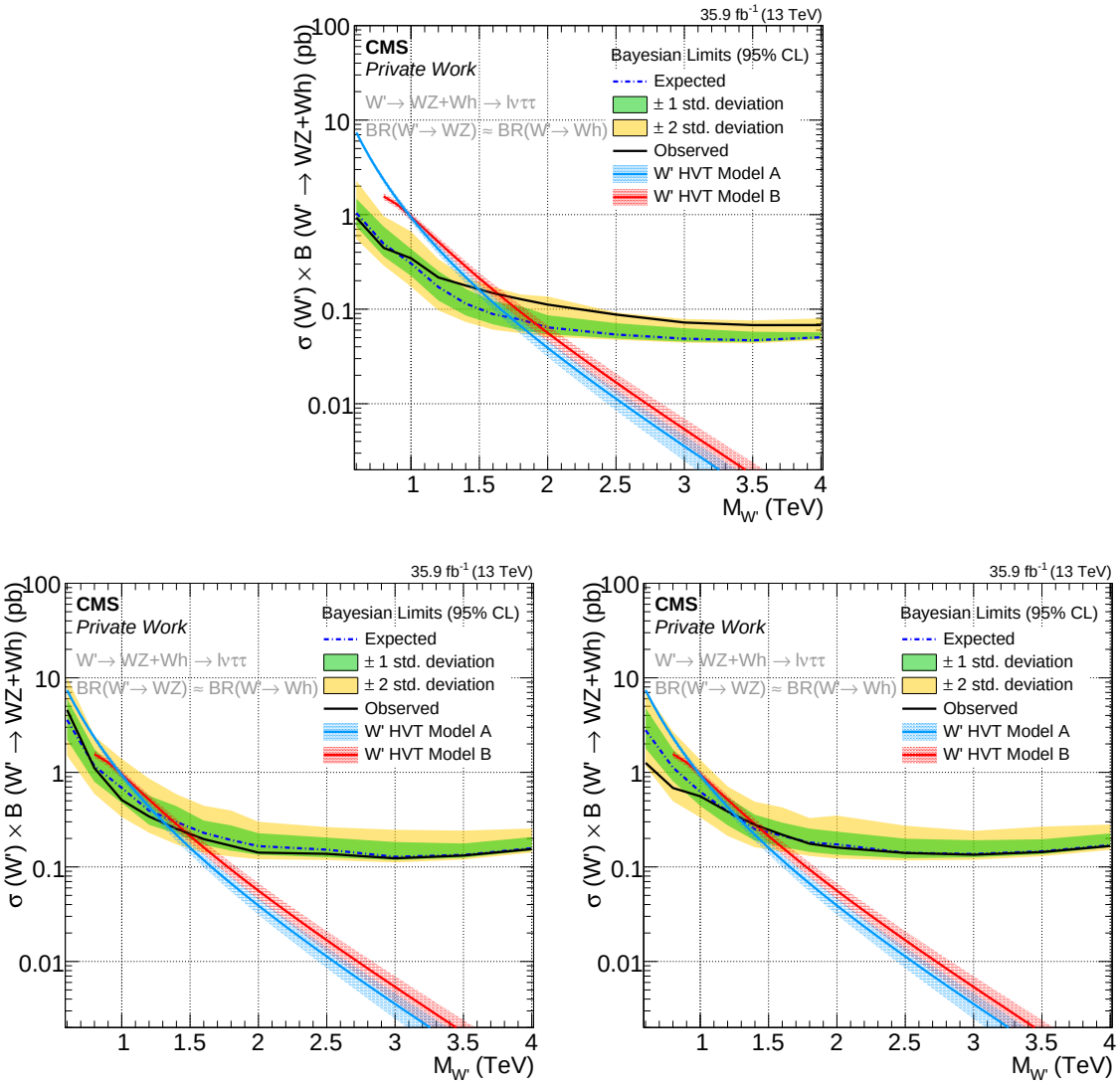

Figure C.10.: Cross section times branching fraction limits for WZ+Wh resonances considering HVT model B for the hadronic (top), semileptonic same lepton flavour (bottom left), semileptonic different lepton flavour (bottom right) channel as a function of the resonance mass.

Bibliography

[1] M. Thomson, "Modern particle physics". Cambridge University Press, New York, 2013.

[2] D. Pappadopulo, A. Thamm, R. Torre et al., "Heavy Vector Triplets: Bridging Theory and Data", *JHEP* **09** (2014) 060, arXiv:1402.4431. doi:10.1007/JHEP09(2014)060.

[3] CMS Collaboration, "The CMS Experiment at the CERN LHC", *JINST* **3** (2008) S08004. doi:10.1088/1748-0221/3/08/S08004.

[4] ATLAS Collaboration, "The ATLAS Experiment at the CERN Large Hadron Collider", *JINST* **3** (2008) S08003. doi:10.1088/1748-0221/3/08/S08003.

[5] CMS Collaboration, "Search for high-mass resonances in final states with a lepton and missing transverse momentum at $\sqrt{s}$ = 13 TeV", *JHEP* **06** (2018) 128, arXiv:1803.11133. doi:10.1007/JHEP06(2018)128.

[6] ATLAS Collaboration, "Search for a new heavy gauge boson resonance decaying into a lepton and missing transverse momentum in 36 fb^{-1} of pp collisions at $\sqrt{s}$ = 13 TeV with the ATLAS experiment", *Eur. Phys. J.* **C78** (2018), no. 5, 401, arXiv:1706.04786. doi:10.1140/epjc/s10052-018-5877-y.

[7] CMS Collaboration, "Search for a W' boson decaying to a τ lepton and a neutrino in proton-proton collisions at $\sqrt{s}$ = 13 TeV", *Submitted to: Phys. Lett.* (2018) arXiv:1807.11421.

[8] ATLAS Collaboration, "Search for High-Mass Resonances Decaying to $\tau\nu$ in pp Collisions at $\sqrt{s}$=13 TeV with the ATLAS Detector", *Phys. Rev. Lett.* **120** (2018), no. 16, 161802, arXiv:1801.06992. doi:10.1103/PhysRevLett.120.161802.

[9] CMS Collaboration, "Search for heavy resonances decaying to a top quark and a bottom quark in the lepton+jets final state in proton-proton collisions at 13TeV", *Phys. Lett.* **B777** (2018) 39–63, arXiv:1708.08539. doi:10.1016/j.physletb.2017.12.006.

[10] CMS Collaboration, "Search for narrow and broad dijet resonances in proton-proton collisions at $\sqrt{s}$ = 13 TeV and constraints on dark matter mediators and other new particles", arXiv:1806.00843.

[11] ATLAS Collaboration, "Search for new phenomena in dijet events using 37 fb^{-1} of pp collision data collected at $\sqrt{s}$ =13 TeV with the ATLAS detector", *Phys. Rev.* **D96** (2017), no. 5, 052004, arXiv:1703.09127. doi:10.1103/PhysRevD.96.052004.

[12] ATLAS Collaboration, "Search for W$'$ $\to$ tb decays in the hadronic final state using pp collisions at $\sqrt{s}$ = 13 TeV with the ATLAS detector", *Phys. Lett.* **B781** (2018) 327–348, arXiv:1801.07893. doi:10.1016/j.physletb.2018.03.036.

[13] ATLAS Collaboration, "Search for vector-boson resonances decaying to a top quark and bottom quark in the lepton plus jets final state in pp collisions at $\sqrt{s}$ = 13 TeV with the ATLAS detector", *Submitted to: Phys. Lett.* (2018) arXiv:1807.10473.

[14] CMS Collaboration, "Search for massive resonances decaying into WW, WZ, ZZ, qW, and qZ with dijet final states at $\sqrt{s}$ = 13 TeV", *Phys. Rev.* **D97** (2018), no. 7, 072006, arXiv:1708.05379. doi:10.1103/PhysRevD.97.072006.

[15] ATLAS Collaboration, "Search for diboson resonances with boson-tagged jets in pp collisions at $\sqrt{s}$ = 13 TeV with the ATLAS detector", *Phys. Lett.* **B777** (2018) 91–113, arXiv:1708.04445. doi:10.1016/j.physletb.2017.12.011.

[16] CMS Collaboration, "Search for a heavy resonance decaying to a pair of vector bosons in the lepton plus merged jet final state at $\sqrt{s}$ = 13 TeV", *JHEP* **05** (2018) 088, arXiv:1802.09407. doi:10.1007/JHEP05(2018)088.

[17] ATLAS Collaboration, "Search for WW/WZ resonance production in $\ell\nu$qq final states in pp collisions at $\sqrt{s}$ = 13 TeV with the ATLAS detector", *JHEP* **03** (2018) 042, arXiv:1710.07235. doi:10.1007/JHEP03(2018)042.

[18] CMS Collaboration, "Search for a new heavy resonance decaying into a Z boson and a Z or W boson in 2ℓ2q final states at $\sqrt{s}$ = 13 TeV", arXiv:1803.10093.

[19] ATLAS Collaboration, "Searches for heavy ZZ and ZW resonances in the $\ell\ell$qq and $\nu\nu$qq final states in pp collisions at $\sqrt{s}$ = 13 TeV with the ATLAS detector", *JHEP* **03** (2018) 009, arXiv:1708.09638. doi:10.1007/JHEP03(2018)009.

[20] ATLAS Collaboration, "Search for resonant WZ production in the fully leptonic final state in proton-proton collisions at $\sqrt{s}$ = 13 TeV with the ATLAS detector", arXiv:1806.01532.

[21] CMS Collaboration, "Search for a heavy resonance decaying into a Z boson and a vector boson in the $\nu\bar{\nu}$q$\bar{\text{q}}$ final state", *JHEP* **07** (2018) 075, arXiv:1803.03838. doi:10.1007/JHEP07(2018)075.

[22] CMS Collaboration, "Search for heavy resonances that decay into a vector boson and a Higgs boson in hadronic final states at $\sqrt{s}$ = 13 TeV", *Eur. Phys. J.* **C77** (2017), no. 9, 636, arXiv:1707.01303. doi:10.1140/epjc/s10052-017-5192-z.

[23] ATLAS Collaboration, "Search for heavy resonances decaying to a W or Z boson and a Higgs boson in the q$\bar{\text{q}}^{(\prime)}b\bar{\text{b}}$ final state in pp collisions at $\sqrt{s}$ = 13 TeV with the ATLAS detector", *Phys. Lett.* **B774** (2017) 494–515, arXiv:1707.06958. doi:10.1016/j.physletb.2017.09.066.

[24] CMS Collaboration, "Search for heavy resonances decaying into a vector boson and a Higgs boson in final states with charged leptons, neutrinos and b quarks at $\sqrt{s}$ = 13 TeV", arXiv:1807.02826.

[25] ATLAS Collaboration, "Search for heavy resonances decaying into a W or Z boson and a Higgs boson in final states with leptons and b-jets in 36 fb^{-1} of $\sqrt{s}$ = 13 TeV pp collisions with the ATLAS detector", *JHEP* **03** (2018) 174, arXiv:1712.06518. doi:10.1007/JHEP03(2018)174.

[26] CMS Collaboration, "Search for heavy resonances decaying into two Higgs bosons or into a Higgs boson and a W or Z boson in proton-proton collisions at 13 TeV", arXiv:1808.01365.

[27] D. Griffiths, "Introduction to Elementary Particles". Physics textbook. Wiley, 2008.

[28] Particle Data Group Collaboration, "Review of Particle Physics", *Chin. Phys.* **C40** (2016), no. 10, 100001. doi:10.1088/1674-1137/40/10/100001.

[29] L. Evans and P. Bryant, "The LHC Machine", *Journal of Instrumentation* **3** (2008), no. 08, S08001.

[30] CMS Collaboration, "Observation of a new boson at a mass of 125 GeV with the CMS experiment at the LHC", *Phys. Lett.* **B716** (2012) 30–61, arXiv:1207.7235. doi:10.1016/j.physletb.2012.08.021.

[31] ATLAS Collaboration, "Observation of a new particle in the search for the Standard Model Higgs boson with the ATLAS detector at the LHC", *Phys. Lett.* **B716** (2012) 1–29, arXiv:1207.7214. doi:10.1016/j.physletb.2012.08.020.

[32] B. Bellazzini, C. Csaki, J. Hubisz et al., "Composite Higgs Sketch", *JHEP* **11** (2012) 003, arXiv:1205.4032. doi:10.1007/JHEP11(2012)003.

[33] R. Contino, D. Marzocca, D. Pappadopulo et al., "On the effect of resonances in composite Higgs phenomenology", *JHEP* **10** (2011) 081, arXiv:1109.1570. doi:10.1007/JHEP10(2011)081.

[34] S. P. Martin, "A Supersymmetry primer", arXiv:hep-ph/9709356. [Adv. Ser. Direct. High Energy Phys.18,1(1998)]. doi:10.1142/9789812839657_0001, 10.1142/9789814307505_0001.

[35] A. Thamm, R. Torre, and A. Wulzer, "Composite Heavy Vector Triplet in the ATLAS Diboson Excess", *Phys. Rev. Lett.* **115** (2015), no. 22, 221802, arXiv:1506.08688. doi:10.1103/PhysRevLett.115.221802.

[36] E. Accomando, A. Belyaev, L. Fedeli et al., "Z' physics with early LHC data", *Phys. Rev.* **D83** (2011) 075012, arXiv:1010.6058. doi:10.1103/PhysRevD.83.075012.

[37] M. Schmaltz and C. Spethmann, "Two simple W′ models for the early LHC", *Journal of High Energy Physics* **2011** (Jul, 2011) 46. doi:10.1007/JHEP07(2011)046.

[38] C. Grojean, E. Salvioni, and R. Torre, "A weakly constrained W' at the early LHC", *JHEP* **07** (2011) 002, arXiv:1103.2761. doi:10.1007/JHEP07(2011)002.

[39] V. Barger, W. Y. Keung, and E. Ma, "Gauge model with light W and Z bosons", *Phys. Rev. D* **22** (Aug, 1980) 727–737. doi:10.1103/PhysRevD.22.727.

[40] G. Altarelli, B. Mele, and M. Ruiz-Altaba, "Searching for New Heavy Vector Bosons in $p\bar{p}$ Colliders", *Z. Phys.* **C45** (1989) 109. [Erratum: Z. Phys.C47,676(1990)]. doi:10.1007/BF01552335, 10.1007/BF01556677.

[41] K. Agashe, R. Contino, and A. Pomarol, "The Minimal composite Higgs model", *Nucl. Phys.* **B719** (2005) 165–187, arXiv:hep-ph/0412089. doi:10.1016/j.nuclphysb.2005.04.035.

[42] M. J. Dugan, H. Georgi, and D. B. Kaplan, "Anatomy of a Composite Higgs Model", *Nucl. Phys.* **B254** (1985) 299–326. doi:10.1016/0550-3213(85)90221-4.

[43] R. Contino, "The Higgs as a Composite Nambu-Goldstone Boson", in *Physics of the large and the small, TASI 09, proceedings of the Theoretical Advanced Study Institute in Elementary Particle Physics, Boulder, Colorado, USA, 1-26 June 2009*, pp. 235–306. 2011. arXiv:1005.4269.

[44] R. Contino, C. Grojean, D. Pappadopulo et al., "Strong Higgs Interactions at a Linear Collider", *JHEP* **02** (2014) 006, arXiv:1309.7038. doi:10.1007/JHEP02(2014)006.

[45] M. Carena, L. Da Rold, and E. Pontón, "Minimal composite Higgs models at the LHC", *Journal of High Energy Physics* **2014** (Jun, 2014) 159. doi:10.1007/JHEP06(2014)159.

[46] F. del Aguila, J. de Blas, and M. Pérez-Victoria, "Electroweak limits on general new vector bosons", *Journal of High Energy Physics* **2010** (Sep, 2010) 33. doi:10.1007/JHEP09(2010)033.

[47] ATLAS Collaboration, "Combination of searches for heavy resonances decaying into bosonic and leptonic final states using 36 fb^{-1} of proton-proton collision data at $\sqrt{s}$ = 13 TeV with the ATLAS detector", arXiv:1808.02380.

[48] LEP Collaboration, "LEP design report". CERN, Geneva, 1984.

[49] F. Marcastel, "CERN's Accelerator Complex. La chaîne des accélérateurs du CERN". https://cds.cern.ch/record/1621583, Oct, 2013. General Photo.

[50] CMS Collaboration, "CMS Luminosity - Public Results, TWiki Website". https://twiki.cern.ch/twiki/bin/view/CMSPublic/LumiPublicResults, 2017.

[51] LHCb Collaboration, "The LHCb Detector at the LHC", *JINST* **3** (2008) S08005. doi:10.1088/1748-0221/3/08/S08005.

[52] ALICE Collaboration, "The ALICE experiment at the CERN LHC", *JINST* **3** (2008) S08002. doi:10.1088/1748-0221/3/08/S08002.

[53] CMS Collaboration, "Detector Drawings". CMS Collection., March, 2012.

[54] CMS Collaboration, "The CMS tracker system project: Technical Design Report", 1997.

[55] CMS Collaboration, "The CMS electromagnetic calorimeter project: Technical Design Report", 1997.

[56] CMS Collaboration, "The CMS hadron calorimeter project: Technical Design Report", 1997.

[57] CMS Collaboration, "Precise Mapping of the Magnetic Field in the CMS Barrel Yoke using Cosmic Rays", *JINST* **5** (2010) T03021, arXiv:0910.5530. doi:10.1088/1748-0221/5/03/T03021.

[58] CMS Collaboration, "The CMS muon project: Technical Design Report". https://cds.cern.ch/record/343814, 1997.

[59] CMS Collaboration, "The performance of the CMS muon detector in proton-proton collisions at sqrt(s) = 7 TeV at the LHC", *JINST* **8** (2013) P11002, arXiv:1306.6905. doi:10.1088/1748-0221/8/11/P11002.

[60] CMS Collaboration, "Performance of the CMS muon detector and muon reconstruction with proton-proton collisions at $\sqrt{s}$ = 13 TeV", *JINST* **13** (2018), no. 06, P06015, arXiv:1804.04528. doi:10.1088/1748-0221/13/06/P06015.

[61] CMS Collaboration Collaboration, C. Battilana, "The CMS muon system status and upgrades for LHC run-2 and performance of muon reconstruction with 13 TeV data", Technical Report CMS-CR-2016-437, CERN, Geneva, Dec, 2016.

[62] CMS Collaboration, "The TriDAS Project: Technical Design Report, The Trigger System". http://cds.cern.ch/record/578006, 2002.

[63] CMS Collaboration Collaboration, S. Ahuja, "Level-1 track trigger for the upgrade of the CMS detector at HL-LHC", Technical Report CMS-CR-2016-462, CERN, Geneva, Dec, 2016.

[64] L. Cadamuro, "The CMS Level-1 trigger system for LHC Run II", *Journal of Instrumentation* **12** (2017), no. 03, C03021.

[65] C. Eck, J. Knobloch, L. Robertson et al., "LHC computing Grid: Technical Design Report. Version 1.06 (20 Jun 2005)". Technical Design Report LCG. CERN, Geneva, 2005.

[66] CMS Collaboration, "CMSSW Application Framework, TWiki Website". https://twiki.cern.ch/twiki/bin/view/CMSPublic/WorkBookCMSSWFramework, Accessed on August 2018.

[67] CMS Collaboration, "Data Formats and Data Tiers, TWiki Website". https://twiki.cern.ch/twiki/bin/view/CMSPublic/WorkBookDataFormats, Accessed on August 2018.

[68] W. Adam, V. Adler, B. Hegner et al., "PAT: the CMS Physics Analysis Toolkit", Technical Report CMS-CR-2009-083, CERN, Geneva, May, 2009.

[69] CMS Collaboration, "Physics Analysis Toolkit (PAT), TWiki Website". https://twiki.cern.ch/twiki/bin/view/CMSPublic/SWGuidePAT, Accessed on August 2018.

[70] III. Physics Institute A, RWTH Aachen University, "Three A Physics Analysis Software (TAPAS), Gitlab Website". https://gitlab.cern.ch/aachen-3a, Accessed on August 2018.

[71] H. P. Bretz, M. Brodski, M. Erdmann et al., "A development environment for visual physics analysis", *Journal of Instrumentation* **7** (2012), no. 08, T08005.

[72] III. Physics Institute A, RWTH Aachen, "The VISPA Project, Website". https://vispa.physik.rwth-aachen.de/, Accessed on August 2018.

[73] "dCache Project, Website". https://www.dcache.org/, Accessed on August 2018.

[74] Rene Brun and Fons Rademakers, "ROOT - An Object Oriented Data Analysis Framework". https://root.cern.ch/, 1996.

[75] CMS Collaboration, "Particle-flow reconstruction and global event description with the CMS detector", *JINST* **12** (2017), no. 10, P10003, arXiv:1706.04965. doi:10.1088/1748-0221/12/10/P10003.

[76] CMS Collaboration, F. Beaudette, "The CMS Particle Flow Algorithm", in *Proceedings, International Conference on Calorimetry for the High Energy Frontier (CHEF 2013): Paris, France, April 22-25, 2013*, pp. 295–304. 2013. arXiv:1401.8155.

[77] CMS Collaboration Collaboration, "Particle-Flow Event Reconstruction in CMS and Performance for Jets, Taus, and MET", Technical Report CMS-PAS-PFT-09-001, CERN, Geneva, Apr, 2009.

[78] CMS Collaboration, "Performance of Electron Reconstruction and Selection with the CMS Detector in Proton-Proton Collisions at $\sqrt{s}$ = 8 TeV", *JINST* **10** (2015), no. 06, P06005, arXiv:1502.02701. doi:10.1088/1748-0221/10/06/P06005.

[79] R. Fruhwirth, "Application of Kalman filtering to track and vertex fitting", *Nucl. Instrum. Meth.* **A262** (1987) 444–450. doi:10.1016/0168-9002(87)90887-4.

[80] W. Adam, R. Frühwirth, A. Strandlie et al., "Reconstruction of Electrons with the Gaussian-Sum Filter in the CMS Tracker at the LHC", 2005.

[81] CMS Collaboration, "Cut Based Electron ID for Run 2, TWiki Website". https://twiki.cern.ch/twiki/bin/view/CMS/CutBasedElectronIdentificationRun2, Accessed on March 2018.

[82] M. Cacciari and G. P. Salam, "Pileup subtraction using jet areas", *Phys. Lett.* **B659** (2008) 119–126, arXiv:0707.1378. doi:10.1016/j.physletb.2007.09.077.

[83] CMS Collaboration, "Performance of CMS muon reconstruction in pp collision events at $\sqrt{s}$ = 7 TeV", *JINST* **7** (2012) P10002, arXiv:1206.4071. doi:10.1088/1748-0221/7/10/P10002.

[84] CMS Collaboration, "Baseline muon selections for Run-II, TWiki Website". https://twiki.cern.ch/twiki/bin/view/CMS/SWGuideMuonIdRun2, Accessed on March 2018.

[85] CMS Collaboration, "Performance of reconstruction and identification of τ leptons decaying to hadrons and ν_τ in pp collisions at $\sqrt{s}$ = 13 TeV", *JINST* **13** (2018), no. 10, P10005, arXiv:1809.02816. doi:10.1088/1748-0221/13/10/P10005.

[86] CMS Collaboration, "Performance of reconstruction and identification of tau leptons in their decays to hadrons and tau neutrino in LHC Run-2", Technical Report CMS-PAS-TAU-16-002, CERN, Geneva, 2016.

[87] CMS Collaboration, "Reconstruction and identification of τ lepton decays to hadrons and ν_τ at CMS", *Journal of Instrumentation* **11** (2016), no. 01, P01019.

[88] K. O. Padeken and T. Hebbeker, "Search for new physics in the tau plus missing energy final states at CMS". https://cds.cern.ch/record/2265826, 2017. Presented 18 Apr 2017.

[89] CMS Collaboration, "TauID for 13 TeV run: recommendation from the Tau POG, TWiki Website". https://twiki.cern.ch/twiki/bin/view/CMS/TauIDRecommendation13TeV, Accessed on March 2018.

[90] CMS Collaboration, "Tau identification in boosted topologies". https://cds.cern.ch/record/2202971, July, 2016.

[91] Christian Veelken, "Tau ID in CMS, Talk at $\tau\tau$ workshop at DESY". https://indico.desy.de/indico/event/9586/contribution/5/material/slides/0.pdf, 2016.

[92] F. Ricci-Tam and M. Chertok, "Search for New Light Higgs Bosons in Boosted Tau Final States with the CMS Experiment". https://cds.cern.ch/record/2137267, March, 2016. Presented 2016.

[93] CMS Collaboration, "Search for Narrow High-Mass Resonances in Proton–Proton Collisions at $\sqrt{s}$ = 8 TeV Decaying to a Z and a Higgs Boson", *Phys. Lett.* **B748** (2015) 255–277, arXiv:1502.04994. doi:10.1016/j.physletb.2015.07.011.

[94] CMS Collaboration Collaboration, "Search for resonant pair production of Higgs bosons decaying to $b\bar{b}$ and $\tau^+\tau^-$ in proton-proton collisions at $\sqrt{s}$ = 8 TeV", Technical Report CMS-PAS-EXO-15-008, CERN, Geneva, 2015.

[95] CMS Collaboration, "A Cambridge-Aachen (C-A) based Jet Algorithm for boosted top-jet tagging", 2009.

[96] CMS Collaboration, "Jet algorithms performance in 13 TeV data", Technical Report CMS-PAS-JME-16-003, CERN, Geneva, 2017.

[97] M. Cacciari, G. P. Salam, and G. Soyez, "The anti-k_t jet clustering algorithm", *JHEP* **04** (2008) 063, arXiv:0802.1189. doi:10.1088/1126-6708/2008/04/063.

[98] CMS Collaboration, "Pileup Removal Algorithms", Technical Report CMS-PAS-JME-14-001, CERN, Geneva, 2014.

[99] CMS Collaboration, "Jet energy scale and resolution in the CMS experiment in pp collisions at 8 TeV", *JINST* **12** (2017), no. 02, P02014, arXiv:1607.03663. doi:10.1088/1748-0221/12/02/P02014.

[100] CMS Collaboration, "Recommended Jet Energy Corrections and Uncertainties For Data and MC, TWiki Website". https://twiki.cern.ch/twiki/bin/view/CMS/JECDataMC, Accessed in March 2018.

[101] CMS Collaboration, "Jet energy scale uncertainty sources, TWiki Website". https://twiki.cern.ch/twiki/bin/view/CMS/JECUncertaintySources, Accessed in March 2018.

[102] CMS Collaboration, "Jet Identification, TWiki Website". https://twiki.cern.ch/twiki/bin/viewauth/CMS/JetID, Accessed in March 2018.

[103] CMS Collaboration, "Identification of b-quark jets with the CMS experiment", *JINST* **8** (2013) P04013, arXiv:1211.4462. doi:10.1088/1748-0221/8/04/P04013.

[104] CMS Collaboration, "Identification of b quark jets at the CMS Experiment in the LHC Run 2", Technical Report CMS-PAS-BTV-15-001, CERN, Geneva, 2016.

[105] CMS Collaboration, "Usage of b/c Tag Objects for 13 TeV Data in 2016 and 80X MC, TWiki Website". https://twiki.cern.ch/twiki/bin/viewauth/CMS/BtagRecommendation80XReReco, Accessed in March 2018.

[106] CMS Collaboration, C. Collaboration, "Performance of missing energy reconstruction in 13 TeV pp collision data using the CMS detector", 2016.

[107] CMS Collaboration, "MET Corrections and Uncertainties for Run-II, TWiki Website". https://twiki.cern.ch/twiki/bin/viewauth/CMS/MissingETRun2Corrections, Accessed in March 2018.

[108] CMS Collaboration, "CMS Luminosity Measurements for the 2016 Data Taking Period", Technical Report CMS-PAS-LUM-17-001, CERN, Geneva, 2017.

[109] T. Sjostrand, S. Mrenna, and P. Z. Skands, "PYTHIA 6.4 Physics and Manual", *JHEP* **05** (2006) 026, arXiv:hep-ph/0603175. doi:10.1088/1126-6708/2006/05/026.

[110] T. Sjostrand, S. Mrenna, and P. Z. Skands, "A Brief Introduction to PYTHIA 8.1", *Comput. Phys. Commun.* **178** (2008) 852–867, arXiv:0710.3820. doi:10.1016/j.cpc.2008.01.036.

[111] J. Alwall, R. Frederix, S. Frixione et al., "The automated computation of tree-level and next-to-leading order differential cross sections, and their matching to parton shower simulations", *JHEP* **07** (2014) 079, arXiv:1405.0301. doi:10.1007/JHEP07(2014)079.

[112] J. Alwall, M. Herquet, F. Maltoni et al., "MadGraph 5 : Going Beyond", *JHEP* **06** (2011) 128, arXiv:1106.0522. doi:10.1007/JHEP06(2011)128.

[113] P. Nason, "A New method for combining NLO QCD with shower Monte Carlo algorithms", *JHEP* **11** (2004) 040, arXiv:hep-ph/0409146. doi:10.1088/1126-6708/2004/11/040.

[114] S. Frixione, P. Nason, and C. Oleari, "Matching NLO QCD computations with Parton Shower simulations: the POWHEG method", *JHEP* **11** (2007) 070, arXiv:0709.2092. doi:10.1088/1126-6708/2007/11/070.

[115] S. Alioli, P. Nason, C. Oleari et al., "A general framework for implementing NLO calculations in shower Monte Carlo programs: the POWHEG BOX", *JHEP* **06** (2010) 043, arXiv:1002.2581. doi:10.1007/JHEP06(2010)043.

[116] CMS Collaboration, "Event generator tunes obtained from underlying event and multiparton scattering measurements", *Eur. Phys. J.* **C76** (2016), no. 3, 155, arXiv:1512.00815. doi:10.1140/epjc/s10052-016-3988-x.

[117] GEANT4 Collaboration, "GEANT4: A Simulation toolkit", *Nucl. Instrum. Meth.* **A506** (2003) 250–303. doi:10.1016/S0168-9002(03)01368-8.

[118] J. Allison et al., "Geant4 developments and applications", *IEEE Trans. Nucl. Sci.* **53** (2006) 270. doi:10.1109/TNS.2006.869826.

[119] CMS Collaboration, "Summary table of samples produced for the 1 Billion campaign, with 25ns bunch-crossing, TWiki Website". https://twiki.cern.ch/twiki/bin/viewauth/CMS/SummaryTable1G25ns, Accessed in 2017.

[120] CMS Collaboration, "Measurement of the WZ production cross section in pp collisions at $\sqrt{(s)}$ = 13 TeV", *Phys. Lett.* **B766** (2017) 268–290, arXiv:1607.06943. doi:10.1016/j.physletb.2017.01.011.

[121] LHC Higgs cross section working group Collaboration, "SM Higgs production cross sections at $\sqrt{s}$ = 13-14 TeV, TWiki Website". https://twiki.cern.ch/twiki/bin/view/LHCPhysics/CERNYellowReportPageAt1314TeV2014, Accessed in 2017.

[122] LHC Higgs cross section working group Collaboration, "SM Higgs Branching Ratios and Partial-Decay Widths, TWiki Website". https://twiki.cern.ch/twiki/bin/view/LHCPhysics/CERNYellowReportPageBR2014, Accessed in 2017.

[123] CMS Collaboration, "Measurement of the ZZ production cross section and $Z \to \ell^+\ell^-\ell'^+\ell'^-$ branching fraction in pp collisions at $\sqrt{s}$=13 TeV", *Phys. Lett.* **B763** (2016) 280–303, arXiv:1607.08834. [Erratum: Phys. Lett.B772,884(2017)]. doi:10.1016/j.physletb.2017.09.030, 10.1016/j.physletb.2016.10.054.

[124] P. Bärnreuther, M. Czakon, and A. Mitov, "Percent Level Precision Physics at the Tevatron: First Genuine NNLO QCD Corrections to $q\bar{q} \to t\bar{t} + X$", *Phys. Rev. Lett.* **109** (2012) 132001, arXiv:1204.5201. doi:10.1103/PhysRevLett.109.132001.

[125] M. Czakon and A. Mitov, "NNLO corrections to top-pair production at hadron colliders: the all-fermionic scattering channels", *JHEP* **12** (2012) 054, arXiv:1207.0236. doi:10.1007/JHEP12(2012)054.

[126] M. Czakon, P. Fiedler, and A. Mitov, "Total Top-Quark Pair-Production Cross Section at Hadron Colliders Through $O(\alpha_S^4)$", *Phys. Rev. Lett.* **110** (2013) 252004, arXiv:1303.6254. doi:10.1103/PhysRevLett.110.252004.

[127] M. Czakon and A. Mitov, "NNLO corrections to top pair production at hadron colliders: the quark-gluon reaction", *JHEP* **01** (2013) 080, arXiv:1210.6832. doi:10.1007/JHEP01(2013)080.

[128] CMS Collaboration, "Standard Model Cross Sections for CMS at 13 TeV, TWiki Website". https://twiki.cern.ch/twiki/bin/viewauth/CMS/StandardModelCrossSectionsat13TeV, Accessed in 2017.

[129] T. Gehrmann, M. Grazzini, S. Kallweit et al., "W^+W^- Production at Hadron Colliders in Next to Next to Leading Order QCD", *Phys. Rev. Lett.* **113** (2014), no. 21, 212001, arXiv:1408.5243. doi:10.1103/PhysRevLett.113.212001.

[130] CMS Collaboration, "MET Filter Recommendations for Run-II". https://twiki.cern.ch/twiki/bin/viewauth/CMS/MissingETOptionalFiltersRun2, 2018.

[131] Laurant Thomas, "2016 Beam Halo Filter Update, CMS Internal Presentation". https://indico.cern.ch/event/518559/contributions/2132815/attachments/1264581/1871184/beamhalostatus.pdf, 2016.

[132] HCAL Noise Working Group, "HCAL Noise and Noise Filters in 2016, CMS Internal Presentation". https://indico.cern.ch/event/534040/contributions/2178680/attachments/1280427/1901837/HCALnoise_JamboreeMeeting_27May2016.pdf, 2016.

[133] Ken Call, Jay Dittmann, Ken Hatakeyama, Hongxuan Liu, Joe Pastika, "EcalDeadCellTriggerPrimitiveFilter & Variations on 2015D data, CMS Internal Presentation". https://indico.cern.ch/event/502965/contributions/2012834/attachments/1240656/1824209/20160309MET.pdf, 2015.

[134] Isabell Melzer-Pellmann on behalf of the MET scanners group, "Report from the MET Scanners, CMS Internal Presentation". https://indico.cern.ch/event/591506/contributions/2387636/attachments/1381281/2099935/2016_12_01_MET_Scanning_Report_PPD.pdf, 2017.

[135] CMS Collaboration, "Utilities for Accessing Pileup Information for Data, TWiki Website". https://twiki.cern.ch/twiki/bin/viewauth/CMS/PileupJSONFileforData#Pileup_JSON_Files_For_Run_II, Accessed in August 2018.

[136] CMS Collaboration, "Electron efficiencies and scale factors, TWiki Website". https://twiki.cern.ch/twiki/bin/view/CMS/EgammaIDRecipesRun2#Electron_efficiencies_and_scale, 2018.

[137] CMS Collaboration, "Electron Scale Factors Run 2, TWiki Website". https://twiki.cern.ch/twiki/bin/view/CMS/ElectronScaleFactorsRun2, 2018.

[138] CMS Collaboration, "Muon Efficiency from Tag-and-Probe for Run 2, TWiki Website". https://twiki.cern.ch/twiki/bin/view/CMS/MuonWorkInProgressAndPagResults, 2018.

[139] CMS Collaboration, "Muon Tag-and-Probe, TWiki Website". https://twiki.cern.ch/twiki/bin/view/CMS/MuonTagAndProbe, 2018.

[140] CMS Collaboration, "Methods to apply b-tagging efficiency scale factors, TWiki Website". https://twiki.cern.ch/twiki/bin/view/CMS/BTagSFMethods, 2018.

[141] CMS Collaboration, "Jet Energy Resolution, TWiki Website". https://twiki.cern.ch/twiki/bin/viewauth/CMS/JetResolution, 2018.

[142] CMS Collaboration, "Energy Calibration and Resolution of the CMS Electromagnetic Calorimeter in pp Collisions at $\sqrt{s}$ = 7 TeV", *JINST* **8** (2013) P09009, arXiv:1306.2016. [JINST8,9009(2013)]. doi:10.1088/1748-0221/8/09/P09009.

[143] CMS Collaboration, "EXO-MUO Documentation for Run2, TWiki Website". https://twiki.cern.ch/twiki/bin/view/CMS/TWikiEXO-MUODocumentationRun2, 2018.

[144] CMS Collaboration, "Search for high-mass resonances in dilepton final states in proton-proton collisions at $\sqrt{s}$ = 13 TeV", *JHEP* **06** (2018) 120, arXiv:1803.06292. doi:10.1007/JHEP06(2018)120.

[145] G. Abbiendi et. al., "Search for High-Mass Resonances Decaying to Muon Pairs in pp Collisions at $\sqrt{s}$ = 13 TeV with the full 2016 data set of 37 fb^{-1} and combination with 2015 result". CMS Note CMS AN-2016/391 (2018).

[146] CMS Collaboration, "Documentation of the RooStats -based statistics tools for Higgs PAG, TWiki Website". https://twiki.cern.ch/twiki/bin/view/CMS/SWGuideHiggsAnalysisCombinedLimit, 2018.

[147] CMS Collaboration, "Higgs Combine Tool Summary Page, Automatic statistical uncertainties". https://cms-hcomb.gitbooks.io/combine/content/part2/bin-wise-stats.html, 2018.

[148] J. S. Conway, "Incorporating Nuisance Parameters in Likelihoods for Multisource Spectra", in *Proceedings, PHYSTAT 2011 Workshop on Statistical Issues Related to Discovery Claims in Search Experiments and Unfolding, CERN,Geneva, Switzerland 17-20 January 2011*, pp. 115–120. 2011. arXiv:1103.0354.

[149] R. Barlow and C. Beeston, "Fitting using finite Monte Carlo samples", *Comput. Phys. Commun.* **77** (Jun, 1993) 219–228. 16 p.

[150] J. Butterworth et al., "PDF4LHC recommendations for LHC Run II", *J. Phys.* **G43** (2016) 023001, arXiv:1510.03865. doi:10.1088/0954-3899/43/2/023001.

[151] CMS Collaboration, "Higgs Combine Tool GitHub Repository". https://github.com/cms-analysis/HiggsAnalysis-CombinedLimit, 2018.

[152] L. Moneta, K. Belasco, K. S. Cranmer et al., "The RooStats Project", in *13th International Workshop on Advanced Computing and Analysis Techniques in Physics Research (ACAT2010).* SISSA, 2010. arXiv:1009.1003. PoS(ACAT2010)057.

[153] The ATLAS Collaboration, The CMS Collaboration, The LHC Higgs Combination Group Collaboration, "Procedure for the LHC Higgs boson search combination in Summer 2011", Technical Report CMS-NOTE-2011-005. ATL-PHYS-PUB-2011-11, CERN, Geneva, Aug, 2011.

[154] CMS Collaboration, "Combine Harvester Introduction, Website". http://cms-analysis.github.io/CombineHarvester/, 2018.

[155] CMS Collaboration, "Combine Harvester GitHub Repository". https://github.com/cms-analysis/CombineHarvester, 2018.

[156] L. Demortier, "P values and nuisance parameters", in *Statistical issues for LHC physics. Proceedings, Workshop, PHYSTAT-LHC, Geneva, Switzerland, June 27-29, 2007*, p. 23. 2008.

[157] G. Cowan, K. Cranmer, E. Gross et al., "Asymptotic formulae for likelihood-based tests of new physics", *Eur. Phys. J.* **C71** (2011) 1554, arXiv:1007.1727. [Erratum: Eur. Phys. J.C73,2501(2013)]. doi:10.1140/epjc/s10052-011-1554-0, 10.1140/epjc/s10052-013-2501-z.

[158] A. Arhrib, R. Benbrik, and S. Moretti, "Bosonic Decays of Charged Higgs Bosons in a 2HDM Type-I", *Eur. Phys. J.* **C77** (2017), no. 9, 621, arXiv:1607.02402. doi:10.1140/epjc/s10052-017-5197-7.

[159] F. Kling, J. M. No, and S. Su, "Anatomy of Exotic Higgs Decays in 2HDM", *JHEP* **09** (2016) 093, arXiv:1604.01406. doi:10.1007/JHEP09(2016)093.

Acknowledgements

In the end, I want to thank everybody who made it possible to write my thesis about this interesting topic. First of all, I want to show my gratitude to Prof. Dr. Thomas Hebbeker for his support and the opportunity to write this dissertation while working at the III. Physics Institute A of the RWTH Aachen University, including the possibility to travel to CERN for six months. In addition, I thank Dr. Oliver Pooth who agreed to serve as a second referee for my thesis.
A special thanks goes to Dr. Kerstin Hoepfner for supporting and advising me and my analysis within the CMS experiment.

I also want to thank everybody else who gave advises for my analysis. In this context, I thank the CMS B2G- and DIB-conveners for their instructions and useful comments to improve this analysis. An additional thank you is addressed to everyone who made/makes the CMS experiment possible, including the people running the LHC. I want to thank everybody who worked at the institute, especially my office colleagues, namely Matthias Endres and Andreas Güth before I went to CERN and Sebastian Thüer, Philipp Millet, and Markus Radziej after I came back to Aachen, for their helpful advises and the good times we had on- and off-work. A special thanks goes to Tobias Pook and Jonas Roemer who were ready to proofread parts of my thesis. In addition, I thank the Aachen computing group who made this complicated and computing time expensive analysis possible.

Finally, a very special thank you goes to my parents who made it possible for me to study physics in Aachen which was the foundation for this thesis. Without their moral support, neither this thesis, nor my general studies of physics would not be possible.